Study of swash motion in an embayed beach based on observations and phase-resolving wave modeling - Case of the Grande Plage of Biarritz

Jonas Pinault

Thèse

Présentée à

L'UNIVERSITÉ DE PAU ET DES PAYS DE L'ADOUR

École doctorale :

Sciences Exactes & leurs applications (ED211)

Par

Jonas PINAULT

Pour l'obtention du grade de

DOCTEUR

Spécialité : Génie civil

Study of swash motion in an embayed beach based on observations and phase-resolving wave modeling Case of the Grande Plage of Biarritz

---

Sous la direction de **Dr. Denis Morichon** et **Dr. Volker Roeber**

Composition du jury :

France Floc'h	MC/HDR	Université de Bretagne Occidentale	Rapporteure
Marion Tissier	Ass. Pr.	TU Delft	Rapporteure
Chris Blenkinsopp	Pr.	University of Bath	Examinateur
Nadia Sénéchal	Pr.	Université de Bordeaux	Examinatrice
Rodrigo Pedreros	Dr.	BRGM	Examinateur
Vicente Gracia Garcia	Pr.	Universitat Politècnica de Catalunya	Examinateur
Matthias Delpey	Dr.	Rivage Pro Tech (SUEZ)	Invité
Denis Morichon	MC/HDR	UPPA	Directeur de thèse
Volker Roeber	Ass. Pr.	UPPA	Co-directeur de thèse

C'était assez dur, et ça a fait mal sur le bonhomme.
- *Hugo Lauras, navigateur.*

Abstract

Study of swash motion in an embayed beach based on observations and phase-resolving wave modeling - Case of the *Grande Plage* of Biarritz

Due to the ever growing anthropogenic pressure at the coast and the perspectives of sea level rise, coastal hazards such as overtoping are more threatening than ever. In this context, accurate estimations of the wave contributions to the total water level (TWL) at the shoreline, namely the run-up, are crucial for coastal engineers and those involved in coastal zone management and engineering design. In this work, we propose to investigate wave run-up in an urbanized embayed beach based on observations and phase-resolving numerical modeling. First, the phase-resolving model based on the Boussinesq equations *BOSZ* is validated against laboratory LiDAR measurements to provide an extensive validation and sensitivity analysis. Then, the model is applied to the real configuration of the *Grande Plage* of Biarritz, a complex urbanized embayed beach. A data-set from a 3-day field campaign carried out in 2018 including pressure measurements and video-derived run-up data is utilized for the model validation. These applications demonstrate that the model reproduces wave transformations and subsequent swash motions reasonably well. The validated model results and observations are then used to investigate the swash motions, under varying conditions of waves and tide. Results show that the tidal level played a key-role in the swash dynamics. At low tide, the conditions were dissipative and the swash was dominated by the infragravity motions. At high tide reflective conditions were observed with a domination of the short-wave frequencies. These changes are explained by the double-slope profile where a low sloping area is found in the intertidal zone and a steep slope on the foreshore. The tidal modulation also influenced the dissipation of infragravity waves, which were found to dissipate energy substantially at low tide through breaking, while at mid and high tide standing wave patterns, characteristic of shoreline reflection, were observed. Under energetic conditions the influence of the tide was minimized as the large waves tended to break on the low sloping portion, regardless of the tide. These results highlight the complexity of the swash behavior in 3D configurations and the potential of phase-resolving models to accurately capture these processes.

Keywords : Coastal processes, run-up, numerical modeling, Boussinesq model, infragravity waves.

Résumé

Étude de la dynamique du jet de rive _dans une plage de poche à partir d'observations et de modélisation numérique à phase-résolue - Cas de la_ Grande Plage _de Biarritz_

Dans le contexte de la montée des eaux associée au réchauffement climatique et d'une pression anthropique dans les zones côtières toujours plus forte, une bonne compréhension et modélisation du niveau d'eau total à la côte sont primordiales pour anticiper au mieux le risque côtier et déployer à temps des solutions efficaces. En particulier, l'action des vagues appelée jet de rive *joue un rôle important le long des côtes exposées aux houles océaniques. Dans cette étude, nous avons étudié la dynamique du* jet de rive *dans une plage de poche urbanisée à forts enjeux car soumise aux aléas submersion. Cette étude s'appuie sur de la modélisation numérique à phase-résolue ainsi que des observations. Dans un premier temps, le modèle numérique est validé sur un jeu de données issu d'une expérience en canal à houle. Ensuite, le modèle est appliqué au cas réel de la Grande Plage de Biarritz, et est comparé à des mesures de pression pour les vagues et à des mesures vidéo-métriques pour le* jet de rive. *Ces applications démontrent les performances du modèle pour estimer le jet de rive, y compris dans un cas réel complexe comme celui de la* Grande Plage. *Ensuite, les résultats du modèle validé et les observations sont utilisés pour analyser les processus physiques observés à la* Grande Plage. *Il a tout d'abord été montré que la marée a un impact significatif sur le* jet de rive. *A marée basse des conditions dissipatives sont observées où le* jet de rive *est dominé par les ondes infragravitaires en raison de la faible pente dans la zone de déferlement (2%). A marée haute, la forte pente présente dans la fin de la zone subtidale et la zone supratidale génère des conditions plutôt réflectives avec une domination des ondes courtes du* jet de rive. *Cette variation du niveau d'eau a aussi pour effet de moduler la dissipation d'énergie associée aux ondes longues. Pour de faibles niveaux d'eau une dissipation de l'énergie de la bande infragravitaire croissante avec la fréquence est observée, suggérant une dissipation des ondes longues par déferlement. Á l'inverse, à marée haute la forte pente a pour effet de ne plus totalement dissiper l'énergie et un régime nodal est mis en place dû à la réflexion des ondes à la côte. Dans des conditions énergétiques, les vagues ont tendance à déferler en partie sur la pente douce qu'importe le niveau d'eau, réduisant la modulation tidale. Ces résultats montrent la complexité du comportement du* jet de rive *dans des configurations tridimensionnelles et le potentiel des modèles à phase-résolue pour capturer ces processus.*

Mots-clés : Processus côtiers, jet de rive, modèle numérique, modèle Boussinesq, vagues infragravitaires.

Remerciements

Tout d'abord, je souhaite remercier **Denis Morichon** et **Volker Roeber** pour l'encadrement de cette thèse. Merci à toi Denis pour m'avoir guidé dans ce doctorat en m'impliquant le plus possible dans les diverses activités (campagnes de mesure, mise en place des webcams...) et pour le temps passé à réécrire les articles et mon manuscrit de thèse. *Volker I'd like to thank you for the help you provided when using the model and the insight you gave me about my work. The knowledge about numerical modeling you gave me will for sure help me in the future.*

J'aimerais remercier **Matthias Depley** de *Rivage Pro Tech* et **Rodrigo Pedreros** du *BRGM* pour avoir pris part à mon comité de thèse et en me donnant des conseils avisés sur la suite de mes travaux. En particulier merci à Matthias pour ton aide tout au long de ce doctorat, notamment sur les travaux portant sur la Grande Plage de la campagne MAREA, mais aussi sur toutes les discussions fructueuses portant sur le modèle *BOSZ* .

J'aimerais remercier le laboratoire *SIAME* de l'UPPA pour m'avoir accueilli pendant cette thèse, et en particulier la chaire *HPC-Waves* portée par Volker Roeber et co-financée par E2S et la Communauté d'Agglomération Pays Basque.

Merci aux équipes techniques qui s'occupent du cluster quotidiennement pour s'assurer que nos simulations puissent tourner sans problème. À ce propos, j'aimerais remercier **Florian Bellafont** pour le temps qu'il m'a consacré à mon arrivée pour m'expliquer comment faire tourner *BOSZ* sur le cluster ! Merci à tous les autres doctorants, **Paul**, **Ximun** et **Fatima-Zarah**, avec qui j'ai passé du temps, malgré les (nombreux) changements de bureau.

I would like to express my deepest gratitude to ***Chris Blenkinsopp*** *and his PhD students at the time* ***Paul Maxime Bayle*** *for providing me data about the GWK experiment. The dataset has been an important part of my work and your availability to answer all my questions quickly has helped me a lot.*

I would like to thank the reviewers, ***France Floc'h*** *and* ***Marion Tissier*** *for agreeing to review my work, and for their constructive comments. I also want to express my gratitude to the entire jury,* ***Chris Blenkinsopp***, ***Nadia Sénéchal***, ***Vincente Gracia Garcia***, ***Rodrigo Pedreros*** *and* ***Matthias Delpey*** *for agreeing to participate to my PhD defense.*

Plus personnellement, j'aimerais remercier mes **parents**, mon **frère** et ma **sœur** pour leur soutien et pour avoir contribué à me vider la tête lors de mes retours en Bretagne. De même, merci à tous mes amis qui m'ont aidé à garder une vie à côté de ce long travail qu'est la thèse. Merci à vous **Lucie**, **Liza**, **Ronan**, **Solal**, **Camille**, **Hugo**, **Mathilde** et **Tristan** ! De même pour mes amis de la côte Nord, merci à **Gaultier**, **Thomas**, **Sacha**, **Max**, **Aëlig**, **Corox**,

Pierre et **Thib** ! Et merci aux Parisiens, même si pour vous mon travail n'a jamais consisté qu'à aller surfer d'après vos dires ... **Matthias**, **Alexis**, **Adri** et **Simon**.

Finalement, j'aimerais remercier plus que tout **Alisée**, qui a su endurer mes nombreux moments de doute et sautes d'humeur. Sans ton soutien inébranlable, je n'aurais probablement pas pu mener à bien ce projet. J'espère être ne serait ce qu'un dixième de ce que tu as été pour moi quand sera venu le moment pour toi de soutenir ta thèse. Merci du fond du cœur.

Contents

List of Figures

List of Tables

List of abbreviations

BOSZ : Boussinesq Ocean and Surf Zone model
BTM : Boussinesq Type Model
BP : Break-point
BW : Bound Wave
CC : Color Contrast
DLT : Direct Linear Transform
EWS : Early Warning System
GCP : Ground Control Point
GPB : Grande Plage de Biarritz
GPS : Global Positioning System
IG : Infra Gravity
LT/MT/HT : Low, Mid and High Tide
NLSW : Non Linear Shallow Water
NRMSE : Normalized Root Mean Square Error
PS : Pressure Sensor
PSD : Power Spectral Density
RMSE : Root Mean Square Error
SW : Short Wave
SWAN : Simulating WAves near Shore
SWASH : Simulating WAves till SHore
TFM : Transfer Function Method
TWL : Total Water Level

List of symbols

Constant

ρ	Volumic mass of water	$1025\ kg.m^{-3}$
g	Gravity acceleration	$9.81\ m.s^{-2}$

Variables

δ_m	Distance between the pressure sensor and the seabed	m
h	Water depth	m
η	Free surface elevation	m
$\tilde{\eta}$	Short wave envelope of η	m
η_{SW}	Free surface elevation of the Short Wave band	m
η_{IG}	Free surface elevation of the Infra Gravity band	m
β_f	Foreshore slope	$-$ or $\%$
f	Frequency	Hz
f_c	Cut-off frequency	Hz
H_s	Significant wave height	m
H_{SW}	Significant wave height of the Short Wave band	m
H_{IG}	Significant wave height of the Infra Gravity band	m
T_p	Peak period	s
η_s	Run-up	m
$\eta_{s_{SW}}$	Swash of the Short Wave band	m
$\eta_{s_{IG}}$	Swash of the Infra Gravity band	m
$\overline{\eta_s}$	Shoreline set-up	m
S	Significant swash height	m
S_{SW}	Significant swash height of the Short Wave band	m
S_{IG}	Significant swash height of the Infra Gravity band	m
$R_{2\%}$	2% run-up exceedence	m
ω	Angular frequency	$rad.s^{-1}$
ϵ	Degree of non-linearity	$-$
μ	Degree of dispersivity	$-$

Chapter 1

Introduction

Contents

1.1 General context

1.1.1 Anthropogenic pressure in coastal areas and climate change

Due to the immediate proximity to the ocean, coastal areas have offered a strategic positioning for marine trade and transport for a very long time. They usually provide abundant resources and valuable services (recreational and cultural activities) making it a preferred settlement locations (Barbier et al., 2011, Neumann et al., 2015, Mehvar et al., 2018). The world population density in these areas is now greater than anywhere else and more over in increase. It is estimated that more than 45% of the world population live on less than 15% of the Earth's land area represented by the coastal zones (Christopher and Robert, 2003) and projected to reach more than 75% in 2035 (IUCN, 2017). Coastal areas are therefore undergoing an all time high anthropogenic and economic pressure (Nicholls and Cazenave, 2010, Barbier et al., 2011, Seto et al., 2011). While the abundance of resources and strategic positioning for trading is not necessarily relevant anymore, coastal zones play still key-role in the economy of entire countries. In Europe, one-third of the gross domestic product is generated within 500 m of the coast and the total value of economic assets was estimated in about 500-1000 billion euros in 2000 (Lombardo et al., 2004).

The coastal zone, being the interface between land and sea, is an extremely complex and dynamic environment affected by numerous processes. These natural processes, including flooding, wave action, coastal erosion and sedimentation threatens human activities and occupations (Davidson-Arnott et al., 2019, Ciavola et al., 2011) and are generally complex to avoid. For instance, all European coastal countries have been affected by coastal erosion over the last decades (Pranzini and Williams, 2013). Mitigation solutions implemented to limit the impact of such coastal hazards are extremely expensive, estimated to average 5400 million euro per year between 1990 and 2020 along European coasts (Lombardo et al., 2004).

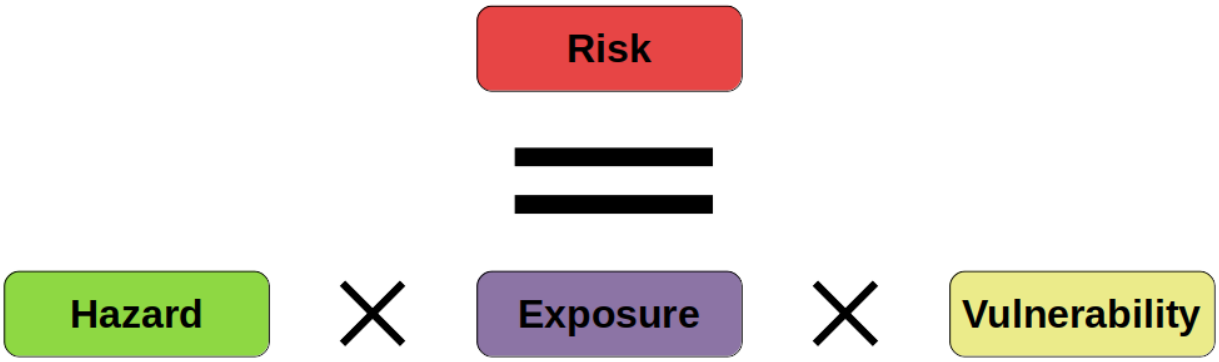

Figure 1.1: The concept of *risk* according to UNGA (2016).

Depending on the intensity of the threat and the stakes, the impacts of coastal hazards can be dramatic and cost thousands of lives while it can go unnoticed. The outcome of such situation, the *risk* is defined in UNGA (2016) as "*the potential loss of life, injury, or destroyed or damaged assets which could occur to a system, society or a community in a specific period*

of time, determined probabilistically as a function of the hazard, exposure, vulnerability and capacity" (see figure 1.1). In this definition, the *hazard* refers to a process that may cause loss of life or property damage for example. Regions exposed to energetic swells are prone to hazards, a situation that will worsen under the effect of climate change. Indeed, the regional sea level is expected to rise (Stocker et al., 2013, Chaigneau et al., 2021), while occurrences and intensities of energetic events such as cyclones are projected to increase (Knutson et al., 2021), inevitably leading to higher coastal risk episodes (Kirezci et al., 2020, Almar et al., 2021, Vitousek et al., 2017). The *exposure* makes reference to the situation of people and infrastructure within the hazard-prone area. The heavy urbanization of coastal zones and the growing anthropogenic pressure drastically increase the level of exposure of these areas.Finally, the *vulnerability* alludes to the various factors increasing the susceptibility to the impacts of the hazard, which here can be associated with the high economic stakes of coastal regions which are generally highly touristic places.

The heavy urbanization and alteration of the shoreline, in combination with the ever increasing anthropogenic pressure and the consequences of climate change will considerably threaten human activities and lives in coastal areas in the near future. Therefore, it appears essential to improve our knowledge of nearshore physical processes to provide tools and solutions to decision makers.

1.1.2 Embayed beaches - A typical feature of the Basque Coast

Rocky coastal zones represent approximately 80% of the world's coast (Trenhaile and Trenhaile, 1987). Within these areas, beaches constrained by rocky headlands are common (Ojeda and Guillén, 2008, Klein et al., 2010, Scott et al., 2011, Castelle and Coco, 2012, Robinet et al., 2020). The presence of lateral boundaries has implications on currents (Castelle and Coco, 2012), cross and longshore sediment transports (Loureiro et al., 2012) and shoreline or dune motion (Robinet et al., 2020). In general, it is recognized that the geological heritage can be a key driver of the hydrodynamics and morphodynamics (Short, 2006, Enjalbert et al., 2011), which differs from open beaches.

These sheltered environments, referred to as embayed beaches, have been originally preferred locations of settlements as they offer a natural protection against climatic and oceanic conditions. Nowadays, embayed beaches are still highly popular for tourism as they provide safe recreational areas due to the sheltering from incident swells and the urbanization offers significant housing capacities, shops and restaurants. The economic values at stakes in these environments are often crucial for the local communities, especially along the Basque Coast, which is the context of this study.

The Basque Coast stretches 150 km (30 km for France and 120 km for Spain) along the Atlantic Ocean. It is widely known as it offers a large variety of landscapes, a strong historical and cultural heritage as well as recreational activities. Historically composed of fishing villages who settled in the different bays sheltered by geological protections (Biarritz, Guéthary, St Jean de Luz, Ciboure...), during the 19th century the Basque Coast rapidly became a popular place

among European Royalty and rich people. The many castles and large houses built by rich owners are a visual testimony of that era and a symbol attracting many visitors. Nowadays, the economy of the Basque Coast mostly relies on tourism as it is a favored holidays destination due to its warm water (up to 24°C in summer), its famous surf spots and the various towns located all along the rocky coast. An example of popular cities along the Basque Coast is given on figure 1.2. The oceanic offshore wave climate ranges from moderately to highly energetic,

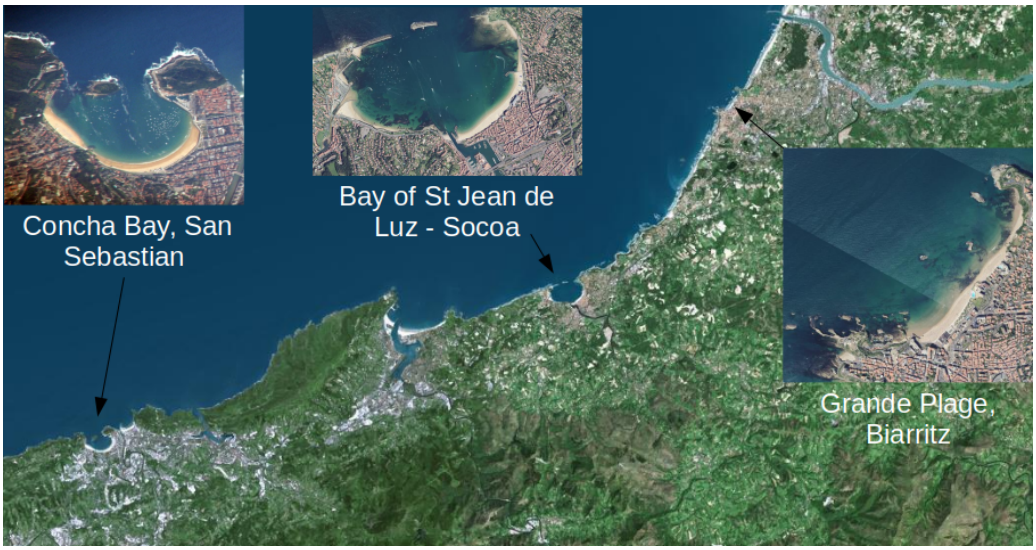

Figure 1.2: Part of the Basque Coast, with highlights on the Concha Bay in San Sebastian (Spain), the bay of Saint Jean de Luz - Socoa (France) and the Grande Plage of Biarritz (France).

with storms, considered as such when H_s and T_p are respectively greater than 3.5 m and 13.8 s, representing 7.24% of the yearly offshore wave climate (Morichon et al., 2018, Abadie et al., 2006). The significant wave height 10-year return period has been statistically computed to $H_s = 6.7m$ with a peak period of $T_p = 18s$ (Morichon et al., 2018). While this context might be favorable for the development of wave energy converter (Lastiri et al., 2020, Delpey et al., 2021), the Basque Coast have faced high levels of coastal floods in the last years (de Santiago et al., 2017, Callens et al., 2020, Arnoux et al., 2021). The consequences of these events can severely damage seafront infrastructures as the coastline presents a succession of embayed beaches of various shapes, densely urbanized and for most of them heavily engineered. An example of an energetic swell hitting the Basque Coast is given on figure 1.3 **(a)** where large waves of several meters are seen slamming the rocks and the wall. The consequences of such energetic events can be disastrous for the neighbouring buildings and infrastructures (**(b)** and **(c)**). For instance the 2014 Hercules storm caused about 700k€ of damages to the city of Biarritz.

Given the high stakes along the urbanized Basque Coast and the perspective of increasing coastal risks due to climate change there is a crucial need for a better understanding of storm impact.

Figure 1.3: Storm impact along the Basque Coast. **(a)** Waves slamming the *Rocher de la Vierge*, © Isabelle Palé, **(b)** waves overtopping the seawall at the Grande Plage of Biarritz during the Hercules storm in 2014 © De Maria, **(c)** damaged sea wall at Anglet after the Justine storm of 2021 © Kty64.

1.1.3 Storm impact assessment

While the estimation of the exposure and vulnerability is of the domain of decision makers, the quantification of the impacts of a storm requires significant knowledge of the various hydrodynamic processes. Asbury H. Sallenger (2000) proposed a scale that describes the different storm impact regimes depending on the limit reached by the total water level. This scale uses the maximum and minimum elevations reached by the waterline, defined as R_{HIGH} and R_{LOW} on figure 1.4 respectively. Even though this scale was initially developed to evaluate storm impact on natural beaches i.e. with a dune system, it works in a similar fashion when the beach is truncated with a vertical wall. Depending on the values of the maximum and minimum waterline elevations, several configurations are found :

- **Swash regime** : $R_{HIGH} < D_{LOW}$
  The swash regime occurs when the upper limit of the waterline is lower than the lower limit of the wall i.e. the waves will run up and down the beach face without any contact with the wall (figure 1.5 **(a)**). This regime is associated with no particular threat in terms of coastal hazard.

- **Collision regime** : $D_{HIGH} > R_{HIGH} > D_{LOW}$

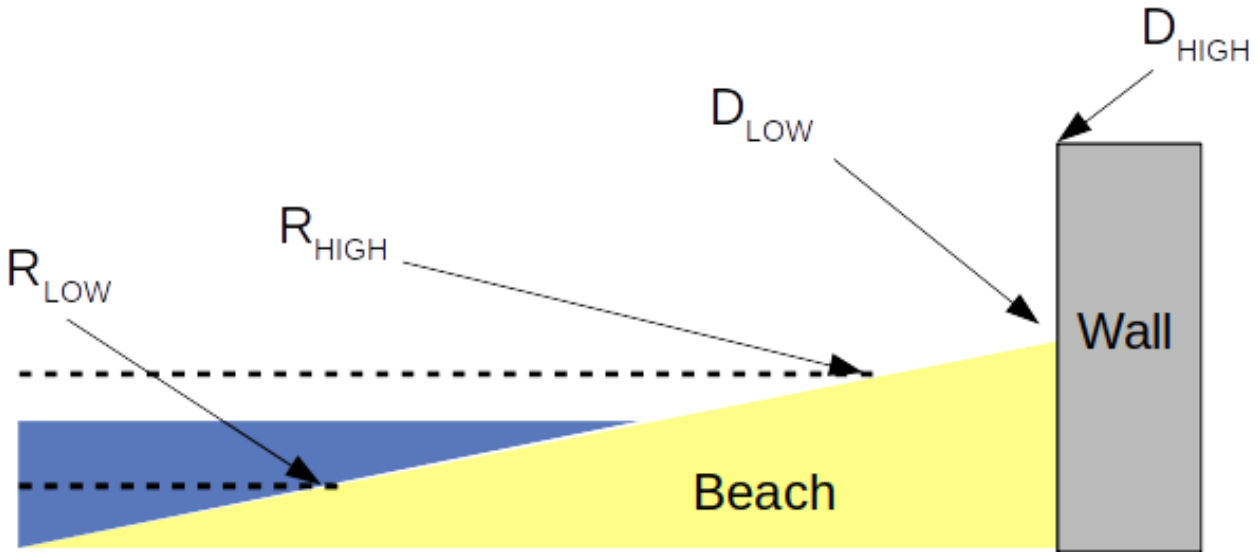

Figure 1.4: Defintion sketch of the variables used for storm impact. Adapted from Asbury H. Sallenger (2000) for the case of engineered beach truncated with vertical wall.

The collision regime is characterized by the waves hitting the wall without overtopping the edge of it (figure 1.5 **(b)**). This regime is associated with limited coastal hazard.

- **Submersion regime** : $R_{HIGH} > D_{HIGH}$
  Under the submersion regime, the waves will run up the beach face slope as well as the wall, resulting in possible damage in the vicinity of the wall and major safety hazards if people are nearby (figure 1.5 **(c)**).

- **Inundation regime** : $R_{LOW} > D_{HIGH}$
  In this case the water continuously flows above the wall, resulting in significant inundation.

Figure 1.5: Different regimes as defined by Asbury H. Sallenger (2000), namely the swash regime **(a)**, the collision regime **(b)** and the submersion regime **(c)**. The black dashed line on image **(c)** indicates the wall location.

The application of the Asbury H. Sallenger (2000) scale is based on the estimation of the total water elevation (TWL) at the coast (R_{HIGH} or R_{LOW}). The TWL is composed of different components, acting at different time and space scales. The TWL is defined as :

$$\text{TWL} = \eta_{tide} + \eta_{su} + \eta_s \tag{1.1}$$

where η_{tide} is the astronomical tide, η_{su} is the storm surge and η_s is the wave run-up (figure 1.6).

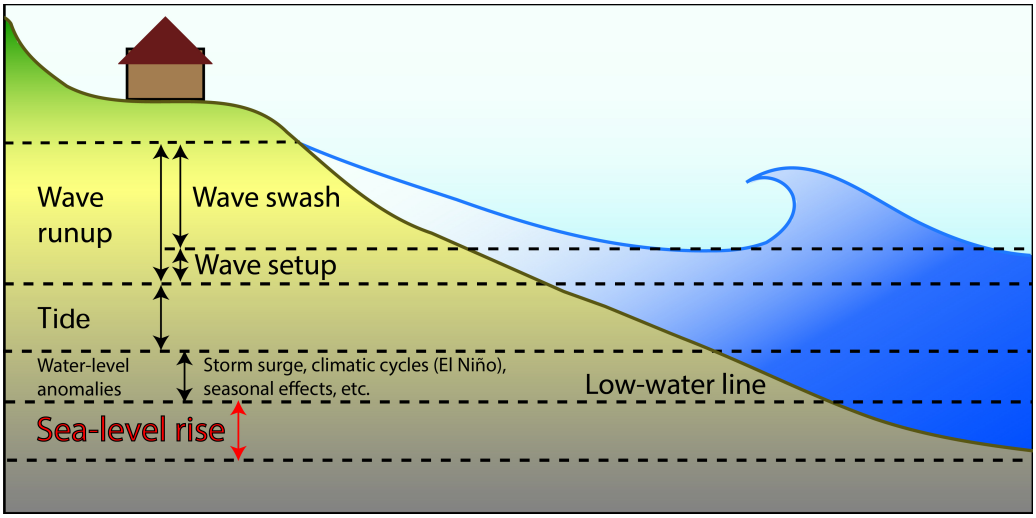

Figure 1.6: Definition sketch of the TWL components, reproduced from Vitousek et al. (2017).

The **astronomical tide** is one the most important components of the TWL (Melet et al., 2018). The tide level oscillates under the effect of the gravitational forces (by the Moon and the Sun) and the rotation of the Earth.

The **storm surge** is the increase of mean water level above the astronomical tidal level due to climatic conditions. Specifically it is the combination of two main processes : the wind and the atmospheric pressure. Under the action of strong wind the still water equilibrium is disturbed and a higher water level is observed at the coast, while lower values in the opposite direction. In a low atmospheric pressure area, such as a cyclone for instance, the water level will rise. Conversely, in areas of high atmospheric pressure the water will be pushed down, lowering the water level. This effect is known as the inverted barometer. As the increase in water level is directly proportional to the difference of pressure, a major storm with a 50 hPa pressure drop would induce locally a 0.5 m water level increase.

The **run-up** η_s corresponds to the vertical oscillations of the waterline on the beach face, under the influence of the waves. The elevation reached by the waterline is an important process when considering extreme water level and associated flooding hazards (Peregrine and Williams, 2001, Hughes et al., 2010, Rodrigues et al., 2012, Serafin and Ruggiero, 2014, Cohn and Ruggiero, 2016, Blenkinsopp et al., 2016). The run-up is usually decomposed into a static component, called the set-up, and a dynamic component called the swash (Holman, 1986) :

$$\eta_s(t) = \overline{\eta_s} + \underbrace{\eta_{s_{SW}}(t) + \eta_{s_{IG}}(t)}_{\text{swash(t)}} \tag{1.2}$$

where $\overline{\eta_s}$ is the shoreline set-up and represents the mean water elevation at the shoreline above the still water level, $\eta_{s_{SW}}$ and $\eta_{s_{IG}}$ are respectively the swash motion associated with the short waves (SW) ($f > 0.05\,H_z$) and the infragravity (IG) ($f < 0.05\,H_z$) frequency bands. The set-up

corresponds to the increase in mean water level above the still water level (in the absence of waves) due to momentum transfer to the water column by breaking waves (Longuet-Higgins and Stewart, 1964). The swash corresponds to the vertical elevation oscillating with the broken waves washing up on the beach face.

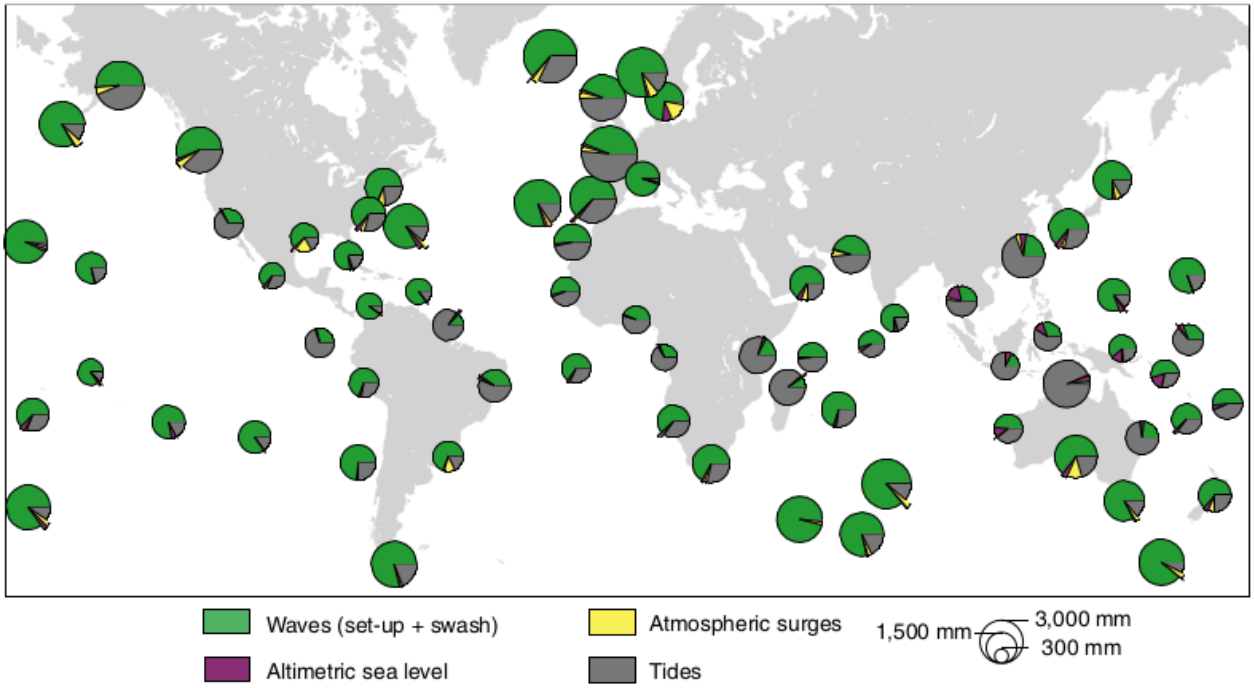

Figure 1.7: Contributions of the different elements to extreme events, reproduced from Melet et al. (2018).

The contributions of the different components of the TWL to extreme events is shown on figure 1.7. The wave run-up (set-up + swash) appears as a driver to extreme TWLs. At a local scale, depending on the wave conditions and the bathymetry configuration the contributions of the set-up and the different swash frequency bands to the run-up vary. A more thorough description of swash zone dynamics is provided in section 1.3. As the ultimate motion of the waves, wave run-up requires to understand all the previous transformations undergone by the waves as they propagate towards the shore.

1.2 Nearshore waves

The nearshore zone is a region of complex coupled processes, combining hydrodynamics, sediment transport and morphodynamics. In the context of our study, waves entering an embayment and propagating up to the shoreline undergo significant interactions with the bathymetry as well as the geology. When propagating over a bathymetry exhibiting strong 3D gradients, changes in wave height, length and direction are observed, ultimately leading to wave breaking close to the shoreline (figure 1.8). These processes govern the nearshore hydrodynamics including wave run-up.

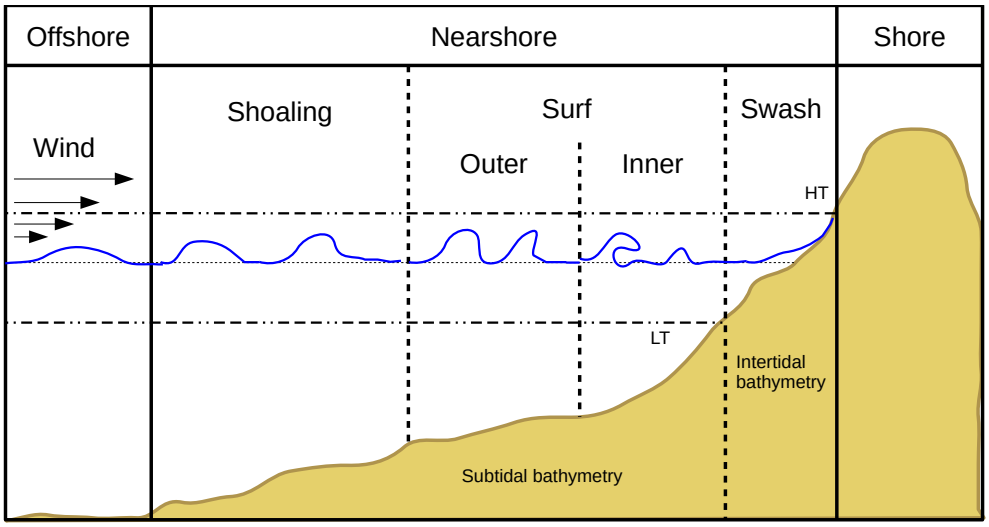

Figure 1.8: Idealised cross-section of a wave-dominated beach system. Wave propagate from the offshore region, where interactions with the bottom are not considered, to the nearshore region.

1.2.1 Short waves

Typical gravity waves, called here *Short Waves* (SW), are water waves with periods ranging from 1 s to 20 s. They originate from the wind blowing over the ocean. When approaching the shoreline, waves entering the nearshore region begin to interact with the bathymetry. When the waves propagate over an irregular bathymetry, the changes in depth modulate the phase celerity, waves in deeper regions going faster and cause the wave crests to bend and align with the isobaths (lines of equal depth). It is the reason why waves appear to approach nearly parallel to the shoreline. An example of wave refraction is given on figure 1.9 panel **(a)**, where the wave crests are seen to bend and align with the shape of the coastline. If obstacles are present, such as rocky headlands (Daly et al., 2014), islands (Kim et al., 2015) or breakwaters (Briggs et al., 1995), the wave energy is redistributed towards the sheltered zone as the energy allows no discontinuity along the wave crests. This phenomenon, called diffraction, is illustrated on figure 1.9 panel **(b)**, where circular wave crests are observed in the sheltered region behind the breakwater.

As the depth decreases, the group celerity decreases causing the wave height to increase as a result of energy flux conservation. In addition, the wavelength decreases causing the steepening of the wave. This process, called the shoaling effect, causes the waves to steepen in the nearshore. An example of wave shoaling is shown on figure 1.9 panel **(c)** where the waves appear steeper closer to the shore. As the depth continues to decrease, excessive steepness causes the waves to break at a location identified as the *surf zone* (see fig. 1.8). Wave breaking is the main dissipation process of wave energy in the nearshore zone. During breaking, the majority of the wave energy is dissipated through viscous effect or air entrapment (Lubin et al., 2006, Iafrati, 2011). An example of a breaking wave is shown on figure 1.9 panel **(c)**. Wave breaking is of great interest in coastal engineering as it drives the hydrodynamics from the surf zone up to the swash zone. For instance, the wave set-up is directly controlled by wave breaking

Figure 1.9: **(a)** Wave refraction around a headland, Scorpion Bay, Mexico. © Jacopo Cosmelli **(b)** Wave diffraction around the tip of a breakwater. Source : Google Earth **(c)** Wave shoaling at the Côte des Basques, Biarritz, France **(d)** Example of a plunging breaker in Brittany. © Tristan Keroullé.

(Longuet-Higgins and Stewart, 1964), as well as longshore and rip currents (Bonneton et al., 2010, Bruneau et al., 2011, Scott et al., 2016), the generation or release of infragravity waves (see section 1.2.2), and swash processes (Guedes et al., 2012).

1.2.2 Infragravity waves

Infragravity waves (IG) are long-period waves, typically between 20 and 200 s, that have not been directly generated by the wind, but by interactions between wind-generated waves. First observations were made by Munk (1949) in the middle of the 20$^{\text{th}}$ century. However, it is only recently that the importance of IG waves on the nearshore dynamics has been recognized (Bertin et al., 2018b, figure 1). The importance of IG waves in various aspects of hydrodynamics, such as rip currents (MacMahan et al., 2004, Greenwood and Brander, 2011), run-up and submersion (Guza et al., 1984, Holman and Sallenger Jr., 1985, Ruessink et al., 1998, Cheriton et al., 2020), sediment transport (de Bakker et al., 2016), dune erosion (Cohn and Ruggiero, 2016) or harbours resonance (Naciri et al., 2004, Thotagamuwage and Pattiaratchi, 2014, Bellafont et al., 2018), has been widely demonstrated justifying the growing attention for these low frequency waves.

In the literature two generation mechanisms are commonly identified : the Bound Wave (BW) and the moving Break-Point (BP) mechanisms. Longuet-Higgins and Stewart (1964) demonstrated that the presence of groups in the incident short-waves generated a wave of similar frequency as the group, called bound wave. In the simple case of the superimposition of two monochromatic waves of slightly different frequencies, wave crests and troughs locally add or cancel each other (figure 1.10). This creates a modulation envelope of the wave height. Furthermore, through non-linear interactions the mean sea level oscillates out of phase with the wave group. Under the assumption of flat bottom, which is the case in Longuet-Higgins and Stewart (1964), the bound wave travels phase-locked with the wave group. Under the action

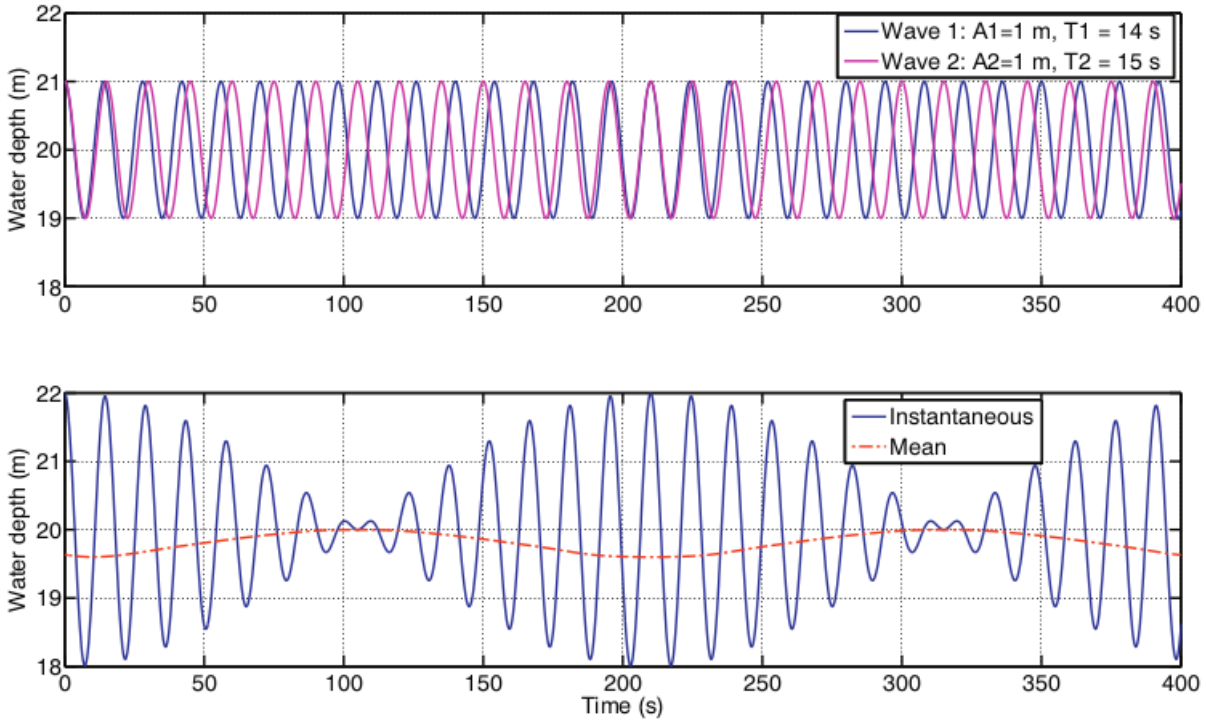

Figure 1.10: Top : Time series of two sinusoidal waves with periods of 14 s (blue) and 15 s (pink) travelling over a flat bottom by 20 m water depth. Bottom : Resulting free surface elevation (blue) and bound wave (red) as computed according to Longuet-Higgins and Stewart (1964). Reproduced from Bertin et al. (2018b).

of the depth-limited short-wave breaking, the envelope no longer exists, and the bound waves are released (List, 1992, Janssen et al., 2003, Inch et al., 2017). The released IG waves now propagate as free waves in the surf zone up to the shoreline.

The second mechanism is based on the consideration that depending on the wave height the depth-induced breaking is initiated at different locations. Under the influence of the short-wave envelope, the breakpoint will oscillate and the associated set-up will oscillate as well, inducing time-varying elevation at the frequency of the wave group i.e. an IG wave. This breakpoint forcing generation mechanism, proposed by Symonds et al. (1982), supposes that IG waves radiate from the breakpoint both shoreward and seaward.

Depending on the conditions, a generation mechanism can be dominating. Consistently with the parametrization from Battjes et al. (2004), a number of studies identified bound IG

waves in low sloping dissipative environments (Janssen et al., 2003, de Bakker et al., 2013, Inch et al., 2017, Poate et al., 2020) while the BP forcing has been highlighted in the presence of high bathymetric gradients, for instance rocky platforms (Poate et al., 2020) or coral reefs (Pomeroy et al., 2012, Van Dongeren et al., 2013).

While it has long been assumed that IG waves fully reflected at the shoreline due to their long wavelengths leading to standing wave structure (Guza and Thornton, 1985), recent studies have highlighted IG wave dissipation near the shoreline based on field (Sheremet et al., 2002, Ruggiero et al., 2004, Senechal et al., 2011, Guedes et al., 2011, 2013, Fiedler et al., 2015, Inch et al., 2017) , laboratory (Battjes et al., 2004, van Dongeren et al., 2007) and numerical (Ruju et al., 2012, de Bakker et al., 2016) data. Two main IG energy dissipation mechanisms are generally adopted : the dissipation through bottom friction and wave breaking. In the first case, it was found that this mechanism is only significant in environments with high friction coefficients such as coral reefs (Pomeroy et al., 2012, Van Dongeren et al., 2013, Péquignet et al., 2014). IG wave breaking is now commonly accepted as the main mechanism on sandy dissipative beaches (Battjes et al., 2004, van Dongeren et al., 2007, de Bakker et al., 2014, Rijnsdorp et al., 2015). As wave breaking is frequency-dependent, the energy dissipation is not constant throughout the IG band and significant reflection can be observed at the shoreline in the lowest frequencies (van Dongeren et al., 2007, Guedes et al., 2013, de Bakker et al., 2014, Inch et al., 2017), possibly resulting in nodal structures characteristic of standing wave patterns (Martins et al., 2017, Bertin et al., 2018a, Matsuba et al., 2021b).

1.3 Swash zone dynamics

The swash zone is characterized as the portion of the beach face that is alternatively covered and uncovered by the waves running up the beach. As a consequence the swash motions are the ultimate result of all the wave transformations up to the shoreline. Run-up on natural beaches is commonly investigated by discriminating the IG and SW bands, as these motions are forced by different processes whose interplay changes depending on beach state. The relation between swash motions, in both frequency bands, and environmental parameters such as wave conditions and beach slope has undergone lots of attention as it provides an understanding of the driving mechanisms of the run-up. Most importantly it allows to derive parametric formulations capable of a rapid run-up estimation based on wave parameters and beach morphology indicators (see section 1.4.1). In this section the contributions of short and long waves and the role of the environmental parameters such as the wave conditions or the beach morphology are described. The parameters contributing to the alongshore variability of the run-up are discussed.

1.3.1 Contribution of short and IG waves

The swash, as mentioned in eq. 1.2, is usually partitioned into SW and IG frequency bands. IG dominated swash motions are commonly observed under dissipative conditions favoured by gently sloping beaches (Ruggiero et al., 2004, Stockdon et al., 2006, Senechal et al., 2018) while

the SW frequency band prevails on steep reflective beaches (Guedes et al., 2012, de Bakker et al., 2016). Typically dissipative / reflective conditions are characterized using the Irribaren number :

$$\xi_0 = \frac{\beta}{\sqrt{H_0/\lambda_0}} \tag{1.3}$$

where H_0 and λ_0 respectively represent the wave height and wavelength in deep water and β the beach slope. Following the Iribarren number, dissipative conditions are generally associated with low values of the Iribarren number ($\xi_0 < 0.3$) (Wright and Short, 1984, Guza and Thornton, 1982, Raubenheimer and Guza, 1996, Ruessink et al., 1998, Ruggiero et al., 2001, Stockdon et al., 2006), whereas reflective conditions are associated with $\xi_0 > 1.25$ and intermediate conditions in between (Holland et al., 1995, Holland and Holman, 1999, Holman, 1986, Holman and Sallenger Jr., 1985, Guedes et al., 2012).

1.3.2 Relation with environmental parameters

Typically, under moderate conditions the run-up is found to increase with the offshore wave height H_0 (Ruessink et al., 1998, Ruggiero et al., 2004) or a combination of the offshore wave height and wavelength such as $\sqrt{H_0 L_0}$ (Stockdon et al., 2006, Vousdoukas et al., 2012). However, under energetic conditions observations showed that the run-up did not increase with increasing offshore wave height, suggesting a *saturation* of the run-up. Huntley et al. (1977) proposed that the swash energy was saturated across the frequency band for which waves are breaking. Since high frequency waves exhibit more breaking than lower frequencies, it implies an energy roll-off from the low to the high frequencies. Numerous studies evaluated energy roll-offs in the SW frequency band proportional to f^{-4} or f^{-3} (Guza and Thornton, 1982, Raubenheimer and Guza, 1996, Ruessink et al., 1998, Holland and Holman, 1999, Ruggiero et al., 2004, Hughes et al., 2013, Guedes et al., 2013). An example of swash spectra corresponding to reflective and dissipative conditions is given on figure 1.11. Under dissipative conditions ($S_{IG}/S_{SW} = 1.95$) the energy decrease extends into the IG band, up to $f = 0.03\,H_z$. Under reflective conditions ($S_{IG}/S_{SW} = 0.38$), a well defined peak in the SW frequency around $f = 0.08\,H_z$ is observed. The saturation has commonly been observed for the SW frequency band (Huntley et al., 1977, Guza and Thornton, 1982, Holman, 1986, Ruggiero et al., 2004, Stockdon et al., 2006, Senechal et al., 2011, Hughes et al., 2013). A number of studies produced evidence that during dissipative conditions the saturation observed in the SW band could extend to the IG band (Ruessink et al., 1998, Ruggiero et al., 2004, Senechal et al., 2011, Guedes et al., 2013), as wave breaking in the low frequencies can be a significant dissipation mechanism (van Dongeren et al., 2007, de Bakker et al., 2014). An example of saturation of the swash in the IG band from Senechal et al. (2011) is shown on figure 1.12. Under extremely energetic conditions ($H_s > 4\,m$) the linear increase of the IG swash stops and a hyperbolic-tangent behaviour is observed. On the other hand, some studies did not observe any saturation in the run-up values even under very energetic conditions (Fiedler et al., 2015), suggesting that more in depth-studies are required to fully understand protosaturation and full run-up saturation.

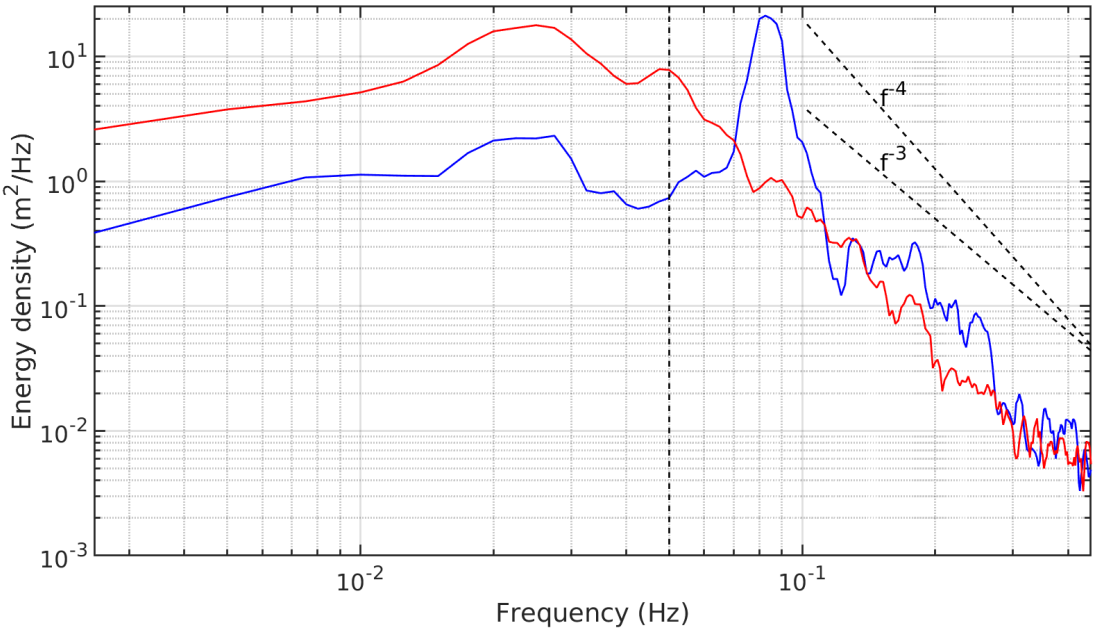

Figure 1.11: Swash energy density spectrum derived from video imagery at the Grande Plage of Biarritz. The blue and red curves respectively represents a the swash spectra under reflective and dissipative conditions. Oblique black dashed line show the f^{-4} and f^{-3} energy roll-off. The vertical black dashed line indicates the separation between IG and SW frequency bands at 0.05 H_z.

Along with the wave conditions the beach morphology over which waves propagate has been found to play a key-role in the swash values. The slope, both in the surf zone and on the foreshore, influences the dissipation of wave energy and consequently the run-up amplitude. Therefore, this dependency is often integrated in the parametric formulations. However, the relation of each component to the slope is still highly discussed. For instance, some studies highlighted the dependency of both S_{SW} and S_{IG} on the foreshore slope (Passarella et al., 2018, Gomes da Silva et al., 2018), while some parametrizations of S_{IG} gave better results without including the slope (Ruessink et al., 1998, Ruggiero et al., 2004, Stockdon et al., 2006, Senechal et al., 2011). In addition, the section of the profile that has the most influence on the run-up is still unclear, especially in the presence of complex morphologies. The foreshore slope is often used in parametrization as the only morphological parameter (Ruggiero et al., 2001, Stockdon et al., 2006). However, it only accounts for a small portion of the profile and excludes the influence of the submerged bathymetry, such as bar systems, which has been shown to have an influence on the run-up Cohn and Ruggiero (2016).

1.3.3 Alongshore variability

While the temporal variability of the run-up amplitude induced by environmental parameters has undergone significant attention, alongshore changes are still poorly understood. Ruggiero et al. (2004) used video measurements of TWL carried out on a dissipative beach under moderate wave conditions to investigate alongshore variability of the run-up. They showed

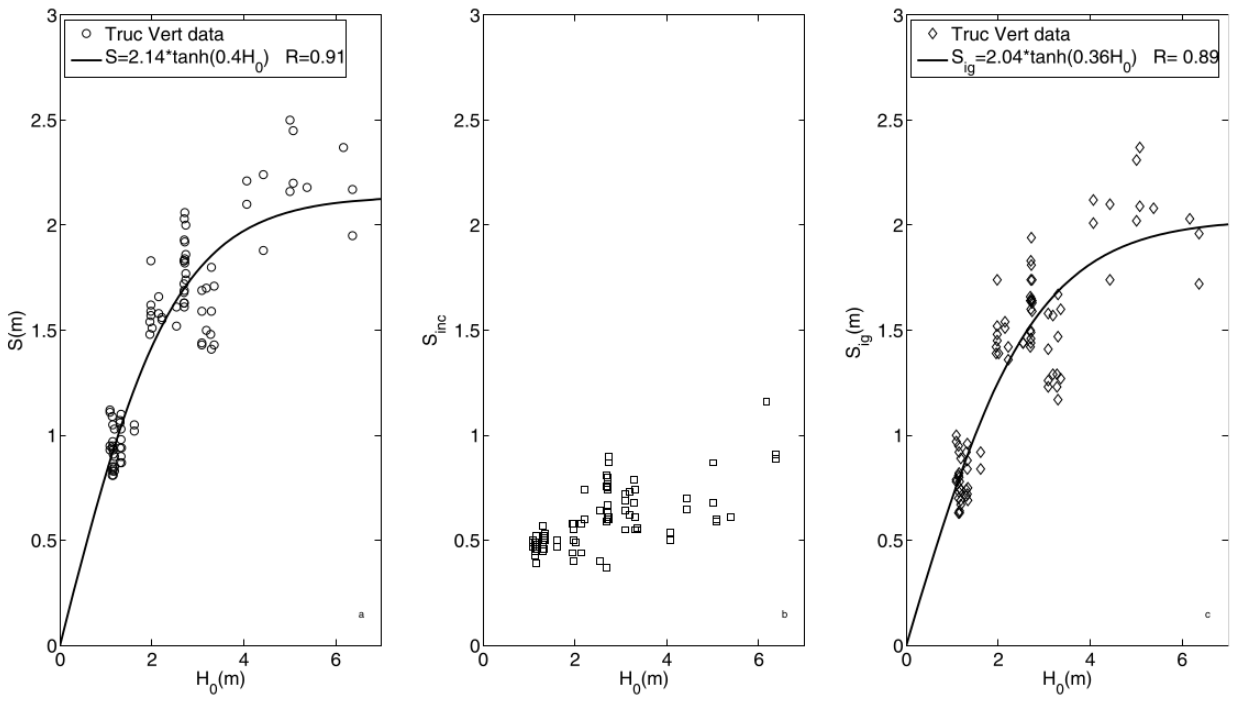

Figure 1.12: Significant swash height S versus offshore wave height H_0. Left S, middle S_{SW} and right S_{IG}. Symbols represent observations, and line is the hyperbolic-tangent fit to observations. Reproduced from (Senechal et al., 2011).

that the highest values of the significant swash height exceeded the lowest values by over a factor of two. This variability was attributed to alongshore differences in the foreshore slope as both swash components (SW and IG) exhibit significant correlation with this parameter. Stockdon et al. (2006) evaluated the longshore variability of the run-up based on video data under intermediate and reflective conditions on the long open beach of Duck (North Carolina, USA). They showed that under moderately energetic wave conditions, the SW swash displayed the highest variability, with a significant correlation with the foreshore slope. Conversely, the IG swash showed a lower variability and no significant correlation with the foreshore slope. Guedes et al. (2012) reported observations of alongshore variability of a factor of 2 under calm conditions on an intermediate pocket beach. Here again, the variability was primarily controlled by the foreshore slope. Nonetheless, the investigation of the wave breaking distribution showed a correlation with the run-up distribution, suggesting a morphological control in the surf zone. More recently, Senechal et al. (2018) investigated the run-up variability under moderate conditions on a natural dissipative open beach. A large variability of a factor 3 was reported for the IG components in similar fashion as previously documented. However, contrary to previous studies, the variability of the foreshore slope alone was not the main control of alongshore distribution of the run-up. Evidence of a control by the inner surf zone morphology was highlighted leading to rapid and localized modifications of the wave field. This result was previously suggested by a numerical study (Nicolae Lerma and Bulteau, 2017), based on the phase-resolving nearshore wave model SWASH (Zijlema et al., 2011) that was carried out on the same site. The SW swash appeared to be sensitive to the local slope, e.g. with higher values

in front of a rip channel. On the other hand, the IG swash component appears to be related to the outer bar system configuration and displays a different alongshore distribution than the SW swash. This numerical study suggests different responses to morphological features depending on the spectral component. The influence of both the underlying bathymetry and the foreshore slope on the run-up has again recently been highlighted in Matsuba et al. (2021a) based on observations and numerical computations.

1.4 Estimation of the swash elevation

1.4.1 Empirical formulae

As a prime indicator for coastal risk assessment, an accurate prediction of the run-up is necessary for coastal engineers and managers. As mentioned in the previous section, empirical formulations have long been used to estimate the run-up, providing a fast and easy tool. These formulations usually relate bulk wave parameters (H_s, T_p), offshore or nearshore, as well as morphological parameters, such as the foreshore slope β_f, to statistical parameters such as $R_{2\%}$ representing the 2% run-up exceedance. Early studies have highlighted that the run-up was related to offshore wave characteristics and beach slope, through the use of the Iribarren number (eq. 1.3) (Hunt, 1961, Guza and Thornton, 1982, Guza et al., 1984, Holman, 1986, Holman and Sallenger Jr., 1985). Holman and Sallenger Jr. (1985) proposed to differentiate the behavior of the run-up components i.e. $\overline{\eta_s}$, S_{SW} and S_{IG}. This approach allows to consider differently the SW and IG components in order to account for the different dependence of S_{SW} and S_{IG} to the offshore wave height or the beach slope. Table 1.1 gives examples of existing formulations. An extensive review of the existing parametric formulations has been compiled by Gomes da Silva et al. (2020).

Table 1.1: Parametric formulations based on field data. Wave conditions are sorted in to moderate ($H_s < 3\,m$) and energetic ($H_s > 3\,m$). Beach slope are differentiated into low and high sloping, with a threshold between the two for $\beta = 0.05$.R_s : significant run-up height. H_0, L_0 : offshore wave height and wave length. β_{SZ} : surf-zone slope. β_f : Foreshore slope.

Reference	Equations	Conditions
Guza and Thornton (1982)	$R_s(cm) = 3.48(cm) + 0.71\overline{H_0}(cm)$	Moderate, low sloping
Holman and Sallenger Jr. (1985)	$S_{SW}/H_0 = -0.19 + 0.69\xi_0$ $S_{IG}/H_0 = 0.09 + 0.53\xi_0$ $\overline{\eta}/H_0 = 0.14(0.06) + 0.35(0.46)\xi_0$ high tide (mid tide)	Moderate to energetic high sloping
Ruggiero et al. (2001)	$S_{IG} = 0.27(\beta_s H_0 L_0)^{0.5}$	Moderate to energetic, low sloping
Raubenheimer et al. (2001)	$\overline{\eta}/H_0 = 0.019 + 0.003(\overline{\beta_{SZ}})^{-1}$	Moderate, low sloping
Ruggiero et al. (2004)	$R_s/H_0 = 0.27 + 1.04\xi_0$	Moderate to energetic, low sloping
Stockdon et al. (2006)	$\overline{\eta} = 0.35\beta_f\sqrt{H_0 L_0}$ $S_{IG} = 0.06\sqrt{H_0 L_0}$ $S_{SW} = 0.75\beta_f\sqrt{H_0 L_0}$	Moderate low to high sloping
Senechal et al. (2011)	$S = 2.14\tanh 0.4H_0$ $S_{IG} = 2.04\tanh 0.36H_0$	Energetic, high sloping
Vousdoukas et al. (2012)	$R_{2\%} = 0.53\beta_f\sqrt{H_0 L_0} + 0.58\sqrt{H_0^3/L_0} + 0.45$	Moderate, high sloping
Didier et al. (2020)	$R_{2\%} = 0.117\sqrt{H_0 L_0}$	Moderate to energetic, high sloping

While the rapidity and simplicity of these formulations make it an attractive tool for coastal risk assessment, the performances of such formulations strongly rely on the fact that the study site and the conditions are within the range of applicability of the formulations. Typically, the performances of these formulations are disputable under energetic conditions (Stockdon et al., 2014, Nicolae Lerma et al., 2017), due to the complexity of instrumenting a beach under extreme conditions. Atkinson et al. (2017) compared 11 existing run-up models again field data under moderate wave conditions, on a variety of beaches. The best models exhibited a mean NRMSE on the run-up of 25%. However, for a better match with a specific site, a calibration of the formulation is possible (Vousdoukas et al., 2012, Da Silva et al., 2017). While it greatly improves the performances of the model, it requires instrumenting the site to retrieve data, which can be costly and even impossible in some beach configurations.

Moreover, even though the majority of wave transformations take place in the surf zone, many parametrizations use the average foreshore slope (Ruggiero et al., 2001, Stockdon et al., 2006, Senechal et al., 2011) as the only morphological parameter which might not be the best indicator (Stockdon et al., 2006, Vousdoukas et al., 2012, Gomes da Silva et al., 2020). For instance, the presence of sand waves, bar systems, rip channels can strongly influence wave transformations along a cross-shore profile. The inclusion of bathymetric effect in a parametrization has been achieved in some studies through the use of the wave height at breaking, called breaker height H_b (Senechal et al., 2018, Blenkinsopp et al., 2016). However, collecting such measurements remains challenging in many sites.

Overall, parametric formulations are now widely used to estimate run-up due to their simplicity of implementation and reliability in most cases. However, they face some serious flaws when conditions are extreme or in complex beach configurations such as embayed beaches.

1.4.2 Process-based numerical models

As an alternative to parametric formulations, process-based numerical models now offer a promising capabilities to estimate wave run-up for various wave and beach conditions, notably thanks to major developments of computing capacities. Wave models are generally sorted into three main categories : spectral models, phase-resolving depth-integrated models and phase- and depth-resolving models also called Navier-Stokes solvers. Spectral models do not actually model the free surface deformation associated with waves and consequent run-up on the beach. Conversely, Navier-Stokes solvers such as *RANS* models resolve the all processes, including air entrapment and turbulence, but at a prohibitive computational cost.

Phase-resolving and depth-integrated models offer a promising alternative. This type of approach allows to account for the main processes of nearshore wave transformations while requiring an acceptable computational time. Similarly to the Navier-Stokes solvers, these models compute the evolution of the free surface elevation in space and time. Furthermore, processes such as refraction, diffraction, IG waves or current generation are intrinsically represented. The major difference with the depth-resolving models is that the equations are averaged along the vertical direction i.e. the free surface and horizontal velocity are only solved in a 2D plan.

This allows to drastically reduce the computation cost of the equations while solving relevant nearshore hydrodynamic processes. An example of a nearshore wave field computed for the Grande Plage of Biarritz with a phase-resolving wave model is shown in figure 1.13 . The relevant nearshore processes such as wave shoaling, refraction and diffraction can be observed as well as the dissipation of energy due to wave breaking.

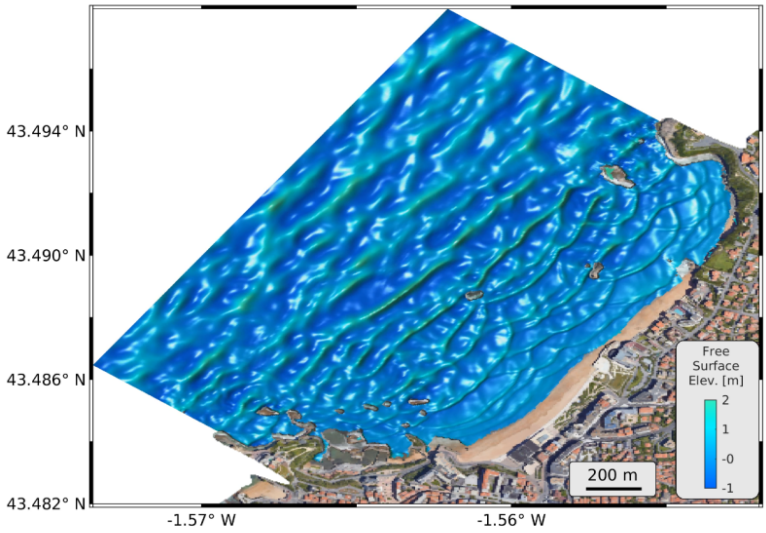

Figure 1.13: Instantaneous free surface elevation computed by the phase-resolving model *BOSZ* used in this study at the site of Grande Plage.

The description of nearshore waves transformations from deep to shallow water requires to account for both non-linear and dispersive effects. Non-linear shallow water (NLSW) models, which assume hydrostatic pressure, are restricted to non-dispersive waves, i.e. long waves such as tsunami or tidal bore, or shallow water applications e.g. at a 2 m depth (Raubenheimer and Guza, 1996), which is often located already within the surf zone. In order to capture nearshore wave transformations numerical models need to include some dispersion degree. Two types of models can be used to account for wave dispersion, Boussinesq-type models (BTM) and non-hydrostatic NLSW models. The difference between these two types of models is that the Boussinesq equations include the vertical variation of pressure in the momentum equation while a non-hydrostatic pressure correction is implemented in the hydrostatic NLSW models. While these models slightly differ in terms of equations or set-up, they are in the end very similar as they solve the same processes under similar assumptions. The main limitation of depth-averaged models is that they do not allow the overturning of waves seen in depth-induced wave breaking. Consequently, the corresponding energy dissipation is externally implemented (a more complete description is given in section 3.2). In addition the undertow current, causing sediment transport, requires a detailed description of the velocity profile along the water column which is not possible with depth-averaged models (Elsayed et al., 2022).

Dispersive phase-resolving models have widely been applied to nearshore wave studies. However, their application to run-up studies is relatively new and still requires comparison with observations for validation. Some of these studies were performed under laboratory conditions,

which offer the advantage of being under completely controlled conditions and therefore allows an extensive validation. Ruju et al. (2014) replicated a GLOBEX laboratory experiment (Ruessink et al., 2013a) with the widely used SWASH model (Zijlema et al., 2011) to investigate the swash response to variable conditions. The model was found to capture irregular wave run-up with relative errors between 1% and 11% depending on the conditions and proved to be able to reproduce the energy transfers that govern the surf and swash zones. More recently, the capacity of the SWASH model to accurately capture wave transformations run-up were demonstrated again on reef profiles at laboratory scales (Peláez-Zapata et al., 2018, Liu et al., 2021). Similarly, the fully nonlinear and dispersive Boussinesq-type model FUNWAVE-TVD (Shi et al., 2012) was utilized to replicate irregular waves propagating over a laboratory scale fringing reef (Liu et al., 2020). Comparisons showed that the model was fit to capture rapid wave transformations occurring on steep faces of reefs, including the run-up.

Recently, depth-integrated models have been applied to investigate swash motions under real conditions on various field sites. For instance, the SWASH model was applied in 1D mode on an urbanized field site (Fiedler et al., 2018) and in 2D mode on a natural open sandy beach (Nicolae Lerma et al., 2017) to compute storm-induced run-up. The studies demonstrated modeled run-up errors of 12 and 10% respectively. Valentini et al. (2019) used the same model but under lowly energetic conditions to reproduce wave run-up in a large embayed beach, yielding run-up errors of the order of 10%. These studies highlight the potential of phase-resoling models to capture wave run-up under real conditions.

The importance of including both short and long waves components was investigated using the non-hydrostatic (NH) and surfbeat (SB) versions of XBeach. Under laboratory conditions the two XBeach versions were found to perform similarly for fringing reefs environments (Lashley et al., 2018). This result can be explained by the dominance of IG motions at the shoreline. Conversely, under field conditions along a reef-lined coast Quataert et al. (2020) found that the NH version was better at capturing run-up, testifying of the importance of modeling both short and long waves. This result was also observed on an intermediate-reflective sandy beach (de Beer et al., 2021). For the NH version, comparisons with video-derived swash data indicated an error of about 14% on $R_{2\%}$.

1.5 Aims and objectives

Under the perspective of climate change and the growing anthropogenic pressure, the increase of extreme sea level events appears inevitable and therefore a deep understanding of run-up processes is needed. Along the Basque coast, the highly urbanized and rugged coastline exposed to energetic swell makes it a specific site with complex hydrodynamic processes coupled to high stakes. For that reason the local authorities are very involved in the shoreline management process and coastal related studies. The *HPC Waves* Chair (High Performance Computing), led by Volker Roeber since its launch in 2019, is part of this synergy and is dedicated to the study of coastal risks and their numerical simulation. The chair is co-funded by

the E2S program, the Region Nouvelle Aquitaine and the Communauté Agglomération Pays Basque. The aim of the chair is to improve accuracy and speed of numerical models, to obtain an accurate and complete description of coastal processes for problematic such as the impact on structure, marine renewable energies, submersion and development of operational forecasting tool at the beach scale. In this context, the overall objectives of this thesis are to provide an effective tool to estimate wave run-up under realistic conditions and to investigate swash motions in a geologically constrained embayed beach. More specifically, the work is organized around two main questions :

1. **Is a phase-resolving nearshore wave model capable of accurately modeling wave induced run-up ?** While the use of depth-integrated phase-resolving models is becoming increasingly popular for coastal applications owing to major improvement of computational capacities, the application of such models to compute the run-up is still rather new. The application of these models would enable extensive investigations of swash zone processes. However, their capacities to capture the run-up need to be assessed. In addition, the sensitivity of the numerical results to the model set-up is of great interest to be able to apply a model to a specific location without the need for prior measurements for validation.

2. **What is the behavior of the swash in a geologically constrained meso-tidal environment ?**
   Hydrodynamics and swash zone processes in complex environments such as embayed beaches exhibiting strong bathymetric gradients and geological features are far from being predictable. Insights about the driving mechanisms in these configurations are thus required to improve run-up estimations and offer reliable tools to decision-makers regarding the submersion hazard.

1.6 Outline of the thesis

To answer the previously stated questions, this work is articulated as follows :

In chapter 2, the methodological aspect of this work is detailed. It includes a presentation of the GPB an urbanized embayed beach that constitutes our study site. Then, we present the conditions and the settings of the field campaign that was carried in 2018 on this site to measure waves transformation and total water level along the beach. The technique used to derive run-up data from the video-monitoring station is also presented. Finally, the different methods that can be performed to reconstruct the free surface elevation from pressure measurements are discussed.

In chapter 3, we assess the ability of *BOSZ* (Roeber et al., 2010), a depth-integrated phase-resolving model, to simulate nearshore wave processes and run-up. The model is first validated for relevant nearshore processes such as diffraction, refraction and shoaling on academic benchmarks (Whalin, 1971, Berkhoff et al., 1982) using monochromatic waves. Then,

the 1D laboratory experiment of Blenkinsopp et al. (2019, 2021) is replicated to assess the performances of the model to estimate wave run-up of irregular waves. A sensitivity analysis is carried out to evaluate parameters that need further attention when modeling wave run-up. This part has been published under Pinault et al. (2020) in the *Journal of Marine Science and Engineering*.

In chapter 4, the model is applied to a real case, at the site of the *Grande Plage* of Biarritz. After a validation based on pressure measurements and video-derived run-up data, the driving mechanisms of the hydrodynamics and wave run-up at the GPB are studied based on numerical computations and observations. Different wave scenarios (H_s and T_p) as well as tide levels are used to evaluate the site behavior under various conditions. This work is currently under review in the journal *Estuarine, Coastal and Shelf Science*. Then, the cross-shore evolution of infragravity waves is analyzed. In particular the dissipation of IG energy near the shoreline is investigated to better understand the swash response to wave forcings.

Finally, in **the chapter 5** we conclude this thesis by summarizing the output of this work, associated with both the methodological aspect of the phase-resolving numerical modeling and the physical analysis of the swash motions in an embayed beach. The perspectives arising from this work are also discussed.

Chapter 2

Study site - Nearshore waves and swash zone monitoring techniques

Contents

2.1 Introduction

In this chapter, first we introduce the field site (section 2.2) of the *Grande Plage* of Biarritz and the field campaign (section 2.3) that took place during winter of 2017/2018. In section 2.4, we then briefly present the advantages and drawbacks of intrusive and non-intrusive techniques that can be deployed in field conditions to measure swash characteristics. The video monitoring station used in this study is then detailed in section 2.5 as it offers the best compromise between a large spatial coverage and a high enough resolution in order to capture the water level evolution at high frequency along our study site. In section 2.6, the procedure to extract the swash line from *timestack* images is detailed, along with the spectral methods used to analyze the swash motions. The second part of the chapter (section 2.7) is dedicated to the determination of the free surface in the surf zone based on pressure sensor measurements. We discuss the different methods that can be used to perform free surface reconstruction from pressure sensor measurements and then present the procedure used to perform spectral analysis of nearshore waves measurements.

2.2 Study site

In this section, the characteristics of the study site of the *Grande Plage* of Biarritz are presented. This site was chosen as it is highly exposed to energetic swells and urbanized, which makes it vulnerable to coastal hazards such as submersion (see figure 1.3 panel **(b)**).

2.2.1 Context

The Grande Plage of Biarritz (GPB) is one of the main attraction of the touristic city of Biarritz. It is also famous for its seafront casino and the *Hotel du Palais* on the northern side of GPB, a historical hotel built during the Napolean III era (see figure 2.1, panel **(b)**), and recreational activities such as surfing.

The GPB has always been exposed to the impact of storms with varying degrees of damage (see figure 2.1 panel **(c)** and **(d)**). In 2014 the energetic wave conditions during the Hercules storm in combination with high tidal coefficients caused significant damage (Abadie et al., 2018) for a cost of 700k€. In recent years, public authorities have tried to limit the impact of flooding events by installing temporary protection measures. These include beach scraping, which consists of pushing sand against the seawall toward the lower portion of the beach, and the placement of sandbags (figure 2.1 panel **(c)**). These counter-measures have the advantage of being temporary and relatively easy to be set up. However, they might not be sufficient under some extreme conditions as damages to neighbouring buildings have been observed during recent storms. Moreover, there is evidence that the intensity of the impact of storms can vary along the GPB; implying that the design of an optimal protection solution could vary according to the exposure of the different beach sections to the incoming wave action.

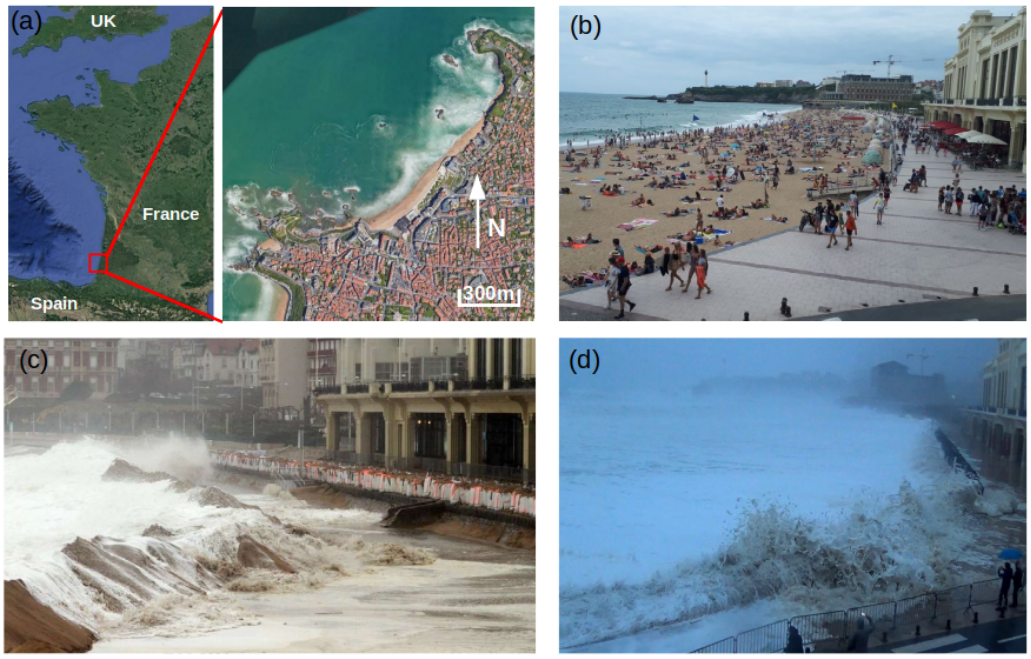

Figure 2.1: Location and situation of the study site Grande Plage of Biarritz. (a) Location of the GPB. (b) : crowded beach in front of the Casino during a calm day. The Hotel du Palais is seen in the background (Credit : Radio France - Céline Arnal). (c) : Sand piles and big bags set-up to mitigate the storm impact (February 2016). Waves are seen overwashing the dunes (Credit : Bertrand Lapègue / Sud Ouest). (d) : Submersion event during the Ciara storm in February 2020, water is seen overtopping the wall (Credit : SurfingBiarritz).

2.2.2 Beach characteristics

The GPB is a 600 m long engineered beach within a 1.2 km long embayment located in the south-west of France (figure 2.1 panel **(a)**). The embayed beach is constrained by two headlands and is backed by a seawall, protecting shops and habitations from high water level and wave overtopping as well as providing a recreational area for walking or restaurant terraces.

The GPB is a mesotidal environment with a spring tidal range of 4.5 m and a mean water level of 2.64 m (charts datum). Highest water levels reach +4.7 m excluding any surge. The elevation of the top of the seawall is +7.65 m. The double-barred profile (figure 2.2 panel **(b)**) exhibits a low sloping region in the subtidal zone ($x < 800\,m$, with the outer bar at $x = 600\,m$) and in the lower part of the intertidal area ($800\,m < x < 1000\,m$), with an inner bar that rather looks like an almost flat terrace around $x = 950\,m$ (slope 2-3%). Conversely, the foreshore is quite steep (slope 8-10%). For that reason, the GPB is characterized as intermediate-reflective (Morichon et al., 2018).

The beach morphology exhibits a large rip channel and a 3D nearshore bar system, as a result of the geological constraints (Enjalbert et al., 2011) visible on figure 2.2 panel **(a)**. In addition, the presence of rocky features in the nearshore bathymetry induces a complex offshore wave height distribution (Varing et al., 2020, Delpey et al., 2021).

The GPB opens to the Bay of Biscay and is mainly exposed to sea swells coming from the WNW direction (315°). The offshore wave climate ranges from moderately to highly energetic, with occasional high storm events. For example, storms with offshore $(H_s, T_p) = (3.5\,m, 13.8\,s)$

represents 7.24% of the yearly offshore climate (Morichon et al., 2018, Abadie et al., 2006). The significant wave height 10-year return period has been statistically computed to $H_s = 6.7\,m$ with a peak period of $T_p = 18\,s$ (Morichon et al., 2018).

2.3 Field campaign

In the framework of the MAREA project (*Modélisation et Aide à la décision face aux Risques côtiers en Euskal Atlantique*), a cross-border European project (INTERREG POCTEFA) aiming at better understanding storm impact along the Basque Coast , a field campaign was carried out during winter 2018 to measure wave transformations and run-up along the GPB. The events targeted in this campaign are energetic events coinciding with spring tides, generally responsible for high water levels, potentially leading to overtopping. Measurements include wave data provided by an array of pressure sensors described in section 2.3.1 as well as video run-up data, described in section 2.3.2.

2.3.1 Nearshore wave measurements

During the 3-days MAREA campaign, pressure sensors were deployed in the nearshore region to capture wave transformations in shallow water. Four pressure sensors were positioned along a cross-shore transect located in the middle of GPB (profile ID02 on figure 2.2 **(a)**) to measure wave transformation across the intertidal zone (figure 2.3). Their elevations were measured with a RTK GNSS and vary between +0.3 m up to +2 m (chart datum). They were complemented with a subtidal bottom-mounted pressure sensor (type *SEABIRD*) moored at 12 m depth that provides wave characteristics in the shoaling zone prior to wave breaking.

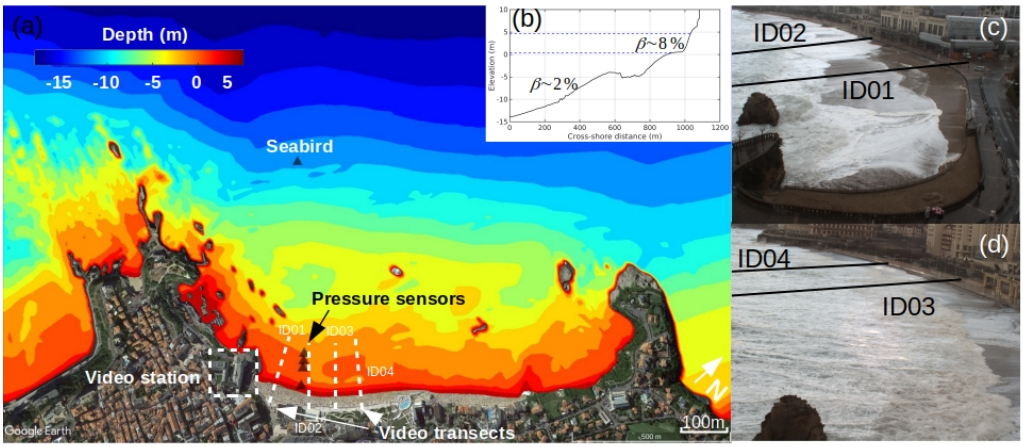

Figure 2.2: Field campaign description. **(a)** bathymetry of the GPB and locations of the measuring devices including pressure sensors and a video station. The white dashed lines represent the cross-shore transects where the swash was video monitored. From left to right : ID01, ID02, ID03 and ID04. **(b)** Cross-shore profile at ID02. Blue dashed lines represents lowest and highest water level at the site. **(c)**/**(d)** View from camera 1/4 and transects locations.

The RBR sensors were tightly attached to metallic poles which were deeply buried in the sand to avoid any loss of material during the energetic events that occurred. The *SEABIRD* was

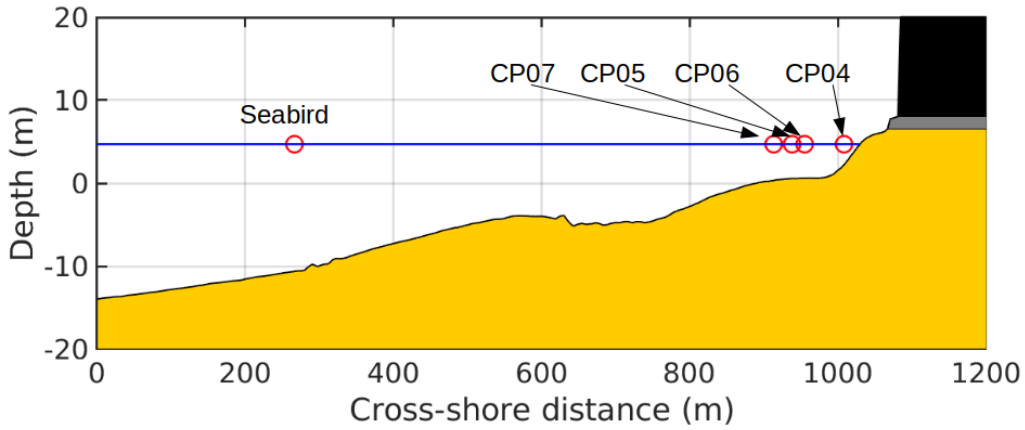

Figure 2.3: Cross-shore profile with pressure sensors locations. Note that the cross-shore axis starts at an arbitrary location but is consistent throughout the thesis.

moored to the bottom by a professional team of divers prior to the campaign when conditions allowed it. All the sensors recorded bottom pressure continuously with a 2 Hz frequency. For spectral analysis purpose, the pressure time series were divided in 30 min bursts. Due to the extensive tidal range (more than 4 m), the four intertidal sensors were located alternatively in the surf or swash zone. Therefore, to avoid any non-physical results, only the moments when the sensors were fully submerged have been used in this study. The method used to reconstruct the free surface from the pressure measurements is detailed in section 2.7.

2.3.2 Video estimation of the swash

The swash motions were measured using *timestack* images from the video monitoring station of the GPB, described in section 2.5. The cameras are sampled at 1 H_z and each *timestack* image represents a duration of 14 min to minimize the contribution of the tide on the water line position (Stockdon et al., 2006, Gomes da Silva et al., 2019). The analysis of the *timestack* images were performed at four longshore locations, spaced by approximately 100 m (figure 2.6) and referred to as ID01 to ID04, resulting in a data-set of more than 160 samples (14 min TWL time series) distributed among the locations. The methodology used to derive swash motions from *timestack* images is further described in section 2.6.

2.3.3 Experimental conditions

Offshore wave data were continuously recorded by a Datawell directional buoy, moored offshore in 50 m depth at about 6 km off the coast. This buoy is part of the french natioanl CANDHIS network (http://candhis.cetmef.developpement-durable.gouv.fr/) operated by the CEREMA. The buoy provides hourly frequency-direction spectra of the sea state.

Tidal data were provided by a tide gauge deployed at the Bayonne-Boucau harbor located 5.5 km north of the study site. It automatically records the level of water measured at regular 10 min intervals. The gauge is operated by the French Naval Hydrographic and Oceanographic Service (SHOM) as part of the REFMAR network (https://data.shom.fr/donnees/refmar).

In this work, a focus is made on a storm recorded from January 31 to February 02, 2018. The window corresponds to spring tide. This period was selected as it potentially represents the highest threat to surrounding buildings due to very high tidal level. The tidal level varied between +0.5 m and +4.8 m. Variable offshore wave conditions were observed during the field experiment (fig 2.4). They were first moderate with $(H_s, T_p) = (1.5\,m, 11\,s)$, followed by storm conditions with values reaching $(H_s, T_p) = (4.5\,m, 15.4\,s)$ from mid-day of the second day. The peak direction of wave propagation was mainly comprised between 300° and 320°, while during the most energetic event, a stable direction of 315° was observed, which corresponds to near-normal incidence of the GPB.

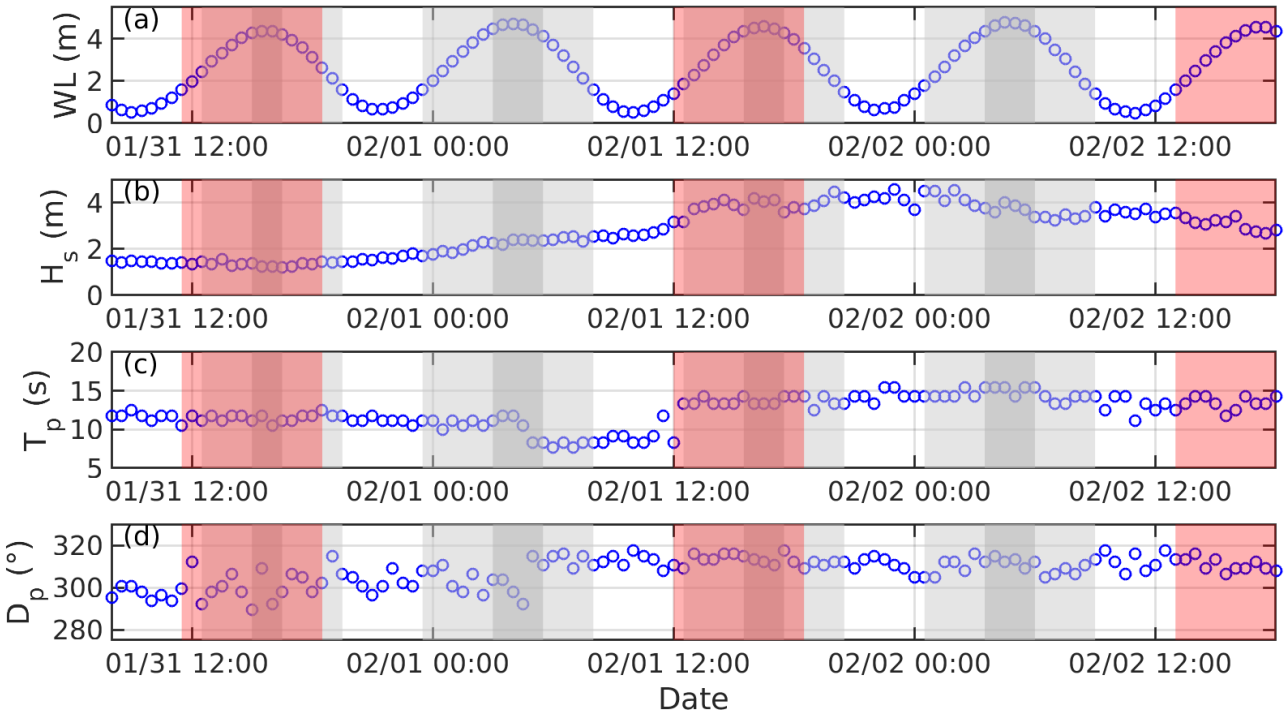

Figure 2.4: Conditions observed during the field campaign. Red shaded areas denote the webcam working hours (day time and from mid to high tide). Light grey and darker grey areas respectively denote CP07 and CP04 working hours (depending on the tide level they were not always submerged).

Finally, the data set was complemented with an extensive topo-bathymetric survey conducted on January 31, covering the beach and the nearshore area up to 25 m meters depth. This dataset was complemented offshore by the national reference dataset from French Naval Hydrodraphic and Oceanographic Service (SHOM).

2.4 Monitoring of the swash motion

2.4.1 Intrusive techniques

Intrusive techniques have been widely used in the past to measure swash motions. One system consists in resistance wires which conductance varies depending on the degree of immersion (Holman and Guza, 1984). To measure the swash excursions along a cross-shore profile, wires

can be placed horizontally over the beach face, at a fixed distance. In this configuration, the wires record the most seaward location at which water depth exceeds the vertical elevation of the wires, allowing to capture the time evolution of the landward limit of the swash motion (Guza and Thornton, 1982, Holman and Guza, 1984, Holland et al., 1995, Raubenheimer et al., 1995, Raubenheimer and Guza, 1996, Ruessink et al., 2013b, Peláez-Zapata et al., 2018, Liu et al., 2020). The main drawback of this method is that the height of the wires is at the basis on the definition of the swash tongue, which implies that measurements are extremely sensitive to this parameter (Holman and Guza, 1984, Holland et al., 1995, Raubenheimer and Guza, 1996). Alternatively, the wire can be placed vertically to evaluate the swash depth (Waddell, 1980, Hughes, 1992). An example of a resistance wire is given on figure 2.5 panel **(a)**. While data post-processing are usually straightforward as they are based on a linear relation between the conductance and the water elevation, the resistance wires suffer a certain number of disadvantages (Foote and Horn, 2002, Pitman, 2014). First, it requires a tedious calibration step prior to on-site deployment. Secondly, the electronic gauges require constant power-supply which can be difficult to provide on-site and are at risk to be damaged in the swash zone under energetic conditions (Masselink and Puleo, 2006).

Pressure sensors (PSs), usually used to measure the free surface elevation in the surf zone or seaward, have also been used to measure swash depth. For example, Masselink and Russell (2006) buried a series of PSs to have them flush with the beach face in order to estimate the amount of water above the bed. However, the swash zone carrying large quantity of sediments, progressively the PSs can be covered with a large thickness of sand which can skew the measurements. In addition, only the swash depth at the PS location is measured, but not the swash extension. More generally, instrumenting a beach with PSs under storm conditions can be complex (Nicolae Lerma et al., 2017), preventing data-set from including highly energetic wave conditions (Senechal et al., 2011). In addition, as surface-piercing objects these instruments can lead to obstruction of the flow and therefore disturb swash events.

2.4.2 Remote sensing

As an alternative technique to intrusive devices, remote sensing methods, that allow to monitor data from a distance without any form of contact with the water, are gaining importance (Pitman, 2014). An emerging method to remotely monitor the swash and surf zone is based on light and radio detection and ranging, LiDAR and RADAR respectively. The use of this type of technology is becoming increasingly popular as it allows a precise 3D mapping of the area of interest. It has been used in recent studies to measure swash zone processes (McNinch, 2007, Blenkinsopp et al., 2010, Brodie et al., 2015, Fiedler et al., 2015, Blenkinsopp et al., 2021). Examples of a LiDAR scanner and X-band radar are shown on figure 2.5 panels **(c)** and **(d)**. These systems can record the free surface elevation in the surf and swash zones by measuring the round trip time of either a laser (LiDAR) or radio (RADAR) pulse. The advantage of this methodology is that it is not limited by daylight and less sensitive to weather conditions (McN-

inch, 2007). It also provides a detail description of the swash zone, including the swash depth, and requires less post-treatment than the video-derived data. However, instrumenting a beach under energetic conditions might be challenging. In addition, these instruments are usually set-up for a given period of time and their area of measurement are usually localized, excluding any long term and large scale monitoring, of the order of the year along an entire beach for example.

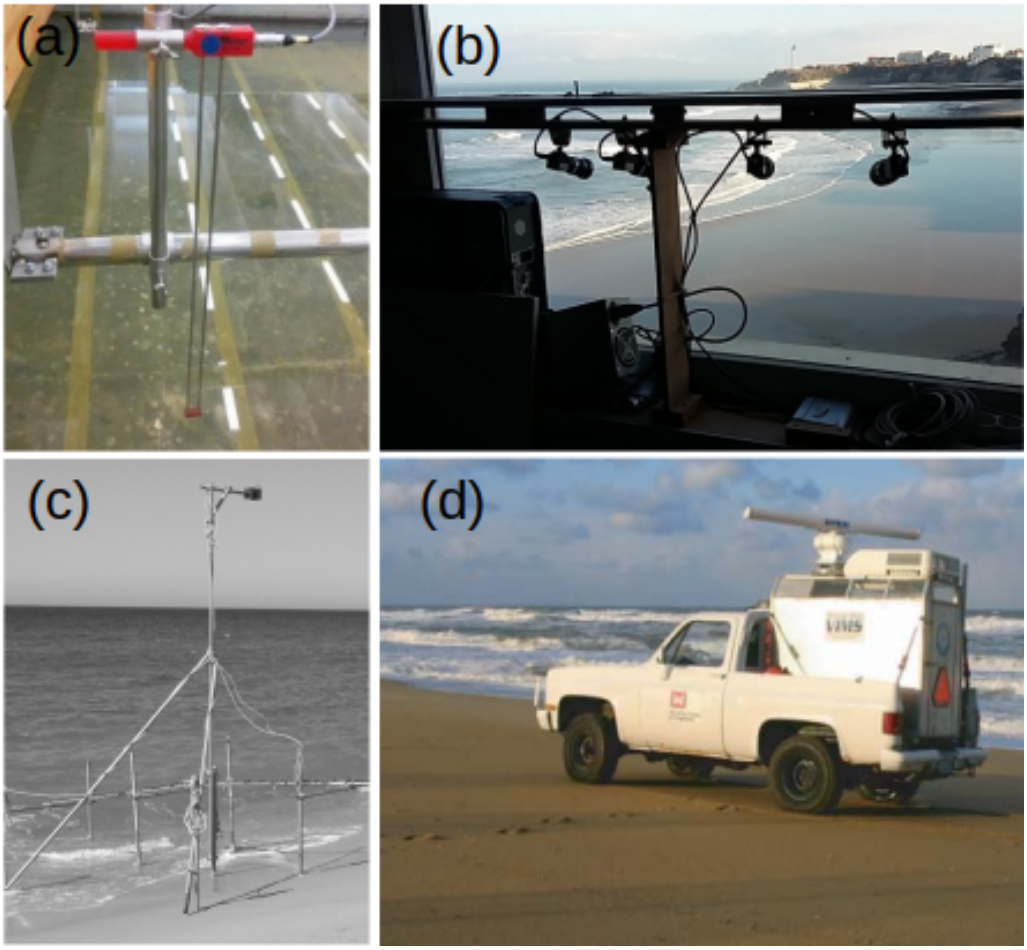

Figure 2.5: Illustration of the different types in-situ measurements of the swash zone **(a)** : resistance wire that can be set horizontally or vertically (reproduced from Martone et al. (2018), **(b)** : video monitoring station looking over the Grande Plage of Biarritz, **(c)** : LiDAR scanner positioned above the swash zone (reproduced from Blenkinsopp et al. (2010)), **(d)** : Car-mounted X-Band radar (reproduced from McNinch (2007)).

Video monitoring systems allow to capture high frequency processes (up to several H_z) during large periods of time (several years), for spatial scales ranging from meter to kilometer (Aarninkhof et al., 2003). For the last decades, they have been used in several coastal studies with typical applications spanning from hydrodynamic processes such as wave breaking (Gal et al., 2011, Guedes et al., 2012, Almar et al., 2012, Robertson et al., 2015, Andriolo, 2019), rip currents (Turner et al., 2007, Orzech et al., 2010, Gallop et al., 2011, Enjalbert et al., 2011), swash motions (Holman and Guza, 1984, Lippmann and Holman, 1989, Guedes et al., 2011, 2012, Senechal et al., 2011, Vousdoukas et al., 2009, 2011) to morphological processes including subtidal and intertidal bathymetry estimation (Collins et al., 2020, Bouvier et al.,

2020), shoreline and dunes monitoring (Blossier et al., 2017, Hein and Winter, 2019). The advantage of measuring swash motion through a video monitoring station is that it can be set-up for a long period of time. In addition, it is usually very resistant to climatic conditions as it is located away from the energetic swash zone and sometimes even indoor (see fig. 2.5 panel **(b)**).

Usually, a video monitoring system is fixed and located high above the ground to minimize the distortion effects. It is composed of several cameras in order to cover the whole study area with a sufficient spatial resolution. Those camera are operated with a software allowing to synchronize the acquisition of images from each camera, to pre-process these images and to transfer them to a server via internet access. Since the installation of the pioneer Argus system in 1992 (Holman et al., 1993, Holman and Stanley, 2007) at Agate Beach in the USA, various video monitoring systems have followed, such as the *Kosta* (https://www.kostasystem.com/en/), The *Beachkeeper* (Dessy et al., 2008), The *Cosmos* (Taborda and Silva, 2012). Along the French Basque coast, the *SIRENA* video monitoring system (https://coo.icm.csic.es/service/video-monitoring) is operated by the SIAME laboratory on three sites to monitor morphology changes, coastal flooding and wave transformation at the foot of a cliff, respectively at the Anglet, Biarritz and Socoa stations (http://sirena.univ-pau.fr/). An example of a video station is given on figure 2.5 panel **(b)**.

2.5 Video station of the GPB

In this study, we use the images collected by a video station deployed in 2017 at the Grande Plage of Biarritz to monitor the swash motion under varying wave conditions. In this section, we present the characteristics of the station and the geo-rectification procedure allowing to estimate metric distances from images necessary to quantify the swash motion.

2.5.1 Settings of the station

The video monitoring station of the GPB is located at +30 m in a neighbouring building on the southern crop of the beach (figure 2.6). The monitoring system is controlled by the open source software *SIRENA* (https://sourceforge.net/projects/sirena-remote/). The station is comprised of four cameras oriented to cover the whole area of interest, spanning from the outer surf zone to the beach front. Cameras 1 and 4 are directed towards the upper part of the beach and provide data for swash and submersion monitoring. Specifically, *timestack* images (described later) are captured along 4 cross-shore transects (ID01 to ID04) spaced by approximately 100 m along the beach (figure 2.6). Cameras 2 and 3, not used in this study, are directed towards the lower part of the intertidal zone and the subtidal zone, to capture incident wave transformation.

Figure 2.6: Video station of the GPB with black lines indicating the positions of cross-shore profiles where swash motion is followed.

2.5.2 Video station products

The Biarritz video-monitoring station produces three different types of images, namely *timestack*, *timex* and *variance* images.

***Timestack* images** represent the temporal evolution of pixels intensity along a cross-shore transect spanning the area of interest, from the shoaling zone up to the swash zone. They have been used in several studies to investigate wave run-up (Guedes et al., 2011, 2012, Senechal et al., 2011, 2018, Stockdon et al., 2006, Vousdoukas et al., 2009, 2011) or wave breaking (Gal et al., 2011, Almar et al., 2012, Robertson et al., 2015, Andriolo, 2019). The *timestack* images generated by the GPB video station are sampled at a rate of 1 H_z during 14 min to limit the effect of tide level on the location of wave breaking and swash zone slope ((Senechal et al., 2011, Stockdon et al., 2006, Vousdoukas et al., 2012)). An example of a *timestack* image is given in figure 2.7 panel **(b)** where the horizontal axis refers to the cross-shore position and vertical axis to the time.

TIMe EXposure images are the result of the time averaged RGB triplets of each individual image collected during a 14 min at 1 H_z (panel **(c)**). The gain of such image is that it smooths out short scale motions (lower than the sampling duration) as well as possible obstacles such as people, ships. It allows to highlight the location of the breaking zone that appears as a white pattern due to the presence of foam as well as the swash zone that is usually the ultimate area of wave breaking at the shore. Various studies based on *timex* images have been carried out to study for example rip currents formation and migration (Turner et al., 2007, Orzech et al., 2010, Gallop et al., 2011, Enjalbert et al., 2011), to investigate wave breaking properties

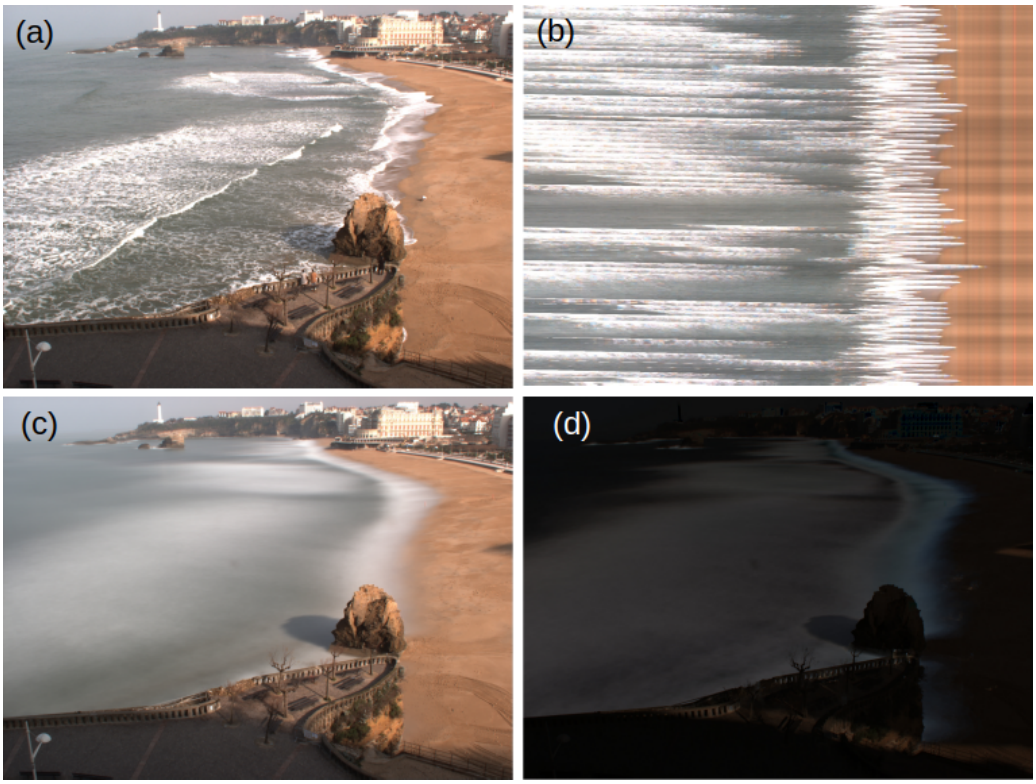

Figure 2.7: Typical output images from the Biarritz video station. **(a)** Snapshot of the Grande Plage of Biarritz , **(b)** *timestack* image, **(c)** *timex* image and **(d)** *variance* image.

(Guedes et al., 2012, Andriolo et al., 2020) and more recently to perform bathymetric inversion (Collins et al., 2020).

Finally, **variance image** represents the standard deviation of pixel intensities over a sampling period. Areas exhibiting large temporal variability appear bright on the image while still areas are darker. For instance, the surf and swash zone appear brighter than the rest of the image on figure 2.7 panel **(d)** due to significant motions in these areas. While variance images are a typical product from coastal video monitoring systems very few studies use them for scientific purposes.

2.5.3 Image geo-rectification

In this study, *timestack* images are geo-rectified in order to quantify swash motions along the GPB. The image geo-rectification is a calibration process in which the oblique image captured by a camera is rectified into a plan image with corresponding real world coordinates. The transformation of real-world coordinates to pixel coordinates (or the other way around) is achieved by applying standard photogrammetric procedures (Holland et al., 1997), which consists in a series of transformations on the basis of the collinearity equations. The relation between image and real-world coordinates involves the camera location $N(x_c, y_c, z_c)$, also called projection center, its focal length f and its orientation, defined through 3 camera angles (the tilt τ, azimuth ϕ and roll σ).

The relation between real world coordinates (x, y, z) and the image-plan reference frame

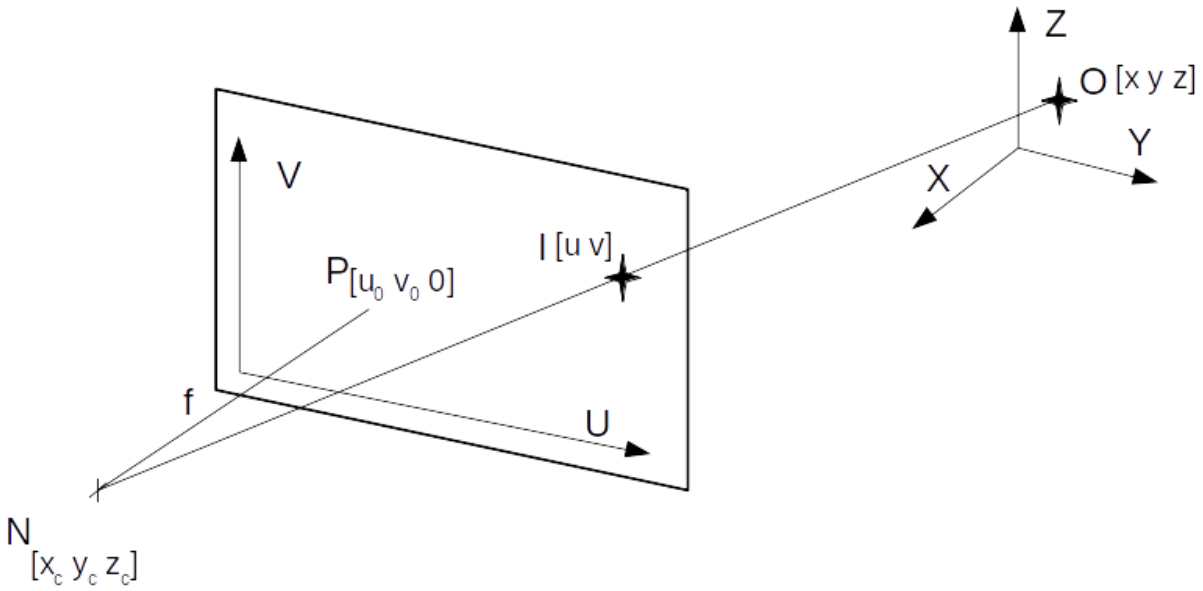

Figure 2.8: Definition of the variables for the DLT where N is the projection center, O the object and I its image.

(u, v) is obtained using a *Direct Linear Transformation* (DLT). The DLT involves that the object O, its image I and the projection center N are collinear (see fig. 2.8). It is given by:

$$\begin{aligned} u &= \frac{L_1 x + L_2 y + L_3 z + L_4}{L_9 x + L_{10} y + L_{11} z + 1} \\ v &= \frac{L_5 x + L_6 y + L_7 z + L_8}{L_9 x + L_{10} y + L_{11} z + 1} \end{aligned} \tag{2.1}$$

where the parameters L_i (called DLT parameters) are functions of 11 unknowns : the coordinates of N in both the object-space (x_c, y_c, z_c) and image-plan reference frame (u_0, v_0, f), the camera angles (τ,ϕ,σ) and horizontal and vertical scale factors (λ_u,λ_v) which are used as a unit conversion factors to express image coordinate unit (pixel) into real world coordinate unit (meter). A more detailed description of the DLT parameters is given in appendix B.1.

2.5.4 Ground Control Points

The resolution of the system of equations 2.1 requires to identify on a reference image a minimum number of points whose Real World coordinates are known. Those points are called *Ground Control Points* (GCPs). Each GCP bringing two new equations, the system needs a minimum of 6 points to solve the equations and find the 11 unknowns of eq. 2.1. More GCPs leads to an over-determined system that can be solved in a least-squares sense. The control points must not be co-planar and therefore should form what is called a *control volume*. Each GCPs is measured in space using a DGPS system (geographic coordinates as well as elevation) and simultaneously recorded with the camera, allowing to precisely determine which pixel was associated with the measured coordinates, as displayed in 2.9. In the context of this study, a

Figure 2.9: GCP pixel identification on the camera image **(a)** and DGPS-RTK measurement of the GCP coordinates **(b)**.

total of 13 GCPs were used for the calibration of the camera. They are shown in figure 2.10 (in red) as well as their recalculated locations using the geo-rectification (green). This procedure

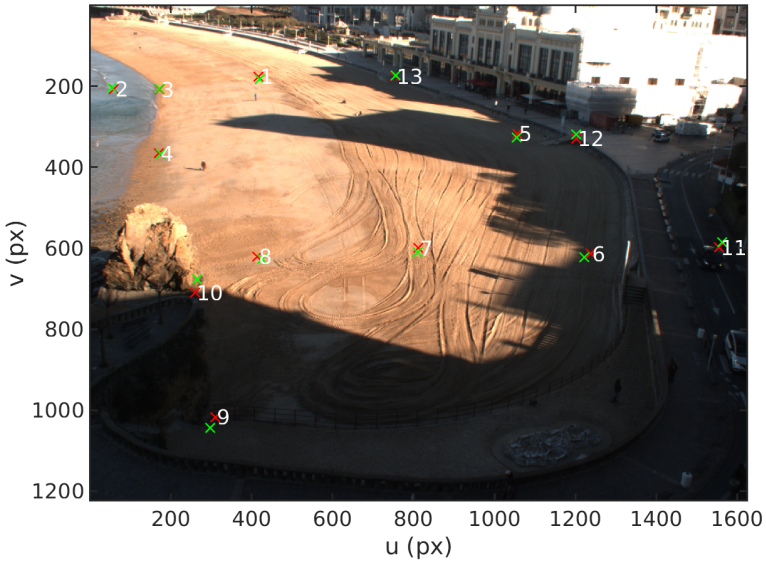

Figure 2.10: GCPs used for the calibration of the camera. Red : original locations, green : re-calculated locations via geo-rectification.

yielded a mean (max) error of $12px$ ($33px$) and $2.5m$ ($6.5m$) in terms of distance. Multiple sources of inaccuracy can be identified : the identification of the GCPs on the image being manually performed by an operator for a distant GCP from the video station a deviation of a few pixels is possible, a bias in the GPS elevation...

The geo-rectification procedure is valid under the ideal assumption of distortion free lenses and square image pixels. In practical applications the spherical shape of the camera lenses impose a certain amount of distortion, which needs to be corrected before applying the geo-rectification. The procedure is detailed in appendix B.2.

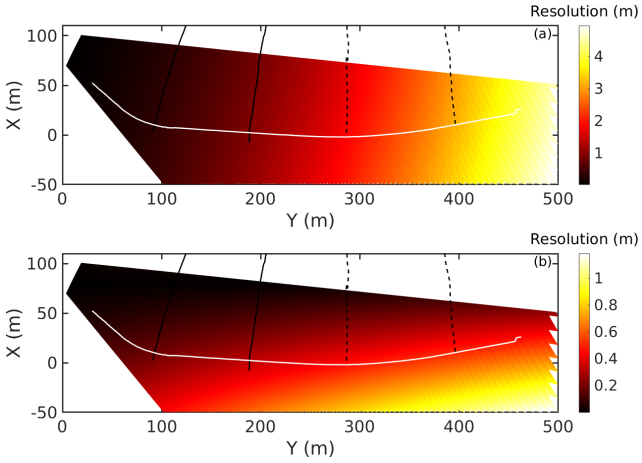

(1) Camera 1 (transects ID01 and ID02)

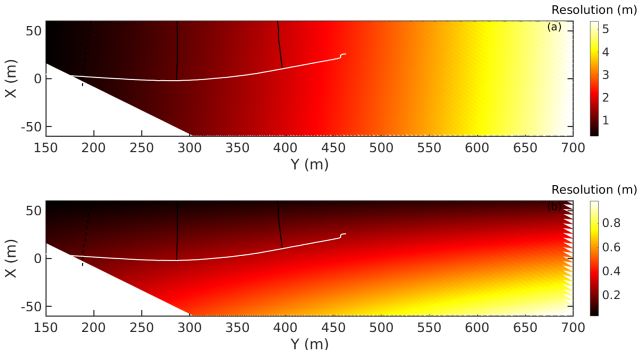

(2) Camera 4 (transects ID03 and ID04)

Figure 2.11: Pixel footprints map for cameras 1 and 4 in the longshore **(a)** and cross-shore **(b)** directions. Solid black and white lines indicate locations of the cross-shore transects and the wall respectively. The black dashed lines on subfigure (1) represent the location of the two transects captured by camera 4.

2.5.5 Pixel resolution map

Pixel footprints are the projection of each pixel in real world coordinates through geo-rectification. The pixel footprints do not have the same size i.e. the resolution varies on the rectified image. The resolution is inversely proportional to the pixel spatial dimension. In practical terms, the pixel footprints far from the camera are the most distorted and largest, yielding therefore the lowest resolution. The theoretical accuracy is approximated as (Lippmann and Holman, 1989) :

$$L_c(x,y) = R(x,y)\frac{\delta}{N_u} \tag{2.2}$$

$$L_a(x,y) = \frac{L_c(x,y)}{cos(\tau(x,y))} \tag{2.3}$$

where L_c (L_a) is the cross-bore (bore sight) size of a single pixel, N_u the number of horizontal pixels composing the image, R the distance between the camera and the location of interest (x, y), τ the tilt camera angle, and δ the lens horizontal field of view. The spatially varying dimensions of L_c and L_a for each camera are projected along a cross-shore- and alongshore-oriented coordinate axis, yielding two maps of pixel footprints within the area of interest. The pixel footprint maps of the Biarritz video station are shown on figure 2.11. In the upper part of the beach, the angular resolution (cross-shore) ranges from 1 to 15 cm and the radial resolution (longshore) from 1 to 5 m.

2.6 Wave run-up estimation from *timestack* images

The estimation of the wave run-up using the *timestack* images captured by the GPB video station includes two steps. First, the water line position is determined using a pixel clustering algorithm. Then, geo-rectified topographic measurements of the beach profile elevation are used to determine the corresponding water level.

2.6.1 Waterline detection method

In our study, the detection of the water line position on the *timestack* images is carried out using a clustering algorithm based on a *Color Contrast* (CC) method. It consists in identifying the interface between the dry part of the beach and the submerged area, namely the extension of the swash zone, by analysing the pixel intensity gradients.

The pixel intensity clustering (PIC) is achieved by regrouping pixels intensities into n similar grey shadings derived from the RGB (Red-Blue-Green) values of the *timestack* images. This method has been successfully used in previous studies (Vousdoukas et al., 2012, Gomes da Silva et al., 2019). The n classes are determined using the Otsu's automatic thresholding method (Otsu, 1979). The threshold between each class is automatically chosen as the one minimizing intra-class intensity variance, or equivalently maximizing inter-class intensity variance. An example of algorithm results for $n = 4$ classes is shown on figure 2.12. Panel **(a)** shows the contour of the automatically defined classes while panel **(b)** shows distribution of pixel intensity as well as the thresholds. The quality of the image segmentation heavily relies

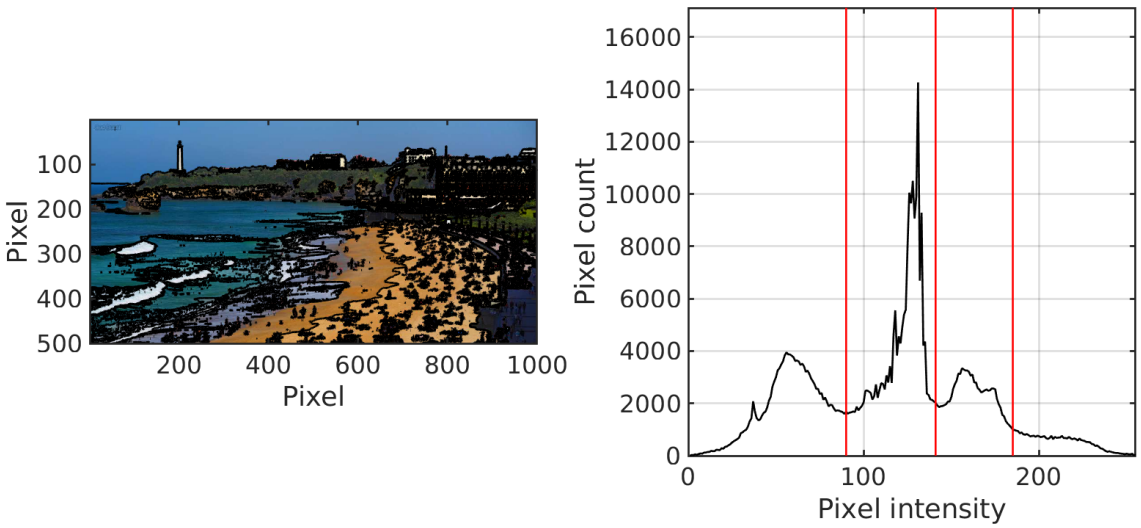

Figure 2.12: Left : Contour of the 3 minimizing intra-class variance thresholds ($n = 4$ segments) over an image of Biarritz. Right : associated pixel intensity distribution and thresholds calculated according to Otsu's method.

on the image itself. If the pixel intensity distribution exhibits sharp peaks, a satisfying result is observed. On figure 2.12 panel **(b)** the distribution shows 3 distinct peaks, allowing for a clear identification of the thresholds.

2.6.2 Sensitivity analysis of the segmentation procedure

Initially, the method assumed a bi-modal distribution of the pixel intensity meaning two classes and one threshold. The upgrade of the algorithm to multi-modal problems is straightforward but the credibility of the thresholds decreases as the number of classes increases (Otsu, 1979). We carried out a sensitivity analysis to assess the dependency of the detected waterline position to the number of classes used in the segmentation algorithm. A comparison between $n = 2, 3, 4$ is shown on figure 2.13. A low number of classes, 2 for instance, usually produces over-smooths swash lines and fails to capture the run down of the swash line, as swell as small scale variations. This results in an underestimation of the swash amplitude, especially in the high frequencies (panel **(b)**). A number of 3 or 4 classes allows to improve the accuracy of the segmentation. A number of classes greater than 4 results in noisy time series that could not be used. In this study, we used a number of $n = 4$ classes.

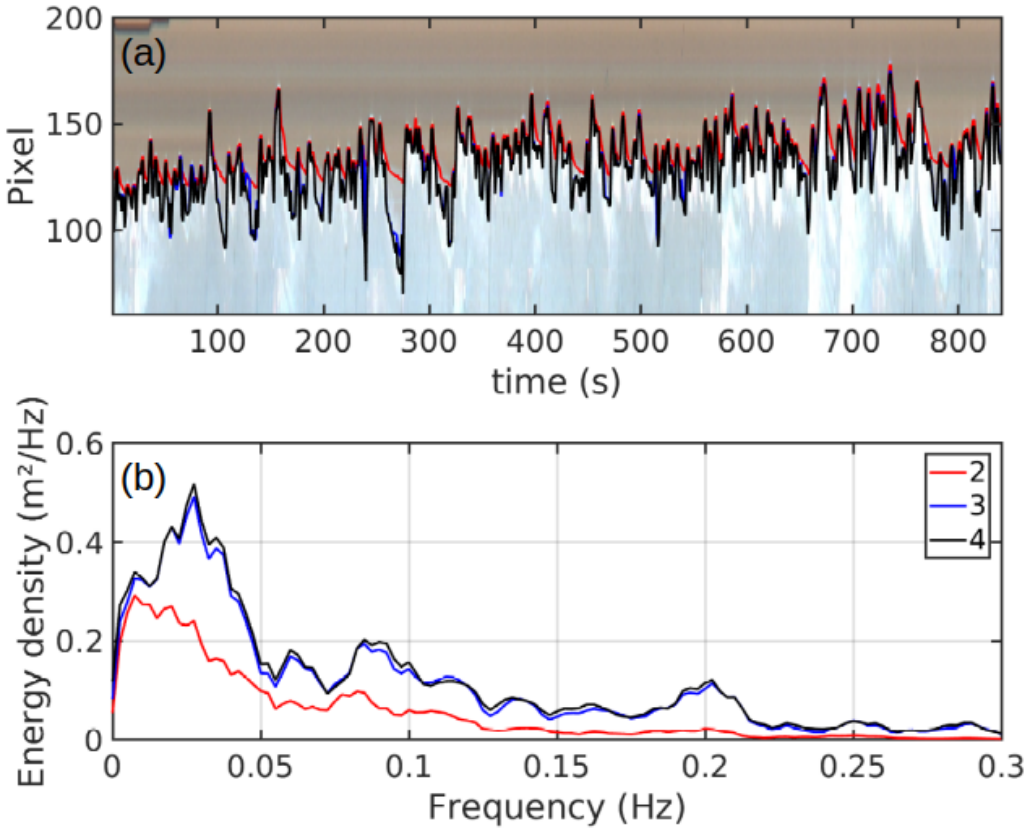

Figure 2.13: Influence of the number of class on the TWL time series **(a)** and resulting swash spectrum **(b)**.

Once the image is segmented, the stack is read seaward (from top to bottom on figure 2.13) and the swash line is detected as being the first maximum pixel value (white). Indeed, the white foam composing the run-up tongue is usually converted to true white whereas the sand is converted to grey. Once the swash line is identified, the resulting product is a time series of pixel locations, corresponding to the location of the swash line along the given transect every second. It is worth to note that the automatic detection is not always robust and manual corrections are sometimes necessary to correctly process some images. In addition, under poor

lighting conditions or during rain episodes the quality of the *timestack* proved to be too poor to be used for analysis.

2.6.3 Swash elevation time series and statistics

The time series of pixel locations, representing the total water level (TWL) motion along a cross-shore transect, are then converted into vertical TWL elevation time series by geo-rectifying the topographic profiles measured with a DGPS, using the DLT coefficients calculated in section 2.5. Each geo-rectified profile is interpolated onto the pixel coordinates to provide each cross-shore pixel the corresponding elevation (see fig. 2.14). The swash motion is then obtained by subtracting the average of the 14-min time series, which consists in removing the astronomical tide and the eventual storm surge and wave set-up components of the TWL.

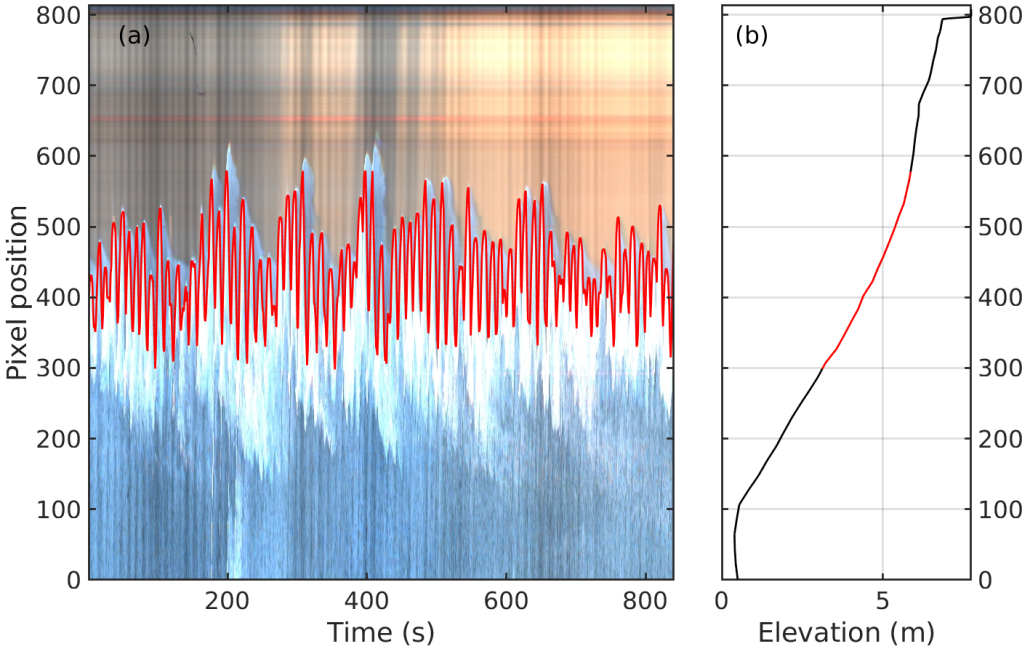

Figure 2.14: **(a)** Identification of the swash line on a *timestack* image. **(b)** Geo-rectified bathymetric profile.

The determination of the contribution of the SW and IG frequency bands to the swash motion that is analysed in 4.1, is based on a spectral analysis of the swash time series. The power spectral density (PSD) is computed using the Welch's method (Welch, 1967). The time series are divided into 50% overlapping segments and each segment is then tappered using a Hanning window. Associated confidence intervals are computed according to Emery and Thomson (2001, equation 5.108) :

$$\frac{(\nu-1)s^2(f)}{\chi^2_{1-\alpha/2,\nu}} < \sigma^2(f) < \frac{(\nu-1)s^2(f)}{\chi^2_{\alpha/2,\nu}} \tag{2.4}$$

where ν is the degree of freedom calculated as in Emery and Thomson (2001, table 5.5), σ^2 and s^2 are the true and calculated variances respectively and α the confidence coefficient at

5%. When represented in a logarithmic scale, the confidence interval becomes constant and expressed as :

$$CI = \left] \frac{(\nu-1)}{\chi^2_{1-\alpha/2,\nu}}; \frac{(\nu-1)}{\chi^2_{\alpha/2,\nu}} \right[\tag{2.5}$$

The calculation of the spectrum allows to compute integrated quantities on defined frequency band. Commonly, the significant swash heights within the IG and SW frequency bands are computed respectively as :

$$S_{IG} = 4\sqrt{\int_{fl}^{fc} E(f)\, df} \tag{2.6a}$$

and

$$S_{SW} = 4\sqrt{\int_{fc}^{fh} E(f)\, df} \tag{2.6b}$$

where E is the spectral density at the frequency f of the swash elevation time series. The cut-off frequency f_c, that separates SW and IG frequency bands, is set equal to $f_c = 0.05\ H_z$, similar than in previous studies (Stockdon et al., 2006, Senechal et al., 2011, Nicolae Lerma et al., 2017, Gomes da Silva et al., 2019). The total significant swash height S is then computed as the sum of the IG and SW components according to:

$$S = \sqrt{S_{IG}^2 + S_{SW}^2} \tag{2.7}$$

Figure 2.15 displays an example of a swash time series and its associated spectrum. The spectrum displays two distinct peaks, one in the SW and one in the IG frequency bands, suggesting a contribution of both wind-forced short waves and IG waves.

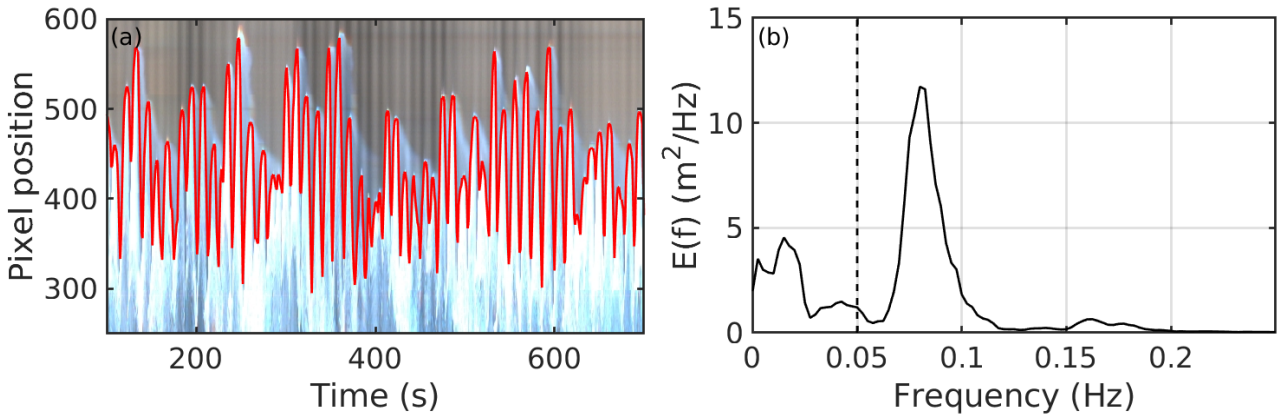

Figure 2.15: Example of the swash line extraction and treatment (data from ID02). **(a)** : swash time series identification on the timestack. **(b)** : Energy density spectrum derived from the measured swash time series in **(a)**. The black dashed line represents the cut-off frequency between the SW and IG band.

2.7 Free surface reconstruction methods

In this section, we present the reconstruction method that was applied to estimate the free surface from pressure sensor measurements carried out during the MAREA field campaign. We present three different methods and discuss their domain of application.

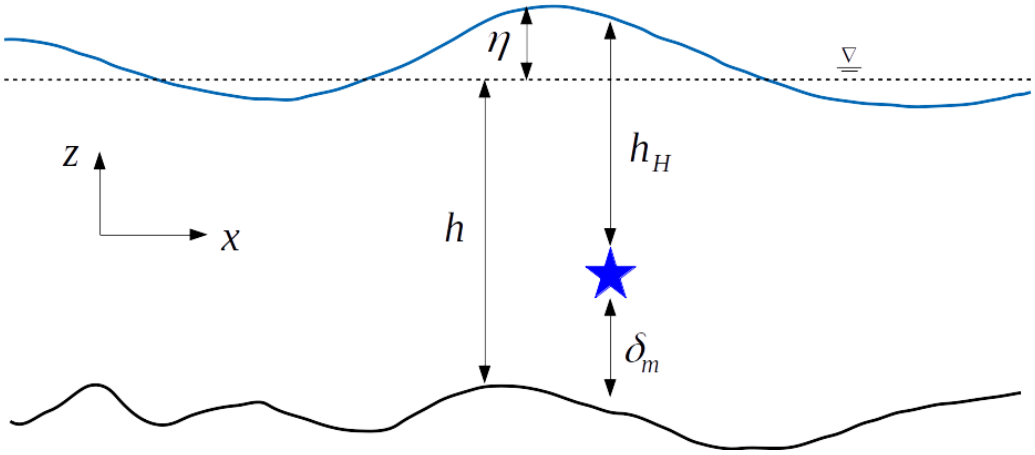

Figure 2.16: Definition sketch of the variables.

2.7.1 Hydrostatic reconstruction

The simplest reconstruction method consists in neglecting vertical acceleration and only considering the pressure as hydrostatic. This implies that the measured pressure is assumed to only depend on the weight of the water column above the sensor and the atmospheric pressure, such as :

$$P_{tot} = P_{atm} + \rho g h_H \tag{2.8}$$

where P_{tot} is the total pressure, h_H is the water depth, P_{atm} is the atmospheric pressure, ρ is the fluid density and g the acceleration of gravity. The corresponding hydrostatic free surface elevation is then given by :

$$\eta_H = h_H + \delta_m - h = \frac{P_{tot} - P_{atm}}{\rho g} + \delta_m - h \tag{2.9}$$

where δ_m is the elevation of the sensor above the bottom and h the still water level at the point of measurement, given by a tidal gauge for instance. The hydrostatic assumption is usually valid for long waves, such as tsunami, coastal seiches (Bellafont et al., 2018), tidal waves or in the breaking zone where the waves propagate as bores (Raubenheimer et al., 1996, Sénéchal et al., 2001). For instance, Lin and Liu (1998) showed based on numerical results from a validated *RANS* model that the pressure under spilling breakers is almost hydrostatic, with a maximum deviation of 7%, occurring under the broken wave front. However, in the shoaling and surf zones the vertical acceleration of the fluid becomes non negligible and the resulting pressure is no longer hydrostatic. Under these conditions, the hydrostatic assumption significantly underestimates the wave height (Bonneton and Lannes, 2017, Bonneton et al.,

2018, Mouragues et al., 2019, Martins et al., 2020).

2.7.2 Linear reconstruction

The derivation of the pressure field based on the linear theory provides a first order estimate of the non-hydrostatic terms. The Transfer Function Method (TFM) is the most common approach (Fiedler et al., 2015, Brodie et al., 2015, Do et al., 2016, Lashley et al., 2019, Risandi et al., 2020, Bertin et al., 2020) to reconstruct the free surface elevation from pressure sensors deployed over the entire neashore zone. This method provides a good estimate of integrated quantities such as H_s (Tsai et al., 2005, Mouragues et al., 2019). Following the linear theory, the derivation of the pressure field using Bernoulli's equation leads to the following transfer function :

$$K_{p,L}(f, h, \delta_m) = \frac{\cosh(hk(f))}{\cosh(\delta_m k(f))} \tag{2.10}$$

This coefficient is a function of the total depth h, the measurement elevation with respect to the bottom δ_m and the wave number $k(f)$. It allows to compensate the pressure attenuation observed under dispersive waves (Tsai et al., 2005, Oliveras et al., 2011). The linear attenuation is frequency-dependent with a higher attenuation of high frequencies in deeper water, as shown on figure 2.17. For $h = 1\,m$, the attenuation is relatively small, even for frequencies higher

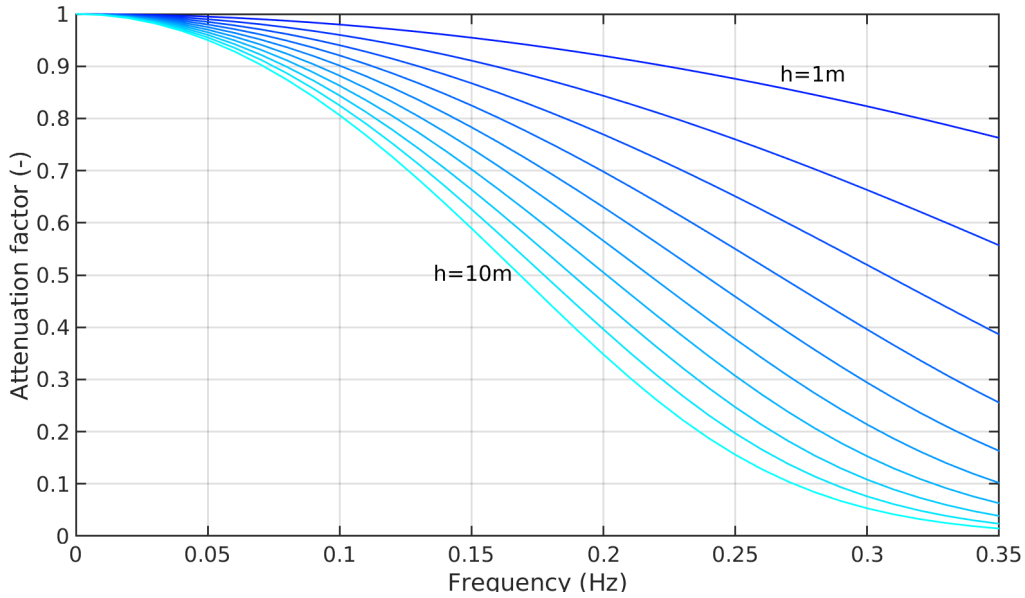

Figure 2.17: Attenuation coefficient at 10 cm above the bottom in function of the frequency for different water depths. A factor of 1 means no attenuation while a factor of 0 means complete attenuation.

than $0.3\,H_z$ (shorter than 3.3 s) with a calculated attenuation of around 20%. However, for $h = 10\,m$ the attenuation is significant and applies lower in the spectrum, with a value of 60% in $f = 0.15\,H_z$ and almost completely dampens the frequencies higher than $0.2\,H_z$.

As the transfer function is also frequency-dependent, for irregular signals such as pressure time

series under oceanic waves it needs to be applied directly on the spectrum :

$$\mathcal{F}(\eta_L)(f) = \begin{cases} K_{p,L}(f)\mathcal{F}(\eta_H)(f) & \text{if} \quad f \leq f_c \\ \mathcal{F}(\eta_H)(f) & \text{if} \quad f > f_c \end{cases} \tag{2.11}$$

where $\mathcal{F}(\eta_H)(f)$ and $\mathcal{F}(\eta_L)(f)$ are respectively the Fourier transforms of the hydrostatic elevation $\eta_H(t)$ and the linear elevation reconstruction $\eta_L(t)$. Due to the exponential growth of the transfer function in the high frequencies, a cut-off frequency f_c is applied above which the spectrum is no longer corrected. This constitutes the main limitation of the linear reconstruction, however energy in the high frequency part of the spectrum is usually low. By retaining the phases, the corrected free surface elevation can then be obtained from an inverse Fourier transform :

$$\eta_L(t) = \mathcal{F}^{-1}(\mathcal{F}(\eta_L)) \tag{2.12}$$

Alternatively the power spectrum density (PSD) can be calculated directly as :

$$\mathcal{PSD}(\eta_L)(f) = \begin{cases} K_{p,L}^2(f)\mathcal{PSD}(\eta_H)(f) & \text{if} \quad f \leq f_c \\ \mathcal{PSD}(\eta_H)(f) & \text{if} \quad f > f_c \end{cases} \tag{2.13}$$

This method allows for a direct computation of the significant wave height H_s and avoids an inverse Fourier transform, necessary to obtain the time series of $\eta_L(t)$. An example of

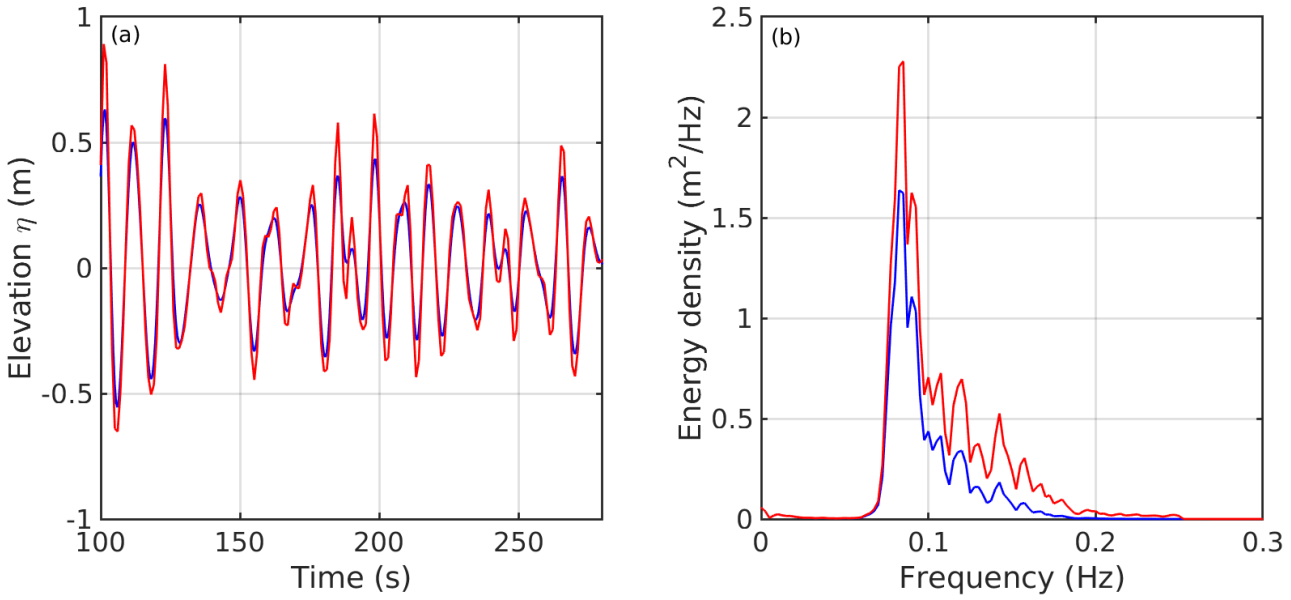

Figure 2.18: Hydrostatic and linear reconstruction of data recovered from a seabird moored at 12m depth during the MAREA campaign of 2018. **(a)** : Hydrostatic elevation (blue) and linear reconstruction elevation (red line). **(b)** : PSD of the hydrostatic elevation (blue) and the linear reconstruction using a cut-off frequency of $f_c = 0.25\ H_z$ (red).

linear reconstruction is provided on figure 2.18. As shown on panel **(b)**, in the low frequencies ($f < 0.07\ H_z$) the two spectra are similar. The transfer function effects are visible in the high frequencies, where the linearly corrected spectrum shows much higher value than the hydrostatic spectrum. For frequencies higher than $f = 0.25 H_z$ the two spectra are identical as no correction

is applied. Computed significant wave heights are $H_s = 0.8m$ and $H_s = 1.0m$ for the hydrostatic and linear reconstruction respectively. In terms of time series (panel **(a)**), the crests are higher and the troughs lower as a result of the high frequency components amplification.

2.7.3 Non linear reconstruction

Recently, nonlinear methods have undergone an increasing attention in order to improve the description of higher harmonics (Oliveras et al., 2011, Constantin, 2012, Clamond and Constantin, 2013), underestimated using the TFM method due to the cut-off frequency. These harmonics are known to be responsible for the shape of the individual waves, such as skewness or asymmetry (Bonneton and Lannes, 2017, Mouragues et al., 2019, Martins et al., 2020). An example of such method is the fully-dispersive non-linear reconstruction method derived by Bonneton and Lannes (2017), which uses the linear reconstruction :

$$\begin{aligned} \eta_{NL} &= \eta_L - \frac{1}{g}\partial_t(\eta_L \partial_t \eta_L) \\ &= \eta_L - \frac{1}{g}(\eta_L \partial_{tt}\eta_L) - \frac{1}{g}(\partial_t \eta_L)^2 \end{aligned} \tag{2.14}$$

The first nonlinear term enables to capture more accurately the wave extrema by increasing the crests and flattening the troughs, while the second term amplifies the wave skewness and asymmetry (Mouragues et al., 2019). This method relies on the previously calculated linear reconstruction η_L and therefore incorporates the effect of the cut-off frequency. Figure 2.19

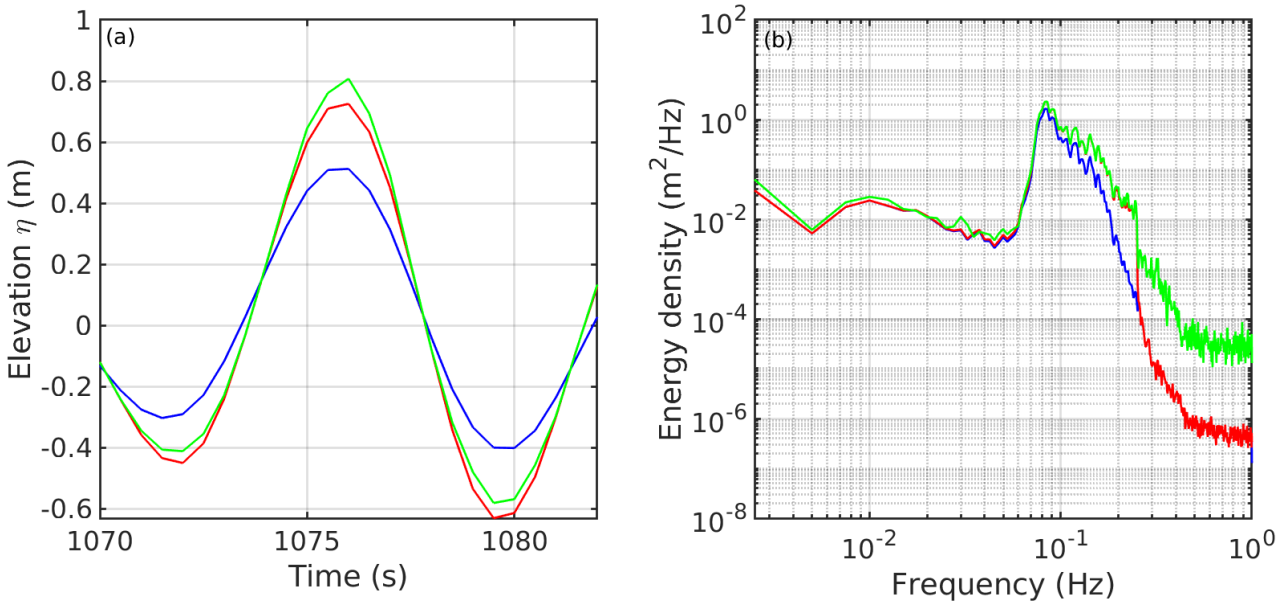

Figure 2.19: Hydrostatic, linear and non-linear reconstruction (computed following Bonneton and Lannes (2017)) of data recovered from a seabird moored at 12m depth during the MAREA campaign of 2018. **(a)** : Hydrostatic elevation (blue), linear reconstruction elevation (red line) and non-linear reconstruction elevation (green line). **(b)** : PSD of the hydrostatic elevation (blue) linear reconstruction using a cut-off frequency of $f_c = 0.25\ H_z$ (red) and non-linear reconstruction (green).

shows the implementation of the nonlinear method described in Bonneton and Lannes (2017) on pressure data recovered from a *Seabird* device. The free surface calculated with the nonlinear method shows an amplification of the crests computed with the linear theory and lower troughs (panel **(a)**), suggesting a more skewed wave profile. This feature is the result of the amplification of the higher harmonics observed in the nonlinear reconstruction spectrum (panel **(b)**). While this part of the spectrum is crucial for the free surface profile (Bonneton and Lannes, 2017, Mouragues et al., 2019, Martins et al., 2020), the resulting H_s is almost identical in the linear and nonlinear reconstructions ($H_s = 1.0\,m$ for both).

2.7.4 Wave statistics

After performing a Fourier transform on the free surface elevation time series, wave statistics are computed in the same way from the PSD as with the swash time series. The significant swash heights within the IG and SW frequency bands are computed respectively as :

$$H_{IG} = 4\sqrt{\int_{fl}^{fc} E(f)\,df} \tag{2.15a}$$

and

$$H_{SW} = 4\sqrt{\int_{fc}^{fh} E(f)\,df} \tag{2.15b}$$

where E is the spectral density at the frequency f of the free surface elevation time series. The total significant wave height S is then computed as the sum of the IG and SW components according to:

$$H_s = \sqrt{H_{IG}^2 + H_{SW}^2} \tag{2.16}$$

2.8 Conclusion

In this chapter, we described the field campaign and monitoring techniques that were used to measure the swash motion and the nearshore waves in the embayed beach of GPB. During the campaign, wave conditions ranged from moderate ($H_s < 2\,m$) to energetic ($H_s > 4\,m$) and the tidal level varied between +0.5 m and +4.8 m, constituting a data-set of a wide range of conditions for analysis and model validation purposes. The swash motions along the embayed beach of the GPB were derived from timestack images acquired by a video-monitoring station, as it allows to capture wave run-up continuously and at different longshore locations. In addition, this type of set-up allows to capture high-energy events, which can be complicated with *in-situ* measurements. The swash line time series was extracted from timestack images by discriminating color contrasts , and then converted to elevation using the geo-rectified topographic profile. To evaluate nearshore wave processes, data from pressure sensors are used in this study. Free surface elevation times series were computed from the

bottom pressure recordings by applying a frequency-domain attenuation correction based on the linear theory. The hydrostatic approximation proved to be too restrictive as some pressure sensors were located too deep, where the non-hydrostatic pressure is non negligible. Conversely, the non-linear approximation improved the details in the high-frequency spectrum tail, enabling to describe more accurately the free surface shape but resulting in almost identical wave energy as the linear theory.

Chapter 3

Computation of swash hydrodynamics with a phase-resolving model

Contents

3.1 Introduction

Measuring wave and swash processes in the field is usually complex and costly, especially under energetic conditions. Thanks to numerical tools, process-based numerical models allow for a reasonable description of the hydrodynamics at a much lower cost. In addition, numerical modeling can be used to compute past events and future events in order to assess the potential impact of climate changes such as sea level rise. As discussed in section 1.4.2, the phase-resolving depth-integrated approach, namely NLSW models or BTM, has become increasingly popular for coastal applications as it resolves the relevant physical processes at a relatively cheap computational cost, allowing to consider numerical domains of up to several square kilometers. Therefore, it is important to estimate the performances and limitations of this approach to ensure the best possible results.

In this chapter, the performances of the BTM *BOSZ* to capture wave transformations and run-up are assessed. After a description of the model in section 3.2, a validation using two 2D laboratory experiments with non-breaking waves (Whalin, 1971, Berkhoff et al., 1982) is presented in section 3.3. Then the high-quality wave and swash measurements from a longshore-uniform laboratory experiment (Blenkinsopp et al., 2019, 2021) are used to perform an extensive validation of the model with respect to run-up processes in section 3.4. A sensitivity analysis is then carried out to evaluate the influence of various model parameters on the results, including the grid size, the initial phase distribution or the wave breaking criterion. This work takes the form of an article published in the *Journal of Marine Science and Engineering* (Pinault et al., 2020).

3.2 Description of the Boussinesq-type model *BOSZ*

Over the past decades, Boussinesq-type models (BTM) have undergone increasing popularity within the coastal engineering community (Brocchini, 2013). Indeed, the capabilities of these dispersive phase-resolving depth-integrated models makes them a suitable tool to capture nearshore wave processes. The BTM *BOSZ* (Boussinesq Ocean & Surf Zone model) (Roeber et al., 2010, Roeber and Cheung, 2012b) was developed for coastal applications including tsunamis studies (Horrillo et al., 2014, Lynett et al., 2017, Roeber and Cheung, 2012a, Morichon et al., 2021), harbor oscillations (Azouri et al., 2018, Bellafont et al., 2018) and wave transformations (Li et al., 2014, Filipot et al., 2019, Varing et al., 2020). In our study, the model is applied to compute nearshore wave transformations and most importantly wave run-up. In this section, the Boussinesq approach along with the BTM *BOSZ* are detailed.

3.2.1 Dispersion errors in Boussinesq-type equations

The idea of the Boussinesq equations (Boussinesq, 1872) is to reduce the three-dimensional problem to a bi-dimensional problem by getting rid of the vertical coordinate in the Navier-Stokes equations (or Euler equations). The horizontal and vertical flow are decomposed as a

truncated finite Taylor expansion as a closing equation for the vertical integration. The starting point of many works is the set of equations derived by Peregrine (1967), where the Taylor series is expressed using the depth averaged horizontal velocity $\bar{\mathbf{u}}$:

$$\begin{aligned} &\eta_t + \nabla.[(h+\epsilon\eta)\bar{\mathbf{u}}] = 0 \\ &\bar{\mathbf{u}}_t + \nabla\eta + \epsilon(\bar{\mathbf{u}}.\nabla)\bar{\mathbf{u}} + \mu^2\left[\frac{h^2}{6}\nabla(\nabla.\bar{\mathbf{u}}_t) - \frac{h}{2}\nabla[\nabla.(h\bar{\mathbf{u}}_t)]\right] = 0 \end{aligned} \tag{3.1}$$

The main limitation is the growing dispersion error as kh increases (see fig. 3.1). This error limits the range of applicability of the model and restricts it to the case of very long waves while the coastal area is largely influenced by short waves such as wind waves. In order to improve the frequency dispersion characteristics of the Peregrine (1967) formulation, Nwogu (1993) used the horizontal velocity at an arbitrary depth, yielding :

$$\begin{aligned} &\eta_t + \nabla[(h+\epsilon\eta)\mathbf{u}_\alpha] + \mu^2\nabla.\big[(\frac{z_\alpha^2}{2} - \frac{h^2}{6})h\nabla(\nabla.\mathbf{u}_\alpha) + (z_\alpha + \frac{h}{2})h\nabla[\nabla.(h\mathbf{u}_\alpha)]\big] = 0 \\ &\mathbf{u}_{\alpha t} + \nabla\eta + \epsilon(\mathbf{u}_\alpha.\nabla)\mathbf{u}_\alpha + \mu^2\big[\frac{z_\alpha^2}{2}\nabla(\nabla.\mathbf{u}_{\alpha t}) + z_\alpha\nabla[\nabla.(h\mathbf{u}_{\alpha t})] = 0 \end{aligned} \tag{3.2}$$

The truncated Taylor series expansion retains of the order of $O(\epsilon, \mu^2)$ where $\epsilon = a_0/h_0$ and $\mu = h_0/L_0$ express the non-dimensional parameters defining respectively the degree of non linearity and frequency dispersion (where a stands for the wave amplitude, h the water depth, L the wavelength and the subscript 0 denotes the deep water values of the associated quantities). The choice of using the velocity at an arbitrary depth rather than the usual depth averaged velocity improves the dispersion properties of the Boussinesq model, making it applicable to a wider range of water depths, from intermediate to shallow water and able to cope with fully non linear waves on a variable bathymetry. The dispersion properties are also improved by retaining contributions of higher order in the governing equations, but it strongly increases the computational costs.

The dispersion capacities of the formulation by Nwogu (1993) is compared to the one of Peregrine (1967) on figure 3.1 with $z_\alpha = -0.531h$. The set of equations from Nwogu (1993) agrees well with the Airy theory dispersion for $kh < \pi$. For $kh > \pi$ the dispersion error grows larger, overestimating the phase celerity and wavelength in deep water. The error reaches about 12% for $kh = 2\pi$. In the formulation from Peregrine (1967), an underestimation of the phase speed and wavelength is noted, with a computed phase speed of 85% of what it should be for $kh = \pi$. An in-depth comparison of the various BTM models can be found in Brocchini (2013).

3.2.2 *BOSZ* formulation of the Boussinesq equations

In the *BOSZ* model the set of equations from Nwogu (1993), consisting of a continuity equation and two momentum equations in the x and y direction, is expressed in a conservative

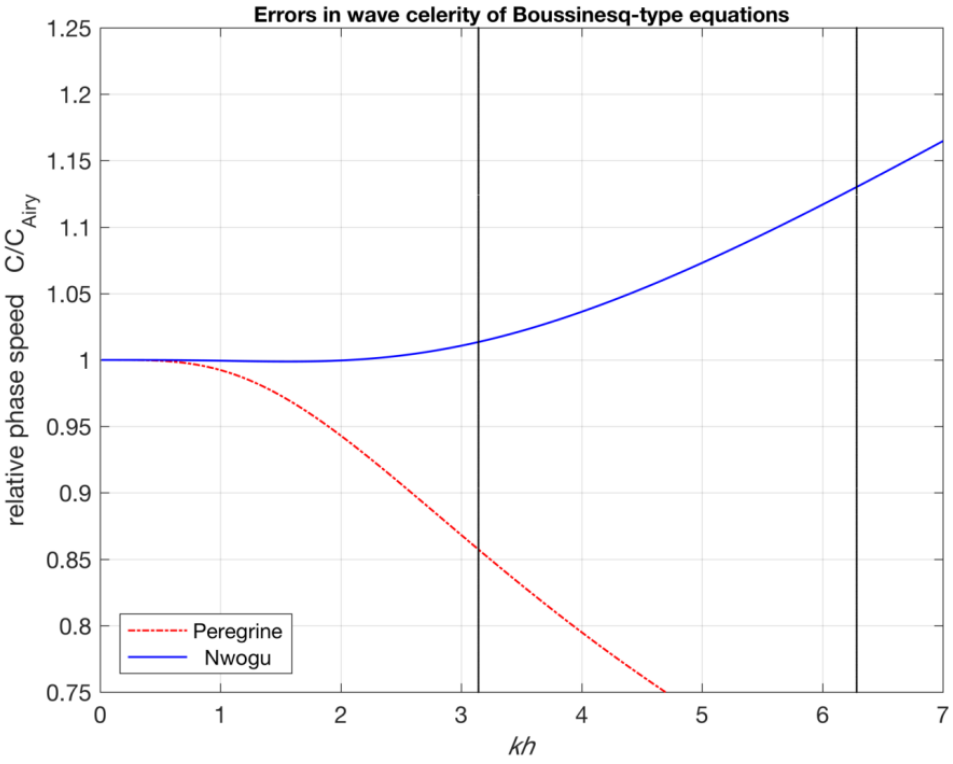

Figure 3.1: Error in kh with $z_\alpha = -0.531h$. Adapted from the *BOSZ* manual.

form and is written as follows :

$$\begin{aligned} & H_t + [Hu]_x + [Hv]_y \\ & + \left[\left(\frac{z_\alpha^2}{2} - \frac{h^2}{6}\right)h\big(u_{xx}v_{xy}\big) + \left(z_\alpha + \frac{h}{2}\right)h\big((hu)_{xx} + (hv)_{xy}\big)\right]_x \\ & + \left[\left(\frac{z_\alpha^2}{2} - \frac{h^2}{6}\right)h\big(v_{yy}u_{xy}\big) + \left(z_\alpha + \frac{h}{2}\right)h\big((hv)_{yy} + (hu)_{xy}\big)\right]_y = 0 \end{aligned} \tag{3.3}$$

$$\begin{aligned} & (Hu)_t + (Hu^2)_x + (Huv)_y + gH\eta_x \\ & H\frac{z_\alpha^2}{2}[u_{xxt} + v_{xyt}] + Hz_\alpha[(hu_t)_{xx} + (hv_t)_{xy}] \\ & + u\left[\left(\frac{z_\alpha^2}{2} - \frac{h^2}{6}\right)h\big(u_{xx}v_{xy}\big) + \left(z_\alpha + \frac{h}{2}\right)h\big((hu)_{xx} + (hv)_{xy}\big)\right]_x \\ & + u\left[\left(\frac{z_\alpha^2}{2} - \frac{h^2}{6}\right)h\big(v_{yy}u_{xy}\big) + \left(z_\alpha + \frac{h}{2}\right)h\big((hv)_{yy} + (hu)_{xy}\big)\right]_y \\ & + \tau_1 = 0 \end{aligned} \tag{3.4}$$

$$
\begin{aligned}
&(Hv)_t + (Hv^2)_x + (Huv)_x + gH\eta_y \\
&H\frac{z_\alpha^2}{2}[v_{yyt} + u_{xyt}] + Hz_\alpha[(hv_t)_{yy} + (hu_t)_{xy}] \\
&+ v\left[\left(\frac{z_\alpha^2}{2} - \frac{h^2}{6}\right)h\big(u_{xx}v_{xy}\big) + \left(z_\alpha + \frac{h}{2}\right)h\big((hu)_{xx} + (hv)_{xy}\big)\right]_x \\
&+ v\left[\left(\frac{z_\alpha^2}{2} - \frac{h^2}{6}\right)h\big(v_{yy}u_{xy}\big) + \left(z_\alpha + \frac{h}{2}\right)h\big((hv)_{yy} + (hu)_{xy}\big)\right]_y \\
&+ \tau_2 = 0
\end{aligned}
\tag{3.5}
$$

where h denotes the water depth, η the free surface elevation and $H = h + \eta$ the flow depth. The subscripts (x, y) and t stand for partial derivative with respect to space and time, g is the gravitational acceleration, (u, v) is the horizontal flow velocity at the reference depth z_α and (τ_1, τ_2) is the Manning roughness coefficient. The variables are defined on figure 2 in section 3.4 (Pinault et al., 2020).

The expression of the equations in a conservative form allows the use of Finite Volume Method. To handle discontinuities, such as the ones observed due to wave breaking, a shock-capturing Riemann solver scheme is used. The use of such scheme is not necessary where no discontinuities are observed, i.e. in most of the computational domain for typical coastal applications. In addition, it proved to be rather diffusive and therefore unusable in conditions where unbroken waves have to propagate over a large distance. To cater for this issue the *BOSZ* model offers the option to use the Finite Volume Riemann solver in the surf zone while a Finite Difference 2$^{\text{nd}}$-order upwind scheme, much less diffusive, is used in the rest of the domain. The

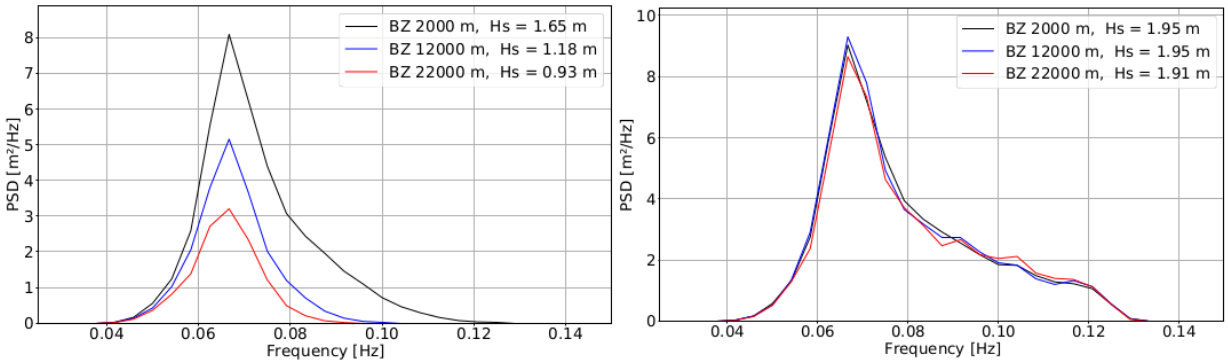

Figure 3.2: Evolution of the PSD of a propagating swell over flat bottom after 2km (black), 12km (blue) and 22km (red) for the Riemann flux (left) and 2$^{\text{nd}}$-order upwind scheme (right) formulations. The initial spectrum is TMA-shaped with $H_s = 2\,m$ and $T_p = 15\,sec$. Adapted from the *BOSZ* manual.

propagation of a TMA-spectrum over a flat bottom on figure 3.2 shows the decay of the wave field when using the Finite Volume, with a decrease of more than 50% of the input level after about 20 km. In comparison, the shape and the overall energy are well conserved in the case of the Finite Difference.

The time step is adaptative and based on the Courant–Friedrichs–Lewy condition (CFL). The Courant number is expressed as such in one dimension :

$$C = \frac{u\Delta t}{\Delta x} < C_{max} \tag{3.6}$$

where u is the velocity, Δx the grid size and Δt the time step. The CFL condition imposes that in one time step, information must not travel more than a cell, hence $C_{max} < 1$. For stability purposes a value of $C_{max} < 0.5$ is recommended.

3.2.3 Wave generation

Depending on the application, several types of wave input for the boundary condition can be used. It includes a sine wave, solitary wave, spectral distribution based on either empirical formulations or data and a free surface time series. The types of input used in this study are developed in the next subsections.

3.2.3.1 Empirical spectrum

Wave input conditions can be set in the model to follow predefined empirical spectral shapes, such as the commonly-used JONSWAP (Hasselmann and Olbers, 1973), Pierson-Moskovitz (Pierson and Moskowitz, 1964), Bretschneider (Bretschneider, 1959) or TMA spectra (Hughes, 1984). The wave spectrum is scaled to match the H_s given in input and shifted to the correct T_p. In order to prevent large over estimations of the phase speed and wavelength due to the frequency-dispersion error, a cut-off frequency is applied to the spectrum above which the energy is redistributed to the lower frequencies. The value of the cut-off depends on the user-defined maximum kh value, generally $kh = \pi$ (or equivalently $L = 2h$), and the offshore water depth. The energy above the frequency cut-off is redistributed to the lower part of the spectrum, to conserve the initial significant wave height H_s. While this limitation due to the weakly-dispersive properties of the equations is generally not too restrictive as the tail of the spectrum contains little energy, under certain conditions, for instance a wind sea in deep water, the energy redistribution will considerably modify the input spectrum. For instance, at a depth of $50\,m$ a cut-off frequency at $kh = \pi$ means that the resulting spectrum will not have energy for periods smaller than $8\,sec$. An example of the energy redistribution is provided on figure 3.3 for two different cases using a Pierson-Moskowitz spectrum. In panel **(a)** the initial spectrum (blue) a significant amount of energy is contained in the high frequencies ($T_p = 8\,sec$) and the water depth is relatively deep ($h = 50\,m$). This results in a relatively low frequency cut-off at $f = 0.1250\,H_z$ ($T = 8\,sec$), and a considerable amount of energy is therefore redistributed in the lower part of the spectrum, for energy conservation purposes. The resulting spectrum (red) is completely distorted from the initial one. In the second case, panel **(b)**, much less energy is contained in the tail of the spectrum and the depth is intermediate, leading to a relatively unchanged spectrum.

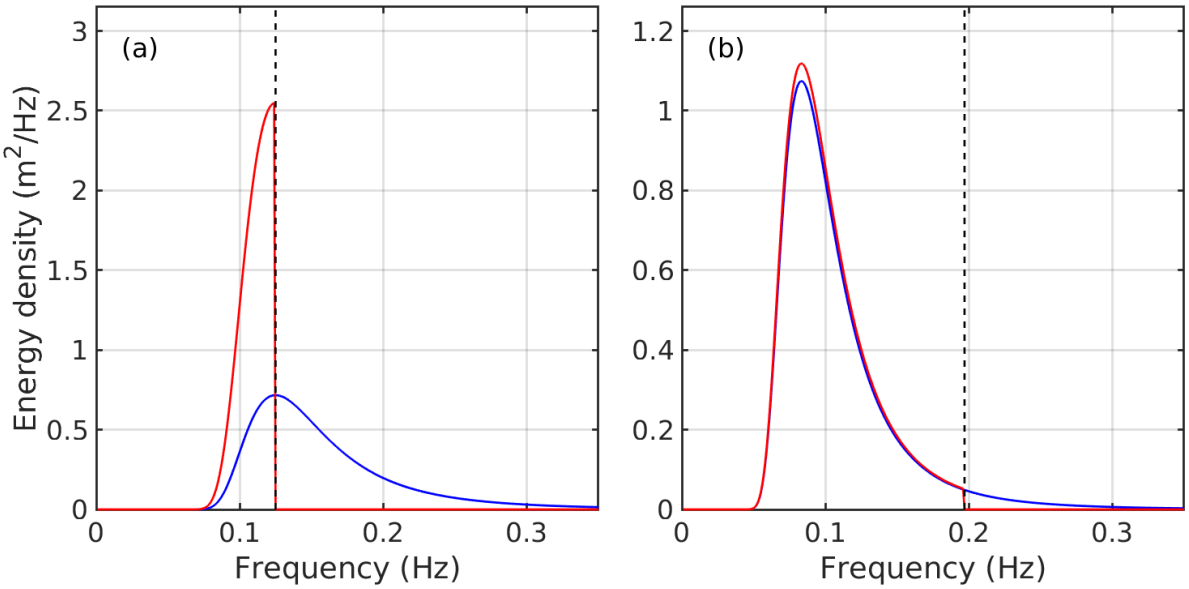

Figure 3.3: Redistribution of the energy above the cut-off frequency ($kh = \pi$) in the case of **(a)** $T_p = 8\,sec$ and $h = 50\,m$ and **(b)** $T_p = 12\,sec$ and $h = 20\,m$ for a Pierson-Moskowitz spectrum shape. Note that the PM spectrum naturally contains a significant amount of energy in the high frequencies, much more than a JONSWAP spectrum for example, amplifying the impact of the energy distribution.

The frequency-discretization of the initial spectrum depends on the user-defined duration of computation. This is made to ensure no recycling of a time series to prevent any artificial wave grouping. The frequency binning is calculated as :

$$\Delta f = \frac{1}{\Delta T} \tag{3.7}$$

where Δf is the frequency binning and ΔT the total length of computation. By doing so, the model ensures no repetition of the input time series at the wavemaker.

3.2.3.2 Spectral input

When the spectral distribution is available, via a wave buoy or a spectral model for example, it is possible to use it as the offshore boundary conditions in the model. The input spectrum undergoes the same treatment as the empirical spectrum i.e. the redistribution of the energy above the cut-off frequency and a frequency binning according to the length of the time series to avoid artificial recycling.

3.2.3.3 Time series

If available, time series of free surface elevation can be used as input in *BOSZ* . In field conditions it is rather rare to be given access to such information, but it is common in laboratory conditions. It has the advantage of providing the phases and thus allowing for extensive

comparisons (see section 3.4).
To initialize the solution, the free surface and and the horizontal particle velocities are needed. If the velocities are not known, which is often the case when the waves are measured using resistive gauges or LiDAR scanners, the velocity can be estimated using the long wave theory approximation :

$$U = \eta\sqrt{\frac{g}{h}} \tag{3.8}$$

This approximation holds within the long wave theory i.e. when waves are not too dispersive. In the case of short waves, for example a wind sea, at a relatively deep location, the approximation could significantly underestimate the velocity and therefore distort the initial solution.

3.2.4 Wave breaking implementation

As a depth-integrated formulation the overturning of the free surface can not be described so the description of the wave breaking processes is challenging. As the water depth decreases the wave steepens and the non-linearity increases, counter balanced by the dispersion terms in the equations. These terms can grow exponentially, to the point of creating numerical artifacts and in some cases instabilities. To avoid these situations the strategy is to deactivate locally and momentarily the dispersion terms over a few grid cells, along the wave breaking front. To identify the cells in which the deactivation might be needed, different criteria are implemented. Here, the strategy used it the wave height to water depth ratio. At each time step and in each grid cell, the ratio of the free surface elevation η and the local water depth h is evaluated. If the ratio exceeds the value of C_b, then the dispersion terms are switched off i.e. the Boussinesq-type equations are reduced to the NLSWE :

$$\frac{\eta}{h} > C_b \tag{3.9}$$

This strategy to determine wave breaking is in fact well known in coastal engineering, and often used to determine the maximum height a wave can reach prior to breaking. For instance, theoretical calculations by McCowan (1894) showed that the maximum ratio of the wave height over the water depth prior to breaking reached a value of 0.78 in the case of a solitary wave.
For numerical applications, the actual wave height, defined from crest to trough, can be calculated in 1D relatively easily by applying a zero up-crossing method for example. In 2D, it becomes more challenging as waves are free to propagate in any direction, the definition of crest to trough becoming more challenging. As an approximation, the free surface elevation η is used. It results in a slight underestimation of the wave height, but not more than 50% as the troughs are generally smaller than the crests in terms of amplitude.

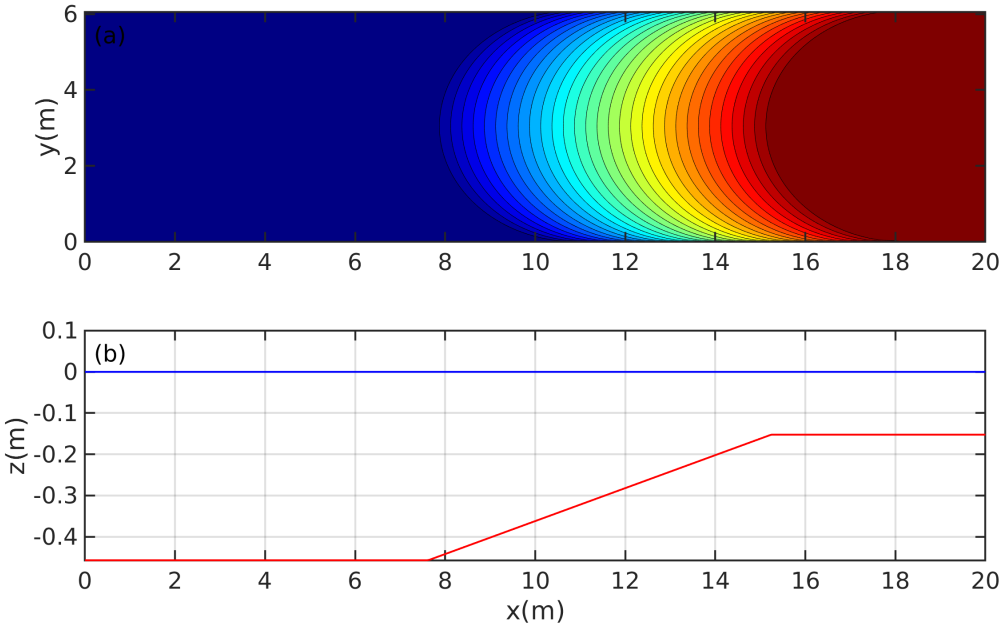

Figure 3.4: Bathymetry of the experiment. **(a)** : Colormap of the bathymetry. **(b)** : cross-shore profile in the middle of the domain.

3.3 Model validation on 2D non-breaking waves

In this section two numerical tests are presented in order to assess the *BOSZ* model for non-linear processes undergone by short-waves in the nearshore, namely refraction, diffraction and shoaling. The numerical tests are based on two-dimensional laboratory experiments performed with non-breaking waves. The laboratory benchmark cases include the wave propagation over a semicircular submerged shoal from Whalin (1971) and over an elliptic shoal from Berkhoff et al. (1982).

3.3.1 Wave propagation over a semicircular shoal

First, the *BOSZ* model is used to replicate a laboratory experiment originally performed by Whalin (1971). This test, which consists in the propagation of a unidirectional monochromatic waves over semicircular shoal, has become a standard to evaluate the ability to handle non linear refraction and diffraction for dispersive wave models (Engsig-Karup et al., 2008, Eskilsson and Sherwin, 2006, Eskilsson et al., 2006, Li et al., 1999, Madsen and Sørensen, 1992, Sørensen et al., 2004, Mara Tonelli, 2009, Walkley and Berzins, 2002, Ricchiuto and Filippini, 2014).

3.3.1.1 Experimental set-up

The original experiment was performed in a wave tank sized 25.6 mx6.069 m with a depth of 0.4572m at the wavemaker. The shoal starts around $x = 8\ m$, with a minimum depth of 0.1524m at the end of the tank, as shown on figure 3.4 panels **(a)** and **(b)**. The cross-shore section is linear with a slope of about 4% along the center-line. The isobaths are semi-circular,

and mathematically described by the set of equations 3.10.

$$h(x,y) = \begin{cases} 0.4572 & x \leq 10.67 - \lambda(y), \\ 0.4572 + 0.04(10.67 - \lambda(y) - x) & 10.67 - \lambda(y) < x < 18.29 - \lambda(y), \\ 0.1524 & x \geq 18.29 - \lambda(y) \end{cases} \tag{3.10}$$

Where $\lambda(y) = \sqrt{6.096y - y^2}$.

In this work, a monochromatic input with a period of $T = 2\,sec$ and amplitude of $A = 0.0075\,m$ is computed. It corresponds to a degree of dispersivity of $kh = 0.73 < 2$ indicating that it is in the range of applicability of the model, as shown on figure 3.1.

3.3.1.2 Model set-up

The computational domain consists in a square grid of $5\,cm$, meaning in case 1 the wave is described initially with 30 cells. The domain is made in total of 112362 cells. Lateral boundary conditions are set to solid reflective walls, consistently with the experiment, with a width of $6.069\,m$. To generate the input conditions an internal wavemaker is used, thus requiring a sponge layer for the outgoing signal generated. In addition, a sponge layer boundary condition is implemented at the end of the domain to prevent any wave reflection. For these reasons the numerical tank is longer than the one in the experiment, starting at $x = -10\,m$ up to $x = 36\,m$. The longer the wave the larger the wavemaker, for example in case 3 , which corresponds to the longest wave, the wavemaker source covers 42 cells, from $-8\,m$ to $-6\,m$ approximately. A standard bottom friction manning coefficient of $n = 0.013\,sm^{-1/3}$ is used to represent the concrete bottom used in the experiment. A standard CFL value of 0.5 was used. The free surface outputs are sampled at a rate of 20Hz.

3.3.1.3 Results

An example of the waves generated are shown on figure 3.5. The top panel shows a snapshot of the fully developed free surface. The shoaling can be noticed as well as the strong 3D effect due to focusing of the wave as it refracts on the elliptic shoal. Indeed, as the energy is gradually directed towards the center, the amplitude of the wave increases along the center-line. The focusing point, where the maximum of amplitude along the center-line is reached, is around $x = 18\,m$. The wave then propagates on a flat bottom and the energy is gradually spread out due to the effect of diffraction, leading to a decrease in amplitude around the center-line and an increase on the side. If the tank was infinite the wave would eventually return to its original shape.

To compare model results and laboratory data, a spectral analysis is performed on the free surface elevation time series along the cross-shore axis at the center of the tank, from $x = 3\,m$ to $x = 25\,m$. The figure 3.6 compares data and numerical results of the evolution of the 1^{st}, 2^{nd} and 3^{rd} harmonics. The wave appears to be very linear for low values of x (amplitude of the 2^{nd} and 3^{rd} harmonics very small corresponding to a sine wave) but as it propagates on the

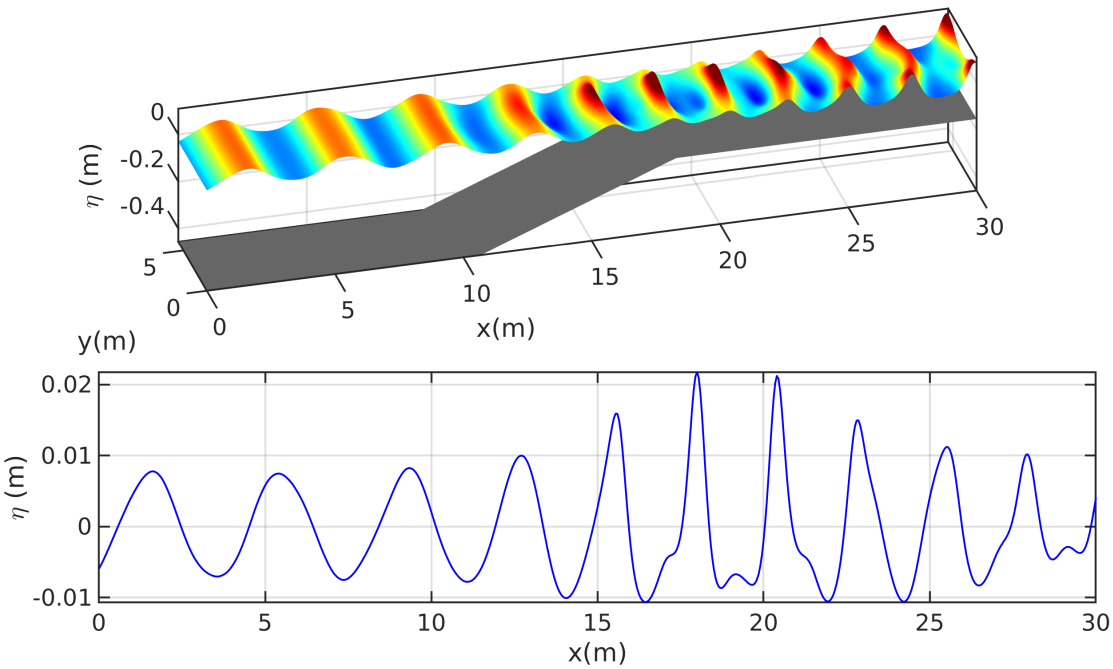

Figure 3.5: Perspective view of the free surface at t=420 s (top panel) and free surface profile in the middle of the domain (bottom panel).

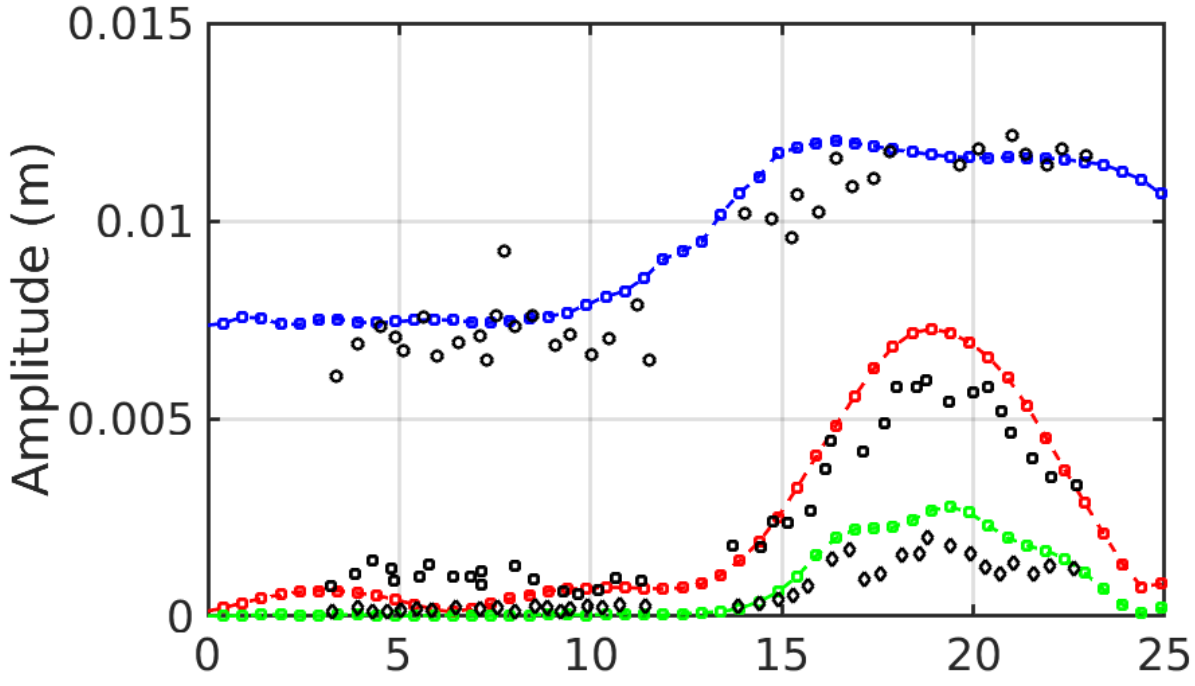

Figure 3.6: Comparison of 1st (blue), 2nd (red) and 3rd (green) computed (dashed line with square markers) and experimental harmonics along the center-line.

shoal the non-linearities increase. On both figure 3.5 and 3.6 it is clearly seen that the focusing point of the energy is around 18 m, where all harmonics show an increase, before decreasing on the flat part under the action of diffraction. The numerical results and the experimental data are in good agreement and show the same trend, suggesting that non-linear processes are correctly handled by the model.

3.3.2 Wave propagation over an elliptic shoal

Similarly to the previous experiment, the *BOSZ* model is compared to a laboratory experiment from Berkhoff et al. (1982). This test case, consisting in a unidirectional monochromatic wave propagating over a tilted slope and a shoal, is a classic test case to evaluate model performances for refraction (Mara Tonelli, 2009, Walkley and Berzins, 2002, Wei et al., 1995, Pengzhi Lin, 2007, Ma et al., 2012, Ricchiuto and Filippini, 2014).

3.3.2.1 Experimental set-up

The laboratory experiment was performed in 20 m wide and 22 m long tank with a depth of 0.45 m at the wave-maker, located in $y = -10\,m$. The bathymetry (figure 3.7) consisted in a tilted slope of 1/50, on top of which an elliptic shoal is placed, centered in $(0; 0)$. The bathymetry is mathematically described by $b(x, y) = b_f(x, y) + b_h(x, y)$ following equation 3.11 :

$$
\begin{aligned}
b_f(x,y) &= \begin{cases} (5.82 + y_r)/50, & \text{if } y_r \leq -5.82, \\ 0, & \text{otherwise} \end{cases} \\
b_h(x,y) &= \begin{cases} -0.3 + 0.5\sqrt{1 - (\frac{x_r}{5})^2 - (\frac{y_r}{3.75})^2}, & \text{if } (\frac{x_r}{5})^2 + (\frac{y_r}{3})^2 \leq 1, \\ 0, & \text{otherwise} \end{cases}
\end{aligned}
\tag{3.11}
$$

where $x_r = x\cos(20°) - y\sin(20°)$, $y_r = x\sin(20°) + y\cos(20°)$.
The input wave is monochromatic and unidirectional, with a period of $T = 1\ sec$ and an amplitude of $A = 0.0232\,m$.

During the experiment, time series of the free surface profile were measured along 5 longshore sections, as shown on the figure 3.7 at y=[1.0, 3.0, 5.0, 7.0, 9.0] and along the cross-section at the center-line (section 7).

3.3.2.2 Model set-up

The numerical domain consists in a square grid of 5 cm, spanning from $x = -20\,m$ up to $y = 16\,m$ and $x = -10\,m$ to $x = 10\,m$, for a total number of 289121 cells. The input sine wave is generate using an internal wavemaker, thus requiring a sponge layer for the outgoing signal. In addition, a sponge layer is applied at the end of the domain to prevent reflected waves from

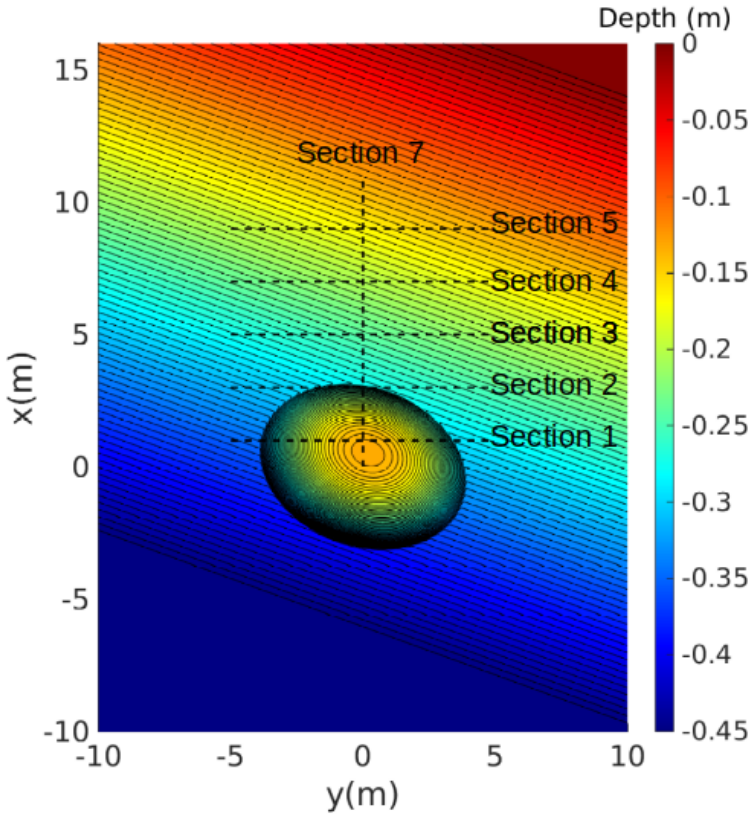

Figure 3.7: Bathymetry of the experiment. Black dashed lines represent the sections used for comparison between numerical results and experimental data.

entering the area of interest. Consistently with the experiment, the lateral boundaries are set to solid reflective walls.

A standard CFL value of 0.5 was used. A 20Hz sampling was used for the free surface elevation. The wave heights are measured using a zero-up crossing method on the last 20 seconds and the mean wave height is calculated consistently with the experiment.

3.3.2.3 Results

The results normalized by the incoming wave amplitude are compared on figure 3.8. As the wave propagates it bends under the action of refraction to align with the tilted isobaths (sections 1 and 2 on figure 3.8). Wave focusing due to the shoal occurs at sections 3 and 4, causing an increase of the wave height along the center-line which reaches a factor of 2 and starts decreasing afterwards in section 5. The cross-shore transect of section 7 clearly shows the increase of the wave height followed by the decrease under the action of diffraction as the wave moves further away from the shoal.

Table 3.1: NRMSE at each section calculated as NRMSE $= \frac{1}{X_{obs}}\sqrt{\frac{1}{N}\sum_{i=1}^{N}(X_{mod} - X_{obs})^2}$.

	Section 1	Section 2	Section 3	Section 4	Section 5	Section 7
NRMSE (%)	6.1	9.9	10.5	16.2	25.9	10.3

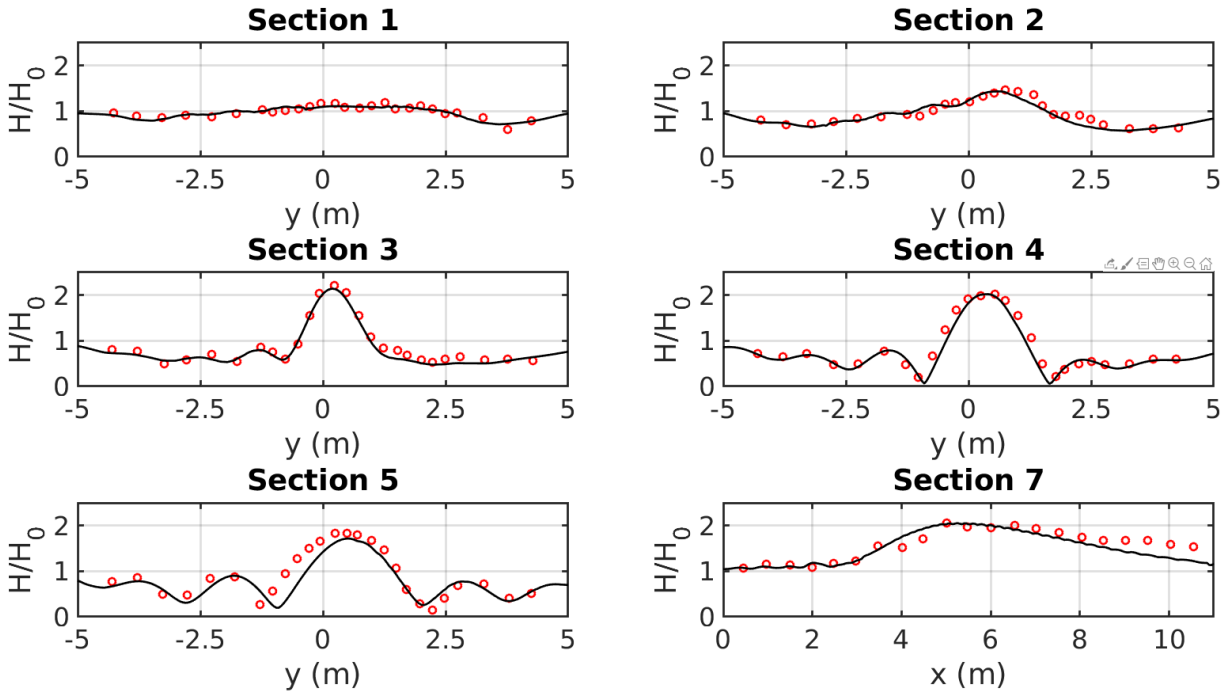

Figure 3.8: Numerical (solid black line) and experimental (red circles) free surface profiles along sections 1 to 5 and 7.

The agreement between laboratory and numerical results are satisfactory and comparable to previous studies found in the literature (Mara Tonelli, 2009, Walkley and Berzins, 2002, Wei et al., 1995, Pengzhi Lin, 2007, Ma et al., 2012, Ricchiuto and Filippini, 2014). These results demonstrate that wave refraction and diffraction can be well simulated by the numerical model.

3.4 Estimation of irregular wave runup on intermediate and reflective beaches using a phase-resolving numerical model - *Article in JMSE 2020*

In this section, the *BOSZ* model is validated against laboratory measurements (Blenkinsopp et al., 2019, 2021) for both wave transformations and run-up in the case of irregular breaking waves. This validation takes the form of an article published in the *Journal of Marine Science and Engineering* (Pinault et al., 2020).

Journal of
Marine Science and Engineering

MDPI

Article

Estimation of Irregular Wave Runup on Intermediate and Reflective Beaches Using a Phase-Resolving Numerical Model

Jonas Pinault *, Denis Morichon and Volker Roeber

Université de Pau et des Pays de lÁdour, E2S UPPA, chair HPC-Waves, SIAME, 64600 Anglet, France; denis.morichon@univ-pau.fr (D.M.); volker.roeber@univ-pau.fr (V.R.)

* Correspondence: jonas.pinault@univ-pau.fr

Received: 15 October 2020; Accepted: 1 December 2020; Published: 5 December 2020

Abstract: Accurate wave runup estimations are of great interest for coastal risk assessment and engineering design. Phase-resolving depth-integrated numerical models offer a promising alternative to commonly used empirical formulae at relatively low computational cost. Several operational models are currently freely available and have been extensively used in recent years for the computation of nearshore wave transformations and runup. However, recommendations for best practices on how to correctly utilize these models in computations of runup processes are still sparse. In this work, the Boussinesq-type model *BOSZ* is applied to calculate runup from irregular waves on intermediate and reflective beaches. The results are compared to an extensive laboratory data set of LiDAR measurements from wave transformation and shoreline elevation oscillations. The physical processes within the surf and swash zones such as the transfer from gravity to infragravity energy and dissipation are accurately accounted for. In addition, time series of the shoreline oscillations are well captured by the model. Comparisons of statistical values such as $R_{2\%}$ show relative errors of less than 6%. The sensitivity of the results to various model parameters is investigated to allow for recommendations of best practices for modeling runup with phase-resolving depth-integrated models. While the breaking index is not found to be a key parameter for the examined cases, the grid size and the threshold depth, at which the runup is computed, are found to have significant influence on the results. The use of a time series, which includes both amplitude and phase information, is required for an accurate modeling of swash processes, as shown by computations with different sets of random waves, displaying a high variability and decreasing the agreement between the experiment and the model results substantially. The infragravity swash S_{IG} is found to be sensitive to the initial phase distribution, likely because it is related to the short wave envelope.

Keywords: Boussinesq-type model; wave runup; LiDAR scanner

1. Introduction

Estimation of the total water level (TWL) at the shoreline is an important asset for coastal engineers and those involved in coastal zone management and engineering design. For instance, the TWL describes one of the key components in forecasting tools for the assessment of coastal flood risk or storm impact intensity [1–3]. The empirical formulae commonly used to design coastal structures, such as sea walls or rubble mound breakwaters, also rely on the determination of the maximum water level [4]. The calculation of the TWL has thus been the subject of many studies [5,6] aiming in particular to improve the estimation of the wave-induced runup [7–12], which is one of the primary contributions to the TWL with tide and atmospheric surge.

Wave runup is composed of a mean time component, the wave setup, and a time-varying component, the swash [13]. The setup depends on an increase in mean sea level at the wave period scale that balances the onshore component of the momentum flux of the waves in the breaking and surf zones [14]. The swash is composed of a short-wave (SW) or incident wave component, corresponding to high frequency oscillations of the water level in the frequency band between 0.04 and 0.25 Hz, and an infragravity (IG) component corresponding to the contribution of long waves with frequency ranging between 0.002 and 0.04 Hz. Therefore, the accurate determination of the runup contribution to the TWL requires tackling a series of challenges associated with the processes of transformation of short waves from intermediate to shallow waters together with the interaction of bound and free long waves. In addition, the respective contribution of SW and IG waves will depend on the type of beach. In the case of a dissipative beach, the dynamics of the swash zone will be dominated by IG waves, whereas for intermediate to reflective beaches both types of waves will contribute to the TWL at the shoreline [15].

One type of approach to estimate the runup consists of applying empirical formulations derived either from laboratory data [16–20] or field observations [13,21–24]. These formulae have the advantage of providing an estimation of the runup essentially based on the knowledge of offshore bulk wave parameters, such as the significant wave height H_s the peak wave period T_p, and the beach geometry as the foreshore beach slope β_f. This type of approach can easily be implemented into coastal risk forecasting tools based on fast and low cost computations. However, their application to beaches with complex 3D features is usually limited [7,10,23]. Indeed, comparing several empirical formulations Atkinson et al. [23] showed that the most accurate models give a relative error of $R_{2\%}$ of up to 25%. Thus, it is often necessary to develop site-specific runup formulations [25,26], which require a significant measurement effort to cover a wide range of oceanographic conditions at a given site [25]. Furthermore, it is often hazardous to collect data in natural environments, especially during extremely energetic events [10,27], which is probably the reason for the sparse existence of runup data from extreme events. Another limitation of empirical formulae is that they do not provide any information on the physical processes that control the wave-induced water level at the shoreline.

The limits of empirical formulae can be overcome through application of process-based deterministic numerical wave models. For instance, a phase-and-depth resolving model based on the Reynolds-averaged Navier–Stokes equations was recently used to study the sources of runup variability on planar beaches [28]. However, the application of this type of wave model is mainly intended for in-depth studies of physical processes that control wave transformations and their interactions with coastal structures [29]. Indeed, the high resolution and long computation time limit their application to real beach configurations. Phase-resolving and depth-integrated models offer a promising alternative. This type of approach allows to account for the main processes of wave transformation in intermediate and shallow waters, including dispersion and nonlinear effects, while requiring an acceptable computation time. For instance, the SWASH model [30], a widely used nonhydrostatic nonlinear shallow water model, was applied in 1D mode on an urbanized field site [11] and in 2D mode on a natural open sandy beach [10] to compute storm-induced runup. The COULWAVE model [31], a weakly dispersive and fully nonlinear Boussinesq-type model, was used to investigate wave processes in a fringing coral reef environment at two atoll sites in the western tropical Pacific [32]. The *BOSZ* model [33], a weakly dispersive and weakly nonlinear Boussinesq-type model was used to compute wave setup induced by energetic breaking waves at a fringing reef site in Hawai'i [34]. The model was incorporated into a full model suite for coastal inundation [35] and later used for probabilistic mapping of storm-induced coastal inundation under climate change scenarios [36]. Both studies involved large computational domains with millions of cells. Most of the previously cited studies demonstrate the ability of phase-resolving depth-averaged models to compute the cross-shore sea and swell waves, the IG waves, and wave-induced setup. This type of approach also succeeds in correctly estimating the 2% exceedance runup value ($R_{2\%}$) , which is usually

used as an indicator of storm impact intensity. However, few studies have focused on the detailed computation of time-varying swash dynamics.

Accurate measurements of water level oscillation at the shoreline under real conditions are usually difficult to perform. It requires one to instrument a thin layer of water, usually during energetic wave conditions in a changing environment. Laboratory data can offer the advantage of providing synchronized high temporal and spatial resolution of wave transformations and wave-driven water level oscillations under controlled conditions. Free surface elevations can be measured using resistance or capacitance wave gauges distributed along a cross-shore transect. The runup oscillation on the beach face is usually measured using a long capacitance wire gauge mounted normal to the beach slope at a fixed height above the bottom. For example, the data collected during the GLOBEX project [37] was used to validate the application of SWASH to compute the runup variability under dissipative conditions corresponding to irregular waves breaking over a gentle slope [38] for three different incident wave conditions. The relative runup errors ranged between 1% and 11%. Laboratory data of free surface elevation for eight gauges and runup oscillations were used to provide a comprehensive and detailed methodology for sensitivity analysis, calibration, and validation of the SWASH model for its application to the computation of runup oscillations over fringing reefs [39]. The fully nonlinear and dispersive Boussinesq-type model FUNWAVE-TVD was tested with laboratory data to assess its ability to predict the cross-shore evolution of significant wave heights in the SW and IG frequency bands, and the runup spectrum for irregular waves propagating over a laboratory scale fringing reef [40]. Detailed data from a laboratory experiment for waves breaking over submerged reef [41] were also used to validate the computation of runup over a steep-sided coastal structure with a Boussinesq-type model [42]. As an alternative to commonly used measuring devices such as pressure sensors or runup wires, the use of LiDAR scanners in coastal research is becoming increasingly common in both field [43–45] and laboratory [46] experiments. The use of a LiDAR scanner provides a continuous description of the area of interest, as opposed to point-by-point measurements with previously cited measuring devices. A single instrument is required to cover a relatively large area. Moreover, LiDAR scanners allow for remote measurements, thus providing data in a nonintrusive way. This can be critical for studies of small-scale processes where surface piercing instruments can lead to obstruction or disturbance of the flow.

In the present work, the Boussinesq-type wave model *BOSZ* [33,34] is compared to an extensive runup laboratory data set based on LiDAR data obtained during the DynaRev large-scale experiment [46]. The study focuses on the ability of a depth-integrated phase-resolving model to accurately compute both the setup and the contribution of SW and IG waves of the time-varying water elevation at the shoreline in intermediate and reflective beach configurations. Furthermore, this work presents a detailed sensitivity analysis of the computed results to the model settings, including the influence of phase distribution of the incident short waves and the definition of the threshold value for runup determination.

The outline of the paper is as follows. In Section 2, the model used in this study is described together with the laboratory data set. The comparisons between the model computations and measurements of spectral wave characteristics, free surface elevation time series, and runup components are presented in Section 3. A discussion of best practices for proper setup of a phase-resolving wave model with the objective to compute runup oscillations over intermediate and reflective beaches is presented in Section 4. Finally, concluding remarks are drawn in Section 5.

2. Methodology

2.1. Laboratory Experiment

The experimental runup data used in this study were collected during the DynaRev physical experiment that was carried out in the Großer Wellenkanal, GWK, (Large Wave Flume) in Hanover, Germany. The experiment originally focused on the investigation of the performance of specific revetments against erosion and runup excursions under varying wave conditions and water levels.

1805

A series of tests was performed in the 309 m long, 7 m deep, and 5 m wide canal equipped with a combined piston-flap type wavemaker. A more comprehensive description of the laboratory experiments is presented in Blenkinsopp et al. [46].

In total, more than 130 runs were completed for a total of 141.6 h of testing. The wave conditions followed the distribution of a JONSWAP spectrum. The tested wave conditions varied from $H_s = 0.6$ m to $H_s = 1.2$ m and from $T_p = 6$ s to $T_p = 12$ s with the water level between 4.5 m and 4.9 m. In the present study, only the 20 min long runs are considered. The sandy bottom was initially composed of a 1/15 planar slope (≈6.6%) (Figure 1). After the first runs, the bed reached an equilibrium with the development of a stable inner bar. Measurements of the bottom profile before and after each 20 min run show no significant bed changes occurred during this time.

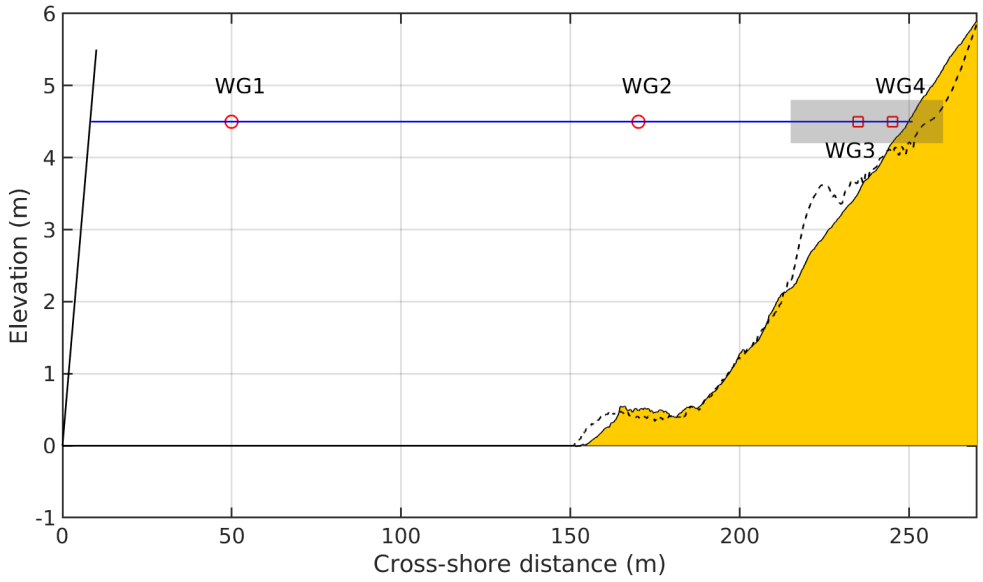

Figure 1. Bathymetric profile for case DR0 (see Table 1) with WG1 and WG2 wave gauge positions (red circles) as well as LiDAR scanner zone (grey area). WG3 and WG4 (red square) refer to virtual wave gauges derived from the LiDAR scanner measurements. The dashed line shows the profile for case SBE2 (see Table 1) indicating the inner bar.

Outside the surfzone, the free surface displacement was measured with two wave gauges WG1 and WG2 (Figure 1) located at $x = 50$ m and $x = 170$ m, respectively. The free surface displacement in the entire surf and swash zones was measured at high resolution using an array of three SICK LMS511 2D LiDAR scanners mounted on the experimental roof. Those scanners allowed to measure the free surface elevation continuously over an extent of 65 m (grey area on Figure 1), starting from the cross-shore position of $x = 215$ m up to the upper part of the beach at $x = 280$ m with a resolution of 10 cm. For detailed comparisons between model results and measurements in the surf and swash zone, two virtual gauges WG3 and WG4 (Figure 1) were set in order to extract water elevation time series from the LiDAR data. WG3 was located at a depth of 1 m and WG4 was positioned deep into the surfzone at a location where the profile is always submerged by at least 10 cm. For case DR0 (see Table 1), cross-shore locations of WG3 and WG4 correspond to $x = 235$ m and $x = 245$ m, respectively. Due to the nature of the LiDAR scanner vertical splashes occurring during the wave overturning process can potentially lead to abnormally high nonphysical values. After careful assessment of the data, these recording were removed from the samples. Wave gauges and LiDAR scanners were sampled at 25 Hz. Each run lasted 20 min and a spin-up time of 1 min was considered to allow the wave field to be fully saturated.

2.2. Selected Test Cases

Three test cases were selected from the DynaRev data set as they are representative of different beach states. Usually, the beach state is defined by the Irribaren number [17] or surf similarity parameter given by:

$$\xi = \frac{\beta_f}{\sqrt{H_0/L_0}} \tag{1}$$

where β_f is the foreshore slope and H_0 and L_0 are the deep-water significant wave height and wavelength, respectively. In the present study, the foreshore slope is calculated as the average slope over the swash zone as defined in Stockdon et al. [22]. Traditionally, a low Iribarren number ($\xi < 0.3$) indicates a dissipative beach. For higher values, ranging between 0.3 and 1.25, the beach is classified as intermediate, and for $\xi > 1.25$, it is classified as reflective [47]. According to this classification, the three selected cases allow to study runup for intermediate and reflective conditions. They are summarized in Table 1. The Ursell number, $U_r = H\lambda^2/h^3$, where H is the total wave height, λ the wavelength, and h the still water depth, expresses the degree of nonlinearity of the waves.

Table 1. Three beach state cases (I: intermediate, R: reflective). WL: water level.

Case Name	H_s (m)	T_p (s)	β_f (-)	ξ (-)	Initial Still WL (m)	Ursell Number U_r (-)	State
DR0	0.8	6	6%	0.50	4.5	11.7	I
SBE2	1.2	8	10%	0.91	4.9	28.2	I
SBA1	0.6	12	10%	1.93	4.9	33.7	R

2.3. Numerical Model

For the present study, the Boussinesq-type wave model *BOSZ* [33,34] is used to compute the runup for irregular waves propagating over intermediate and reflective beaches. This phase-resolving depth-integrated numerical model is based on a conserved variable formulation of Nwogu's equations [48]. Contrary to the nonlinear shallow water equations (NLSWE), Boussinesq equations naturally include dispersion terms to account for the nonhydrostatic pressure effects of periodic waves. To account for frequency dispersion, Nwogu [48] expressed the vertical gradient of the horizontal velocity at an arbitrary depth z_α through a truncated Taylor series expansion in combination with the irrotationality condition $u_z = w_x$. This allows for an approximation of the horizontal velocity's vertical variation in terms of only the horizontal velocity components at z_α. The third momentum equation in the z-direction vanishes from depth integration and a pseudo-3D solution is obtained in the 2D horizontal plane. The resulting set of equations agrees well with the Airy theory in terms of its dispersion properties for $kh < \pi$ or a little beyond that. For $kh > \pi$, the dispersion error increases, which causes an overestimation of the wavelength in deep water typical for most equations of this type. The value of z_α can be adjusted for an optimal compromise between linear dispersion and shoaling properties. For most applications, $z_\alpha = -0.531 \cdot h$ works reasonably well and is used throughout this study. The set of equations, expressed in conservative form, consists of a continuity equation and two momentum equations in the x- and y-directions. In 1D, only the terms in the x-direction are retained:

$$H_t + (Hu)_x + \psi_C + \psi_{wm} = 0 \tag{2}$$

$$(Hu)_t + H\frac{z_\alpha^2}{2}u_{xxt} + Hz_\alpha(hu_t)_{xx} + (Hu^2)_x + gH\eta_x + u\psi_C + \tau_1 = 0 \tag{3}$$

$$\psi_C = \left[\left(\frac{z_\alpha^2}{2} - \frac{h^2}{6}\right)hu_{xx} + \left(z_\alpha + \frac{h}{2}\right)h\,(hu)_{xx}\right]_x \tag{4}$$

The second and third term in the momentum equation arise from the Boussinesq-type approximation derived by Nwogu [48] and account for nonhydrostatic pressure correction. The term $u\psi_C$ is not part of the original equation by Nwogu [48] and due to conserved variable formulation of

Roeber et al. [33]. The term results from the following expression of the momentum equation of the NLSWE with the local acceleration term expressed with the conserved variable (Hu) instead of with only u:

$$H(u_t + uu_x + g\eta_x) = (Hu)_t + (Hu^2)_x + Hg\eta_x - u[H_t + (Hu)_x] = (Hu)_t + (Hu^2)_x + Hg\eta_x + u[\psi_C], \quad (5)$$

as $H_t + (Hu)_x = -\psi_C$ from the continuity equation. The momentum equation therefore includes information from the continuity equation that supports the correct representation of a shock front in terms of flow depth, speed, and dissipation. The mass source term, ψ_{wm}, serves as the internal wavemaker for the generation of periodic waves (see Wei et al. [49]). Here, h denotes the water depth, η denotes the free surface elevation, and $H = h + \eta$ denotes the total flow depth. The variables are defined on Figure 2. The subscripts x and t stand for partial derivatives with respect to space and time, g is the gravitational acceleration, u is the horizontal flow velocity at the reference depth z_α, and τ_1 is the Manning roughness term.

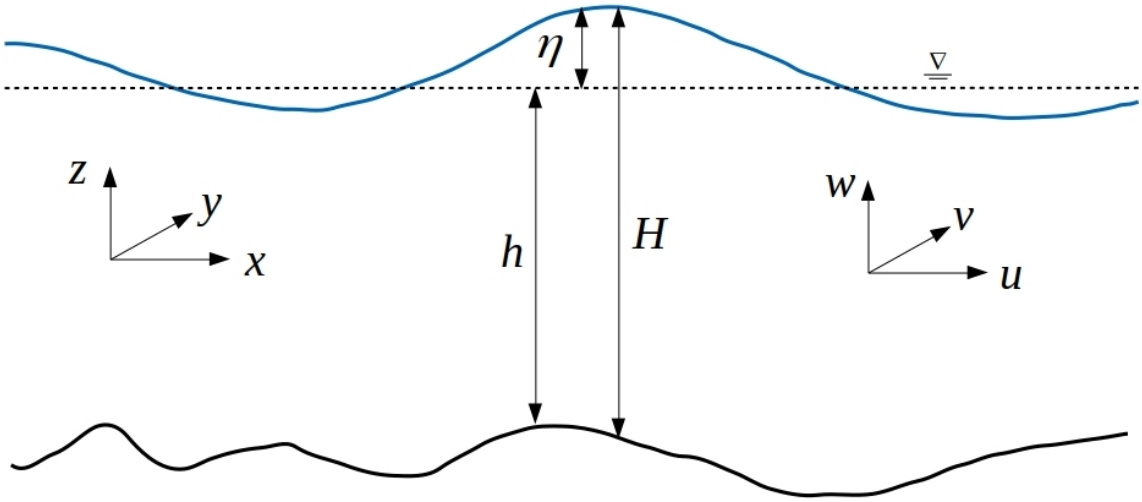

Figure 2. Definition sketch of the free surface flows.

Since the equations are depth-integrated, the solution cannot describe wave overturning, which essentially requires more than one value of the solution in the vertical direction. Therefore, a breaking wave is approximated as bore or hydraulic jump with a discontinuous profile. Since the governing equations contain the elliptic dispersion terms, discontinuous solutions are not directly possible, but they require special treatment along the breaking wave front. One possibility is the deactivation of the dispersion terms locally and momentarily based on particular conditions queried in each time step. The *BOSZ* code offers several options to identify individual cells along the wavefront where the dispersion terms can be ignored and the solutions from the subset of the NLSWE can be used instead. These options include criteria based on geometry and kinematics. Here, the criterion based on a free surface elevation to water depth ratio is used, expressed as follows:

$$\frac{\eta}{h} > C_b \quad (6)$$

If the ratio of free surface to water depth is larger than a given value C_b, the dispersion terms are deactivated. It is important to note that no additional term is strictly required to account for the energy dissipation under breaking waves, since the shock-solution of the underlying NLSWE in combination with a shock-capturing numerical scheme properly accounts for the dissipation rate. The approach of deactivation of dispersion terms has been used in multiple previous studies and provides a robust solution as long as the grid spacing is not excessively fine.

Theoretical calculations from McCowan [50] showed that the highest ratio of η/h in shallow water prior to breaking was 0.78, which is the value adopted here. However, the study by McCowan [50] refers to the ratio of wave height to water depth that includes the leading trough, which is difficult to compute on the fly. The sensitivity of the results to the value of C_b is addressed in the discussion.

2.4. Model Settings

The upstream boundary of the numerical domain is lined up with the first gauge WG1 of the physical experiment. The total length of the numerical domain is 222 m long. The grid size of the computational domain is constant and set to $dx = 0.5$ m. For each test case, the free surface elevation time series measured at WG1 is prescribed at the offshore wave boundary, allowing the model to be forced with the exact incident wave phases. Since the incident wave velocity imposed at the offshore boundary is not available from the experiment measurements, it is computed using the shallow water approximation based on Airy wave theory that relates wave speed to the local water depth:

$$U = \eta \cdot \sqrt{\frac{g}{h}} \tag{7}$$

where U is the horizontal particle velocity. Though the time series clearly shows dispersive waves, the selected conditions are of relatively low frequency dispersion ($kh < 0.25\pi$), which reasonably justifies the long wave approximation. In order to match the conditions of the experiment, a constant Manning friction coefficient of $n = 0.02$ sm$^{-1/3}$ is used to account for sand of medium grain size. The time step is adaptive to ensure stability under the Courant-Friedriechs-Lewy (CFL) condition of a fixed value of 0.5. The free surface was saved to output files at a frequency of 10 Hz.

2.5. Data Analysis

The power spectral density (PSD) of the free surface elevation is computed by applying a fast Fourier transform (FFT) algorithm to 5 min segments of the 19 min time series using a 50% overlapping Hanning window, resulting in about 20 degrees of freedom and a frequency resolution of $df = 0.0033$ Hz. Associated 95% confidence intervals are calculated according to Emery and Thomson [51]. While 19 min is relatively short for low frequency analysis, it is a common duration in runup studies[7,10,22,52], as the results over this time span are hardly influenced by tidal fluctuations or offshore conditions. Nonetheless, given the short duration of the experimental data, the results of low frequency components, i.e., periods longer than 1 min, are subject to uncertainty. The significant wave height is then calculated as:

$$H_s = 4\sqrt{m_0} \tag{8}$$

where m_0 denotes the zero-order spectrum moment.

Instantaneous free surface elevation is averaged over the 19 min at each cross-shore location to provide spatial distribution of the setup $\bar{\eta}$. The time-varying shoreline elevation $\eta_s(t)$ is tracked as the last cell in the shoreward direction where the water depth is greater than a threshold depth δ. The value of δ was fixed to 10 cm as recommended in previous studies [7]. This value was applied to process both numerical and physical data. An example of the results of shoreline tracking carried on scanner data is shown in Figure 3.

In the numerical experiment, all calculations are performed using fixed bathymetry. Comparisons of the bathymetric profiles before and after each 20-min trial showed that no significant changes were observed, validating the use of fixed bathymetry. Alternative methods that take small-scale bed variations into account [44] are not reproducible with a numerical model such as *BOSZ* . For the sake of consistency in the analyses, the data from the numerical model and from the experiment were processed in an identical way, i.e., over a fixed profile. The swash time series is obtained by removing the shoreline setup $\bar{\eta}_s$ from the shoreline elevation time series $\eta_s(t)$. The swash power spectral density is derived in a manner similar to that of the free surface spectra. The significant swash height $S_{[f_l:f_h]}$

of a given frequency band obtained between f_l and f_h is calculated by computing the power spectral density of the swash time series according to:

$$S_{[f_l:f_h]} = 4\sqrt{\sum_{f_l}^{f_h} PSD(f)df} \tag{9}$$

where f_l and f_h denote the low and high frequency cutoff, respectively, and df is the frequency resolution (first non-null value of the frequency vector). The total significant swash height is then computed according to:

$$S = \sqrt{S_{SW}^2 + S_{IG}^2} \tag{10}$$

where S_{SW} and S_{IG} denote the significant swash heights computed in the SW frequency band ($f_l = f_p/2$ and $f_h = 3f_p$), and in the IG frequency band ($f_l = df$ and $f_h = f_p/2$), respectively.

Finally, the 2% runup exceedence ($R_{2\%}$) corresponding to the maximum water elevation reached by 2% of the highest runup is computed according to Stockdon et al. [22] consistently with other studies [11,28,52]:

$$R_{2\%} = 1.1(\bar{\eta}_s + S/2) \tag{11}$$

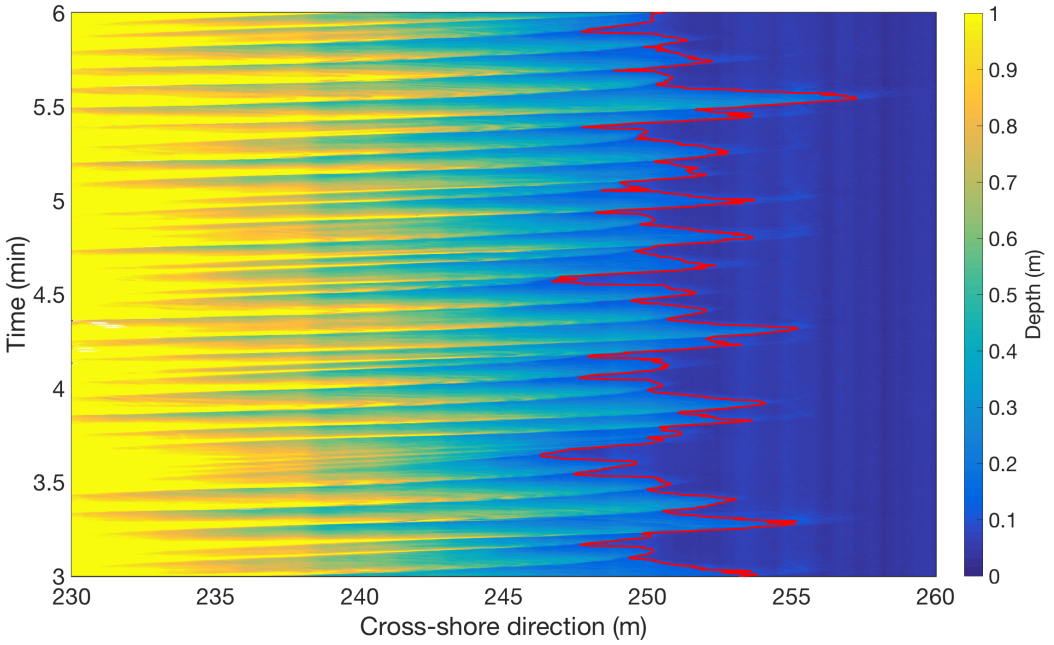

Figure 3. LiDAR scanner flow depth measurement using a threshold depth of 10 cm.

3. Results

The *BOSZ* model computes wave transformation processes including shoaling, breaking, and energy transfer between SW and IG waves. These quantities are compared with measurements for the three test cases from Section 2.1. Moreover, the detailed scanner data are used to examine the model for the calculation of wave-induced oscillations of the shoreline water elevation and runup statistics.

3.1. Wave Propagation

3.1.1. Spectral Wave Characteristics

The depth-induced wave breaking between gauges WG2 and WG3 results in a significant energy dissipation that is well captured by the model for the three cases (Figure 4). In addition, the transfer

1810

of energy from the SW frequency band to the IG band caused by time variations of the breaking point position is also accurately computed. Measurements carried out deep in the surf zone, at gauge WG4 for the intermediate beach cases DR0 and SBE2, reveal that most of the peak energy has been dissipated and the energy is now distributed between the IG and SW frequency bands (Figure 4c,f). For the reflective beach case SBA1 (Figure 4i), the energy at WG4 is distributed between the two frequency bands with a clear peak in the SW band. The detailed wave transformation patterns from the surf zone up to the swash zone for the three beach state configurations are well reproduced by the model.

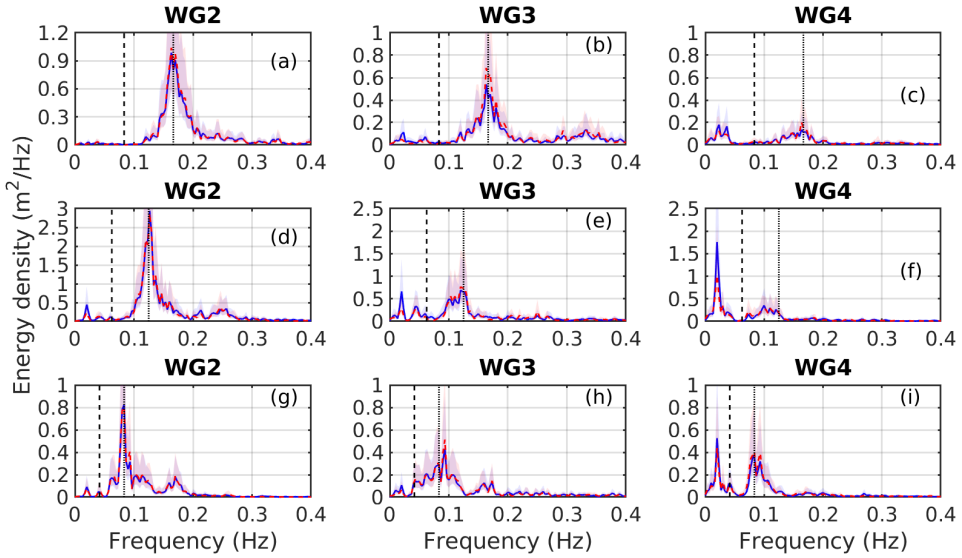

Figure 4. Comparisons between the observed (red dashed line; mostly obstructed) and computed (blue solid line) spectra at the three wave gauge locations for case DR0 (**a**–**c**), SBE2 (**d**–**f**), and SBA1 (**g**–**i**). The vertical dotted line represents the peak frequency and the black dashed line represents the frequency cutoff between the SW and IG band. Shaded areas define the 95% confidence intervals. The bathymetric profile was assumed fixed in the numerical computation for each of the three scenarios.

The model's accuracy to compute wave energy transfers in the surf and swash zones is evaluated by computing the relative error of H_s at the different gauge locations that is defined as:

$$E(\%) = 100\frac{H_s^p - H_s^m}{H_s^m} \tag{12}$$

where H_s^p and H_s^m stand for the predicted and the measured significant wave heights H_s, respectively. The errors of the total significant wave height H_s, the short-wave significant wave height H_{SW} and the infragravity significant wave height H_{IG} are summarized in Table 2. The highest error is reached for case SBE2 at WG3 due to an overestimation of H_{IG}, while it is low for the two other cases. The IG component H_{IG} appears to be slightly overestimated in all cases. Deeper into the surfzone, at WG4, the discrepancy reduces. The absolute errors, the difference between the modeled and measured setup, are less than 3.1 cm, which is low given the overall scale of the test. The errors are of the same order of magnitude as the precision of the initial still water level measurements.

Continuous cross-shore LiDAR measurements of the evolution of the significant wave heights associated with the different frequency bands are compared to the numerical results on Figure 5 for all cases. As Table 2 showed, H_{IG} is slightly overestimated in the outer surfzone but reduces in the inner surfzone. The free surface profiles modeled are in good agreement with the LiDAR measurements as shown in the bottom panels of Figure 5.

Table 2. Relative error of H_s, H_{SW}, and H_{IG}, and absolute errors of the setup $\bar{\eta}$ at the different wave gauges locations. The still water level is indicated for reference.

Case Name		WG2	WG3	WG4
DR0	depth (m)	4	1	0.30
	H_s (%)	−1.95%	−2.52%	−1.36%
	H_{SW} (%)	−1.70%	−6.70%	−3.17%
	H_{IG} (%)	+5.24%	+23.3%	+3.25%
	$\bar{\eta}$ (cm)	−1.0	−2.0	−3.1
SBE2	depth (m)	4.5	1	0.45
	H_s (%)	1.28%	8.51%	6.90%
	H_{SW} (%)	+0.58%	−1.23%	−2.47%
	H_{IG} (%)	+13.4%	+19.5%	+16.6%
	$\bar{\eta}$ (cm)	2.7	−0.3	−1.4
SBA1	depth (m)	4.5	1	0.45
	H_s (%)	−1.14%	−0.55%	−0.91%
	H_{SW} (%)	−2.01%	−3.06%	−6.06%
	H_{IG} (%)	+10.4%	+23.9%	+9.58%
	$\bar{\eta}$ (cm)	0.08	−1.5	−2.6

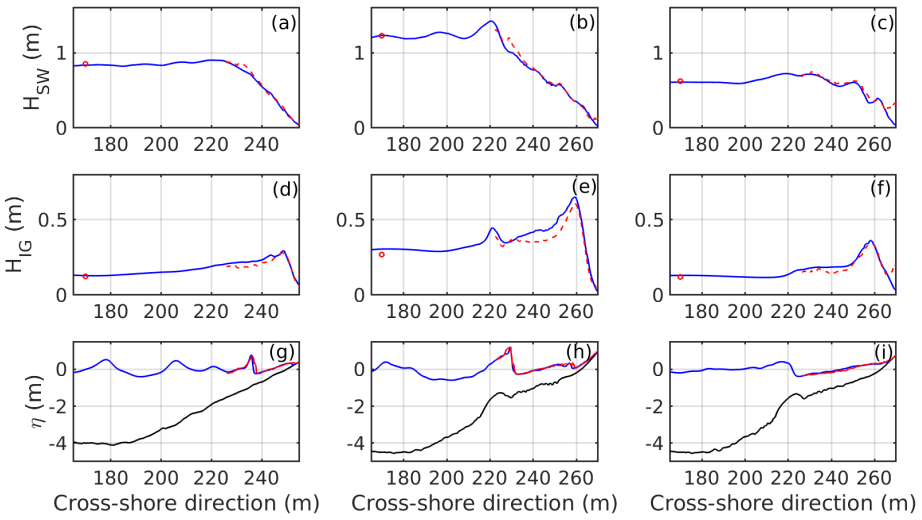

Figure 5. Cross-shore evolution of computed (blue solid line) and observed (red dashed lines) significant wave heights. Values at WG2 are shown as circles at $x = 170$ m. (**a**–**c**): H_{SW} of cases DR0, SBE2, and SBA1. (**d**–**f**): H_{IG} of cases DR0, SBE2, and SBA1. (**g**–**i**): bed profiles with modeled (blue) and LiDAR measurements (red) of the instantaneous free surface at $t = 961$ s.

3.1.2. Free Surface Elevation

Comparisons of the free surface time series are shown for case DR0 at the four wave gauges (Figure 6). The agreement between physical and numerical model results is fairly good. The wave amplitudes and phases computed with the model generally match the measurements. The asymmetry of the waveform that resembles a sawtooth wave as a result of wave shoaling and the amplitude attenuation by friction and breaking are well reproduced. The results for cases SBE2 and SBA1 are of comparable agreements and are therefore not shown for brevity.

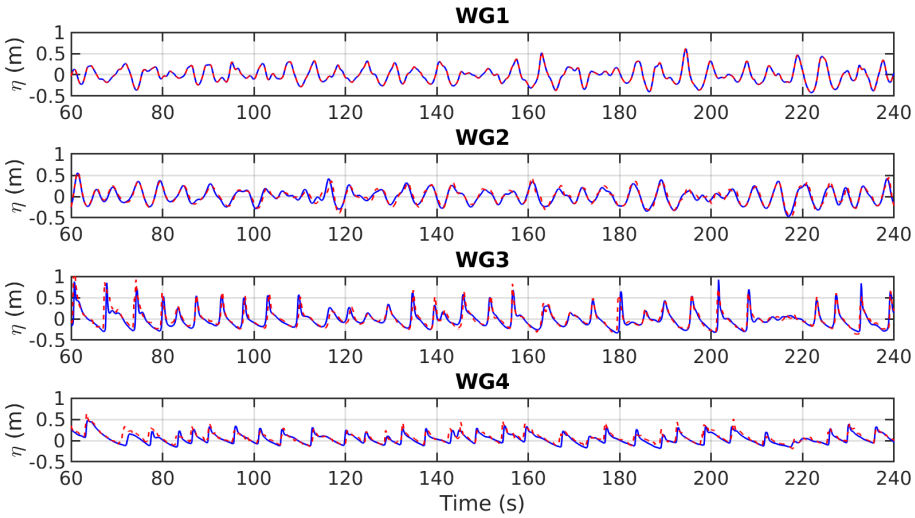

Figure 6. Comparisons between observed (red dashed line) and computed (blue solid line) free surface time series at different cross-shore locations for case DR0.

The ability of the model to reproduce the evolution of the free surface along the flume as well as the shoreline motion is evaluated through the root mean square error (RMSE), bias, coefficient of determination R^2, and Willmott's index of agreement. Willmott's index [53] is computed as:

$$d = 1 - \frac{\sum_{i=1}^{n}(C_i - O_i)^2}{\sum_{i=1}^{n}(|C_i - \bar{O}| + |O_i - \bar{O}|)^2} \tag{13}$$

where C and O denote the computed and observed values, respectively, and n the total number of points. The agreement index has values between 0 and 1, $d = 1$ meaning a perfect agreement between the observed and computed values and, conversely, $d = 0$ indicating no agreement at all between the values. The results for the three wave gauges are summarized in Table 3.

Table 3. RMSE, bias, R^2, and Willmott's index of agreement d at the three wave gauges.

	RMSE (m)	Bias (m)	R^2 (-)	Willmott's d (-)
DR0				
WG2	0.06	−0.01	0.93	0.98
WG3	0.09	−0.02	0.67	0.90
WG4	0.09	−0.04	0.60	0.87
SBE2				
WG2	0.11	0.03	0.90	0.97
WG3	0.17	−0.003	0.55	0.86
WG4	0.13	−0.01	0.60	0.88
SBA1				
WG2	0.04	0.01	0.95	0.99
WG3	0.1	−0.01	0.74	0.93
WG4	0.1	−0.03	0.68	0.89

The Willmott's index of 0.86 and higher confirms the satisfying agreement between computed and measured time series for all cases and at all locations. The coefficient R^2 shows a decreasing correlation between the model and the experiment in the surfzone at WG3 and WG4. A continuous cross-shore analysis of the coefficient R^2 in the LiDAR scanner area (not shown here) shows that high values of R^2 are observed prior to breaking and that the values decrease continuously throughout the surfzone. The limitation of depth-integrated equations in the breaking zone is a possible explanation for this trend. Moreover, LiDAR scanners are known to capture large vertical splashes occurring during energetic

breaking events, locally leading to overestimation in the free surface measurements. A negative bias is observed for all experiments at WG3 and WG4. A possible explanation, consistent with the analysis of R^2, is a slightly excessive dissipation of wave energy around the onset of wave breaking due to the selected condition of deactivation of the dispersion terms in the governing equations of the model.

The ability of the numerical model to capture second order statistics is evaluated with the comparisons of wave skewness S_k and asymmetry A_s, calculated as [54]:

$$S_k = \frac{\langle (\eta - \bar{\eta})^3 \rangle}{\langle (\eta - \bar{\eta})^2 \rangle^{3/2}} \tag{14}$$

$$S_k = \frac{\langle \mathcal{H}(\eta - \bar{\eta})^3 \rangle}{\langle (\eta - \bar{\eta})^2 \rangle^{3/2}} \tag{15}$$

where $\mathcal{H}$ denotes the Hilbert transform and $\langle . \rangle$ denotes the time-average operator. These two quantities provide information on the wave-by-wave shape in contrast to the computed and measured comparison of the free surface elevation. Increasing values in wave skewness mean more asymmetry in the vertical direction, i.e., the wave crests increase proportionally more than the troughs decrease. Negative values in the waves' asymmetry indicate a steepening of the wave face toward the beach with a sharper leading edge and a flattened back. Especially for breaking waves, where the local wave dissipation can influence the shape of the individual waves significantly, it is difficult to obtain close agreement between measured and computed skewness and the asymmetry value. The cross-shore evolution of S_k and A_s are shown for all cases on Figure 7.

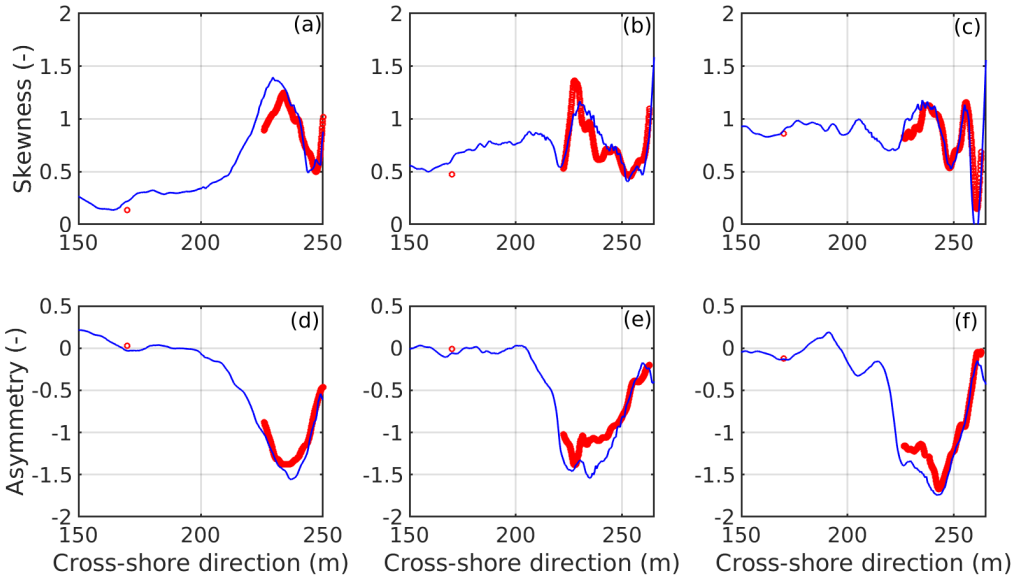

Figure 7. Cross-shore evolution of the computed (blue solid line) and observed (red circles) skewness S_k and asymmetry A_s for all cases. Values at WG2 are shown as circles at $x = 170$ m. (**a**–**c**): S_k of cases DR0, SBE2, and SBA1. (**d**–**f**): A_s of cases DR0, SBE2, and SBA1.

The sharp decrease of the wave asymmetry A_s, due to the steepening of the face as the depth decreases, is well captured by the model. The vertical deformation characterized by increasing values in skewness is observed similarly in both numerical and laboratory data. Considering the challenging conditions in the surf zone, the agreement between model and laboratory data is satisfying.

Overall, these comparisons show that the wave transformation processes in the surf and swash zones on intermediate and reflective beaches can be computed with a high degree of accuracy and confidence by a phase-resolving depth-integrated model such as *BOSZ* .

3.2. Wave Runup

3.2.1. Shoreline Elevation Oscillations

The LiDAR scanner allows for accurate measurements of the shape of the runup tongue from which the water line position can be inferred. The measured and computed shoreline elevation time series $\eta_s(t)$ are compared on Figure 8. The model succeeds in reproducing the amplitude and phases of the shoreline oscillations.

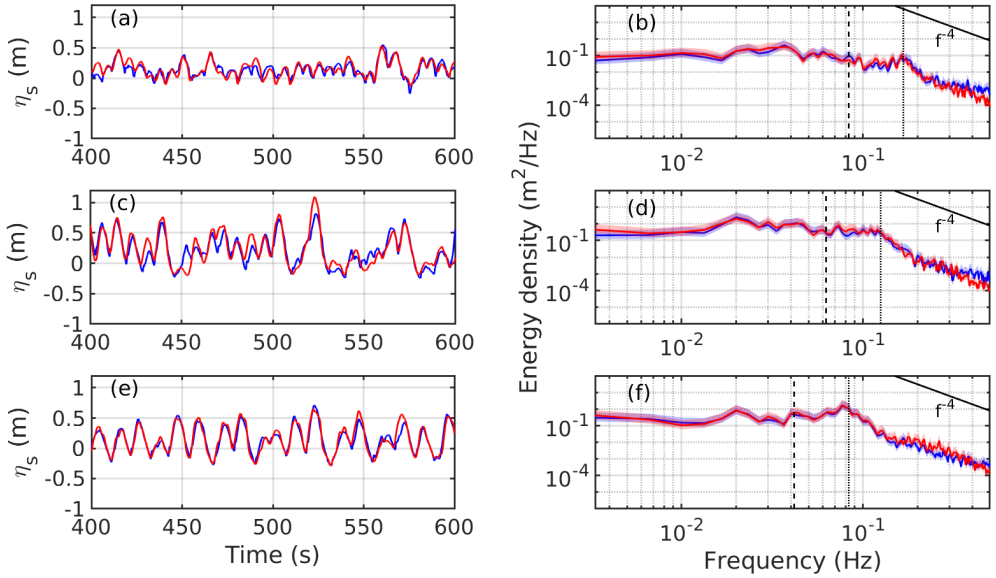

Figure 8. Comparisons between the observed (red) and simulated (blue) continuous shoreline elevation η_s and swash spectra for cases DR0 (**a**,**b**), SBE2 (**c**,**d**), and SBA1 (**e**,**f**). Blacked dashed line: IG cutoff frequency ($f_p/2$). Black dotted line: peak frequency f_p. Shaded areas define the 95% confidence intervals.

The swash energy distribution is also well captured by the model. For instance, the model shows that the swash spectrum at high frequencies exhibits a spectral decay of f^{-4}, which is consistent with the measured spectra and other studies [21,55]. Furthermore, for the two intermediate beach state cases DR0 (Figure 8b) and SBE2 (Figure 8d), the swash is mainly dominated by low-frequency or infragravity oscillations, whereas for the reflective case SBA1 (Figure 8f), the SW contributions to the shoreline oscillations become more important. For all cases, the results show good agreement between the measured and modeled swash spectra. Following the statistical analysis of the wave gauges from Table 3, the RMSE, bias, R^2 coefficient, and Willmott's index for the shoreline motion η_s are presented in Table 4.

Table 4. RMSE, bias, R^2, and Willmott's index of agreement d for η_s.

Case Name	RMSE (m)	Bias (m)	R^2 (-)	Willmott's d (-)
DR0	0.07	−0.01	0.71	0.87
SBE2	0.13	−0.02	0.79	0.91
SBA1	0.08	−0.01	0.89	0.96

Willmott's index indicates a close match between the numerical and experimental time series, with values higher than 0.87. A negative bias is observed for all cases, suggesting that the model underestimates the amplitude of the oscillations. It is consistent with Table 3 where all bias at WG4 are negative. A possible explanation is a slight overdissipation of energy in the surfzone due to the breaking parametrization. Interestingly, the values presented in this table indicate a better match of η_s

1815

than for η at WG4. Overall, the statistics show that the model is capable of capturing the time series oscillations with a satisfying accuracy.

3.2.2. Runup Statistics

To quantify the ability of the model to compute the different contributions to $R_{2\%}$, SW and IG swash components (S_{SW} and S_{IG}, respectively) and the shoreline setup $\bar{\eta}_s$ are computed and compared to the measured values. The results are displayed in Table 5. The relative discrepancy between the observed and computed $R_{2\%}$ is low, ranging between -3.4% and -6.0% which is comparable to the SWASH model performance for dissipative beach [38]. The underestimation of $R_{2\%}$ is consistent with Tables 3 and 4, suggesting that an overdissipation of the short wave energy in the surfzone results in underestimation of $R_{2\%}$ values. The infragravity component S_{IG} is well reproduced by *BOSZ* for the three cases with a maximum relative error of the order of 3%. Discrepancies are more pronounced for the computation of S_{SW}. However, the relative errors are smaller than 10%. Similarly to S_{SW}, the shoreline setup $\bar{\eta}_s$ displays error smaller than 10%.

Table 5. Relative errors of the $R_{2\%}$ and the different runup components. Values from the numerical model are shown after the vertical bar.

Case Name	$R_{2\%}$		S_{SW}		S_{IG}		$\bar{\eta}_s$	
DR0	−3.4%	0.44 m	−1.2%	0.28 m	−3.3%	0.42 m	−4.7%	0.15 m
SBE2	−6.0%	0.84 m	−9.8%	0.63 m	−1.7%	0.86 m	−8.7%	0.23 m
SBA1	−3.9%	0.65 m	−5.9%	0.77 m	+2.5%	0.47 m	−4.4%	0.14 m

Despite the minor discrepancies with the LiDAR data, the model satisfactorily computes the dynamics of the shoreline elevation oscillations, including interaction between incoming bore and the receding runup. The results attest the ability of the model to compute the different components of the runup with a high degree of accuracy for the intermediate and reflective beach states considered in this study.

4. Discussion

4.1. Model Sensitivity to the Grid Size

A sensitivity analysis of the computed $R_{2\%}$ and its components S_{SW}, S_{IG}, and $\bar{\eta}_s$ to the grid size is conducted for all cases by varying the grid resolution from $dx = 0.30$ m to $dx = 2$ m by a 0.1 m step. Previous studies have shown a strong correlation between $R_{2\%}$ and the quantity $\sqrt{H_0 L_0}$, where H_0 is the deep-water significant wave height and and L_0 is the wavelength [22]. In order to relate the grid size to the incident offshore wave parameters, a normalized grid size based on this parameter is proposed. Considering that, according to the linear theory, $L_0 = \frac{g}{2\pi} T_p^2$, this normalized grid size χ can be expressed as:

$$\chi = \sqrt{H_0 L_0} \Big/ (dx.\beta_f) = \sqrt{\frac{g}{2\pi} H_0 T_p^2} \Big/ (dx.\beta_f) \tag{16}$$

The model's performance is evaluated using the relative error given by Equation (12). The results are displayed on Figure 9. It is worth noting that the higher the normalized grid size χ, the finer the grid. Overall, the model's accuracy increases consistently with the grid resolution. For large grid sizes, $R_{2\%}$ and its components are underestimated by up to 40% for the majority of the beach states and even up to nearly 60% for the shoreline setup computed for case DR0. Only the IG swash component S_{IG} is slightly overestimated for coarse grids in the case SBA1—a reflective beach. In general, S_{IG} has a lower sensitivity to the grid size, which is consistent with the previous numerical study carried out with SWASH on a fringing reef [39]. The relative error curve shows an asymptotic shape from $\chi \sim 200$, which is close to the value corresponding to the grid size $dx = 0.5$ m used in the present

study. To further verify the relevance of the parameter χ, synthetic cases are carried out at two different scales. A TMA spectrum is propagated over a straight slope with different H_s, T_p, and still water levels. The conditions are summarized in Table 6.

Table 6. Synthetic tests and their graphic markers. WL: water level.

	H_s (m)	T_p (s)	Intial Still WL (m)	β_f (-)	ξ (-)	Marker
L1.1	3	13	20	5%	0.47	blue stars
L1.2	5	15	20	5%	0.42	blue circles
L2.1	3	13	20	10%	0.94	green stars
L2.2	5	15	20	10%	0.84	green circles
S1.1	0.15	2.9	1	5%	0.47	black stars
S1.2	0.25	3.35	1	5%	0.42	black circles
S2.1	0.15	2.9	1	10%	0.94	red stars
S2.2	0.25	3.35	1	10%	0.82	red circles

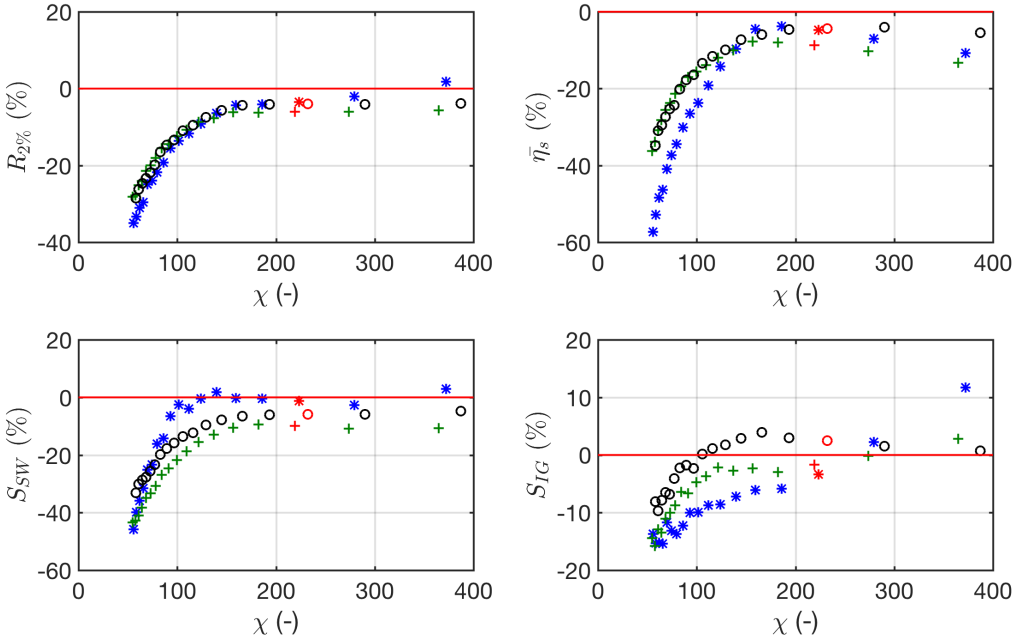

Figure 9. Relative error of the runup components between the numerical results and the laboratory experiment in function χ for case DR0 (blue stars), SBE2 (green plus signs), and SBA1 (black circles). The corresponding χ to $dx = 0.5$ m is shown in red. Note that χ increases for decreasing values of dx.

The computed cases exhibit fairly different wave conditions to represent a wide range of scenarios and to generalize the previous finding. The evolution of $R_{2\%}$ and its components are displayed on Figure 10. Similarly to what is observed in Figure 9, the values tend to converge as χ increases. Again, $\chi \sim 200$ appears to be a reasonable value to ensure correct computation of the total runup and its components. Though this value is model-dependent to a certain extent, other numerical models of a similar kind should not behave entirely differently.

This result can serve as a recommendation for properly setting up a phase-resolving model for runup computation. For instance, a runup computation along a 1D transect over an intermediate to reflective beach with incident irregular waves of $H_0 = 3$ m and $T_p = 13$ s offshore would require a grid size of around 2 m (foreshore slope $\beta_f \sim 7\%$).

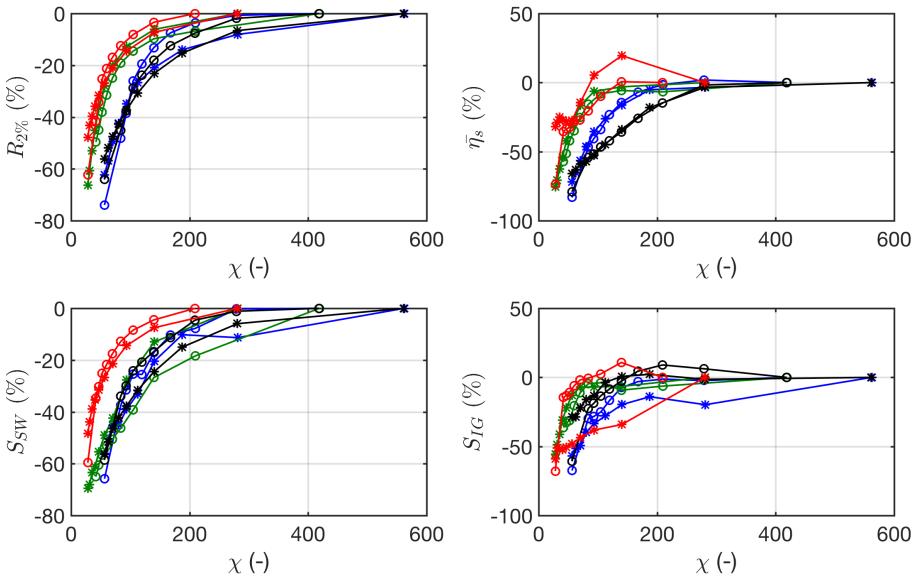

Figure 10. Self-contained deviation of the runup components from the results obtained with the smallest grid size as a function of χ. For markers and curves colors, refer to Table 6.

4.2. Runup Sensitivity to the Wave Breaking Detection Criterion

The simulation of wave breaking in depth-integrated wave models is generally a challenging task. Indeed, this type of model cannot solve for the free surface overturning of a breaking wave and does not include the 3D turbulent dissipation process. To overcome this limitation, the dispersive term of the governing equations can be deactivated once an onset breaking criterion is reached. Thus, the set of equations reduces to the NLSWE, which are a subset of the Boussinesq-type equations. The NLSWE have the advantage that they can describe a discontinuity in the free surface and implicitly treat the dissipation in the hydraulic jump. The solution benefits from a finite volume method such as it is the case in *BOSZ* . In the *BOSZ* version used in the present study, the onset breaking criterion is based on the free surface height to water depth ratio C_b given by Equation (6). A sensitivity analysis of the runup computation to the value of C_b is conducted by running the model for the three cases with C_b values varying from 0.4 to 1.2 (Figure 11).

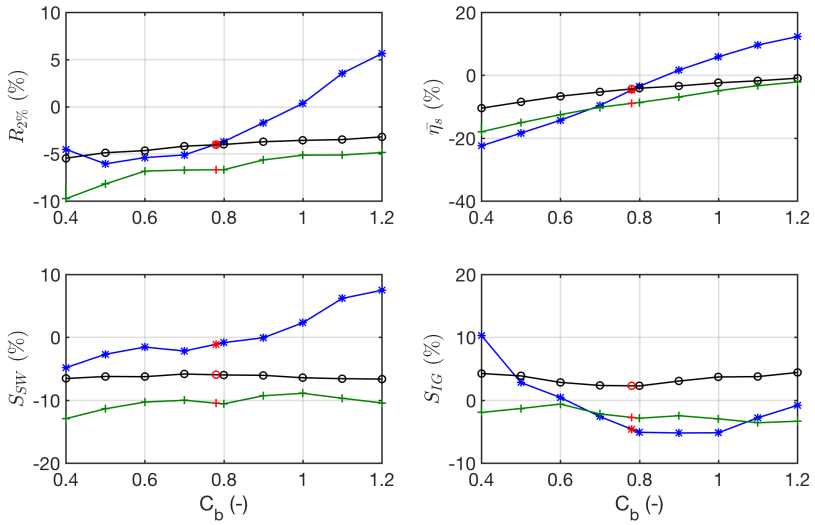

Figure 11. Evolution of the relative errors of $R_{2\%}$ and its components depending of the breaking coefficient C_b for case DR0 (blue stars), SBE2 (green plus signs), and SBA1 (black circles).

For case DR0, the intermediate beach configuration without inner bar, $R_{2\%}$ and its components are more sensitive to C_b than for the two other cases. For this case, relative errors increase with C_b except for the IG swash component, for which the relative error decreases. In the SBA1 and SBE2 cases, the swash components are insensitive to C_b. In contrast, the relative error of the mean shoreline setup increases linearly with C_b, a trend that can be seen in the relative error evolution of $R_{2\%}$. Overall, the best results for all of the components are obtained for C_b ranging between 0.6 and 0.8, which is consistent with the value used in this study ($C_b = 0.78$), based the theoretical work from McCowan [50], and with other studies [42,56].

4.3. Sensitivity of the Runup Determination to the Threshold Depth

The determination of the leading edge of runup requires to define an ad hoc criterion. In the present study, the threshold depth δ used to track the limit between dry and wet cells was set to 10 cm according to recommendations from previous studies based on field data [57,58] and numerical results [7,12]. In this section, the influence of the value of δ on R_2% and its components is investigated for both the numerical results and the laboratory data by varying δ from 4 cm up to 20 cm (Figure 12). In general, a threshold depth resembles a low-pass filter. Overall, low values of δ result in higher runup, swash, and shoreline setup values regardless of the beach type, even if this trend is less pronounced for the determination of S_{SW} in case DR0. Moreover, for small δ lower than 6 cm, it is worth noting that runup components computed from laboratory data are particularly variable, especially for the SBE2 case. It is hypothesized that for this case, small changes in the measured bed profile of the order of 5 cm have an influence on the determination of the runup tongue. This tendency is not observed in the numerical results. In fact, all the computations were carried out using a fixed bottom. Additional tests (not shown here) reveal that when the experimental shoreline position is extracted using a variable profile, the runup components show a behavior similar to that of the numerical results, confirming the influence of small changes of the foreshore slope when using low values of δ to identify the runup limit. Finally, the 10 cm threshold value used in this study provides similar runup values between experimental data and numerical results, which is consistent with other studies (e.g., [22,57]).

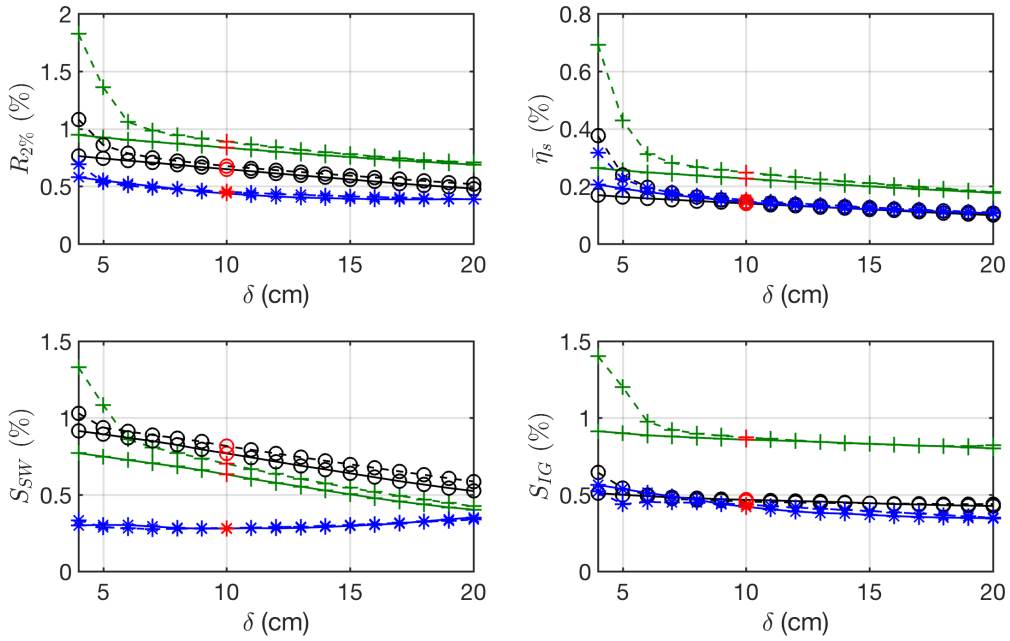

Figure 12. Experimental (dashed line) and numerical (solid line) runup components depending on the threshold depth δ for the DR0 (blue stars), SBE2 (green plus signs), and SBA1 (black circles) cases.

4.4. Influence of Phase Distribution of Incident Waves on Runup

For the comparisons between measured and computed runup, the *BOSZ* model was forced using the free surface times series measured at the wave gauge WG1. The results confirm the ability of the model to accurately compute the oscillations of the shoreline elevation in case the phase distribution is known (Figure 8). However, for practical applications of the model, an empirical offshore wave spectrum or a spectrum from a phase-average model such as SWAN or WaveWATCH III is commonly used to generate the input free surface elevation time series. In this case, the phases are not known and a distribution of random phases is used instead. Obviously, these random phases remain fixed throughout the computation.

The influence of incident phase distribution on the assessment of overtopping volumes has been highlighted in previous studies [42,59,60], showing that the overtopping volume can be overestimated by more than 100%. Wave runup sensitivity to phasing of incident waves was also studied for sloping beach [28,61] and fringing reef environments [32], showing significant differences between $R_{2\%}$ computed with measured phases and random phases. In particular, the significant IG wave height computed near the shoreline of an idealized fringing reef profile was overestimated by 20% using randomly distributed phases.

The influence of the phase distribution on the shoreline elevation is investigated here for the three test cases. Ten runs are computed with the same input energy spectrum as the one measured, but with different uniform random phase distributions within the interval $[-\pi : +\pi]$.

The runup components, normalized by the mean value of the ten runs, are compared in Figure 13 to assess the variability of the runup in dependence of the random phase distribution. The results show that S_{IG} is the most sensitive component of the runup with significant variations in all cases. The total IG signal is composed of both bound and free long waves, where bound waves are phased-locked to the wave group traveling at the group speed [62]. The wave groups are the result of the effect of the dispersion relation on the initial superposition of the different spectral components; their shape and appearance in time depend essentially on the initial phase distribution. The bound components in the IG band are directly affected by the wave phases. Consequently, changes in the phases lead to some variability of the bound waves, which are released as free IG waves after wave breaking. Moreover, Yao et al. [32] suggested that the short waves envelope, which is highly dependent on the interaction of the swell waves with each other, partially controls the IG wave transformations. On the other side, S_{SW} and the averaged quantity of setup at the shoreline $\bar{\eta}_s$ change only slightly with the phase angles. The SW swash and setup are mainly controlled by the depth-induced breaking of individual short waves and might be less sensitive to the SW envelope and, therefore, to the phase distribution. As reported by Torres-Freyermuth et al. [28], the variability increases with decreasing values of ξ, suggesting that the runup variability is larger on dissipative beaches. One possible reason for that is the increasing contribution of the IG band to the runup on dissipative beaches.

The relative errors between $R_{2\%}$ and its components from the random phases and the laboratory data are summarized in Table 7. The errors in $R_{2\%}$ are much larger than when the measured time series is used directly as input in the model (see Table 5). On average, the use of random phases overestimates the measured runup, with a maximum overestimation of 35% for the DR0 case. This highlights the aleatory nature of the runup and the notorious difficulties of comparing numerical results to measured laboratory or field data when no phase information is available. Furthermore, the IG swash is largely overestimated in all cases.

Table 7. Maximum and mean relative errors of the computed scenarios in comparison with the laboratory experiment.

			$R_{2\%}$		S_{SW}		S_{IG}		$\bar{\eta}_s$	
DR0	Max	mean rel. err.	+35.0%	+22.5%	+6.8%	+3.5%	+71.0%	+47.3%	+3.9%	−0.3%
SBE2	Max	mean rel. err.	+20.0%	+9.8%	+12.9%	+2.8%	+40.0%	+24.8%	−10.4%	−6.0%
SBA1	Max	mean rel. err.	+8.5%	+4.32%	−8.9%	−3.2%	+62.8%	+30.4%	−6.3%	−0.01%

1820

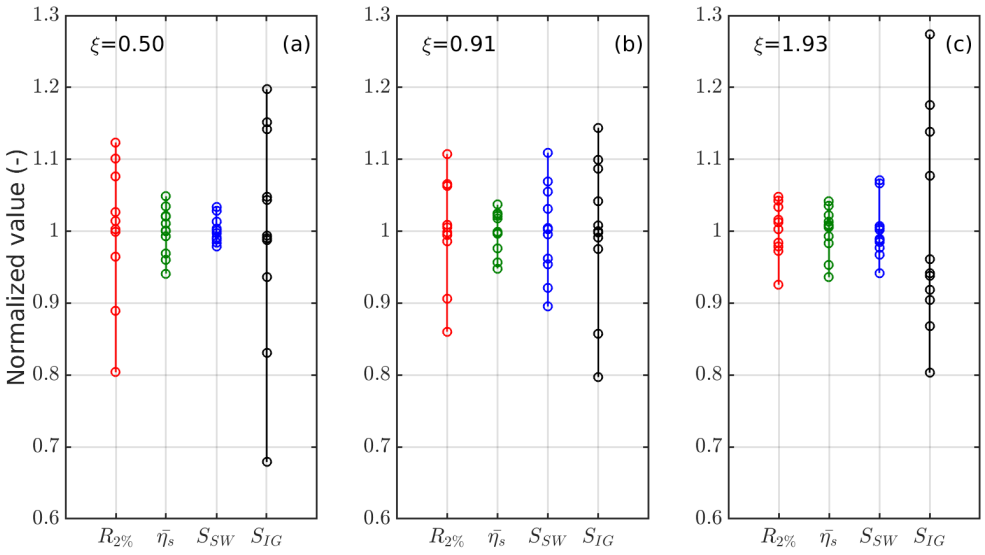

Figure 13. Runup components normalized by the mean value for the 10 random tests for case DR0 (**a**), case SBE2 (**b**), and case SBA1 (**c**). Red: $R_{2\%}$, green: $\bar{\eta}_s$, blue: S_{SW}, and black: S_{IG}.

5. Conclusions

As phase-resolving depth-integrated models are gaining importance for runup studies, precise validations under controlled conditions and recommendations for best practice are required. In this work, a high-quality laboratory data set is used to investigate the capability and sensitivity of the Boussinesq-type model *BOSZ* for the computation of nearshore wave transformations, including swash processes over intermediate and reflective beaches. The data set includes accurate LiDAR measurements of the free surface elevation in the surf and swash zone as well as shoreline elevation oscillations.

Wave transformations are accurately captured with low cross-shore errors for both the significant wave height H_s and the wave setup $\bar{\eta}$. Time series from the numerical model output of shoreline elevation oscillations as well as swash spectra show a satisfying agreement with the laboratory data. The statistical runup quantity $R_{2\%}$ is successfully computed with relative errors of less than 6%. The IG swash is well predicted with errors smaller than 3.5%. The SW swash and shoreline setup are reasonably well predicted with errors of less than 10%.

The discussion evaluates the sensitivity of the results to the model settings for general numerical computations of wave runup by depth-integrated phase-resolving models. Multiple computations with different breaking indices show that in the range of $C_b = 0.6$ to 0.8, the numerical results show little variability overall. Some parameters, such as the grid size or the threshold depth defining the edge of the runup tongue, are found to have a significant impact on the results, and thus the performance of the model. A nondimensional parameter is proposed to find the optimal grid size to improve numerical accuracy. A depth threshold of 10 cm, consistent with other studies [11,22], is found to be the most appropriate value for systematic comparisons of numerical and laboratory data to prevent small changes in the beach profile from having a disproportional impact. For model/data comparison, a free surface time series is used as the boundary condition for the numerical model, thus providing information of both amplitude and phase angles. Computations with different sets of random phases demonstrate that accurate replication of the laboratory data can only be achieved when the exact phases are not known. Moreover, a significant variability is observed among the runs with different random phases due to the sensitivity of the IG swash to the initial phase distribution. For beaches with high influence of IG energy, i.e., intermediate to dissipative beaches, the variability of the runup can be

significant. If the goal is to reproduce particular runup values, which were previously measured in the laboratory or field, the lack of information of the incident wave phases can contribute to substantial uncertainty. It should also be noted that special attention is necessary when data from laboratory experiments such as the one in this study are used. The generation of irregular waves in a laboratory environment essentially relies on the same technique as that which is used in phase-resolving models, i.e., a wave spectrum is decomposed into a series of individual waves. Laboratory data are inevitably subject to the same problem related to the waves' phases as phase-resolving wave models.

Overall, the phase-resolving depth-integrated *BOSZ* model shows satisfying capabilities in modeling irregular wave runup on intermediate and reflective beaches. It proves that this type of numerical model can be a powerful tool for coastal risks assessment and hazard mitigation projects. The sensitivity analysis performed provides guidelines on how to utilize the model and, more generally, any phase-resolving depth-integrated model to find the best accuracy at the lowest computational cost and ensure quality results for runup modeling studies.

Author Contributions: Conceptualization, J.P. and D.M.; methodology, J.P.; software and model development, V.R.; validation, J.P.; formal analysis, J.P.; writing—original draft preparation, J.P.; writing—review and editing, D.M. and V.R.; visualization, J.P.; supervision, D.M. and V.R.; project administration, V.R.; funding acquisition, D.M. and V.R. All authors have read and agreed to the published version of the manuscript.

Funding: The authors acknowledge financial support from the Isite program Energy Environment Solutions (E2S), the Communauté d'Agglomération Pays Basque (CAPB), and the Communauté Région Nouvelle Aquitaine (CRNA) for the chair HPC-Waves.

Acknowledgments: The authors express appreciation to Chris Blenkinsopp and Paul Bayle for providing data from the DynaRev project and guidance. The DynaRev project has received funding from the European Union's Horizon 2020 research and innovation programme under grant agreement No 654110, HYDRALAB+. The authors gratefully acknowledge European POCTEFA Program funding under the research project MARLIT EFA344/19.

Conflicts of Interest: The authors declare no conflict of interest. The funding agencies had no role in the design of the study; in the collection, analyses, or interpretation of data; in the writing of the manuscript; or in the decision to publish the results.

Abbreviations

The following abbreviations are used in this manuscript:

TWL	Total Water Level
SW	Short Waves
IG	Infra-Gravity
LiDAR	Light Detection And Ranging
NLSWE	Non Linear Shallow Water Equations
SWASH	Simulating WAves till SHore
BOSZ	Boussinesq Ocean & Surf Zone
SWAN	Simulating WAves Nearshore

References

1. Didier, D.; Baudry, J.; Bernatchez, P.; Dumont, D.; Sadegh, M.; Bismuth, E.; Bandet, M.; Dugas, S.; Sévigny, C. Multihazard simulation for coastal flood mapping: Bathtub versus numerical modelling in an open estuary, Eastern Canada. *J. Flood Risk Manag.* **2019**, *12*, e12505. [CrossRef]
2. Xie, D.; Zou, Q.P.; Mignone, A.; MacRae, J.D. Coastal flooding from wave overtopping and sea level rise adaptation in the northeastern USA. *Coast. Eng.* **2019**, *150*, 39–58. [CrossRef]
3. Sallenger, A. Storm impact scale for barrier islands. *J. Coast. Res.* **2000**, *16*, 890–895.
4. Van der Meer, J.W.; Allsop, N.; Bruce, T.; De Rouck, J.; Kortenhaus, A.; Pullen, T.; Schüttrumpf, H.; Troch, P.; Zanuttigh, B. *EurOtop 2018. Manual on Wave Overtopping of Sea Defences and Related Structures. An Overtopping Manual Largely Based on European Research, but for Worldwide Application*, 2nd ed.; EurOtop: London, UK, 2018 ; p. 320.
5. Ruggiero, P.; Komar, P.D.; McDougal, W.G.; Marra, J.J.; Beach, R.A. Wave Runup, Extreme Water Levels and the Erosion of Properties Backing Beaches. *J. Coast. Res.* **2001**, *17*, 407–419.

6. Serafin, K.A.; Ruggiero, P. Simulating extreme total water levels using a time-dependent, extreme value approach. *J. Geophys. Res. Ocean.* **2014**, *119*, 6305–6329. [CrossRef]
7. Stockdon, H.; Thompson, D.; Plant, N.; Long, J. Evaluation of wave runup predictions from numerical and parametric models. *Coast. Eng.* **2014**, *92*, 1–11. [CrossRef]
8. Silveira, T.M.; Taborda, R.; Carapuço, M.M.; Andrade, C.; Freitas, M.C.; Duarte, J.F.; Psuty, N.P. Assessing the extreme overwash regime along an embayed urban beach. *Geomorphology* **2016**, *274*, 64–77. [CrossRef]
9. Medellín, G.; Brinkkemper, J.; Torres-Freyermuth, A.; Appendini, C.; Mendoza, E.; Salles, P. Run-up parameterization and beach vulnerability assessment on a barrier island: A downscaling approach. *Nat. Hazards Earth Syst. Sci.* **2016**, *16*, 167–180. [CrossRef]
10. Lerma, A.N.; Pedrero, R.; Robinet, A.; Sénéchal, N. Simulating wave setup and runup during storm conditions on a complex barred beach. *Coast. Eng.* **2017**, *123*, 29–41. [CrossRef]
11. Fiedler, J.; Smit, P.; Brodie, K.; McNinch, J.; Guza, R. Numerical modeling of wave runup on steep and mildly sloping natural beaches. *Coast. Eng.* **2018**, *131*, 106–113. [CrossRef]
12. Fiedler, J.; Young, A.; Ludka, B.; O'Reilly, W.; Henderson, C.; Merrifield, M.; Guza, R. Predicting site-specific storm wave run-up. *Nat. Hazards* **2020**, *104*, 493–517. [CrossRef]
13. Holman, R. Extreme value statistics for wave run-up on a natural beach. *Coast. Eng.* **1986**, *9*, 527–544. [CrossRef]
14. Longuet-Higgins, M.; Stewart, R. Radiation stresses in water waves; a physical discussion, with applications. *Deep Sea Res. Oceanogr. Abstr.* **1964**, *11*, 529–562. [CrossRef]
15. De Bakker, A.; Tissier, M.; Ruessink, B. Beach steepness effects on nonlinear infragravity-wave interactions: A numerical study. *J. Geophys. Res. Ocean.* **2016**, *121*, 554–570. [CrossRef]
16. Hunt, I. Design of seawalls and breakwaters, US Corps Eng. *Lake Surv. Detroit* **1959**, *49, 123–152* .
17. Battjes, J. Surf similarity. In Proceedings of the14th International Conference on Coastal Engineering, Copenhagen, Denmark, 24–28 June 1974; Volume 9, pp. 446–480.
18. Mase, H. Random Wave Runup Height on Gentle Slope. *J. Waterw. Port Coast. Ocean Eng. ASCE* **1989**, *115*, 649–661. [CrossRef]
19. Hedges, T.; Mase, H. Modified Hunt's Equation Incorporating Wave Setup. *J. Waterw. Port Coast. Ocean Eng. ASCE* **2004**, *130*, 109–113. [CrossRef]
20. Khoury, A.; Jarno, A.; Marin, F. Experimental study of runup for sandy beaches under waves and tide. *Coast. Eng.* **2019**, *144*, 33–46. [CrossRef]
21. Ruggiero, P.; Holman, R.; Beach, R. Wave run-up on a high-energy dissipative beach. *J. Geophys. Res. C Ocean.* **2004**, *109*. [CrossRef]
22. Stockdon, H.; Holman, R.; Howd, P.; Sallenger, A. Empirical parameterization of setup, swash, and runup. *Coast. Eng.* **2006**, *53*, 573–588. [CrossRef]
23. Atkinson, A.; Power, H.; Moura, T.; Hammond, T.; Callaghan, D.; Baldock, T. Assessment of runup predictions by empirical models on non-truncated beaches on the south-east Australian coast. *Coast. Eng.* **2017**, *119*, 15–31. [CrossRef]
24. Didier, D.; Caulet, C.; Bandet, M.; Bernatchez, P.; Dumont, D.; Augereau, E.; Floc'h, F.; Delacourt, C. Wave runup parameterization for sandy, gravel and platform beaches in a fetch-limited, large estuarine system. *Cont. Shelf Res.* **2020**, *192*, 104024. [CrossRef]
25. Vousdoukas, M.; Wziatek, D.; Almeida, L. Coastal vulnerability assessment based on video wave run-up observations at a mesotidal, steep-sloped beach. *Ocean Dyn.* **2011**, *62*, 123–137. [CrossRef]
26. Da Silva, G.; Gomes da Silva, P.; Araujo, R.; Klein, A.; Toldo, E. Wave run-up on embayed beaches. Study case: Itapocorói Bay, Southern Brazil. *Braz. J. Oceanogr.* **2017**, *65*, 187–200. [CrossRef]
27. Senechal, N.; Coco, G.; Bryan, K.; Holman, R. Wave runup during extreme storm conditions. *J. Geophys. Res.-Ocean.* **2011**, *116*. [CrossRef]
28. Torres-Freyermuth, A.; Patiño, J.P.; Pedrozo-Acuña, A.; Puleo, J.; Baldock, T. Runup uncertainty on planar beaches. *Ocean Dyn.* **2019**, *69*, 1359–1371. [CrossRef]
29. Martin-Medina, M.; Abadie, S.; Mokrani, C.; Morichon, D. Numerical simulation of flip-through impacts of variable steepness on a vertical breakwater. *Appl. Ocean Res.* **2018**, *75*, 117–131. [CrossRef]
30. Zijlema, M.; Stelling, G.; Smit, P. SWASH: An operational public domain code for simulating wave fields and rapidly varied flows in coastal waters. *Coast. Eng.* **2011**, *58*, 992–1012. [CrossRef]

31. Lynett, P.; Tso-Ren, W.; Liu, P.F. Modeling wave runup with depth-integrated equations. *Coast. Eng.* **2002**, *46*, 89–107. [CrossRef]
32. Yao, Y.; Zhang, Q.; Becker, J.M.; Merrifield, M.A. Boussinesq modeling of wave processes in field fringing reef environments. *Appl. Ocean Res.* **2020**, *95*, 102025. [CrossRef]
33. Roeber, V.; Cheung, K.; Kobayashi, M. Shock-capturing Boussinesq-type model for nearshore wave processes. *Coast. Eng.* **2010**, *57*, 407–423. [CrossRef]
34. Roeber, V.; Cheung, K. Boussinesq-type model for energetic breaking waves in fringing reef environments. *Coast. Eng.* **2012**, *70*, 1–20. [CrossRef]
35. Li, N.; Roeber, V.; Yamazaki, Y.; Heitmann, T.W.; Bai, Y.; Cheung, K.F. Integration of coastal inundation modeling from storm tides to individual waves. *Ocean Model.* **2014**, *83*, 26–42. [CrossRef]
36. Li, N.; Yamazaki, Y.; Roeber, V.; Cheung, K.F.; Chock, G. Probabilistic mapping of storm-induced coastal inundation for climate change adaptation. *Coast. Eng.* **2018**, *133*, 126–141. [CrossRef]
37. Ruessink, B.G.; Michallet, H.; Bonneton, P.; Mouazé, D.; Lara, J.; Silva, P.A.; Wellens, P. Globex: Wave dynamics on a gently sloping laboratory beach. In Proceedings of the HYDRALAB IV Joint User Meeting, Lisbon, Portugal, 1–9 July 2014; pp. 1351–1362.
38. Ruju, A.; Lara, J.; Losada, I. Numerical analysis of run-up oscillations under dissipative conditions. *Coast. Eng.* **2014**, *86*, 45–56. [CrossRef]
39. Pelaez-Zapata, D.; Montoya, R.; Osorio, A. Numerical study of run-up oscillations over fringing reefs. *J. Coast. Res.* **2018**, *34*, 1065–1079. [CrossRef]
40. Liu, W.; Shao, K.q.; Ning, Y. Numerical Study of the Impact of Climate Change on Irregular Wave Run-up Over Reef-Fringed Coasts. *China Ocean Eng.* **2020**, *34*, 162–171. [CrossRef]
41. Mase, H.; Miyahira, A.; Hedges, T.S. Random Wave Runup on Seawalls Near Shorelines with and without Artificial Reefs. *Coast. Eng. J.* **2004**, *46*, 247–268. [CrossRef]
42. McCabe, M.; Stansby, P.; Apsley, D. Random wave runup and overtopping a steep sea wall: Shallow-water and Boussinesq modelling with generalised breaking and wall impact algorithms validated against laboratory and field measurements. *Coast. Eng.* **2013**, *74*, 33–49. [CrossRef]
43. Blenkinsopp, C.; Mole, M.; Turner, I.; Peirson, W. Measurements of the time-varying free-surface profile across the swash zone obtained using an industrial LIDAR. *Coast. Eng.* **2010**, *57*, 1059–1065. [CrossRef]
44. Brodie, K.; Raubenheimer, B.; Elgar, S.; Slocum, R.K.; McNinch, J. Lidar and pressure measurements of inner-surfzone waves and setup. *J. Atmos. Ocean. Technol.* **2015**, *32*, 1945–1959. [CrossRef]
45. Fiedler, J.; Brodie, K.; McNinch, J.; Guza, R. Observations of runup and energy flux on a low slope beach with high-energy, long-period ocean swell. *Geophys. Res. Lett.* **2015**, *42*. [CrossRef]
46. Blenkinsopp, C.; Bayle, P.; Conley, D.; Masselink, G.; Gulson, E.; Kelly, I.; Almar, R.; Turner, I.; Baldock, T.; Beuzen, T.; et al. Dynamic coastal protection: Resilience of dynamic revetments (DYNAREV). In Proceedings of the HYDRALAB+ Joint User Meeting, Bucharest, Romania, 21–25 May 2019.
47. Wright, L.; Short, A. Morphodynamic variability of surf zones and beaches: A synthesis. *Mar. Geol.* **1984**, *56*, 93–118. [CrossRef]
48. Nwogu, O. An alternative form of the Boussinesq equations for nearshore wave propagation. *J. Waterw. Port Coast. Ocean Eng.* **1993**, *119*, 618–638. [CrossRef]
49. Wei, G.; Kirby, J.T.; Sinha, A. Generation of waves in Boussinesq models using a source function method. *Coast. Eng.* **1999**, *36*, 271–299. [CrossRef]
50. McCowan, J. XXXIX. On the highest wave of permanent type. *Lond. Edinb. Dublin Philos. Mag. J. Sci.* **1984**, *38*, 351–358. [CrossRef]
51. Emery, W.J.; Thomson, R.E. Time-series Analysis Methods. In *Data Analysis Methods in Physical Oceanography*; Emery, W.J., Thomson, R.E., Eds.; Elsevier Science: Amsterdam, The Netherlands, 2001; Chapter 5, pp. 371–567. [CrossRef]
52. de Beer, A.; McCall, R.; Long, J.; Tissier, M.; Reniers, A. Simulating wave runup on an intermediate–reflective beach using a wave-resolving and a wave-averaged version of XBeach. *Coast. Eng.* **2020**, *163*, 103788. [CrossRef]
53. Willmott, C.J. On the Validation of Models. *Phys. Geogr.* **1981**, *2*, 184–194. [CrossRef]
54. Elgar, S. Observations of bispectra of shoaling surface gravity waves. *J. Fluid Mech.* **1985**, *161*, 425–448. [CrossRef]

55. Hughes, M.; Aagaard, T.; Baldock, T.; Power, H. Wave runup (Swash) spectra on natural beaches: Morphodynamic controls. In Proceedings of the Coasts Ports 2013, Sydney, Australia, 11–13 September 2013; pp. 412–417.
56. Tonelli, M.; Petti, M. Hybrid finite volume – finite difference scheme for 2DH improved Boussinesq equations. *Coast. Eng.* **2009**, *56*, 609–620. [CrossRef]
57. Holland, K.; Raubenheimer, B.; Guza, R.; Holman, R. Runup kinematics on a natural beach. *J. Geophys. Res.* **1995**, *100*, 4985–4993. [CrossRef]
58. Raubenheimer, B.; Guza, R.; Elgar, S. Swash on a gently sloping beach. *J. Geophys. Res.* **1995**, *100*, 8751–8760. [CrossRef]
59. Romano, A.; Bellotti, G.; Briganti, R.; Franco, L. Uncertainties in the physical modelling of the wave overtopping over a rubble mound breakwater: The role of the seeding number and of the test duration. *Coast. Eng.* **2015**, *103*, 15–21. [CrossRef]
60. Williams, H.E.; Briganti, R.; Pullen, T. The role of offshore boundary conditions in the uncertainty of numerical prediction of wave overtopping using non-linear shallow water equations. *Coast. Eng.* **2014**, *89*, 30–44. [CrossRef]
61. McCabe, M.; Stansby, P.K.; Apsley, D.D. Coupled wave action and shallow-water modelling for random wave runup on a slope. *J. Hydraul. Res.* **2011**, *49*, 515–522. [CrossRef]
62. Longuet-Higgins, M.S.; Stewart, R.W. Radiation stress and mass transport in gravity waves, with application to 'surf beats'. *J. Fluid Mech.* **1962**, *13*, 481–504. [CrossRef]

3.5 Conclusion

In this chapter, the performances of the BTM *BOSZ* were extensively assessed to capture short-wave nearshore coastal processes such as refraction, diffraction, shoaling, wave breaking and most importantly run-up, under different conditions. The model proved to be handling satisfactorily refraction, diffraction and shoaling of non-breaking waves as showed in sections 3.3.1 and 3.3.2. The increasing non-linearity of waves traveling over decreasing depth is well captured, which is important especially for wave shape as high-order terms mostly contribute to skewness and asymmetry rather than overall energy.

The replication of the large-scale run-up experiment performed in the GWK by Blenkinsopp et al. (2019, 2021) published in Pinault et al. (2020) allowed to precisely validate the model performances for the propagation of irregular breaking waves up to the run-up. Specifically, it was shown that the model accurately captured the wave height and set-up. Regarding the run-up, both the time series and the spectra showed a satisfying match with the experimental data. The quantities $R_{2\%}$, S_{IG}, S_{SW} and $\overline{\eta_s}$ were well predicted with errors lower than 6%, 3.5%, 10% and 9% respectively. The high-quality data-set enabled a detailed sensitivity analysis of the results to the model settings common to all depth-integrated phase-resolving models. For instance, it was shown that the model results were particularly sensitive to the grid-size, with an under-estimation of the run-up values when coarse grids are used, due to numerical diffusion. The influence of the initial phase-seeding was also investigated, as phase-resolving models usually assume a random distribution of phases when no time series is available. In this experiment, the use of random initial phases considerably decreased the match between model and laboratory data and significant variability of the IG swash was observed among the different runs. Rutten et al. (2021) reported a similar behavior, and showed that the phase distribution induced more variability than morphodynamic changes under storm conditions.

The validations cases showed that the model is capable of handling nearshore coastal processes and most importantly run-up. These validations further prove that phase-resolving depth-integrated models are valuable tools for the investigation of the different hydrodynamic processes, with acceptable computational times and limitations. The sensitivity analysis showed that some parameters can have a significant influence on the results, for instance the grid size or the initial phase distribution, and suggest more work on this aspect to fully understand the behaviors of such numerical models and the possible improvements.

Chapter 4

Swash motion and hydrodynamics in a meso-tidal embayed beach - Case of the *Grande Plage* of Biarritz

Contents

4.1 Introduction

In this chapter, the hydrodynamics and swash motions at the GPB during moderate and energetic wave conditions are investigated for different water levels. The study combines both the analysis of measurements carried out during a 3-days field campaign and numerical results computed with the phase-resolving model *BOSZ* described in the previous chapter. The objective of this study was twofold. First, the data are used to assess the performance of *BOSZ* to compute the run-up along a constraint embayed beach and to capture the different frequency components of the swash motion in real conditions. Secondly, the model results are used to analyse the influence of environmental and morphological parameters to the swash motion at this meso-tidal intermediate reflective beach. The results of this work are presented in section 4.3 as an article, currently under review in the journal *Estuarine, Coastal and Shelf Science*. This section is preceded with a description (section 4.2) of the regional wave model, based on *SWAN* , that was used to provide input spectra for the *BOSZ* computations.

In alongshore uniform environment, 1D model configurations are often implemented to reduce computational time. It assumes that longshore wave processes are negligible compared to cross-shore processes. However in constrained environments such as embayed beaches this assumption might not hold due to the alongshore gradients in the bathymetry. In particular, the study site of the GPB is characterized by the presence of 3D morphological and geological features, such rip channels or rocks. To evaluate the importance of modeling longshore processes, a 1D model configuration is set-up to capture wave transformations and run-up, and compared to the performances of the 2D model configuration in section 4.4.

Understanding the cross-shore transformations of infragravity waves is crucial for accurate estimations of the IG swash response to variable incident forcings. In particular, the mechanism of IG energy dissipation under varying wave conditions on an intermediate reflective beach are largely unexplored. In section 4.5, the IG wave processes at the site of the GPB are further investigated, to provide explanations of the swash variability highlighted in section 4.3. After an analysis of the cross-shore processes, the generation mechanism of the IG waves is investigated. Then, the dissipation of IG energy is explored, under varying conditions of waves and tide levels. The influence of environmental conditions on the dissipation rates of the IG energy is investigated to provide explanations to the swash behavior.

4.2 Modeling of the incident wave conditions

The numerical modeling of waves using a nearshore model configuration requires knowledge of the boundary conditions i.e. a description of the waves as they underwent transformations from deep water. Boundary conditions are typically provided by either regional spectral wave models (Valentini et al., 2019), offshore wave buoys (Nicolae Lerma et al., 2017) or nearshore pressure sensors (de Beer et al., 2021). The chosen strategy depends on the availability of measurements at the offshore boundary of the nearshore wave model but also on the alongshore distribution of offshore wave conditions. Here, the location of the *BOSZ* offshore boundary was

limited by the dispersion capacities of the model (see section 3.2), restricting offshore conditions to intermediate water depth. The Anglet buoy, the only measurement providing information about the offshore wave climate at the site (figure 4.1), is located at a depth 50 m. This deep water regime prevents any period smaller than 8 *sec* from being generated at the *BOSZ* boundary. In addition, the alongshore variability at the site imposes a wide numerical domain.

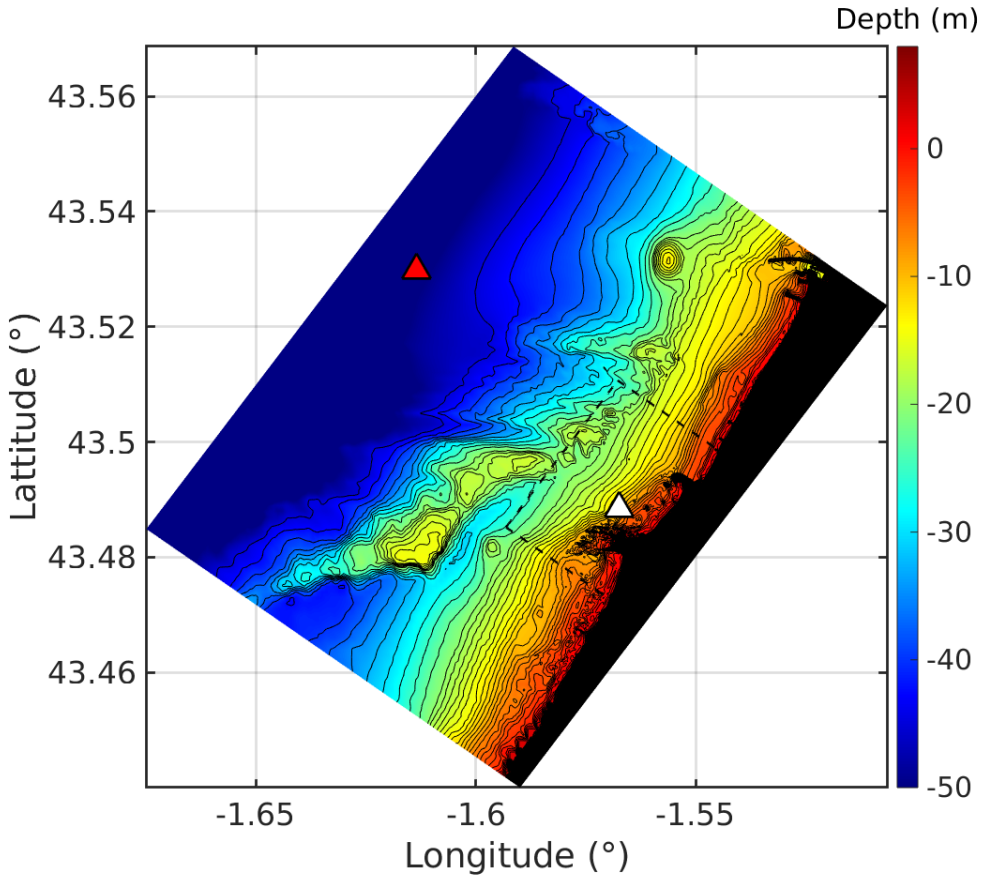

Figure 4.1: *SWAN* and *BOSZ* (inside the black dashed lines) numerical domains with locations of the Anglet wave buoy (red triangle) and *seabird* (white triangle) used for the *SWAN* validation.

Therefore, an offshore boundary corresponding to the Anglet buoy location would result in an extremely large numerical domain, which would be too costly in terms of computation or would require a large grid size preventing a correct computation of small scale processes such as wave run-up. As a workaround, a *SWAN* model configuration (Booij et al., 1999) was implemented to propagate offshore wave conditions up to an acceptable location for the *BOSZ* boundary, at a depth of about $h = 20\,m$. At this depth, the highest frequency input in the model is around 5 *sec*.

In this section, the *SWAN* model configuration is first described. Then, a validation at two different locations is proposed, to ensure consistency of the results and identify possible bias into the *BOSZ* model. Finally, an analysis of the large scale wave patterns is proposed, to provide insights of the wave field prior to the *BOSZ* numerical domain.

4.2.1 Settings of the spectral wave model *SWAN*

The *SWAN* model domain extends 6.5 km offshore up to a depth of 50 m and spans 13.5 km alongshore (figure 4.1). The unstructured grid is composed of cells varying from 10 to 50 m, with higher resolution focusing on large bathymetric variations (Delpey et al., 2021). *SWAN* is run in non-stationary mode with a time step of 5 min. Incident wave energy conditions obtained from the frequency-directional spectra of the Anglet wave buoy are prescribed uniformly along the offshore boundary. Tide-induced water level variations are also taken into account in the computation using the local tide gauge of Bayonne-Boucau harbor located 5.5 km north of the study site. An exponential frequency discretization is considered, using 50 frequencies, f_i , from 0.04 to 0.5 H_z so that $f_{i+1} = 1.05 f_i$. The directional grid is regular with a 5°resolution. Wave generation by wind is not considered in the simulation because of the small extension of the domain considered. Triad interactions, susceptible of generating super-harmonics, are included in the computation. Finite-depth wave-bottom interactions processes such as shoaling, bottom friction (Madsen et al., 1988) and refraction are taken into account. Depth-induced breaking is accounted for using Battjes and Janssen (1978) formulation with a breaker index $\gamma = 0.73$.

4.2.2 Validation

The *SWAN* model configuration is validated against wave measurements in order to evaluate its accuracy in representing coastal wave propagation up to the nearshore area where the *BOSZ* boundary is found. The measurements from the Anglet wave buoy, located in deep water ($h = 50\,m$), and the *Seabird*, located in intermediate depth ($h = 12\,m$), are used. Their are shown in figure 4.1 as red and white triangles respectively.

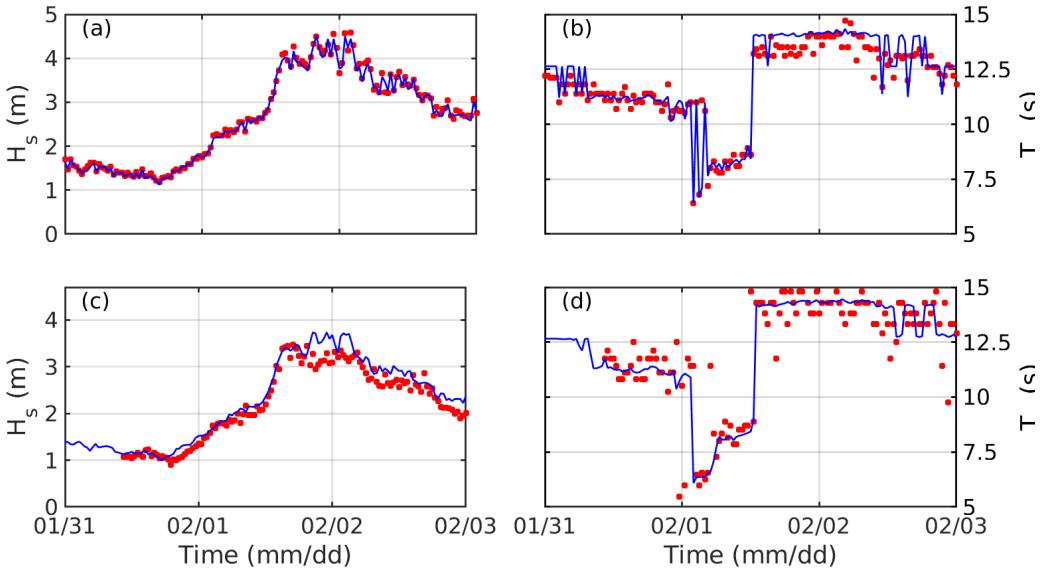

Figure 4.2: Comparisons of bulk parameters H_s and T_p observed (red) and modeled using *SWAN* (blue) at the Anglet wave buoy (**(a)**, **(b)**) and Seabird (**(c)**, **(d)**).

The comparison of model results with observations on figure 4.2 shows that the model

reproduces well the variations of wave regime encountered during the field experiment. During this period a highly energetic event occurred, with a H_s of more than 4.5 m measured at the buoy, allowing to assess the model in extreme conditions. Under such conditions, an underestimation of the wave height can be noticed at the *seabird* (panel **(c)**). Corresponding statistics are shown in table 4.1. Four metrics are used to assess the model performance : the Root Mean Square error (RMSE), the Normalized Root Mean Square error (NRMSE), the correlation coefficient R^2 and the bias. At the Anglet wave buoy the model shows an excellent

Table 4.1: Statistics evaluating the fit between observed and modeled values for the significant wave height H_s and peak period T_p at the wave buoy and seabird locations.

		Wave buoy	Seabird
H_s	RMSE (m)	0.07	0.22
	NMRSE (-)	0.02	0.09
	Bias (m)	-0.03	0.14
	R^2 (-)	0.99	0.96
T_p	RMSE (s)	0.61	1.25
	NMRSE (-)	0.19	0.13
	Bias (s)	0.23	0.21
	R^2 (-)	0.93	0.78

correlation for H_s, which is expected as the wave buoy is located at the offshore boundary of the model and is used as an input. The statistics show a RMSE of 0.07 m corresponding to a NRMSE of 2%, with a correlation coefficient of $R^2 = 0.99$. For the peak period T_p results are more scattered, with a R^2 of 0.93 and a positive bias of 0.23 s. Nonetheless the RMSE is less than a second, which is acceptable. At the Seabird location the *SWAN* models gives satisfying results despite a slight positive bias of the significant wave height of +0.14 m, identified during the extreme event on figure 4.2. Nonetheless, statistics show a satisfying correlation with $R^2 = 0.96$ and $R^2 = 0.78$ for H_s and T_p respectively, with associated NRMSEs around 10%. The visible scatter for T_p comes from the wind sea present during some events of the campaign, resulting in a bi-modal spectrum with a peak in the wind-sea frequency band, around 6 s, and a peak in the sea-swell band, around 11 s. As the peak energy was relatively close in both bands it results in strong variability of T_p, as it only represents the period with the highest energy and not an averaged value.

4.2.3 Implementation of the offshore boundary conditions in *BOSZ*

An example of the significant wave height distribution computed with *SWAN* is given on figure 4.3. Due to the heterogeneous bathymetry, strong refraction patterns are observed leading to significant variability of the wave field with focusing areas alternating with shadowing areas. Along the offshore *BOSZ* boundary (black dashed lines), the significant wave height varied by up to 1.5 m during the campaign, representing an increase by up to 40% between the lowest and highest longshore value. In order to have a representative offshore wave energy spatial

distribution as input in *BOSZ* , the model is forced at the offshore boundary by 20 equally-distributed directional wave spectra given by the *SWAN* configuration.

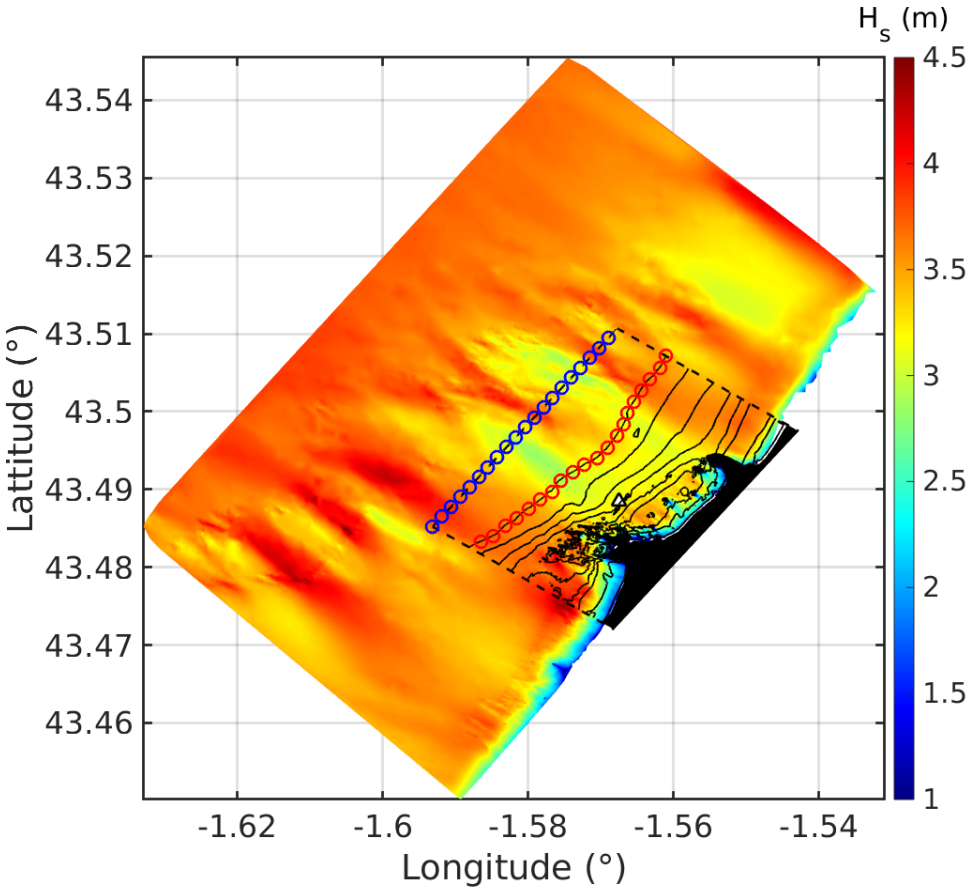

Figure 4.3: H_s map from *SWAN* around the GPB on the 2nd of February at 05 am. Red and blue circles respectively represent the locations where *SWAN* spectra were extracted and used as input in *BOSZ* . Black dashed lines delimitate the *BOSZ* domain. Black lines indicate the isoline within the *BOSZ* domain.

According to the wave-maker theory a flat bottom is required at the offshore boundary. On figure 4.3 the area between the offshore boundary and the first isoline is flat and fixed at -17 m. For that reason, *SWAN* spectra were extracted along the -17 m isoline (blue circles on figure 4.3 and used at the offshore boundary (red circles).

Each component of the *SWAN* spectrum is represented by a linear monochromatic wave with an individual amplitude, frequency, direction and random phase. The same set of random phases is used for the model runs to ensure identical phase locking. The differences between the computed scenarios are then solely due to differences in the magnitudes of the input spectra but not due to changes in phase locking. The waves are generated near the offshore boundary using an internal wavemaker and the resulting superpositions of all components form an irregular sea state. To avoid recycling of the input time series and generation of artificial wave grouping, the *SWAN* spectra are sub-sampled to frequency bins of 0.00018 H_z. A description of the complete *BOSZ* model set-up, including the grid size, the boundary conditions or the wave breaking implementation is provided in section 4.3.

4.3 Characterization of the swash zone dynamics based on field data and model results : *Article currently under review*

Phase-resolving modeling of swash motions at an engineered embayed beach under moderate to energetic conditions

Jonas Pinault[a,*], Denis Morichon[b], Matthias Delpey[c] and Volker Roeber[a,d]

[a] Université de Pau et des Pays de l'Adour, E2S UPPA, chair HPC-Waves, Anglet, 64600, France
[b] Université de Pau et des Pays de L'Adour, E2S UPPA, SIAME, Anglet, 64600, France
[c] SUEZ, Smart & Environmental Solutions, Center Rivages Pro Tech, Bidart, 64210, France
[d] University of Hawai'i at Mānoa, Department of Oceanography, Honolulu, 96822, USA

ARTICLE INFO

Keywords:
Run-up
Swash motions
Video monitoring
Boussinesq model
Embayed beach
Tide
Dissipative to reflective beach type

ABSTRACT

Wave run-up is a key factor for the assessment of coastal flood risk during large swell events. The behavior of swash motions along embayed beaches is strongly influenced by particular features such as rocky headlands, irregular morphology, or tides, that have not received much attention in the past. In the present paper, swash motions along an engineered embayed beach were investigated under moderate to energetic wave conditions through field observations and numerical computations. Using pressure sensors and video-derived run-up data a Boussinesq-type nearshore wave model was found to fairly captures the relevant wave transformation and swash zone processes. The tidal water level variations were found to have a significant impact on the overall swash amplitude and it to condition the respective role of short- and long-wave components to the swash motions. In the studied configuration, the tidal level rise was shown to cause a transition from a very dissipative to a reflective or intermediate beach configuration depending on incident wave energy. Moreover, swash amplitudes were observed to vary significantly alongshore with differences of up to a factor of 2.2. Numerical results suggest that both the foreshore slope and the sub-tidal morphology play a key-role in the alongshore swash distribution.

1. Introduction

Rocky coastal zones represent approximately 80% of the world's coast (Trenhaile and Trenhaile, 1987). Within these areas, beaches constrained by rocky headlands are common (Ojeda and Guillén, 2008; Klein et al., 2010; Scott et al., 2011; Castelle and Coco, 2012; Robinet et al., 2020). These partially sheltered environments, herein referred to as embayed beaches, have been traditionally preferred for settlements as they offer a natural protection against large waves and currents. Nowadays, many embayed beaches are highly urbanized but still threatened by energetic open-ocean swells; a situation, which tends to get worse with climate change. With the likely increase in storm frequency (Knutson et al., 2021) combined with sea level rise, the occurrence of coastal flooding is expected to be more frequent and potentially devastating in populated shorelines (Kirezci et al., 2020; Knutson et al., 2021). It is thus essential to well understand the hydrodynamics functioning of this type of beaches. This knowledge can especially support the implementation of management strategies by local authorities, including the development of efficient early warning systems to mitigate the consequences of hazardous coastal flooding event.

The estimation of the total water elevation (TWL) at the shoreline is often a key element in coastal risk management strategies (Asbury H. Sallenger, 2000; Didier et al., 2019; Xie et al., 2019). This quantity can be considered as the final product of all contributions to a flood hazard. It is often used as an indicator to assess the risk of coastal flooding by comparing the estimate of the two percent TWL exceedence with the elevation of coastal defenses for a given storm (de Santiago et al., 2017). The assessment of the TWL requires considering the contributions from tides (η_{tide}), storm surge (η_{su}), and nearshore waves through the local wave run-up ($\eta_s(t)$) :

$$\mathrm{TWL}(t) = \eta_{tide} + \eta_{su} + \eta_s(t) \tag{1}$$

The wave run-up can be largely influenced by local features in the beach topography over much smaller spatial scales than the other TWL contributions. This makes the run-up often the most challenging contribution to be assessed. The estimation of the wave run-up requires consideration of a static component, the wave set-up, and a dynamic component, the swash (Holman, 1986). The swash, as a time varying component, can be divided into two parts : the incident band that refers to short waves (SW) with frequencies ranging from 0.05 to 0.25 H_z, and the infragravity band (IG) describing the frequency range from 0.002 to 0.05 H_z. IG dominated swash motions are commonly observed under dissipative conditions favoured by gently sloping beaches (Ruggiero et al., 2004; Stockdon et al., 2006; Senechal et al., 2018) while the SW frequency band prevails on steep reflective beaches (Guedes et al., 2012; de Bakker et al., 2016).

Previous studies have shown that the amplitude of the swash and the respective contribution of its spectral components vary depending on environmental parameters. For

*Corresponding author
jonas.pinault@univ-pau.fr (J. Pinault); denis.morichon@univ-pau.fr (D. Morichon); matthias.delpey@suez.com (M. Delpey); volker.roeber@univ-pau.fr (V. Roeber)
ORCID(s): 0000-0003-3449-3440 (J. Pinault); 0000-0003-4264-0412 (D. Morichon); 0000-0001-7596-8524 (M. Delpey); 0000-0002-3768-9863 (V. Roeber)

instance, it has been demonstrated that the tidal modulation of nearshore wave processes can have a significant impact on the swash motions (Guedes et al., 2011; Brinkkemper et al., 2013; Khoury et al., 2019; Gomes da Silva et al., 2020). Guedes et al. (2011) observed variability of the significant swash height by a factor of 2 between low and high tide on a microtidal intermediate barred-beach. The influence of the tide in the presence of sandbars has been further examined under laboratory conditions by Khoury et al. (2019). It was shown in this experimental study that position, height, and type of wave breaking were significantly impacted by the tidal level and ultimately affect the run-up.

While environmental parameters affecting the temporal variability of the run-up has received a lot of attention, studies focusing on the spatial variability of the run-up are sparse. Ruggiero et al. (2004) used video measurements of TWL carried out on a dissipative beach under moderate wave conditions to investigate alongshore variability of the run-up. They showed that the highest values of the significant swash height exceeded the lowest values by over a factor of two. This variability was attributed to alongshore differences in the foreshore slope as both swash components (SW and IG) exhibit significant correlation with this parameter. Stockdon et al. (2006) evaluated the longshore variability of the run-up based on video data under intermediate and reflective conditions on the long open beach of Duck (North Carolina, USA). They showed that under moderately energetic wave conditions, the SW swash displayed the highest variability, with a significant correlation with the foreshore slope. Conversely, the IG swash showed a lower variability and no significant correlation with the foreshore slope. Guedes et al. (2012) reported observations of alongshore variability of a factor of 2 under calm conditions on an intermediate pocket beach. Here again, the variability was primarily controlled by the foreshore slope. Nonetheless, the investigation of the wave breaking distribution showed a correlation with the run-up distribution, suggesting a morphological control in the surfzone. More recently, Senechal et al. (2018) investigated the run-up variability under moderate conditions on a natural dissipative open beach. A large variability of a factor 3 was reported for the IG components in similar fashion as previously documented. However, contrary to previous studies, the variability of the foreshore slope alone was not the main control of alongshore distribution of the run-up. Evidence of a control by the inner surf zone morphology was highlighted leading to rapid and localized modifications of the wave field. This result was previously suggested by a numerical study (Nicolae Lerma and Bulteau, 2017), based on the phase-resolving nearshore wave model SWASH (Zijlema et al., 2011) that was carried out on the same site. The SW swash appeared to be sensitive to the local slope, e.g. with higher values in front of a rip channel. On the other hand, the IG swash component appears to be related to the outer bar system configuration and displays a different alongshore distribution than the SW swash. This numerical study suggests different responses to morphological features depending on the spectral component.

Despite the numerous studies dedicated to run-up characterization, very few were carried out in embayed beaches. As opposed to open beaches, embayed beaches are constrained by lateral boundaries and as a result often exhibit complex 3D morphological features such as rip channels (Enjalbert et al., 2011; Castelle and Coco, 2012). Thus, the hydrodynamics of the swash zone of those natural or man-made embayments is expected to differ from those observed at open beaches. For instance, Valentini et al. (2019) have shown that empirical models, which are widely used to assess run-up, often fail at estimating the run-up at an embayed beach. These results confirm what has been reported in a previous study carried out by Da Silva et al. (2017) who assessed various parametric formulations for run-up estimation on an embayed beach under varying conditions and who found that the performances were poor in the region where the wave field is affected by the headlands.

The intention of the present study is the documentation and investigation of swash motion characteristics in a meso-tidal engineered embayed beach influenced by 3D morphological features. The study is based on the analysis of TWL times series derived from timestack images, which were recorded with a video monitoring station during moderate to energetic incident wave conditions and different water levels. Those data are complemented with the results of a phase-resolving model that serve as surrogate to measurements and help to investigate the contributions to the run-up for this type of beach. The characteristics of the study site, Grande Plage of Biarritz (GPB) in southwest France, are first presented in section 2. This site was selected as it is representative for embayed beaches with high societal and historic stakes, which are highly exposed to storm hazards. The details of the field campaign and the methodology used to estimate the swash along the beach are described in section 3. The data is then used in section 4 to assess the performance of a phase-resolving model. The combined field data and numerical results are analyzed in section 5 to provide a better understanding of the swash dynamics. The numerical set-up and swash behavior are then discussed in section 6. The main results are summarized in the conclusion section.

2. Study site

The Grande Plage of Biarritz (GPB) is a 600 m long engineered beach within a 1.2 km long embayment located in the south-west of France (figure 1 panel **(a)**). The embayed beach is constrained by two headlands and is backed by a sea-wall, protecting shops and habitations from high water level and wave overtopping as well as providing a recreational area for walking or restaurant terraces. The beach is well known around the world for its surfing. It is also famous for its seafront casino and the *Hotel du Palais* on the northern side of GPB, a historical hotel built under the Napolean III era (see fig. 1, panel **(b)**).

The GPB opens to the Bay of Biscay and is mainly exposed to sea swells coming from the WNW direction (315°). The offshore wave climate ranges from moderately

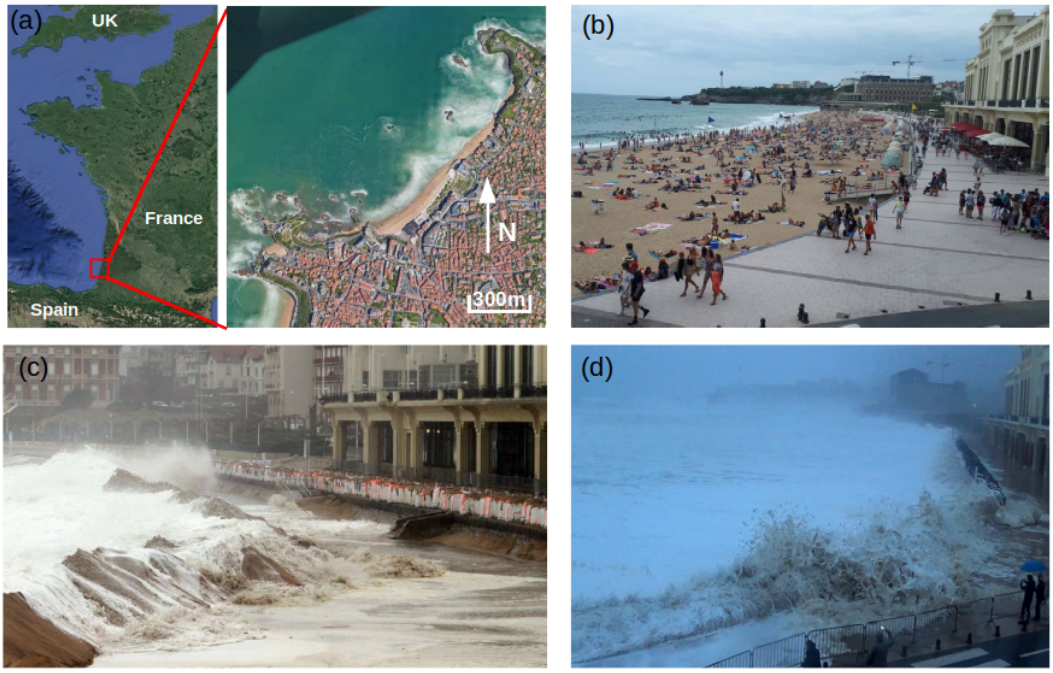

Figure 1: Location and situation of the study site Grande Plage of Biarritz. **(a)** Location of the GPB. **(b)** Crowded beach in front of the Casino during a calm day. The Hotel du Palais is seen in the background (Credit : Radio France - Céline Arnal). **(c)** Sand piles and big bags set-up to mitigate the storm impact (February 2016). Waves are seen overwashing the dunes (Credit : Bertrand Lapègue / Sud Ouest). **(d)** Submersion event during the Ciara storm in February 2020, water is seen overtopping the wall (Credit : SurfingBiarritz).

to highly energetic, with occasional high storm events. The significant wave height 10-year return period has been statistically computed to $H_s = 6.7\ m$ with a peak period of $T_p = 18\ s$ (Morichon et al., 2018). The GPB is a mesotidal environment with a spring tidal range of 4.5 m and a mean water level of 2.64 m (charts datum). Highest water levels reach +4.7 m excluding any surge. The elevation of the top of the seawall is +7.65 m. The double-barred profile (figure 3 panel **(b)**) exhibits a low sloping region in the subtidal zone (x < 800 m, with the outer bar at x = 600 m) and in the lower part of the intertidal area (800 m < x < 1000 m), with an inner bar that rather looks like an almost flat terrace around x = 950 m (slope 2-3%). Conversely, the foreshore is quite steep (slope 8-10%). For that reason the GPB is characterized as intermediate-reflective (Morichon et al., 2018). The beach morphology exhibits a large rip channel and a 3D nearshore bar system, as a result of the geological constraints (Enjalbert et al., 2011) visible on figure 3 panel **(a)**. In addition, the presence of rocky features in the nearshore bathymetry induces a complex offshore wave height distribution (Varing et al., 2020; Delpey et al., 2021).

The GPB has always been exposed to the impact of storms with varying degrees of damage (see figure 1 panel **(c)** and **(d)**). In recent years, public authorities have committed to limit the impact of flooding events by installing temporary protection measures. These include beach scraping, which consists of pushing sand against the seawall toward the lower portion of the beach, and the placement of sandbags (figure 1 panel **(c)**). These counter-measures have the advantage of being temporary and relatively easy to be set up. However, they might not be sufficient under some extreme conditions as damages to neighbouring buildings have been observed during recent storms. Moreover, there is evidence that the intensity of the impact of storms can vary along the GPB; implying that the design of an optimal protection solution could vary according to the exposure of the different beach sections to the incoming wave action.

3. Field data

During the winter 2018, a field campaign was launched between January 31 and February 2 to measure nearshore wave transformations and subsequent swash motion along the GPB during energetic incident wave conditions.

3.1. Offshore wave, tidal and topographic data

Offshore wave data were recorded by a directional buoy moored in 50 m depth at about 6 km from the coast. Hourly frequency-direction wave spectra were derived from the vertical and horizontal displacements recorded by the buoy.

Tidal data were provided by a tide gauge deployed at the Bayonne-Boucau harbor located 5.5 km north of the study site. It automatically records the level of water measured at regular 10 min intervals.

In this paper, a focus will be made on a storm recorded from January 31 to February 02, 2018. The window corresponds to spring tide. The tidal level varied between +0.5m and +4.8m. Variable offshore wave conditions were observed during the field experiment. They were first moderate with $(H_s, T_p) = (1.5\ m, 11\ s)$, followed by storm conditions with values reaching $(H_s, T_p) = (4.5m, 15.4s)$ from mid-day of the second day. The peak direction of wave propagation was mainly comprised between 300° and 320°, while during the most energetic event, a stable direction of 315° was observed, which corresponds to near-normal incidence of the GPB.

An extensive topo-bathymetric survey was conducted on January 31, covering the beach and the nearshore area up to 25 m meters depth. This dataset was complemented offshore by the national reference dataset from French Naval Hydrodraphic and Oceanographic Service (SHOM).

3.2. Video swash monitoring

Run-up motion along the swash zone of the GPB was tracked with video cameras installed at +30 m in a neighbouring building on the southern crop of the beach (figure 3). The video monitoring system is controlled by the open source software *SIRENA* (`https://sourceforge.net/projects/sirena-remote/`). The system is comprised of four cameras oriented to cover the whole area of interest, spanning from the outer surfzone to the beach front. In the upper part of the beach, the angular resolution (cross-shore) ranges from 1 to 15 cm and the radial resolution (longshore) from 1 to 5 m (Morichon et al., 2018).

Four cross-shore time series of pixel intensities sampled at 1 H_z, commonly referred to as *timestack* images, are generated at each camera. Those transects are spaced by approximately 100 m (fig. 3 panel **(a)**) and referred to as ID01 to ID04. Each timestack image represents a duration of 14 min to minimize the contribution of the tide on the water line position (Stockdon et al., 2006; Gomes da Silva et al., 2019).

The TWL position is automatically detected on the georectified timestack images based on a Color Contrast method (CC) using a modified Otsu (1979) segmentation algorithm, similar to the approach described by Vousdoukas et al. (2012). An example of the swash line detection and associated swash spectrum is given on figure 2). The automatic extraction of the swash line was not always possible and manual corrections were sometimes necessary for some images, especially under poor lighting or rainy conditions. The TWL pixel positions were then converted to TWL elevation time series using topographic measurements carried out with a NRTK-GNSS each day, at low tide, along the four cross-shore transects.

The timestack images collected during the 3-day studied time window were processed resulting in a data-set of more than 160 samples. To ensure consistent results when evaluating the alongshore variability of the swash, only the events when data at all four transects were available have been conserved resulting in a data-set of 26 events (104 timestack images), covering different tide levels and wave conditions.

3.3. Nearshore and surfzone wave measurements

Four pressure sensors were positioned along a cross-shore transect located in the middle of GPB to measure wave transformation in the intertidal zone (figure 3). Their elevations were measured with a RTK GNSS and vary between +0.3 m up to +2 m (chart datum). They were complemented with a subtidal bottom-mounted pressure sensor (type SEABIRD) at 12 m depth that provides wave characteristics in the shoaling zone prior to wave breaking.

All the sensors recorded bottom pressure continuously with a 2 H_z frequency. For spectral analysis purpose, the pressure time series were divided in 30 min bursts. Due to the extensive tidal range (more than 4 m) the four intertidal sensors were located alternatively in the surf or swash zone. Therefore, to avoid any non-physical results, only the moments when the sensors were fully submerged have been used in this study.

3.4. Data Processing

Free surface elevation times series $\eta(t)$ are computed from the bottom pressure recordings by applying a frequency-domain attenuation correction based on the linear theory (Tsai et al., 2005; Oliveras et al., 2011) with a cut-off frequency of 0.25 H_z to avoid the blow up of the solution due to the presence of secondary harmonics (Bonneton and Lannes, 2017). The swash time series $\eta_s(t)$ (eq. 1) are obtained after detrending the video estimated TWL(t) time series to remove the static components such as the tide, the surge and the wave set-up (Vousdoukas et al., 2011).

Power densities (PSD) of $\eta(t)$ and $\eta_s(t)$ are then computed using Welch's method (Welch, 1967) on 400 s segments using a 50% overlapping Hanning window. This results in a frequency resolution of $\mathrm{df} = 0.0025 H_z$ and 24 and 12 DOF for the free surface elevation and the swash respectively. IG (0.003-0.05 H_z) and SW (0.05-0.25 H_z) components of the significant wave heights and significant swash heights are calculated respectively as :

$$H_{IG}, S_{IG} = 4\sqrt{\int_{0.003 H_z}^{0.05 H_z} E(f)\,\mathrm{df}} \tag{2}$$

and

$$H_{SW}, S_{SW} = 4\sqrt{\int_{0.05 H_z}^{0.25 H_z} E(f)\,\mathrm{df}} \tag{3}$$

where E is the spectral density at the frequency f of either the free surface or the swash elevation time series. The total significant wave or swash height are computed as the sum of the IG and SW components :

$$H_s, S = \sqrt{H_{IG}^2 + H_{SW}^2}, \sqrt{S_{IG}^2 + S_{SW}^2} \tag{4}$$

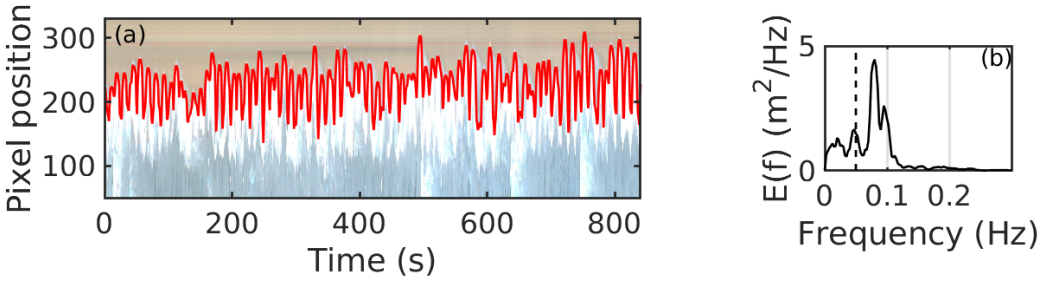

Figure 2: Example of the swash line extraction and treatment (data from ID02). **(a)** swash time series identification on the timestack. **(b)** Energy density spectrum derived from the measured swash time series in **(a)**. The black dashed line represents the limit between the SW and IG band (see section 3.4).

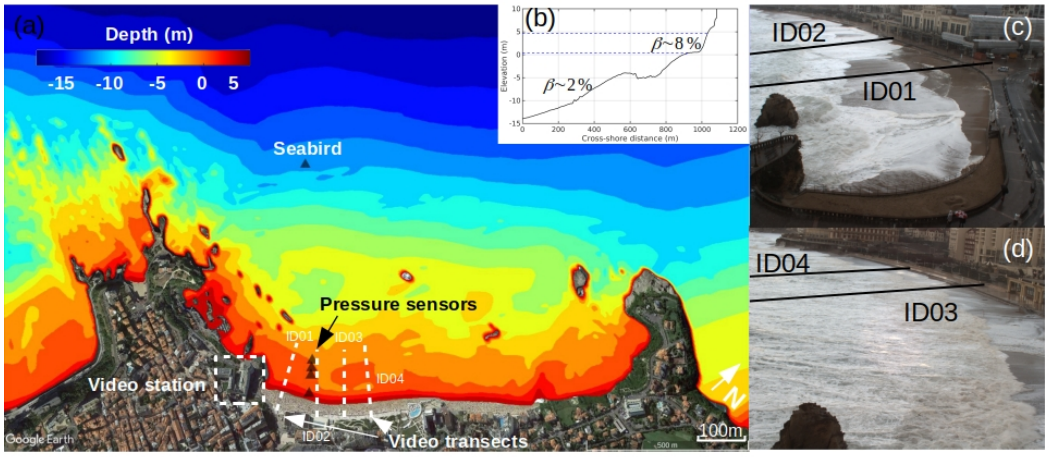

Figure 3: Field campaign description. **(a)** bathymetry of the GPB and locations of the measuring devices. Four pressure sensors were deployed close to the shore, one Seabird sensor was located at a depth of about 10m. A video station was recording high frequency cross-shore transects at different locations. The white dashed lines represent the cross-shore transects where the swash was video monitored. From left to right : ID01, ID02, ID03 and ID04. **(b)** Cross-shore profile at ID02. Blue dashed lines represents lowest and highest water level at the site. **(c)**/**(d)** View from camera 1/4 and transects locations.

4. Numerical modelling

4.1. BOSZ model

The BOSZ model (Roeber et al., 2010; Roeber and Cheung, 2012b) is used to compute the hydrodynamics of the surf and swash zones. It is a phase-resolving depth-averaged Boussinesq-type model based on the set of equations from Nwogu (1993), but alternately expressed in conservative form. Previous studies using BOSZ include tsunamis and long waves (Horrillo et al., 2014; Lynett et al., 2017; Roeber and Cheung, 2012a; Morichon et al., 2021), harbor oscillations (Azouri et al., 2018; Bellafont et al., 2018), wave transformations (Li et al., 2014; Filipot et al., 2019; Varing et al., 2020) and wave run-up (Pinault et al., 2020b).

This numerical model inherits the properties of the set of equations, being weakly nonlinear and weakly dispersive, enabling the modeling of wave transformations from intermediate to shallow water. Typical for depth-integrated solutions, overturning of the free surface cannot be described and the breaking process is approximated through a discontinuity in the flow analogous to a bore. To allow for the formation of discontinuous flows, the dispersion terms are locally and momentarily deactivated, which reduces the equations cell-wise to the hydrostatic nonlinear shallow water equation. In this study, the initiation of wave breaking relies on a wave height to water depth ratio. A shock-capturing Finite Volume scheme with HLLC Riemann solver is used for the computation of the numerical solution in the surf zone, whereas a Finite Difference 2nd-order upwind scheme of lower diffusivity and computational expense is used for the cells outside the surf zone where the local water depth is larger than $2 \cdot H_S$.

4.2. Model set-up

The computational domain extends 2.5 km offshore and spans 3.5 km in the longshore direction. The offshore boundary of the model corresponds to the 18 m isobath depth. The bathymetry is derived from the topo-bathymetric datasets described earlier.

A constant grid size of 3.5 m by 3.5 m is used, resulting in a total of 714,000 cells. The grid size was selected as reasonable compromise between numerical accuracy, stability, and computational cost for the assessment of the swash hydrodynamics as detailed in Pinault et al. (2020b).

For all computations, the bathymetry is stationary as no morphological change is considered in the computations.

The wave height to water depth ratio for the initiation of wave breaking is set to $\eta/H = 0.65$. Pinault et al. (2020b) suggested that any value within the range of 0.6 to 0.8 gave satisfactory results when comparing model run-up values to laboratory observations under the condition that the grid spacing is not excessively fine.

Each run corresponds to a constant tide level and represents the sea state conditions observed over a window of 15 minutes. The assumption of a constant water level is justified as only minimal changes of less than 20 cm were observed at the tidal gauge over the 15 min period. The model is run for 1.5 hrs where the first half hour was allocated for model spin-up and 1 h of simulation data. The run time ensures a full saturation of the wave-field across the entire domain and a sufficiently long time series for statistical analyses. The computational time for a single run is about 20 hours on a cluster machine with 16 CPUs. The time step is adaptive and based on a CFL number of 0.45. The Manning coefficient representing the roughness was set to constant $n = 0.02\ sm^{-1/3}$ over the whole domain to account for sand of medium grain size. The free surface elevation data is output at a rate of 1 H_z.

4.3. Boundary conditions

The model is forced at the offshore boundary by directional wave spectra computed from a spectral model over the inner shelf with the code SWAN (Booij et al., 1999). The SWAN domain extends 6.5 km offshore up to a depth of 50 m. The unstructured grid is composed of cells varying from 10 to 50 m, with higher resolution focusing on large bathymetric variations (Delpey et al., 2021). The outputs consist of 20 frequency-directional spectra equally distributed along the BOSZ offshore boundary. The use of a spatial distribution for the input conditions is meant to represent the variability of the wave field which is present over the particular sea floor trajectory (Varing et al., 2020). Each component of the spectrum is represented by a linear monochromatic wave with an individual amplitude, frequency, direction and random phase. The same set of random phases is used for the model runs to ensure identical phase locking. The differences between the computed scenarios are then solely due to differences in the magnitudes of the input spectra but not due to changes in phase locking. The waves are generated near the offshore boundary using an internal wavemaker and the resulting superpositions of all components form an irregular sea state. To avoid recycling of the input time series and generation of artificial wave grouping, the SWAN spectra are sub-sampled to frequency bins of 0.00018 H_z. Sponge layers are applied at the offshore and lateral boundaries of the numerical domain to absorb possible outgoing wave energy and to mimic open ocean conditions. To prevent any loss of energy within the area of interest, the domain is extended beyond the site of the GPB. While it increases the computational time it ensures a fully saturated wave field in the area. It should be noted that no other forcing is applied to the model, i.e. the wave field is solely generated from the offshore spectra. It is understood that these spectra are only an approximation of the sea state and that local currents or wind fields cannot be accounted for with this method.

4.4. Model result analysis

The TWL elevation time series is derived from the model results using a depth threshold of 5 cm to detect the waterline position. This approach is similar to previous studies (Ruju et al., 2014; Fiedler et al., 2018; Pinault et al., 2020b). The value of the depth threshold used in our study is consistent with recent studies (Almar et al., 2017; de Beer et al., 2021). As with the processing of the video measurements of the TWL, the swash time series is derived from the computed TWL time series by subtracting the mean value, which removes both the tide level and wave set-up. The PSD are computed in the same way for the computed data as for the observations, as well as significant wave and swash heights and their spectral components (equations 2 and 3). For consistency, wave heights are computed over two 30 min windows and averaged, whereas swash heights are computed over four 15 min windows.

The model performance is evaluated by computing the *Root Mean Square Error* (RMSE), the *Normalized Root Mean Square Error* (NRMSE), the bias, the coefficient of determination (R^2) and the scatter index (SCI) according to:

$$\mathrm{RMSE} = \sqrt{\frac{1}{n}\sum_{i=1}^{n}(C_i - O_i)^2} \tag{5a}$$

$$\mathrm{NRMSE} = \frac{\mathrm{RMSE}}{\max(O_i) - \min(O_i)} \tag{5b}$$

$$\mathrm{bais} = \frac{1}{n}\sum_{i=1}^{n}(C_i - O_i) \tag{5c}$$

$$\mathrm{SCI} = \frac{\sqrt{\frac{1}{n}\sum_{i=1}^{n}(C_i - O_i)^2}}{\max\left(\sqrt{\frac{1}{n}\sum_{i=1}^{n}|O_i|^2}, \bar{O}\right)} \tag{5d}$$

where O and C respectively denotes the observed and computed values, and n the number of points.

4.5. Model validation

A total of 80 runs was carried out to test the capacity of the BOSZ model configuration to compute the observed wave transformation in the surf zone and the subsequent swash motion. Those runs cover most of the incident wave conditions and tidal levels that occurred during the 3-day period.

2010

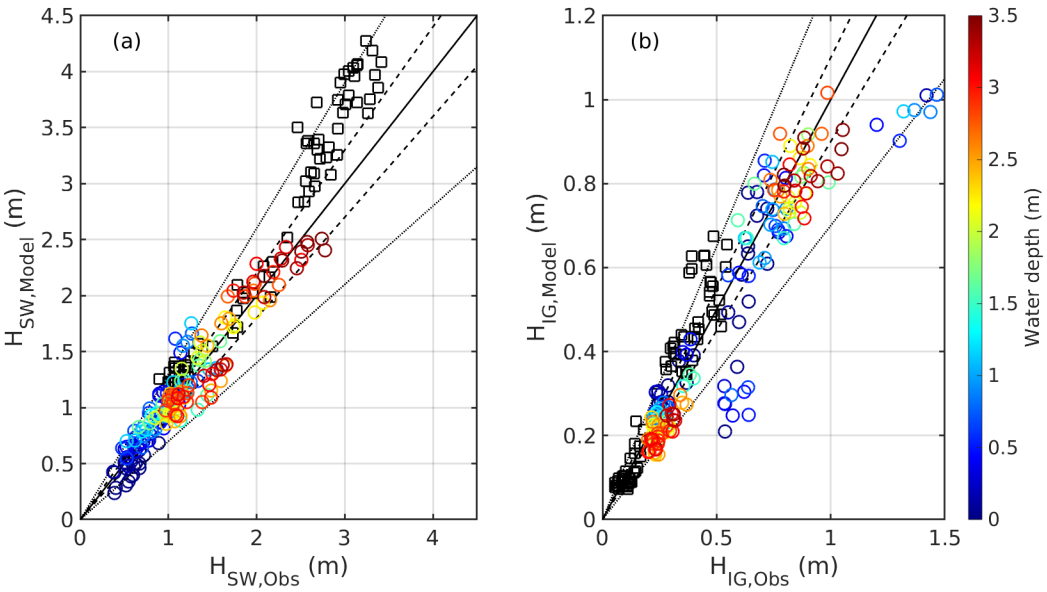

Figure 4: Comparison between modeled and observed significant wave heights of the SW (panel **(a)**)) and IG (panel **(b)**) bands. The color scale indicates the water depth at the sensor locations. Black squares represent the Seabird data. Solid, dashed and dotted lines respectively represents the 1:1, 10% and 30% error lines.

4.5.1. Nearshore wave transformation

A detailed comparison between computed and measured significant wave heights is given in Figure 4. It shows that the model consistently reproduces H_{SW} and H_{IG}. A positive bias is obtained at the SEABIRD location where the model tends to overestimate H_{SW} for the most energetic conditions (table 1). It seems that this discrepancy is rather local or somehow compensated by the rest of the propagation, as model statistics in the intertidal area are overall good (CP05 to CP07) with a low scatter index SCI of the order of 10%. At CP04, the shallowest location, the statistics for H_s are good, however biases of 0.23 and -0.34 m respectively for H_{SW} and H_{IG} are observed. It is worth to note that the CP04 sensor was often emerged during the field campaign, which limits the amount of data available to assess the performance of the model at this depth.

An example of comparison between computed and observed wave spectra is displayed in figure 5. The model correctly reproduces the cross-shore evolution of the wave energy frequency distribution as the waves propagate from intermediate to shallow waters (panel **(d)**). In particular, it captures well the energy transfer between the SW and the IG frequency bands in the surfzone. Discrepancies appear at some frequencies and are expected, since the exact wave conditions remain unknown and only an approximation from a spectral model is used as forcing for the Boussinesq model. The total amount of energy (H_s) is well reproduced and the agreement between model and observations is very close at the shallowest pressure sensor (figure 5 panel **(c)**). In addition, the biases obtained at this point (CP04 in table 1) could be due to a shift in location rather than an erroneous energy distribution when looking at the cross-shore transect in figure 5 panel **(d)**. Indeed, the remarkable increase in H_{IG} up to approximately 1.3 m at CP04 location, is reproduced by the model but slightly further shoreward. This is also suggested by the comparison with the spectrum extracted 2 grid cells shoreward of CP04 location (light blue curve in panel **(c)**), which shows a better match with the observations.

4.5.2. Swash motion

The ability of the BOSZ model to compute the swash dynamics is illustrated by the comparisons between the computed and the video-derived swash components (S,S_{SW} and S_{IG}) at transect ID01 to transect ID04 (figure 6). The total significant swash height S and the infragravity significant swash height S_{IG} are overall well reproduced for the entire field campaign. The major discrepancies are observed for the short wave significant swash height S_{SW}, whose distribution is more scattered.

Error statistics for the swash motion are given in table 2. In total, the model captures reasonably well the significant swash height with a RMSE of 0.42 m (corresponding to a NRMSE of 0.16), a R^2 of 0.74 indicating a good linear correlation and a SCI of 0.19. A negative bias of 0.30 m is noted, suggesting that the model tends to underestimate the total significant swash height S. The IG swash shows a higher correlation coefficient R^2 than the SW swash. However, a stronger negative bias is observed for S_{IG} at almost all locations compared to the one of S_{SW} suggesting that most of the underestimation of S is due to the IG component. When looking at each longshore location, model and observations show the best match at ID04 with a RMSE of 0.27 m. In contrast, a RMSE of 0.54 m is observed at ID03. The southern locations, ID01 and ID02, show similar behaviors with a RMSE of 0.43 m at both locations. Both

Table 1
Statistics evaluating the fit between observed and modeled values of wave heights. The statistics are evaluated at each cross-shore location and for all locations together (total).

		Total	Seabird	CP07	CP06	CP05	CP04
H_s	RMSE (m)	0.31	0.49	0.16	0.16	0.13	0.11
	NMRSE (-)	0.10	0.20	0.08	0.07	0.08	0.13
	Bias (m)	0.11	0.38	-0.05	-0.05	0.01	0.01
	R^2 (-)	0.94	0.96	0.95	0.92	0.93	0.92
	SCI (-)	0.18	0.21	0.10	0.11	0.10	0.07
H_{SW}	RMSE (m)	0.32	0.48	0.16	0.17	0.15	0.30
	NMRSE (-)	0.10	0.20	0.07	0.08	0.09	0.76
	Bias (m)	0.13	0.38	-0.05	-0.03	0.03	0.23
	R^2 (-)	0.94	0.96	0.94	0.91	0.91	0.36
	SCI (-)	0.18	0.21	0.11	0.12	0.13	0.27
H_{IG}	RMSE (m)	0.11	0.07	0.07	0.08	0.07	0.35
	NMRSE (-)	0.08	0.15	0.08	0.10	0.09	0.38
	Bias (m)	-0.02	0.03	-0.01	-0.04	-0.05	-0.34
	R^2 (-)	0.88	0.92	0.95	0.93	0.96	0.97
	SCI (-)	0.18	0.24	0.11	0.14	0.12	0.34

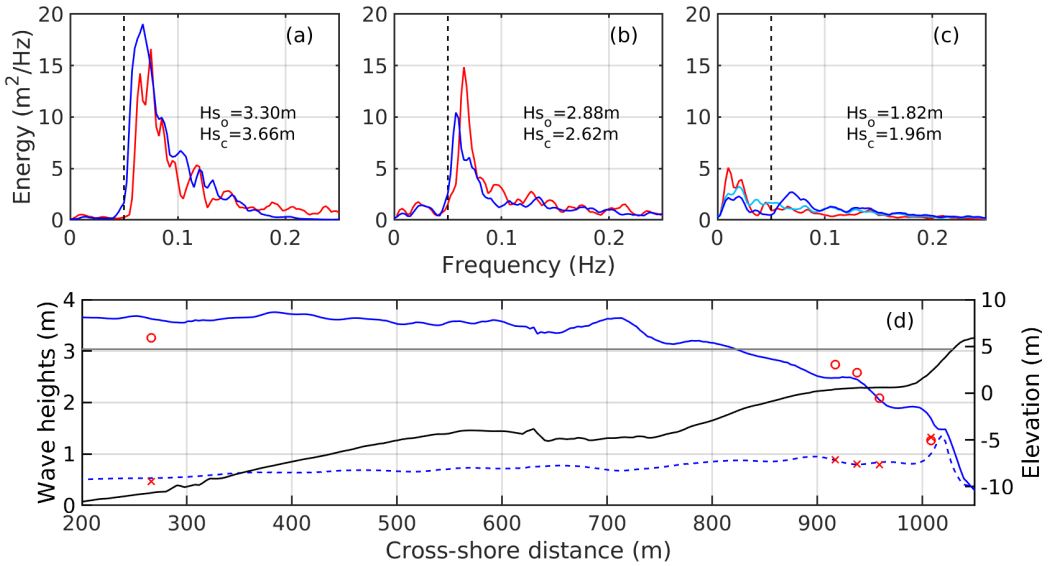

Figure 5: Comparison between observations (red) and model (blue) results on the 02/02 at 4.30am ($H_s = 3.5\ m$ $T_p = 14\ s$, WL=+4.7 m). Spectra at locations of **(a)** seabird (depth of 15.5 m), **(b)** CP07 (3.8 m) and **(c)** CP04 (1.2 m). Light blue on **(c)** corresponds to the numerical spectrum extracted 2 grid cells further shoreward. The vertical black dashed line represents the limit between the SW and IG frequency band. H_{s_o} and H_{s_c} respectively indicate H_s observed and computed. **(d)** Cross-shore transect of H_{SW} (solid line, circles) and H_{IG} (dashed line, crosses), left axis. The bathymetric profile and still water level are indicated in black and grey lines, right axis.

the IG and SW bands behave similarly with better statistics at ID04.

Overall, the statistical model performance parameters show that the BOSZ model performs reasonably well in computing the nearshore wave propagation in the GPB for moderate and energetic wave conditions and different tide levels. Though, some discrepancies between computed and observed data remain. These differences are expected, since not all processes are taken into account by the model and the exact wave conditions at the time of the campaign are unknown. Nevertheless, figures 7 and 8, which are presented in the results section, show that the model reproduces well the variability induced by the tide and incident wave energy. These qualities indicate that the model is a suitable tool for studying swash motion at an embayed beach such as the GPB.

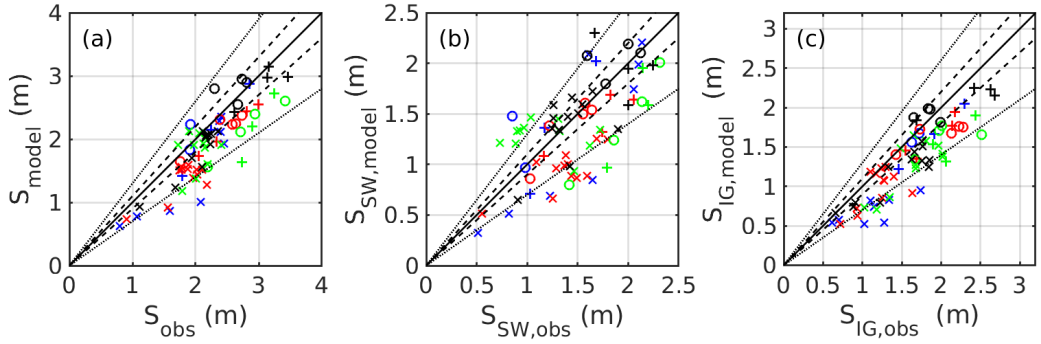

Figure 6: Comparison of modeled and observed S (a) , S_{SW} (b), S_{IG} (c). Blue, red, green and black colors respectively represent the longshore locations ID01, ID02, ID03 and ID04. Crosses, pluses and circles respectively represent the different dates (31/01, 01/02 and 02/02). Solid, dashed and dotted lines respectively represents the 1:1, 10% and 30% error lines.

Table 2
Statistics evaluating the fit between observed and modeled values of swash heights. The statistics are evaluated at each longshore location and for all locations together (total).

		Total	ID01	ID02	ID03	ID04
S	RMSE (m)	0.42	0.43	0.43	0.54	0.27
	NRMSE (-)	0.16	0.21	0.21	0.32	0.11
	Bias (m)	-0.30	-0.26	-0.39	-0.41	-0.14
	R^2 (-)	0.74	0.75	0.85	0.51	0.85
	SCI (-)	0.19	0.21	0.20	0.22	0.11
S_{SW}	RMSE (m)	0.38	0.40	0.38	0.46	0.29
	NRMSE (-)	0.21	0.30	0.25	0.29	0.22
	Bias (m)	-0.13	-0.16	-0.29	-0.13	0.02
	R^2 (-)	0.44	0.62	0.53	0.23	0.49
	SCI (-)	0.25	0.27	0.26	0.30	0.18
S_{IG}	RMSE (m)	0.37	0.41	0.31	0.46	0.30
	NRMSE (-)	0.18	0.29	0.20	0.31	0.15
	Bias (m)	-0.29	-0.40	-0.24	-0.41	-0.20
	R^2 (-)	0.76	0.78	0.80	0.66	0.79
	SCI (-)	0.22	0.28	0.20	0.25	0.17

5. Results

5.1. Significant swash height evolution

The evolution of the significant swash height S during the 3-day case study are analysed at the four timestack transects based on video observations and model results (figure 7). Video captures cannot be performed at night time and detection of the TWL line was challenging during some of the most energetic conditions. Thus the model is used as surrogate when video data are not available. The alongshore averages of S vary from 0.4 m to 3.5 m with a mean of 1.8 m. This represents a range of 172% around the mean value. At the four locations, the values of S are highly modulated by the tide. For example, under similar incident wave conditions, S varies by a factor of 8 between low tide (LT) and high tide (HT) at ID01 with respectively $S = 0.3\,m$ and $S = 2.5\,m$. The varying wave conditions, which include moderate swell ($H_s = 1.5\,m$, $T_p = 11\,s$) to storm conditions ($H_s = 3.5\,m$ and $T_p = 14\,s$), also influence the swash statistics. As expected, increasing wave heights and periods induce higher values of S all along the GPB. For instance at ID02, S is 2.3 times larger under energetic conditions than under moderate conditions for a similar tide level.

The tide in combination with the incoming storm swell during the second day abruptly increases the swash heights. At ID01, a swash height of 0.33 m is observed at 11:30 am and reaches 3.3 m at 2:30 pm, representing an increase by a factor of 10 over the span of 3 h.

5.2. Tidal modulation of the swash

To quantify more precisely the impact of the tide on the swash amplitude in this meso-tidal environment, the evolutions of (S, S_{SW}, S_{IG}) normalized by the offshore wave height H_0 are displayed on figure 8 as a function of the water level (WL) for the two distinct wave regimes of the studied time window. The WL corresponds here to the astronomical tide η_{tide} plus the potential surge η_{su} (see eq. 1) as measured by the tidal gauge. Both the observations (circles) and the numerical results (crosses) are displayed and exhibit similar trends, testifying again of the model results consistency. The influence of WL on the amplitude of the significant swash is pronounced for moderate wave conditions (blue). For this wave regime, S varies by a factor of 4.5 from $0.3H_s$ at LT up to $1.4H_s$ at HT based on numerical results (crosses). Observations (circles) show a similar trend as the numerical results although no data were available at low tide. In contrast, under energetic conditions the variability of S and S_{SW} is less pronounced. The evolution of S_{IG} is less dependent of the wave regime, with the ratio S_{IG}/H_S increasing almost linearly with WL from 0.3 at LT to 1.2 and 1 at HT respectively for moderate and energetic conditions.

5.3. Analysis of the longshore variability of S

Significant variability of swash height was observed along the beach during the studied events. The experimental data-set shows that under energetic conditions, S varied by up to 1.5 m alongshore during a single event, which corresponds to a 90% difference between the minimum and maximum values. Under moderate conditions, this difference

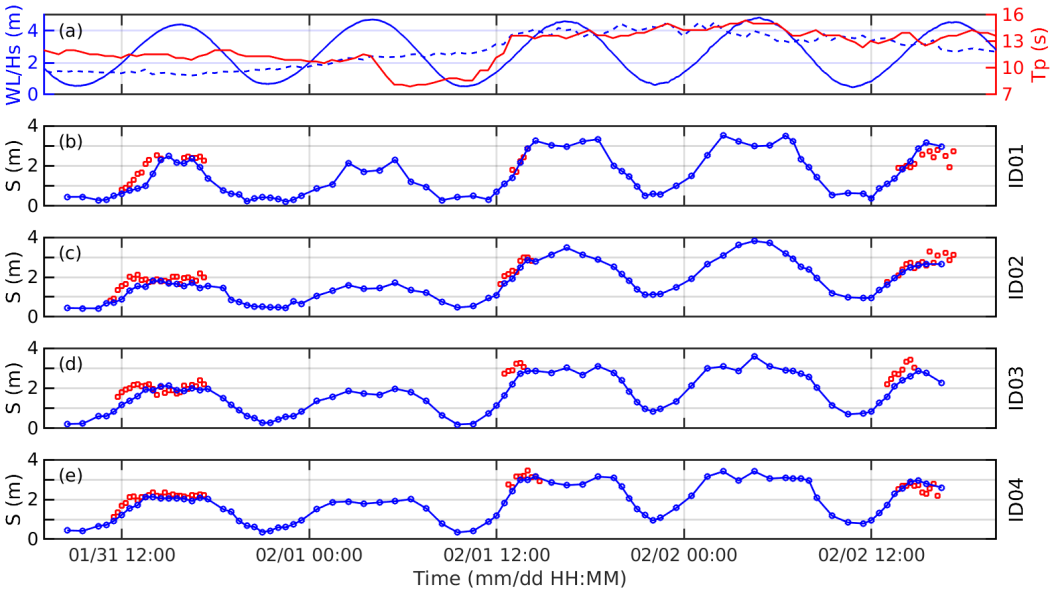

Figure 7: Evolution of the significant swash height through time. **(a)** : Time series of H_s (blue dashed line), T_p (red solid line) and the tide level (blue solid line). **(b)**, **(c)**, **(d)** and **(e)** : Time series of the significant swash height S at the different longshore locations, respectively at ID01, ID02, ID03 and ID04. Blue line : numerical data, red squares : observations.

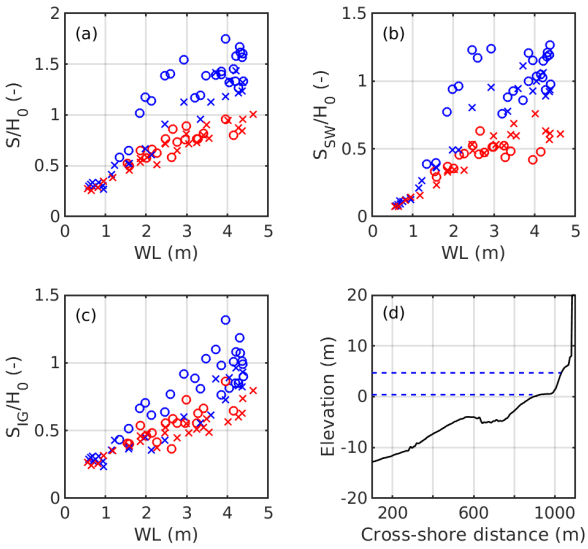

Figure 8: Evolution of the significant swash heights normalized by the offshore significant wave height at the ID02 location as a function of the water level, under moderate (blue) and storm (red) conditions. **(a)** : S, **(b)** : S_{SW}, **(c)** : S_{IG}. Circles denote the observations and crosses the numerical data. The bathymetric profile is shown on panel **(d)**, the two blue dashed lines indicating the low and high water levels.

reached 120% or 1 m. Numerical results exhibit a similar behavior with ranges of 1.0 m (66%) and 1.13 m (112%) under energetic and moderate conditions respectively. The location of highest swash values, or *hotspot*, appears to be modulated by the environmental conditions.

To further examine this aspect, the numerical dataset was divided into six classes, each representative of a specific type of conditions, combining wave characteristics and water levels that occurred during the studied time window. The number of events observed and simulated in each class are given in table 3. The longshore standard deviation of the swash frequency components computed for each class are used as statistics to quantify the alongshore variability of the swash (table 4). Only the numerical results were considered as they provide a continuous longshore distribution and by consequence a better representation of each class of events. The longshore standard deviations of S ranges between 13 cm and 46 cm. The variability of S is greater for higher water levels for both moderate and energetic conditions, with for example $\sigma(S) = 22\ cm$ at LT and $\sigma(S) = 46\ cm$ at HT. The alongshore swash variability appears driven by both frequency components as $\sigma(S_{SW})$ and $\sigma(S_{IG})$ are of the same order of magnitude. At LT, for moderate and storm conditions, the variability is slightly dominated by the infragravity frequency band ($\sigma(S_{IG}) > \sigma(S_{SW})$), as well as the swash motions ($\overline{S_{IG}/S_{SW}}$>2.5). At MT and HT, while S_{SW} and S_{IG} are more balanced (with a slight prevalence of IG for the two energetic classes), S_{SW} appears to be leading the alongshore variability.

5.4. Spectral distribution of the swash energy

The energy density spectra computed from the 15 min swash times series are averaged over the classes defined in table 3 to further characterize the dependency to environmental conditions (fig. 9). At LT, the class-averaged spectra are highly dominated by the IG band along the entire beach regardless of the incident wave conditions (panels **(a)** and **(d)**), with a mean ratio of 2.5 and 2.9 under moderate and energetic conditions respectively (table 4). At MT, under moderate conditions (panel **(b)**) the energy distribution presents

Table 3
Classes separating the dataset into events of similar conditions and corresponding number of events modeled. The number of observed events is shown between brackets.

Wave energy	Low tide (LT) 0.5 m < WL < 1.8 m	Mid tide (MT) 1.8 m < WL < 3.5 m	High tide (HT) 3.5 m < WL < 4.7 m
Moderate 1.2 m<H_s<1.7 m 10 s<T_p<12 s	Computations : 10 (0)	Computations : 5 (8)	Computations : 8 (9)
Storm 3 m<H_s<4 m 13.5 s<T_p<14.5 s	Computations : 7 (0)	Computations : 10 (9)	Computations : 10 (0)

Table 4
Statistics of the longshore variability of the swash for each class of conditions. The standard deviation (σ) is given by columns 3, 4 and 5 for S, S_{SW} and S_{IG} respectively. The last column provides the averaged (mean), minimum (min) and maximum (max) ratio S_{IG}/S_{SW}.

Wave energy	Tide	$\sigma(S)$ (m)	$\sigma(S_{SW})$ (m)	$\sigma(S_{IG})$ (m)	S_{IG}/S_{SW} mean | min | max
Moderate					
	Low tide	0.13	0.08	0.11	2.5 | 1.6 | 4.1
	Mid tide	0.26	0.25	0.13	0.8 | 0.6 | 1.4
	High tide	0.28	0.29	0.27	1.0 | 0.4 | 1.7
Storm					
	Low tide	0.22	0.12	0.19	2.9 | 2.0 | 5.1
	Mid tide	0.27	0.25	0.20	1.2 | 1.0 | 2.0
	High tide	0.46	0.49	0.41	1.3 | 0.6 | 2.1

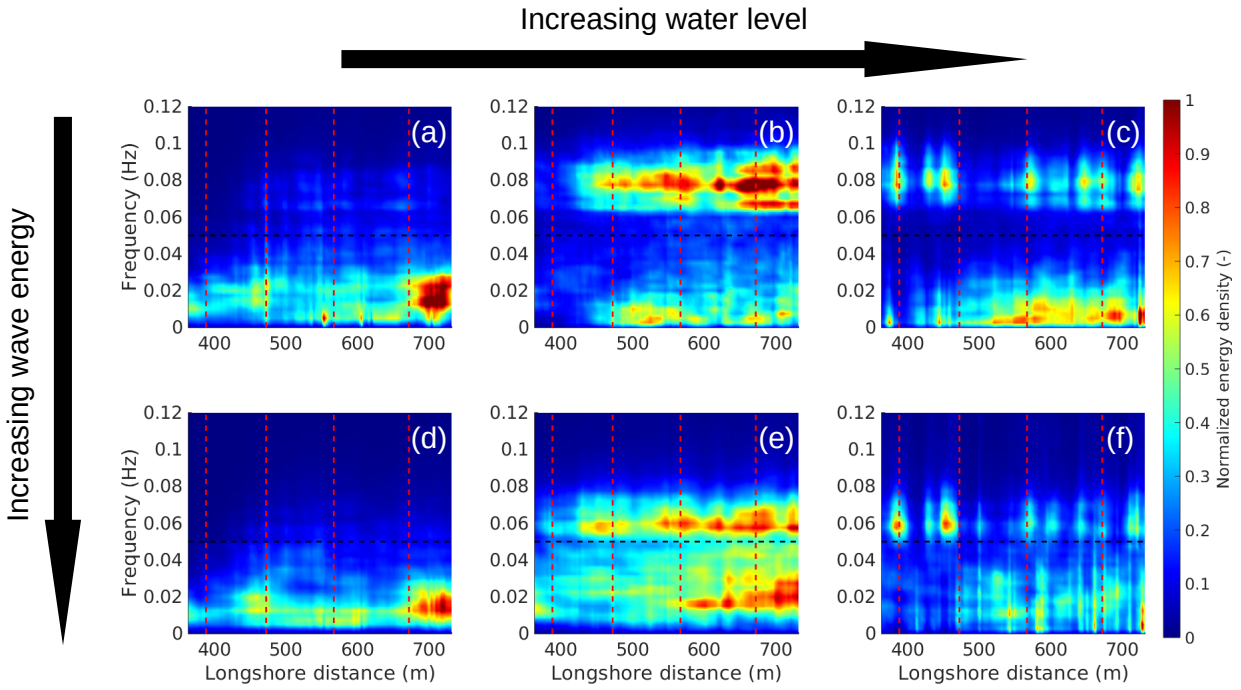

Figure 9: Modeled swash spectra as a function of the alongshore distance. Each spectrum is an average of all events in each class defined in 3 and normalized by its maximum value. The horizontal black dashed line represents the limit between the IG and SW frequency bands. The vertical red dashed lines indicate longshore positions of the webcam transects (see fig. 3 **(a)**). For reference of the alongshore position see figure 11.

a bi-modal pattern with higher energy in the SW frequency band, typical from reflective behaviors. For similar water level conditions but under storm conditions (panel **(e)**), the distribution is more spread out despite the presence of two distinct peaks in the lower IG band and in the lower SW frequency band. At HT (panels **(c)** and **(f)**), both frequency bands are visible in similar intensities (mean ratio around 1, table 4). Those results confirm the strong tidal modulation of the swash motion and the secondary influence of the incident wave conditions.

Alongshore differences of swash energy distribution between frequency bands are clearly visible for each class. Generally, a lower energy is found in the southern part of the domain ($y < 450\,m$) while several hotpots of energy both in the SW and IG frequency bands are observed at different longshore locations. At LT (panels **(a)** and **(d)**), most of the energy is clearly in the IG band and exhibits lower values in the southern part of the domain. A strong concentration of IG energy is found around $y = 700\ m$.

At MT, under storm conditions (panel **(e)**), the spectrum is saturated at all frequencies over the entire beach with the energy gradually increasing from south to north (i.e. with increasing algonshore distance). Similarly to LT, a stronger concentration of IG energy is found around $y = 700\ m$. Under moderate conditions (panel **(b)** the decrease of energy in the south is abrupt, with virtually no energy found before $y = 430\ m$. The low energy zone extends even further into the IG band. In the SW frequency band, three distinct peaks are well defined in the northern part of the domain (y>600 m) while only the main peak is visible souther from this limit .

At HT, the low frequencies display a similar behavior as at LT and MT, exhibiting an increase from south to north, gradual under moderate conditions (panel **(c)**) and more abrupt under storm conditions (panel **(f)**). However, the energy distribution in the SW frequency band displays a highly variable behavior, with several distinct *hotspots* of energy. These features are disseminated along the beach centered around the frequency $f = 0.08\ H_z$ under moderate conditions and $f = 0.06\ H_z$ under storm conditions which correspond to the incident swell peak frequency. As a result, the southern part of the domain appears SW dominated while some locations in the northern part are clearly IG dominated.

6. Discussion

6.1. Short and long wave contributions to the swash under varying conditions

The water level has been shown to have a significant influence on the wave and swash dynamics in an environment exhibiting complex morphologies such as bar systems (Guedes et al., 2011, 2012; Vousdoukas et al., 2012; Cohn and Ruggiero, 2016; Khoury et al., 2019; Matsuba et al., 2021). In this study, a significant tidal-induced variability of a factor of 4.5 was observed under moderate conditions (figure 8), with low values found at LT. Cross-shore evolution of H_s (see example in figure 5) supported by visual observations show that wave breaking primarily occurs on the low sloping region at LT. This results in a wide surf zone dissipating a substantial amount of SW energy ultimately leading to predominant control of the swash by long waves. In contrast, at HT plunging breakers on the steep foreshore are observed, dissipating less wave energy before reaching the shoreline.

Furthermore, differences in the tidal level also result in contrasted relative contributions of the SW and the IG to the swash motion. To highlight these variable situations, figure 10 shows the evolution of the alongshore averaged ratio $\overline{S_{IG}/S_{SW}}$ as a function of the water level. For low water levels (WL<2 m) the swash appears largely dominated by low frequency motions ($1.5<\overline{S_{IG}/S_{SW}}<3.5$), typical of low sloping beaches (Ruggiero et al., 2004; Stockdon et al., 2006). As the tide level increases, the relative contribution of the IG swash decreases. For moderate wave conditions, the swash becomes SW dominated from WL = 2.5 m (MT) to 3.5 m. For comparable WL in energetic conditions, $\overline{S_{IG}/S_{SW}}$ is close to 1. At high tide (WL > 3.5 m), the relative IG contribution increases again and the configuration is back to IG predominance. Thus, depending primary on the water level and secondary on the incident wave energy, the same studied beach may alternatively exhibit dissipative or reflective or intermediate configurations. An explanation for these contrasted situations can be found again in the tidal modulation of the surfzone location and the related slope, especially under moderate wave conditions. Under energetic conditions, large waves tend to break deeper. At HT, waves still break over the flat terrace, resulting in a rather dissipative behavior despite the higher WL. This behavior is consistent with the lower variability of S and S_{SW} under energetic conditions on figure 8. In addition, the low values of S_{IG} observed at LT on figure 8 suggest that a portion of the IG wave energy is dissipated through breaking, consistently with previous studies carried out under dissipative conditions (van Dongeren et al., 2007; de Bakker et al., 2014). While averaged values clearly show a trend depending on the tide level, significant alongshore variations of the dominating swash contribution are observed, especially at HT and LT, where the IG component is dominating. For example, under energetic conditions (red curve) for a water level of 4.5 m the swash ratio varies between 0.7, characteristics of reflective conditions, and 2.0 more representative of dissipative conditions. Thus, remarkably, both reflective and dissipative swash regimes may be simultaneously present along the same studied beach.

6.2. Alongshore variability of the swash

We observed a pronounced alongshore variability of the swash and its frequency components with a ratio of 2.2 between the lowest and the highest value of S measured along the beach. This result is comparable to the alongshore variability previously documented at a dissipative open beach (Senechal et al., 2018), a dissipative semi-open

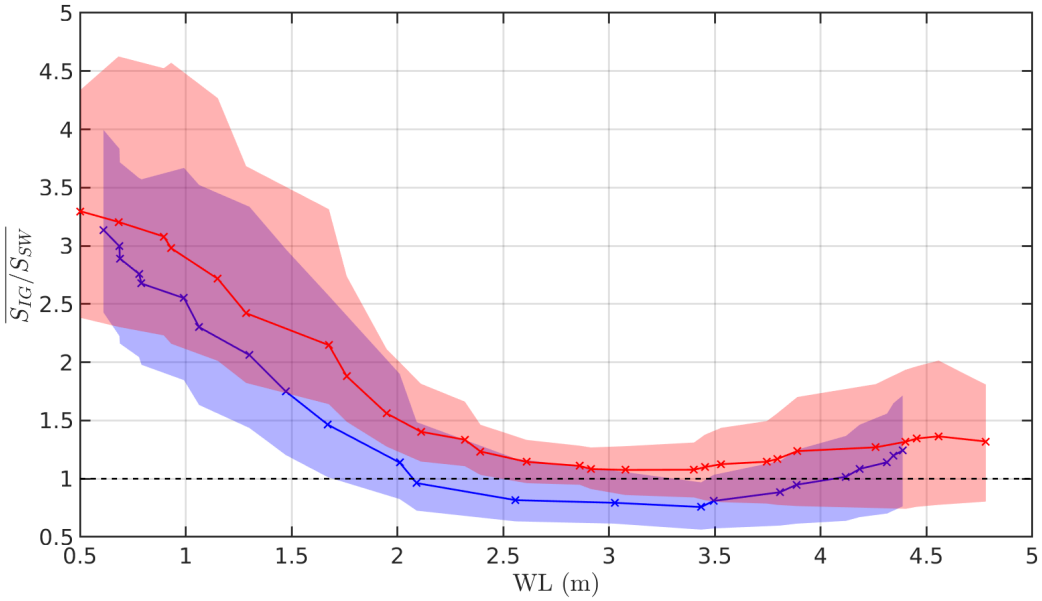

Figure 10: Alongshore averaged ratio $\overline{S_{IG}/S_{SW}}$ against the water level. The solid line and crosses denote the numerical data, and shaded areas indicate the 25 and 75 percentile of the alongshore values. Blue and red colors respectively indicate moderate ($H_s < 1.5m$) and storm conditions ($H_s > 3m$).

beach (Ruggiero et al., 2004) and at a reflective pocket beach (Guedes et al., 2012). The measured longshore variability of the swash was confirmed by our numerical computations that allow to supplement the data set with additional wave and water level conditions. The averaged variability of S computed within each class of conditions (defined in table 3) also shows a significant variability with a standard deviation ranging from 0.13 m up to 0.46 m (table 4). This is comparable to Stockdon et al. (2006), whose study was carried out on dissipative and reflective beaches. In our study, we show that the contribution of S_{SW} and S_{IG} to the alongshore variability of the swash is usually balanced in most of the cases studied. This result contrasts with previous studies both for dissipative beaches where the variability was contained within the IG band (Ruggiero et al., 2004; Senechal et al., 2018; Pinault et al., 2020a), and for reflective beaches where S_{SW} was the predominant component of the swash amplitude's variability (Guedes et al., 2012).

6.2.1. Beach slope influence

The spatial correlations between the alongshore distribution of the swash and the foreshore slope are calculated (table 5) to assess the influence of the beach slope. The foreshore slope β_f was calculated here as the slope over a region of $\pm 0.5m$ around the still water level. The total swash S exhibits a positive correlation with β_f (90% of the time) : an increase of β_f results in an increase of the amplitude of S. S_{SW} is significantly correlated (at the 95% confidence level) to β_f 95% of the time, while for S_{IG} it is only 63% of the time. This result is consistent with previous studies showing that S_{SW} and the foreshore slope are linearly dependent (Stockdon et al., 2006; Ruggiero et al., 2004; Nicolae Lerma and Bulteau, 2017), while the influence of the beach slope on S_{IG} is often omitted in run-up estimation formula (Stockdon et al., 2006; Senechal et al., 2011; Brinkkemper et al., 2013). Values of R^2 averaged over the whole data-set ($\overline{R^2}$) suggest that the alongshore variability of S_{SW} can be partially explained by the foreshore slope variation ($\overline{R^2} = 0.52$). The influence is much less pronounced for S_{IG} ($\overline{R^2} = 0.33$).

Table 5
$\%R^2$: Percentage of spatial correlations significant at the 95% level. The value in parenthesis indicates the percentage of significant correlations that are positive. $\bar{R}^2$: averaged correlation over all events.

	$R^2(S,\beta_f)$	$R^2(S_{SW},\beta_f)$	$R^2(S_{IG},\beta_f)$
$\%R^2$	93 (90)	95 (98)	63 (100)
$\overline{R^2}$	0.48	0.52	0.33

The analysis of R^2 computed for the different classes of conditions highlights that the influence of the foreshore slope can vary according to the wave and water level conditions (table 6). The influence of β_f on the variability of S is the highest at mid tide for both moderate and energetic wave regimes. Both S_{SW} and S_{IG} exhibit the same trend, with higher values for S_{SW} consistently with table 5. Poor correlation is found between S_{IG} and β_f at both LT and HT. Consistently with previous results, S_{SW} is (partially) correlated with β_f at HT under moderate conditions, while this not the case anymore during the storm.

6.2.2. Nearshore morphology influence

In order to better understand the role of the nearshore morphology on the swash dynamics, maps of significant

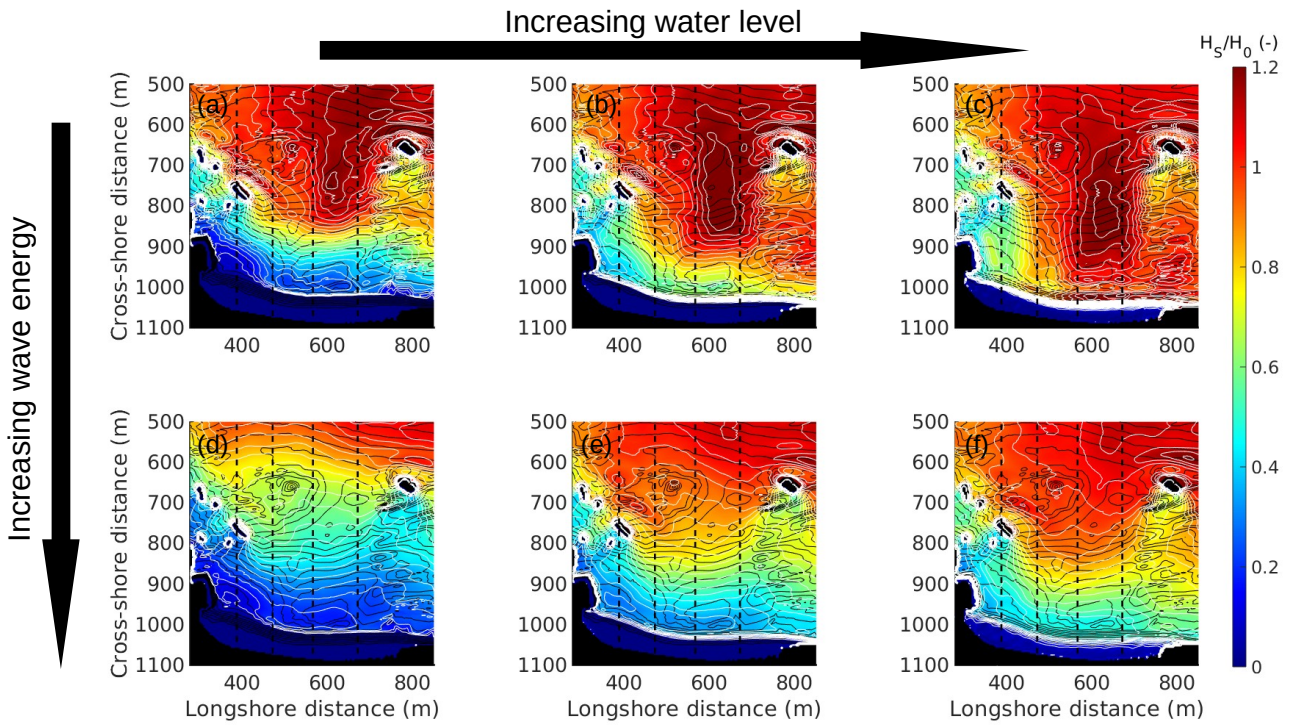

Figure 11: Significant wave height H_s normalized by the offshore wave height. Black lines display the contour of the bathymetry and white lines the contour of the values plotted in the colormap (H_s/H_0).

Table 6
Squared correlation coefficients between the alongshore distributions of the swash and the foreshore slope. Values shown are significant at the 95% percentage confidence level. All calculated coefficients were positive.

Wave energy	$R^2(S,\beta_f)$	$R^2(S_{SW},\beta_f)$	$R^2(S_{IG},\beta_f)$
Moderate			
Low tide	0.29	0.34	0.19
Mid tide	0.68	0.70	0.43
High tide	0.41	0.57	0.08
Storm			
Low tide	0.24	0.42	0.17
Mid tide	0.61	0.59	0.40
High tide	0.31	0.26	0.12

wave heights H_s are computed for each class of wave conditions and water levels defined in table 3 (figure 11). These maps reveal that the influence of the tide on the nearshore wave field characteristics varies according to incident energetic conditions. Under moderate conditions, the surf zone gets narrower and moves further onshore as the water level increases, while for energetic conditions the influence of the tide is less pronounced, since waves mostly break further offshore. As a consequence, while the alongshore distribution of the wave-field in intermediate water depth is relatively uniform, with a variability of less than 10% between maximum and minimum at a depth of 15 m for all conditions, the nearshore wave-field exhibits clearly non-uniform patterns. Furthermore, the presence of geological and three-dimensional morphological features influences the distribution of H_s in different ways along the beach. The most obvious effect is the significant decrease of wave energy in the lee-side of the rocks that corresponds to the area of low swash energy observed on figure 9 for x<450 m. Furthermore, as suggested in previous studies (Guedes et al., 2012; Nicolae Lerma and Bulteau, 2017; Senechal et al., 2018), the uneven distribution of wave energy induced by the nearshore topography can influence the swash components. Under moderate conditions, lower energy is observed in the rip channel (around $x = 500m$), which corresponds to a de-focusing area due to refraction above the channel's sides. In this region a lower swash energy is found at LT in the IG frequency (figure 9 panel **(a)**) but is less visible at mid or high tide. Morphology-induced variations of the wave-field are also observed over the large channel located at $x = 700\ m$. While a higher swash energy is observed at LT in that region, under both moderate and energetic conditions (see figure 9 panels **(a)** and **(d)**), H_s values are smaller suggesting that in this particular case, higher waves in the nearshore do not necessarily lead to higher swash values. Under energetic conditions the wave-field displays considerably less alongshore variability in the nearshore except in the vicinity of the rocky islands, as a result of wave breaking that occurs much further offshore.

Finally, the correlation between the wave and swash height distributions are given in table 7. At MT, under both moderate and energetic conditions the alongshore distributions

Table 7
Squared correlation coefficients between the alongshore distributions of the swash and the significant wave height at a depth of 1 m. Values shown are significant at the 95% percentage confidence level.

Wave energy	$R^2(S, H_s)$	$R^2(S_{SW}, H_s)$	$R^2(S_{IG}, H_s)$
Moderate			
Low tide	0.10	0.38	-
Mid tide	0.95	0.93	0.87
High tide	0.49	-	0.84
Storm			
Low tide	0.17	0.53	0.09
Mid tide	0.73	0.73	0.57
High tide	0.08	0.05	0.48

of the wave and swash heights are highly correlated ($0.57 < R^2 < 0.95$). At LT S_{IG} displays very low correlations with H_s, whereas for S_{SW} poor correlations are found at HT. The variability observed in table 7 suggests that the influence of the morphology on the swash distribution is frequency-dependent. A deeper analysis to understand exactly how each frequency is affected by morphological features is required to fully explain the alongshore variability of the run-up.

6.3. Phase-resolved modeling of swash motion

While the use of phase-resolving models, especially Boussinesq-type, is becoming increasingly popular for coastal engineering applications, only few studies present comparisons between model results and and run-up observations in realistic study cases. The SWASH model (Zijlema et al., 2011) has been assessed against run-up data on open dissipative beaches under moderate conditions (H_s<2.3 m) in 2D by Guimarães et al. (2015), under highly energetic conditions (H_s>6 m) in 2D by Nicolae Lerma et al. (2017) and in 1D by Fiedler et al. (2018). More recently, the model was applied to lowly-energetic conditions (H_s<2 m) in an embayed beach by Valentini et al. (2019). The non-hydrostatic version of XBeach was applied by de Beer et al. (2021) under mildly energetic conditions (H_s<3.1 m) on an intermediate open beach.

In the present study, the BOSZ model is validated against data obtained in the constrained environment of an intermediate reflective embayed beach under wave conditions varying from moderate (H_s=1.5 m) to highly energetic (H_s=4.5 m). Moreover, the studied time window corresponds to a large spring tidal range (0.5 m<WL<4.7 m), which results in a wide range of swash values (0.8 m<S<3.5 m for the observations). The study site is characterized by a significant morphological complexity, being an urbanized embayed beach with many bathymetric heterogeneities at various depths. This configuration required the use of a large numerical domain. The domain is 3.5 km in the longshore compared to only 2 km in Nicolae Lerma et al. (2017), 380 m in de Beer et al. (2021) and 203 m in Valentini et al. (2019). The offshore boundary is set at about 20 m depth compared to about 10 m in Fiedler et al. (2018); de Beer et al. (2021) and 6 m in Valentini et al. (2019). At the offshore model limit, the boundary condition was derived from an inner shelf spectral model (SWAN) to account for the variability induced by strong bathymetric gradients to be found between 50 m and 20 m , when other studies (Nicolae Lerma et al., 2017; Fiedler et al., 2018; de Beer et al., 2021) used direct measurements carried out at a single offshore position assuming longshore uniform incident wave conditions. Due to the large numerical domain, the grid size was limited to reduce the computational cost. It was set to 3.5 m in both directions, which is larger than that in most of the previous studies, where a mesh size of 0.5 m (Fiedler et al., 2018; de Beer et al., 2021) to 2 m (Nicolae Lerma et al., 2017) was used. Additional tests (not shown here) showed that most of the dominant processes were sufficiently resolved with a 3.5 m grid size and decreasing the cell dimensions did not significantly add to the quality of the computed results, but instead, considerably increased the computational cost. Moreover, the strong bathymetric gradients pose a challenge to numerical stability when small grid sizes are used. Nonetheless, normalized errors NRMSE computed here are about 15% for S which is comparable with previous studies (Nicolae Lerma et al., 2017; Fiedler et al., 2018; Valentini et al., 2019; de Beer et al., 2021). Most important, the trends observed in the large space-time variability of the swash motions are consistently captured by the model.

7. Conclusions

In this study, the swash zone dynamics in a mesotidal embayed beach is investigated based on the combination of field measurements and numerical computations covering moderate to energetic incident wave conditions. The following conclusions can be drawn from this work:

- The phase-resolving Boussinesq-type model *BOSZ* (Roeber et al., 2010; Roeber and Cheung, 2012a) was found to accurately compute nearshore wave transformation and swash motion for this geologically constrained and urbanized pocket beach. In particular, it allows to capture the evolution of the contribution of both incident and infragravity waves on the swash motion in dependence of the tide level. This result demonstrates that this type of nearshore wave model can serve as a promising complementary tool to better understand the functioning of complex beach configurations where it is notoriously challenging to carry out extensive field measurements.
- The measurements and the model computations reveal that the intermediate-reflective profile of the beach combined with a large tidal range results in a strong modulation of the swash motions along the tide cycle. The significant swash height varied from $0.3H_s$ up to $1.4H_s$ respectively at low and high tide. The tide was found to modulate the swash motion by controlling the

breaking zone location and thus the spatial distribution of energy dissipation. This leads to a wide dissipative surfzone with an IG dominated swash at low tide, as well as at high tide under storm conditions. In contrast at high tide under moderate wave conditions, a narrow surfzone on the steep foreshore results in a SW dominated swash motion.

- Observations showed that the significant swash height varies by up to a factor of 2.2 alongshore, and is of the same order of magnitude as previous studies. The analysis of the characteristics of the wave field shows that the geology and nearshore morphology contribute to the alongshore non-uniformity of the swash by rapidly and locally redistributing and focusing wave energy through refraction. In addition, the foreshore topography also conditions the short wave contribution to the swash, with more or less influence depending on the tide level.

Acknowledgement

This research was carried out under the framework of the joint laboratory KOSTARISK, which is part of the E2S UPPA program managed by the French National Research Agency (ANR-16-IDEX-0002) and supported by the French Government's "Investissements d'Avenir" (PIA). The joint laboratory KOSTARISK is co-funded by E2S UPPA, the AZTI Foundation and the center Rivages Pro Tech of SUEZ. The authors acknowledge financial support from the I-site program Energy Environment Solutions (E2S), the Communauté d'Agglomération Pays Basque (CAPB), and the Communauté Région Nouvelle Aquitaine (CRNA) for the chair HPC-Waves and the European Union Horizon 2020 project ALPHEUS - DLV-883553. The authors gratefully acknowledge European POCTEFA Program funding under the research project MAREA EFA046/15. The authors would like to thank the CEREMA for operating the french national CANDHIS wave buoy network and the REFMAR network deployed by the SHOM providing tidal recordings.

CRediT authorship contribution statement

Jonas Pinault: Conceptualization, methodology, validation, formal analysis, writing : original draft preparation, visualization. **Denis Morichon:** Conceptualization, methodology, formal analysis, writing : review and editing, supervision, project administration. **Matthias Delpey:** Conceptualization, methodology, formal analysis, writing : review and editing. **Volker Roeber:** Software and model development, writing : review and editing, supervision, project administration, funding acquisition.

References

Almar, R., Blenkinsopp, C., Almeida, L. P., Cienfuegos, R., and Catalán, P. A. (2017). Wave runup video motion detection using the radon transform. *Coastal Engineering*, 130:46–51.

Asbury H. Sallenger, J. (2000). Storm impact scale for barrier islands. *Journal of Coastal Research*, 16(3):890–895.

Azouri, A., Roeber, V., and Luther, D. S. (2018). The response of harbor environments protected by irregular fringing reef systems to strong gravity wave forcing - a case study. *Coastal Engineering Proceedings*, 1(36).

Bellafont, F., Morichon, D., Roeber, V., Andre, G., and Abadie, S. (2018). Infragravity period oscillations in a channel harbor near a river mouth. In *Coastal Engineering Proceedings*, volume 1.

Bonneton, P. and Lannes, D. (2017). Recovering water wave elevation from pressure measurements. *Journal of Fluid Mechanics*, 833:399–429.

Booij, N., Ris, R. C., and Holthuijsen, L. H. (1999). A third-generation wave model for coastal regions: 1. model description and validation. *Journal of Geophysical Research: Oceans*, 104(C4):7649–7666.

Brinkkemper, J., Torres-Freyermuth, A., Mendoza, E., and Ruessink, B. (2013). Parameterization of wave run-up on beaches in yucatan, mexico: A numerical study. *Coast. Dynam.*, pages 225–234.

Castelle, B. and Coco, G. (2012). The morphodynamics of rip channels on embayed beaches. *Continental Shelf Research*, 43:10–23.

Cohn, N. and Ruggiero, P. (2016). The influence of seasonal to interannual nearshore profile variability on extreme water levels : Modeling wave runup on dissipative beaches. *Coastal Engineering*, 115:79–92. Swash-zone Processes.

Da Silva, G., Gomes da Silva, P., Araujo, R., Klein, A., and Toldo, E. (2017). Wave run-up on embayed beaches. study case: Itapocorói bay, southern brazil. *Brazilian Journal of Oceanography*, 65:187–200.

de Bakker, A., Tissier, M., and Ruessink, B. (2014). Shoreline dissipation of infragravity waves. *Continental Shelf Research*, 72:73–82.

de Bakker, A. T. M., Tissier, M. F. S., and Ruessink, B. G. (2016). Beach steepness effects on nonlinear infragravity-wave interactions: A numerical study. *Journal of Geophysical Research: Oceans*, 121(1):554–570.

de Beer, A., McCall, R., Long, J., Tissier, M., and Reniers, A. (2021). Simulating wave runup on an intermediate–reflective beach using a wave-resolving and a wave-averaged version of xbeach. *Coastal Engineering*, 163:103788.

de Santiago, I., Morichon, D., Abadie, S., Reniers, A. J. H. M., and Liria, P. (2017). A comparative study of models to predict storm impact on beaches. *Natural Hazards*, 87:843 – 865.

Delpey, M., Lastiri, X., Abadie, S., Roeber, V., Maron, P., Liria, P., and Mader, J. (2021). Characterization of the wave resource variability in the french basque coastal area based on a high-resolution hindcast. *Renewable Energy*, 178:79–95.

Didier, D., Baudry, J., Bernatchez, P., Dumont, D., Sadegh, M., Bismuth, E., Bandet, M., Dugas, S., and Sévigny, C. (2019). Multihazard simulation for coastal flood mapping: Bathtub versus numerical modelling in an open estuary, eastern canada. *Journal of Flood Risk Management*, 12(S1).

Enjalbert, C., Castelle, B., Rihouey, D., and Dailloux, D. (2011). High-frequency video observation of a geologically-constrained barred-beach: La grande plage de biarritz (france). *J. Coastal Res.*, SI 64.

Fiedler, J., Smit, P., Brodie, K., McNinch, J., and Guza, R. (2018). Numerical modeling of wave runup on steep and mildly sloping natural beaches. *Coastal engineering*, vol. 131.

Filipot, J.-F., Guimaraes, P., Leckler, F., Hortsmann, J., Carrasco, R., Leroy, E., Fady, N., Accensi, M., Prevosto, M., Duarte, R., Roeber, V., Benetazzo, A., Raoult, C., Franzetti, M., Varing, A., and Le Dantec, N. (2019). La jument lighthouse: a real-scale laboratory for the study of giant waves and their loading on marine structures. *Philosophical Transactions of the Royal Society A: Mathematical, Physical and Engineering Sciences*, 377(2155):20190008.

Gomes da Silva, P., Coco, G., Garnier, R., and Klein, A. H. (2020). On the prediction of runup, setup and swash on beaches. *Earth-Science Reviews*, 204:103148.

Gomes da Silva, P., Medina, R., González, M., and Garnier, R. (2019). Wave reflection and saturation on natural beaches: The role of the morphodynamic beach state in incident swash. *Coastal Engineering*, 153:103540.

Guedes, R. M., Bryan, K. R., and Coco, G. (2012). Observations of alongshore variability of swash motions on an intermediate beach. *Continental Shelf Research*, 48:61–74.

2020
Guedes, R. M. C., Bryan, K. R., Coco, G., and Holman, R. A. (2011). The effects of tides on swash statistics on an intermediate beach. *Journal of Geophysical Research: Oceans*, 116(C4).

Guimarães, P. V., Farina, L., Toldo, E., Diaz-Hernandez, G., and Akhmatskaya, E. (2015). Numerical simulation of extreme wave runup during storm events in tramandaí beach, rio grande do sul, brazil. *Coastal Engineering*, 95:171–180.

Holman, R. (1986). Extreme value statistics for wave run-up on a natural beach. *Coastal Engineering*, 9(6):527–544.

Horrillo, J., Grilli, S., Nicolsky, D., Roeber, V., and Zhang, J. (2014). Performance benchmarking tsunami models for nthmp's inundation mapping activities. *Pure Appl. Geophys.*, vol. 172:869–884.

Khoury, A., Jarno, A., and Marin, F. (2019). Experimental study of runup for sandy beaches under waves and tide. *Coastal Engineering*, 144:33–46.

Kirezci, E., Young, I. R., Ranasinghe, R., Muis, S., Nicholls, R. J., Lincke, D., and Hinkel, J. (2020). Projections of global-scale extreme sea levels and resulting episodic coastal flooding over the 21st century. *Scientific Reports*, 10.

Klein, A. H., Óscar Ferreira, Dias, J. M., Tessler, M. G., Silveira, L. F., Benedet, L., de Menezes, J. T., and de Abreu, J. G. (2010). Morphodynamics of structurally controlled headland-bay beaches in southeastern brazil: A review. *Coastal Engineering*, 57(2):98–111. Hydrodynamics and Applications of Headland-Bay Beaches.

Knutson, T. R., Chung, M. V., Vecchi, G., Sun, J., Hsieh, T.-L., and Smith, A. J. P. (2021). Climate change is probably increasing the intensity of tropical cyclones.

Li, N., Roeber, V., Yamazaki, Y., Heitmann, T. W., Bai, Y., and Cheung, K. F. (2014). Integration of coastal inundation modeling from storm tides to individual waves. *Ocean Modelling*, 83:26–42.

Lynett, P., Roeber, V., Heitmann, T., Cheung, K., David, C., and et al., J. B. (2017). Inter-model analysis of tsunami-induced coastal currents. *Ocean Modelling*, vol. 114:14–32.

Matsuba, Y., Shimozono, T., and Tajima, Y. (2021). Tidal modulation of infragravity wave dynamics on a reflective barred beach. *Estuarine, Coastal and Shelf Science*, 261:107562.

Morichon, D., de Santiago, I., Delpey, M., Somdecoste, T., Callens, A., Liquet, B., Liria, P., and Arnould, P. (2018). Assessment of Flooding Hazards at An Engineered Beach during Extreme Events: Biarritz, SW France. *Journal of Coastal Research*, 85(sp1):801 – 805.

Morichon, D., Roeber, V., Martin-Medina, M., Bellafont, F., and Abadie, S. (2021). Tsunami impact on a detached breakwater: Insights from two numerical models. *Journal of Waterway, Port, Coastal, and Ocean Engineering*, 147(2):05021001.

Nicolae Lerma, A. and Bulteau, T. (2017). A numerical study of extreme wave runup behavior : spectral and statistical analysis. In *Coastal Dynamics 2017*, Helsingør, Denmark.

Nicolae Lerma, A., Pedrero, R., Robinet, A., and Sénéchal, N. (2017). Simulating wave setup and runup during storm conditions on a complex barred beach. *Coastal engineering*, vol. 123.

Nwogu, O. (1993). An alternative form of the boussinesq equations for nearshore wave propagation. *Journal of Waterway, Port, Coastal, and Ocean Engineering*.

Ojeda, E. and Guillén, J. (2008). Shoreline dynamics and beach rotation of artificial embayed beaches. *Marine Geology*, 253(1):51–62.

Oliveras, K., Vasan, V., Deconinck, B., and Henderson, D. (2011). Recovering the water-wave profile from pressure measurements. *SIAM Journal on Applied Mathematics*, 72.

Otsu, N. (1979). A threshold selection method from gray-level histograms. *IEEE Transactions on Systems, Man, and Cybernetics*, 9(1):62–66.

Pinault, J., Morichon, D., Abadie, S., and Roeber, V. (2020a). Numerical study of the longshore variability in run-up along an idealized embayed beach. In *XVI èmes Journées Nationales Génie Côtier – Génie Civil*, pages 139–148.

Pinault, J., Morichon, D., and Roeber, V. (2020b). Estimation of irregular wave runup on intermediate and reflective beaches using a phase-resolving numerical model. *Journal of Marine Science and Engineering*, 8(12).

Robinet, A., Castelle, B., Idier, D., Harley, M., and Splinter, K. (2020). Controls of local geology and cross-shore/longshore processes on embayed beach shoreline variability. *Marine Geology*, 422:106118.

Roeber, V. and Cheung, K. (2012a). Bosz - boussinesq ocean and surf zone model. *NOAA, Special Report, Proceedings and Results of the 2011 NTHMP Model Benchmarking Workshop, Galveston, Texas, 437 p.*

Roeber, V. and Cheung, K. (2012b). Boussinesq-type model for energetic breaking waves in fringing reef environments. *Coastal Engineering*, vol. 70:1–20.

Roeber, V., Cheung, K., and Kobayashi, M. (2010). Shock-capturing boussinesq-type model for nearshore wave processes. *Coastal Engineering*, vol. 57:407–423.

Ruggiero, P., Holman, R. A., and Beach, R. A. (2004). Wave run-up on a high-energy dissipative beach. *Journal of Geophysical Research: Oceans*, 109(C6).

Ruju, A., Lara, J., and Losada, I. (2014). Numerical analysis of run-up oscillations under dissipative conditions. *Coastal engineering*, vol. 86.

Scott, T., Masselink, G., and Russell, P. (2011). Morphodynamic characteristics and classification of beaches in england and wales. *Marine Geology*, 286(1):1–20.

Senechal, N., Coco, G., Bryan, K. R., and Holman, R. A. (2011). Wave runup during extreme storm conditions. *Journal of Geophysical Research: Oceans*, 116(C7).

Senechal, N., Coco, G., Plant, N., Bryan, K. R., Brown, J., and MacMahan, J. H. M. (2018). Field observations of alongshore runup variability under dissipative conditions in the presence of a shoreline sandwave. *Journal of Geophysical Research: Oceans*, 123(9):6800–6817.

Stockdon, H. F., Holman, R. A., Howd, P. A., and Sallenger, A. H. (2006). Empirical parameterization of setup, swash, and runup. *Coastal Engineering*, 53(7):573–588.

Trenhaile, A. and Trenhaile, D. (1987). *The Geomorphology of Rock Coasts*. Oxford research studies in geography. Clarendon Press.

Tsai, C.-H., Huang, M.-C., Young, F.-J., Lin, Y.-C., and Li, H.-W. (2005). On the recovery of surface wave by pressure transfer function. *Ocean Engineering*, 32(10):1247–1259.

Valentini, N., Saponieri, A., Danisi, A., Pratola, L., and Damiani, L. (2019). Exploiting remote imagery in an embayed sandy beach for the validation of a runup model framework. *Estuarine, Coastal and Shelf Science*, 225:106244.

van Dongeren, A., Battjes, J., Janssen, T., Noorloos, J., Steenhauer, K., Steenbergen, G., and Reniers, A. (2007). Shoaling and shoreline dissipation of low-frequency waves. *Journal of Geophysical Research, 112, 2007 ; doi:10.1029/2006JC003701*, 112.

Varing, A., Filipot, J.-F., Delpey, M., Guitton, G., Collard, F., Platzer, P., Roeber, V., and Morichon, D. (2020). Spatial distribution of wave energy over complex coastal bathymetries: development of methodologies for comparing modeled wave fields with satellite observations. *Coastal Engineering*, page 103793.

Vousdoukas, M., Ferreira, P., Almeida, L. P., Dodet, G., Psaros, F., Andriolo, U., Taborda, R., Silva, A., Ruano, A., and Ferreira, O. (2011). Performance of intertidal topography video monitoring of a meso-tidal reflective beach in south portugal. *Ocean Dynamics*, 61:1521–1540.

Vousdoukas, M., Wziatek, D., and Almeida, L. (2012). Coastal vulnerability assessment based on video wave run-up observations at a mesotidal, steep-sloped beach. *Ocean Dynamics*, 62:123–137.

Welch, P. (1967). The use of fast fourier transform for the estimation of power spectra: A method based on time averaging over short, modified periodograms. *IEEE Transactions on Audio and Electroacoustics*, 15(2):70–73.

Xie, D., Zou, Q.-P., Mignone, A., and MacRae, J. D. (2019). Coastal flooding from wave overtopping and sea level rise adaptation in the northeastern usa. *Coastal Engineering*, 150:39–58.

Zijlema, M., Stelling, G., and Smit, P. (2011). Swash: An operational public domain code for simulating wave fields and rapidly varied flows in coastal waters. *Coastal Engineering*, 58(10):992–1012.

4.4 Swash motion computation with a 1D model configuration

For operational purposes, such as integration in an *Early Warning System* (EWS), 1D model configurations offer the advantage of being much faster to run and easier to implement than 2D configurations. In this section, we study the potential of a 1D model configuration to reproduce the observed wave transformations and swash motions at three longshore locations corresponding to timestacks ID02, ID03 and ID04. This study aims to quantify the differences with a 2D model configuration in a highly alongshore non-uniform environment.

The 1D model configuration implemented at GPB is derived from the 2D model configuration. The entire campaign was computed at the three longshore locations. ID01 was not modeled as it is located directly behind a rock. A constant grid size of 3.5 m was used. The closest *SWAN* spectrum were used as offshore spectral wave forcing (figure 4.3). For comparison, the computation of the 1.5 hrs model runs took around 20 hours for the 2D model and 5 min for the 1D model.

4.4.1 Nearshore wave transformation

A comparison of significant wave heights and spectral energy distributions computed with the 1D and 2D model configurations is given on figure 4.4. This event was characterized by energetic conditions with $(H_s, T_p) = (4.1\ m, 14.3\ s)$ at mid tide (+2.7 m). Before the surf zone the two model implementations exhibit a difference of about 70 cm for H_{SW}, which is responsible for the overestimation of the 2D version at the *seabird*. In the 1D configuration the offshore input spectrum corresponds to a defocus zone (figure 4.3). This could explain the lower values observed at the *seabird*. In addition, the overestimation is also observed in the *SWAN* results which supports that the bias originated from the *SWAN* configuration rather than from *BOSZ* . Within the surf zone ($x > 500m$), the two curves are superimposed suggesting a similar dissipation rate in both configurations, and very little refraction in the 2D model. A higher H_{IG} is observed in the 1D model, especially close to the shoreline, which results in an overestimation of the IG wave height at the sensors locations.

At CP07 location, the deepest sensor in the intertidal zone (panel **(b)**), the 1D configuration does not exhibit the correct peak at $f = 0.0675 H_z$ observed contrary to the 2D configuration. In addition, the two peaks observed in the IG band, $f = 0.005/0.0225 H_z$ are largely overestimated, while the lowest peak tends to be underestimated by the 2D configuration. At the CP06 and CP05 locations (panels **(c)** and **(d)**) all spectra display the same 3 peaks. However, the 1D configuration shows a considerable increase of energy in the frequencies lower than $0.05 H_z$. The sharp spectral peaks observed at CP06 and CP05 suggests a nodal structure due to reflected wave at the shoreline, explored into details in section 4.5). The 1D configuration shows a much more pronounced nodal structure, probably as both the incoming and reflected IG waves are overestimated. At the shallowest location (panel **(e)**), the energy is contained in the IG band and largely increased in the 1D case. The fact that the 1D configuration considerably increases

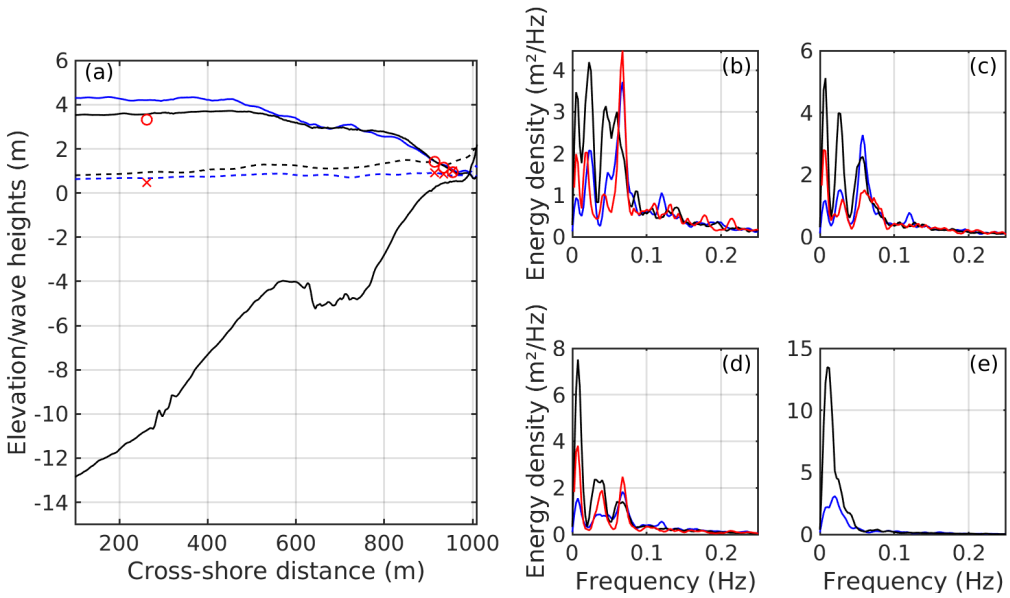

Figure 4.4: **(a)** : Significant wave heights H_{SW} (solid line, circles) and H_{IG} (dashed line, crosses) for the observations (red) the 1D (black) and 2D (blue) configuration. **(b)**, **(c)**, **(d)** wave spectra at the deepest to shallowest pressure sensors locations (CP07, CP06, CP05) and **(e)** at the shallowest submerged location of the observations (red), 1D (black) and 2D (blue) configurations.

energy unevenly with respect to the frequencies is problematic as it does not reflect the correct spectral shape.

Performance statistics of the 1D configuration over the whole 3-days data-set are shown in table 4.2, in green when it represents an improvement and in red when a deterioration compared to the 2D configuration is observed. In total, a better performance of the 1D configuration is noted, with a RMSE decreasing from 0.31 m to 0.22 m for H_s. This is due to a better match with the *seabird* data, mostly visible for H_{SW}, where the RMSE is reduced to 0.18 m instead of 0.48 m in the 2D configuration, and the bias from +0.38 m down to +0.09 m. However, for H_{IG} the 1D configuration significantly overestimates values at the *seabird*, with a bias increasing from +0.03 m to +0.15 m. The values are more scatter (SCI of 0.58). The increase is also observed at the other pressure sensors locations with significant positive bias ($> 0.15\,m$) while the 2D configurations slightly underestimates the values. The SCI values indicate a more scattered distribution compared to the 2D configuration. For H_{SW}, the results at the pressure sensors are very similar between the 1D and 2D configurations, with a slight increase in the 1D case, resulting in a slight positive bias instead of slight negative bias. The more conservative behavior of the 1D configuration is consistent with results reported in previous studies (Stockdon et al., 2014, Nicolae Lerma et al., 2017, Valentini et al., 2019).

4.4.2 Swash motion

The performances of the 1D and 2D models during the 3-days campaign are now compared for the swash values and shown in table 4.3. Overall, when compiling the results at all longshore locations (from ID02 to ID04) the 1D configuration yields similar results with a RMSE of 0.43

Table 4.2: Statistics evaluating the fit between observed and modeled values for wave heights in the 1D configuration. The statistics are evaluated at each cross-shore location and at the all locations (total). Green : better performances of the 1D model, red : better performances of the 2D model.

		Total	Seabird	CP07	CP06	CP05	CP04
H_s	RMSE (m)	0.22	0.20	0.22	0.20	0.23	0.29
	NMRSE (-)	0.07	0.08	0.09	0.10	0.13	0.35
	Bias (m)	0.15	0.11	0.15	0.15	0.2	0.26
	R^2 (-)	0.96	0.97	0.95	0.94	0.94	0.94
	SCI (-)	0.13	0.09	0.14	0.13	0.18	0.19
H_{SW}	RMSE (m)	0.18	0.18	0.17	0.13	0.14	0.34
	NMRSE (-)	0.06	0.07	0.07	0.06	0.08	0.86
	Bias (m)	0.07	0.09	0.03	0.04	0.07	0.32
	R^2 (-)	0.96	0.97	0.94	0.94	0.92	0.75
	SCI (-)	0.13	0.08	0.11	0.09	0.12	0.30
H_{IG}	RMSE (m)	0.25	0.18	0.29	0.26	0.28	0.20
	NMRSE (-)	0.17	0.36	0.35	0.32	0.36	0.21
	Bias (m)	0.19	0.15	0.25	0.23	0.24	-0.03
	R^2 (-)	0.90	0.95	0.93	0.94	0.96	0.92
	SCI (-)	0.13	0.58	0.48	0.44	0.47	0.19

Table 4.3: Statistics evaluating the fit between observed and modeled values for swash heights in the 1D configuration. The statistics are evaluated at each longshore location and at the all locations (total). Green : better performances of the 1D model, red : better performances of the 2D model.

		Total	ID02	ID03	ID04
S	RMSE (m)	0.43	0.47	0.33	0.45
	NRMSE (-)	0.17	0.22	0.20	0.19
	Bias (m)	-0.05	0.08	-0.20	-0.04
	R^2 (-)	0.76	0.77	0.87	0.79
	SCI (-)	0.18	0.22	0.14	0.19
S_{SW}	RMSE (m)	0.45	0.43	0.51	0.41
	NRMSE (-)	0.25	0.29	0.32	0.30
	Bias (m)	-0.31	-0.35	-0.29	-0.3
	R^2 (-)	0.39	0.44	0.29	0.50
	SCI (-)	0.29	0.29	0.33	0.25
S_{IG}	RMSE (m)	0.57	0.60	0.49	0.60
	NRMSE (-)	0.28	0.38	0.33	0.29
	Bias (m)	0.17	0.36	-0.04	0.18
	R^2 (-)	0.56	0.77	0.59	0.6
	SCI (-)	0.33	0.38	0.27	0.33

m against 0.42 m in 2D. However, the bias is reduced from -0.31 m in 2D to -0.05 m 1D, which is consistent with the higher values of H_s observed in table 4.2 and the general observation that 1D model configurations lead to less energy dissipation (Stockdon et al., 2014, Nicolae Lerma

et al., 2017, Valentini et al., 2019).

While overall 1D and 2D performances are similar, when looking in details at the respective frequency contributions the 1D configuration appears less accurate than the 2D one. Indeed, a larger negative bias is observed for S_{SW} (-0.31 m), compensated by a positive bias of S_{IG} (+0.17 m), whereas in the 2D configuration both components were underestimated. In addition, the RMSE of each component has increased under the 1D configuration (from 0.38 to 0.45 m for S_{SW} and from 0.36 to 0.57 m for S_{IG}). The RMSE for S_{IG}/S_{SW} (not shown) in the 1D configuration is twice the one of the 2D, proving that the spectral distribution is wrongly captured.

4.5 Role of infragravity waves to swash motion

In section 4.3, we have shown the critical influence of IG waves on swash motion. Indeed, the swash motion was IG dominated on more than 50% of the data-set (see figure 10 in section 4.3). The IG swash response to the offshore wave height was seen to be modulated by the incident wave conditions and most importantly by the tidal level, primarily by controlling the slope in the area of the SW breaking. In this section, we propose a detailed study of the transformation of incoming IG waves under different water levels and wave conditions along one representative cross-shore profile of the GPB. In particular, the dissipation of IG energy near the shoreline is investigated to provide further insights on the control of environmental parameters on the IG swash. The study is based on the previously validated numerical data-set. The same classification of conditions as in section 4.3 (table 3) is used, consisting in 3 averaged water levels, +1.2 m (LT), +2.7 m (MT) and +4.5 m (HT), and two averaged wave regimes : $(H_s, T_p) = (1.5m, 11s)$ and $(3.5m, 14s)$. Results along the cross-shore transect corresponding to ID02 are used since the pressure sensors used for validation were deployed along this transect.

4.5.1 Cross-shore transformation of infragravity waves

Figure 4.5 shows the evolution of H_{SW}, H_{IG} and their ratio for the six classes of wave and water level conditions. Under moderate wave conditions (panel **(a)**), the location of the surf zone is tidally-modulated. At LT wave breaking occurs on the second part of the low sloping area ($x > 600\,m$) where SW energy is strongly dissipated across a wide surf zone. At HT, waves break on the high sloping foreshore dissipating much less energy. The evolution of H_{IG} is relatively similar under all tides with a gradual increase, followed by an abrupt section on the foreshore at HT.

Under energetic conditions (panel **(b)**), the large waves start breaking deeper. This results in a similar dissipation of the SW energy at all tides, occurring on a wide surf zone and starting on the low sloping part around $x = 500\,m$. The increase of IG energy is gradual up to the outer bar ($x = 600\,m$). Then, it continues to grow before abruptly increasing at the shoreline at MT and HT. However, H_{IG} remains constant or slightly decreases after the bar at LT.

The importance of the IG waves decreases as the tide increases under both moderate and

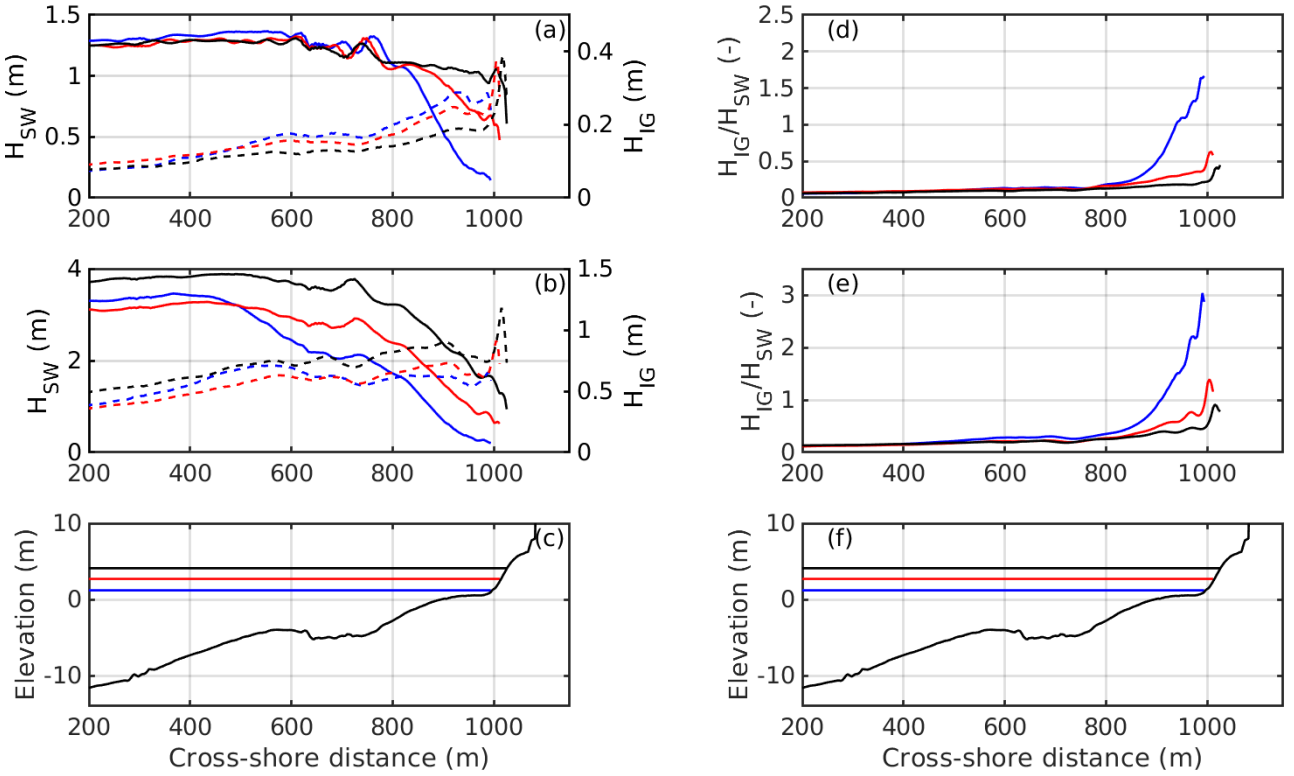

Figure 4.5: Cross-shore evolution of H_{SW} (solid lines) and H_{IG} (dashed lines) along ID02 under moderate **(a)** and energetic conditions **(b)** at LT (blue), MT (red) and HT (black). The ratio of H_{IG}/H_{SW} is indicated on panels **(d)** and **(e)**. The cross-shore profile (black) along with the still water levels (colors) are shown on panels **(c)** and **(f)**.

energetic conditions (panels **(d)** and **(e)**). Under energetic conditions, we observe IG dominated wave motions near the shoreline at LT and MT. At HT, the contribution s of the two spectral components are more balanced. Under moderate conditions, waves are IG dominated at LT while SW dominated at MT and HT ($H_{IG}/H_{SW} < 0.5$).

4.5.2 Cross-shore energy spectrum distribution

Figure 4.6 displays the computed cross-shore variation of the wave spectrum for the six scenarios. The high-energy spectra (lower row) exhibit a broader peak saturated in the SW frequency from the lowest part of the band (about $0.05\,H_z$) up to more than $0.015\,H_z$ compared to the moderate cases which show a clear peak around $f = 0.08\,H_z$. As the waves propagate on the bar (around $x = 600\,m$), an increase of SW super-harmonic components, corresponding to approximately $2f_p$ is observed suggesting an increase of non-linearity at this location. This high-frequency energy contributes to locally increasing the asymmetry and skewness of the individual waves (Mouragues et al., 2019). When reaching shallow waters, the energy across the SW frequency band decreases, starting with the highest frequencies. Simultaneously, an increase of IG energy is noticeable starting around $x = 800\,m$ and $x = 500\,m$ under moderate and energetic conditions respectively.

The wave spectra also highlight the presence of a standing wave pattern in the IG frequency

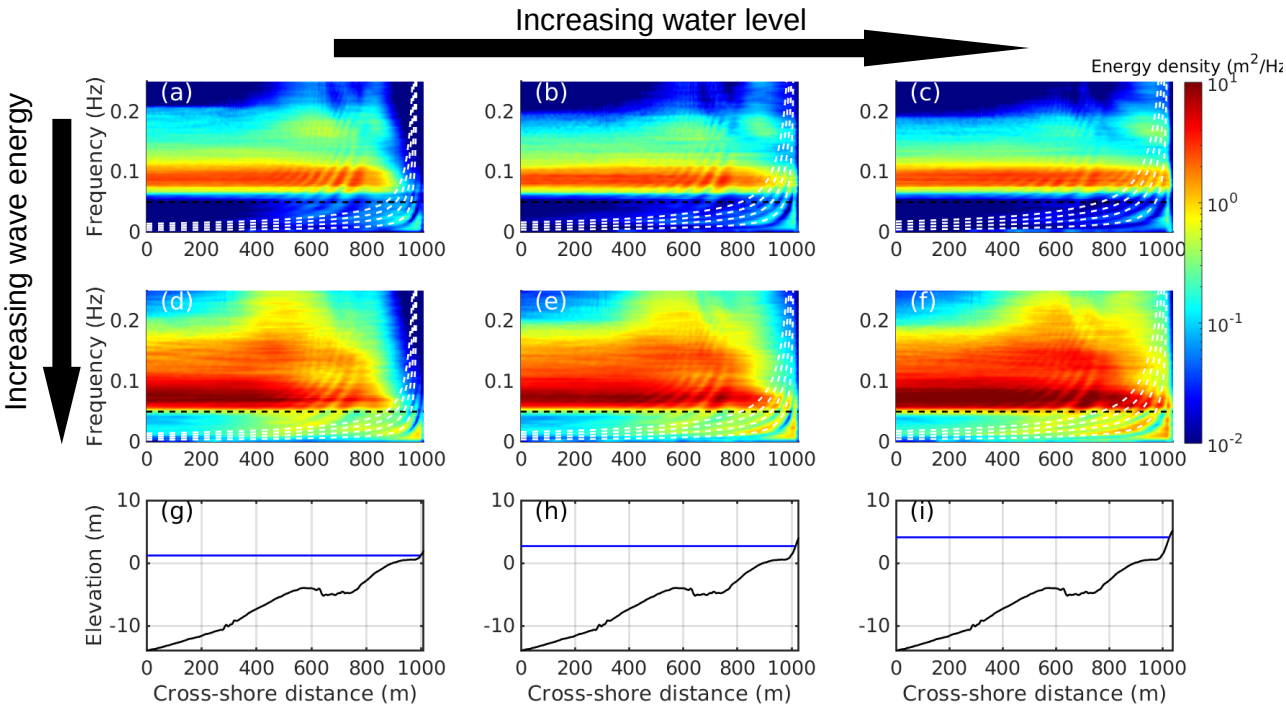

Figure 4.6: Cross-shore wave spectrum along the ID02 transect, for each class of event. Note that the color scale is logarithmic to emphasize lower values. Black dashed line represents the cut-off frequency of $f_c = 0.05Hz$. White dashed lines indicate natural frequencies for a given cross-shore location as calculated using eq. A.8. The cross-shore profiles (black) and still water levels (blue) are shown on panels **(g)-(i)**.

band. Indeed, regions of nearly null energy that could correspond to nodes location are followed by regions of high energy typical of anti-nodes (de Bakker et al., 2014, Martins et al., 2017, Bertin et al., 2018a, Matsuba et al., 2021b). This is further corroborated using equation A.8 as the anti-node locations observed correspond well with predicted anti-nodes locations (white dashed lines on figure 4.6). The presence of a nodal structure appears both tide and wave conditions dependent. At LT only the first mode (around $f = 0.02\ H_z$) is excited, really close to the shoreline (around $x = 900\ m$). At MT and HT the nodes/anti-nodes are much more visible, especially under energetic conditions. The nodal structure is a consequence of reflection at the shoreline of waves that have not been dissipated. The influence of the tide and wave conditions on the dissipation of IG waves is further explored in section 4.5.4.

4.5.3 Mechanisms of infragravity waves generation

In the literature, two mechanisms of IG waves generation are commonly identified : the Bound Wave (BW) and the moving Break-Point (BP) mechanisms. The first mechanism says that IG waves are generated through non-linear interactions within the wave groups and traveled bound to the group until released in the surf-zone. The second mechanism states that the depth-induced wave breaking occurring at different cross-shore locations depending on the wave height, the associated set-up will oscillate and create an IG wave propagating both sea- and shore-ward from the break-point. In this section, the contribution of these two mechanisms to the generation of the observed IG waves is investigated by comparing the cross-shore evolution

of the wave group $\tilde{\eta}$ to the IG waves η_{IG}. The method used to determine $\tilde{\eta}$ and η_{IG} is detailed in appendix A.

The cross-correlation between the upper envelope of the wave groups $\tilde{\eta}$ at the location $x_0 = 520\ m$ (before the surf zone) and IG wave signal η_{IG} at each cross-shore location is presented on figure 4.7. Under all conditions, a negative correlation is observed at increasing

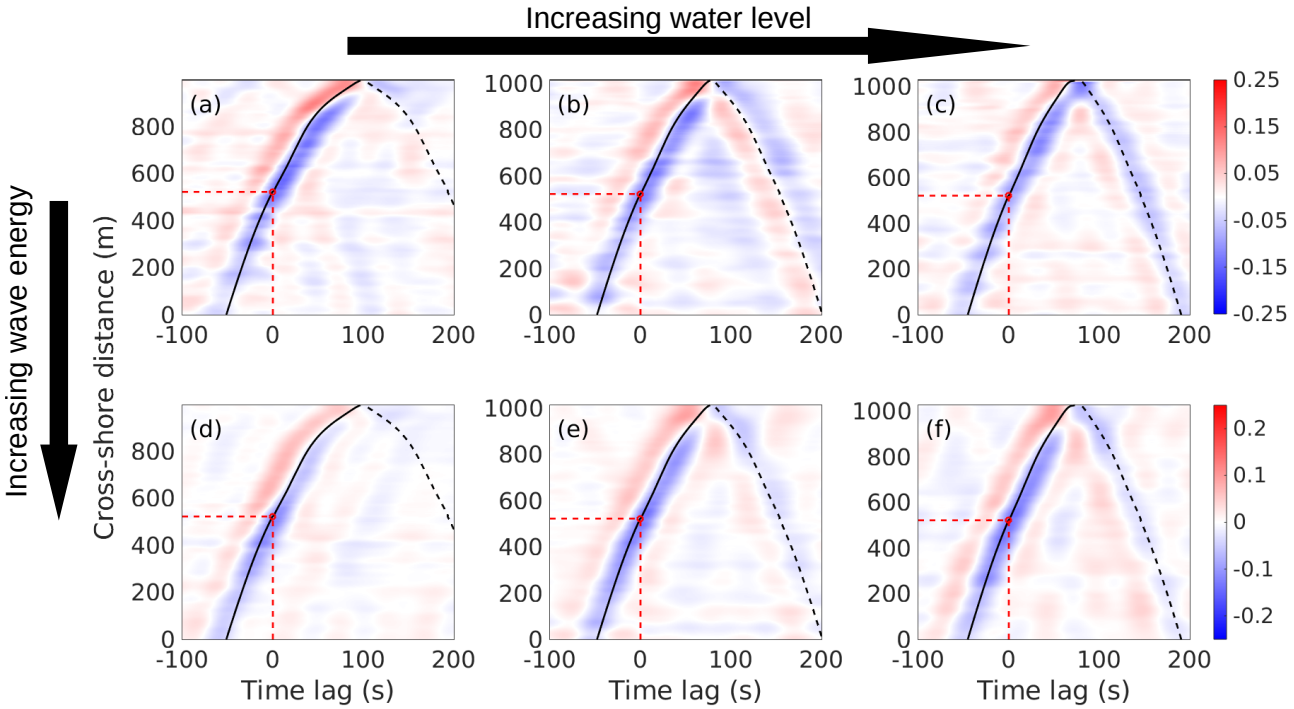

Figure 4.7: Cross-correlation between the upper envelope of wave groups $\tilde{\eta}$ before the outer-bar ($x_0 = 520\ m$) and IG waves η_{IG} at all locations. Red indicates positive correlations and blue indicates negative correlations. The red circle corresponds to the location x_0 where $\tilde{\eta}$ is calculated. Solid black lines correspond to the trip time of shallow water waves from each location to x_0. Black dashed lines indicate the trip time from each location, to the shore and back to x_0.

time lags as the distance to the shoreline decreases. This pattern follows the predicted time lag of a wave propagating at the shallow water celerity $\sqrt{gh}$ (black solid line). This feature has commonly been reported in the literature (Janssen et al., 2003, de Bakker et al., 2013, Inch et al., 2017) and suggests that the IG signal travels out of phase and bound with the SW envelope and at the shallow water celerity. The negative correlation extends all the way to the shoreline, indicating that the bound IG waves persist through the surf zone where they are released due to depth-induced breaking of the SW and propagate to the shoreline (Janssen et al., 2003). This result is consistent with Poate et al. (2020) who suggested that BW mechanism is expected to dominate on sloping platforms, such as sandy beaches, whose slope is less 0.1, whereas the BP mechanism is expected to dominate on steep sloping environment such as sub-horizontal platforms.

A negative correlation is observed at MT and HT (panels **(b)**, **(c)**, **(e)** and **(f)**) for increasing time lags as the distance from the shoreline increases. This pattern highlights possible shoreline reflection as it corresponds well to the predicted lag of reflected wave traveling at $\sqrt{gh}$ indicated

by the black dashed lines, consistently with previous studies (Ruju et al., 2012, Janssen et al., 2003, Poate et al., 2020, Matsuba et al., 2021b).

4.5.4 Dissipation of IG waves

As concluded from figures 4.6 and 4.7, IG wave reflection at the shoreline is observed only at MT and HT. The absence of reflection at LT is investigated here by evaluating the dissipation of IG waves near the shoreline. This analysis is based on the separation between the incoming ($E^+(f)$ or H_{IG}^+) and reflected ($E^-(f)$ or H_{IG}^-) IG components. The separation is performed using the collocated measurements of horizontal cross-shore velocities and free surface elevation, as described in Sheremet et al. (2002) (see appendix A.2).

Bulk reflection coefficients $R^2 = {H_{IG}^-}^2/{H_{IG}^+}^2$ (eq. A.5) of the partitioned IG band are presented on figure 4.8 for the different classes of conditions. The cross-shore evolution of R^2

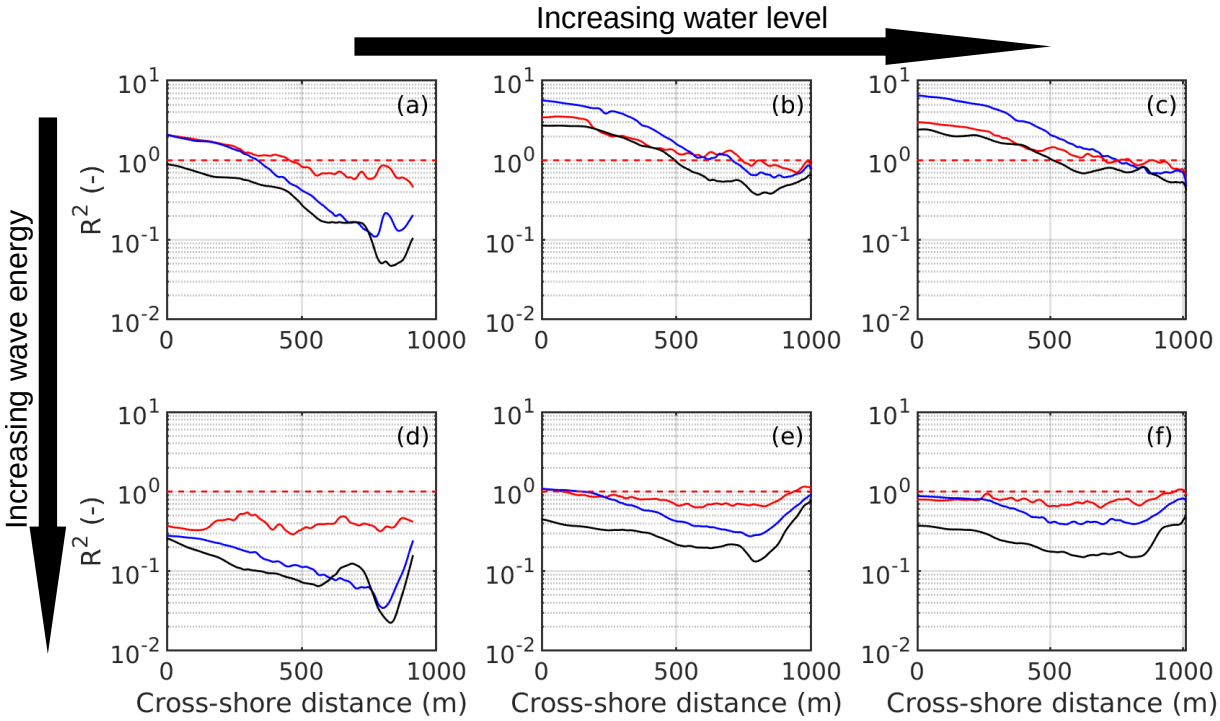

Figure 4.8: Cross-shore evolution of bulk-IG reflection coefficient R^2 for the different frequency bands for each class of conditions. Red : $0.003 - 0.017\ H_z$, Blue : $0.017 - 0.034\ H_z$, Black : $0.034 - 0.05\ H_z$. Top row : moderate conditions, bottom row : energetic conditions. From left to right : low, mid and high tide.

generally indicates that under moderate conditions (panels **(a)-(c)**) leaky IG waves (free reflected IG waves) dominate the low frequency wave motions outside the surf zone ($R^2 > 1$) and seawards while released incident bound IG wave are prevailing from the surf zone up to the shoreline ($R^2 < 1$). Under energetic conditions (panels **(d)-(f)**), IG motions are dominated by incident IG waves. Consistently with previous field studies (Guedes et al., 2013, de Bakker et al., 2014, Inch et al., 2017), the infragravity dissipation observed is frequency-dependent with generally more energy being conserved at lower frequencies. At MT and HT, R^2 is close to 1 at the shoreline, which allows the development of standing wave patterns.

Table 4.4: Bulk R^2 coefficients for the partitioned IG band. Coefficients are given at the shoreline and minimum cross-shore value (shoreline | minimum).

Wave energy	$0.003 - 0.017 H_z$	$0.017 - 0.034 H_z$	$0.034 - 0.05 H_z$
Moderate			
Low tide	0.46 | 0.46	0.21 | 0.11	0.11 | 0.05
Mid tide	0.78 | 0.70	0.77 | 0.60	0.64 | 0.37
High tide	0.47 | 0.47	0.48 | 0.47	0.42 | 0.42
Storm			
Low tide	0.43 | 0.29	0.24 | 0.03	0.16 | 0.02
Mid tide	1.10 | 0.63	0.91 | 0.27	0.77 | 0.13
High tide	0.89 | 0.62	0.74 | 0.38	0.48 | 0.15

Values of R^2 at the shoreline and cross-shore minimum are given in table 4.4. Generally, the values show a higher bulk reflection coefficient, i.e. lower dissipation, for the lowest part of the IG band. This is especially true under energetic conditions and at LT under moderate conditions. For instance at LT under moderate conditions R^2 values at the shoreline are 0.46, 0.21 and 0.11 for the low, middle and high IG band. The difference between the values at the shoreline and the minimum reflection coefficient indicates that part of the dissipation happens before the swash zone, hence in the shallow surf zone, consistently with previous observations (Guedes et al., 2013).

To further investigate the frequency-dependency of the IG waves dissipation at the shoreline, the coefficient of reflection $R(f)$ (eq. A.4) is shown on figure 4.9 as a function of the normalized bed slope β_H computed from Battjes et al. (2004) as :

$$\beta_H = \frac{h_x}{\omega}\sqrt{\frac{g}{H^+}} \tag{4.1}$$

where h_x is the bed slope, ω the angular frequency of the IG waves and H^+ is the height of the incoming IG wave.

Under energetic conditions (panel **(b)**), the distribution agrees quite well with the parametrization proposed by van Dongeren et al. (2007). It implies that the reflection coefficient R increases with the slope and decreases with the frequency. The transition from mild-to-steep sloping regime, where the IG energy dissipation is no longer frequency-dependent, is observed to be around $\beta_h \approx 3$ which is higher than reported by Van Dongeren et al. (2013) under laboratory experiment but consistent with field data from de Bakker et al. (2014), Inch et al. (2017). The water level indicates at LT only the lowest frequencies are not dissipated ($R > 0.8$) while the highest IG frequencies undergo almost complete dissipation ($R < 0.2$), which is consistent with the dissipative conditions due to the low sloping terrace. At MT and HT the dissipation is less significant, with minimum values of $R = 0.75$ and $R = 0.45$ respectively, but still shows an increasing trend with β_h.

Under moderate conditions (panel **(a)**), the values agree well with parametrization from van

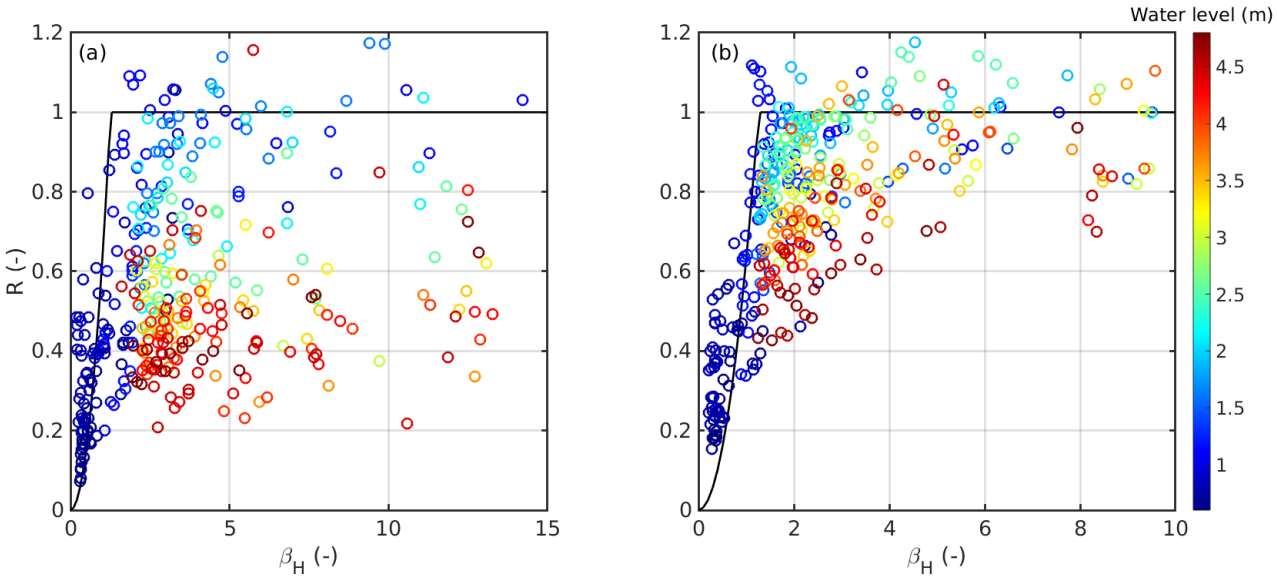

Figure 4.9: Amplitude reflection coefficient R at the shoreline versus normalized bed slope β_H for $f = 0.0033 - 0.05\ H_z$ with a $0.005\ H_z$ step size under moderate **(a)** and energetic **(b)** conditions. The black solid line represents $min(1, 0.2\pi\beta_H^2)$ as found in van Dongeren et al. (2007). The incoming and reflected components are computed according to Sheremet et al. (2002). The color scale indicates the water level (m).

Dongeren et al. (2007) at LT only. As under energetic conditions, the shortest IG waves are the most dissipated, with values as low as $R < 0.1$, suggesting an almost complete dissipation, while the longest IG waves exhibit almost full reflection ($R > 0.9$). At HT a considerable scatter is observed, all frequencies showing a similar reflection coefficient of about $R = 0.4$ and hence exhibiting only partial reflection. At MT, the values show a slight increasing trend with β_h, with values of R ranging from 0.6 to more than 1.

The relationship between R and β_h suggests that wave breaking is the dominant dissipation mechanism at the shoreline. Indeed, under all tides for energetic conditions and only at LT for moderate conditions all but the lowest frequency waves are in the mild sloping regime. This result is consistent with previous studies led on dissipative beaches (Guedes et al., 2013, Inch et al., 2017) even though the GPB is considered as intermediate-reflective, suggesting that the low sloping part of the profile is acting on the IG energy dissipation even at high tide. However, under moderate conditions at MT and HT, mainly the high sloping foreshore is active, which results in an almost constant dissipation rate across the IG band.

4.5.5 IG waves and swash motions

In this section, the relationship between IG waves and swash is investigated. The study is based on the comparison between the IG swash amplitude $A_{S_{IG}}$ and the amplitudes of the incoming and outgoing IG waves, referred to A_{IG}^{+} and A_{IG}^{-} respectively. Those amplitudes are calculated as $A^{\pm}(f) = \sqrt{\mathrm{df} E^{\pm}(f)}$ where $E^{\pm}(f)$ is either the incoming/outgoing wave spectra or the swash spectrum and df the associated frequency resolution. Results are shown on figure 4.10 for different given frequencies. The amplitude of the IG swash $A_{S_{IG}}$ agrees well with the

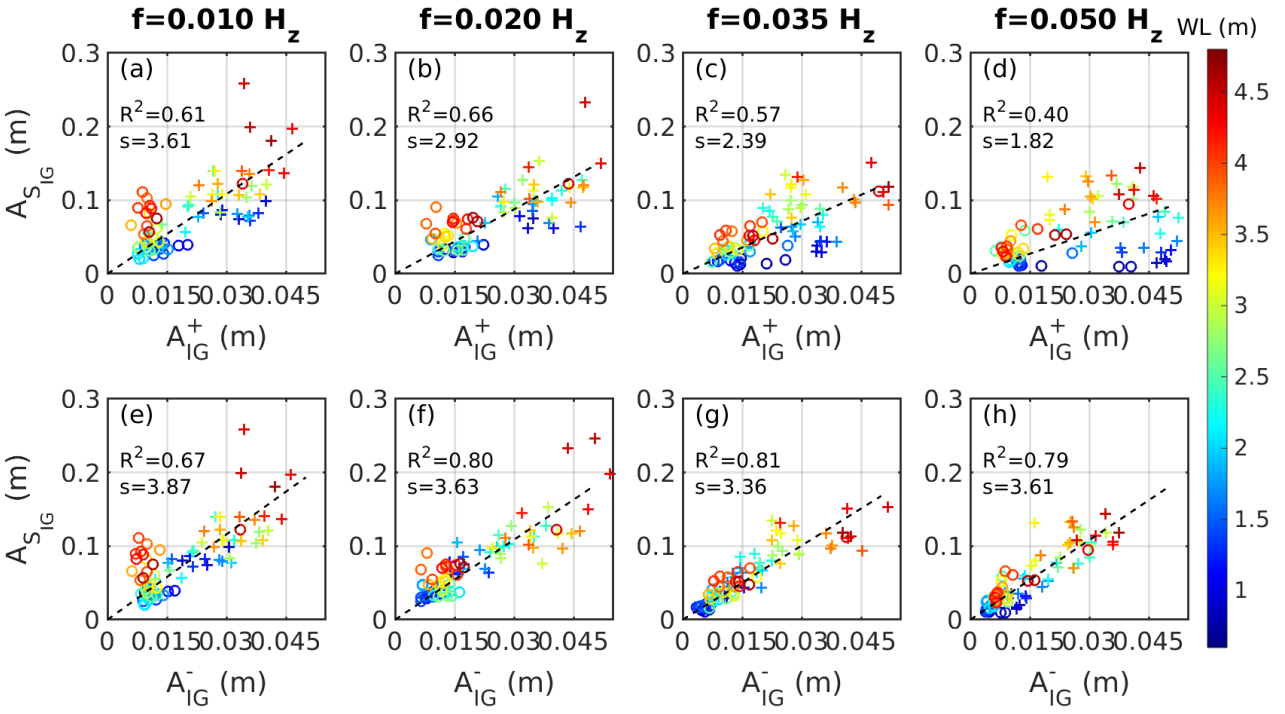

Figure 4.10: Comparison of the incoming/outgoing IG wave amplitudes measured at a depth of 2 m and IG swash amplitudes of each frequency component. **(a)-(d)** Incoming IG waves. **(e)-(h)** Outgoing IG waves. The color scale indicates the water level. Circles and plus signs respectively show the intermediate (H_s <3 m) and energetic (H_s >3 m) offshore wave conditions. R^2 and s respectively indicate the correlation coefficient and the slope of the linear relationship.

outgoing IG component A_{IG}^- with R^2 values ranging between 0.67 and 0.81 (panels **(e)**, **(f)**, **(g)** and **(h)**). The same response is observed at each frequency, with a linear fit slope s between 3.4 and 3.9. The water level, which has been seen to modulate the entire surf zone and associated energy dissipation mechanisms, is not seen to particularly influence the relationship. However, the relationship between $A_{S_{IG}}$ and A_{IG}^+ appears more frequency dependent, with R^2 values between 0.57 and 0.66 at 0.01, 0.02 and 0.035 H_z while it is only of 0.4 at $f = 0.05$ H_z. The linear fit slope decreases as the frequency increases, indicating a weaker response of the swash for the same IG forcing. This is consistent with previous observations of decreasing IG wave energy near the shoreline, especially for the high frequencies. Conversely to A_{IG}^-, the water level appears to play a significant role in the IG swash response, especially in the high frequencies. For $f = 0.05$ H_z (panel **(d)**), which represents the cut-off frequency between the IG and SW bands, at low tide the swash response is much weaker than at high tide, which is consistent with energy dissipation through IG wave breaking. The response of the swash over the whole IG wave band to the incoming and outgoing IG components H_{IG}^+ and H_{IG}^- are shown on figure 4.11. As expected, the outgoing component H_{IG}^- (panel **(b)**) appears to be a better scaling parameter for S_{IG} than H_{IG}^+ (panel **(a)**), with correlation coefficients R^2 of 0.65 and 0.85 respectively.

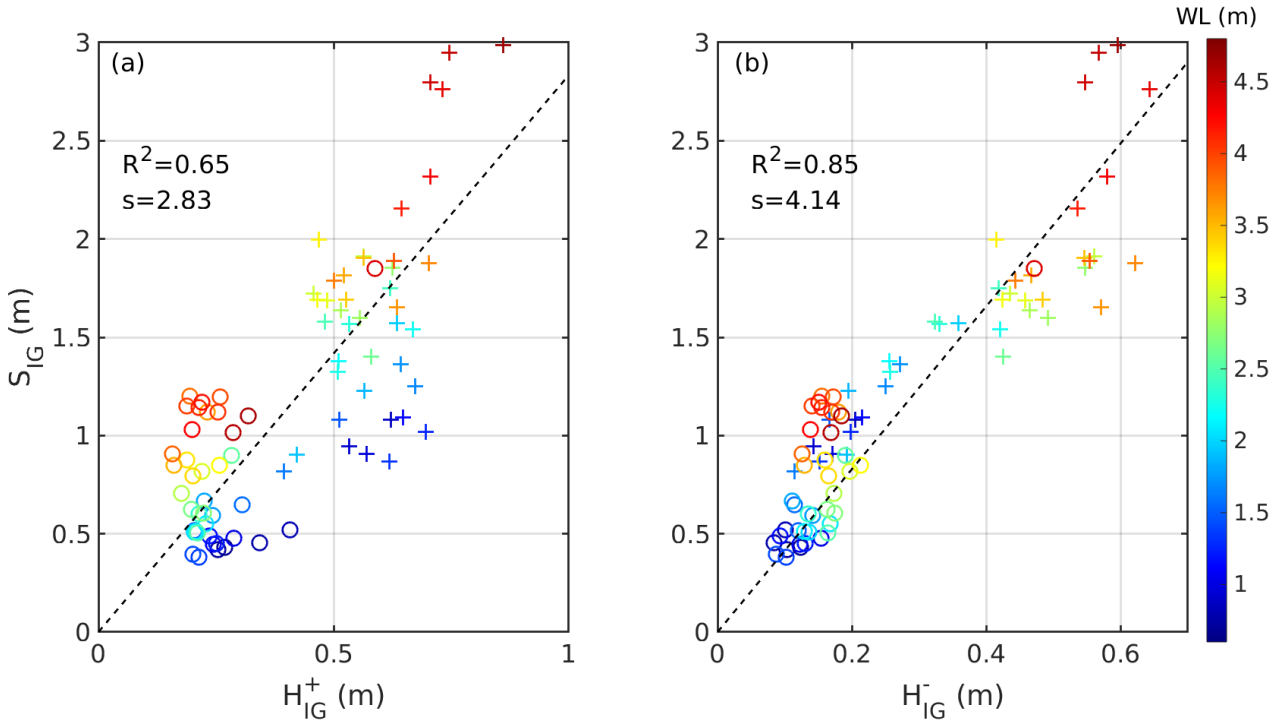

Figure 4.11: Comparison of the **(a)** incoming and **(b)** outgoing IG wave heights measured at a depth of 2 m and IG swash height. The color scale indicates the water level. Circles and plus signs respectively show the intermediate (H_s <3 m) and energetic (H_s >3 m) offshore wave conditions. R^2 and s respectively indicate the correlation coefficient and the slope of the linear relationship.

4.6 Conclusion

In this chapter, the hydrodynamics and the swash motions were investigated in an embayed beach exhibiting complex 3D morphological and geological features using both observations and validated numerical data. The numerical study is based on a 2D configuration of the BOSZ model forced at the offshore boundary by the output of a regional *SWAN* model. Prior to the results analysis, the *BOSZ* model configuration was validated against pressure measurements and video-derived swash data at the site of the Grande Plage of Biarritz (section 4.3). The model showed satisfying performances despite the complexity of the site where high bathymetric gradients are found. The significant swash heights S, S_{SW} and S_{IG} were captured with NRMSEs of 16%, 21% and 18% respectively. These results clearly show the potential of phase-resolving depth-integrated models to compute the run-up, even in highly rugged configurations exhibiting strong bathymetric gradients.

The implementation of a 1D model configuration, evaluated in section 4.4, showed in overall a more conservative behavior with higher values observed, where the 2D configuration tends to underestimate run-up data. However, the spectral distribution was not conserved resulting in a much larger increase of IG energy compared to the SW band. This suggests that the 1D configuration might not be fully representative of the processes undergone in the surf and swash zone, compared to the 2D configuration. This result suggests that in beach configurations where strong bathymetric gradients are present, the use of a 2D model configuration is crucial to capture the relevant wave transformation processes and ultimately compute the details of swash motions. However, such implementation requires a considerably higher computational cost, 20 h against 5 min for the 1D model, which prevents its application for operational purposes.

Based on the validated model results and video estimations of the total water level reached along the shore, the swash motions were first investigated, under moderate to energetic conditions and different tidal levels. The shape of the cross-shore profile, which exhibits two distinct sections with one low sloping area in the subtidal and intertidal zone and a high sloping foreshore, has a strong influence on the hydrodynamics regimes. Indeed, dissipative conditions associated with low swash values were observed at low tide, while reflective conditions were characteristics of mid and high tides. The tidal modulation was less significant under energetic conditions as the large waves tend to break further offshore, on the low sloping area under all tides.

The alongshore variability of the swash motions was also addressed. The analysis of the nearshore wave field shows that the distribution of the swash along the beach is strongly linked to the distribution of the wave heights. It is hypothesized that the geology and nearshore morphology contribute to the alongshore non-uniformity of the swash by rapidly and locally redistributing and focusing wave energy through refraction. Similarly to previous studies, the foreshore topography was seen to have an influence on the SW swash. However, further work is needed to fully understand the influence of the geological and morphological features on the different frequency bands of the wave field.

Finally, the dynamics of IG waves at the site were investigated in section 4.5 to better

understand the high tidally-induced modulation of the swash values. The released bound IG waves exhibit partial reflection at the shoreline depending on the water level, leading to nodal structures typical of standing wave patterns. The dissipation of IG waves was observed to be frequency-dependent, suggesting IG wave breaking as the main energy dissipation mechanism. As a result the tidal level induced a variable response of the swash for identical incident IG wave amplitudes. This was especially noted in the highest IG frequencies, where most of the dissipation is observed. This suggests that a precise prediction of the IG swash would require to consider partitioned incoming IG wave frequency bands and the inclusion of a morphological parameter to represent the influence of the "active" slope.

Chapter 5

Conclusions and perspectives

In the following, a number of aspects are discussed related to the results presented in previous chapters. In section 5.1, we first summarize the answers to the scientific questions laid out in the general introduction. The implications, limits and perspectives of this work are developed in section 5.2.

5.1 Main results

In recent years, under the threat of global warming and the ever growing anthropogenic pressure along coastal areas, many studies have focused on providing a better estimation and understanding of wave run-up for coastal risk prediction. Following the development of computational capabilities, process-based numerical models are rapidly evolving and allow to capture wave transformations in the nearshore up to the run-up. In light of this, this thesis aimed to :

Assess the capabilities of a numerical model to capture wave run-up and provide a better understanding of run-up processes in a complex highly-urbanized embayed beach.

This objective was first achieved by carefully validating the Boussinesq-type model *BOSZ* against an extensive laboratory data-set (chapter 3), and then using field data collected at the site of *Grande Plage* (chapter 4 section 4.3). The swash behavior under varying conditions was then investigated in sections 4.3 and 4.5.

The main results of this thesis are first that depth-integrated phase-resolving models provide a promising tool to evaluate wave run-up, even in a complex configuration such as a meso-tidal intermediate-reflective embayed beach. Secondly, it was found that in meso-tidal configurations exhibiting 3D morphologies the influence of the tide on the wave transformations led to significant variability of the swash values. The specific scientific findings are detailed in the following sections as answers to the questions laid out in the introduction chapter.

5.1.1 Is a phase-resolving model capable of accurately modeling wave run-up ?

The model was first compared to high-quality laboratory data of wave and run-up data under intermediate-reflective conditions (chapter 3). The model showed excellent accuracy at capturing irregular wave run-up, including the individual phases of up and down rush that compose the swash motion. Wave transformations from intermediate to shallow water were also well captured, not only in terms of wave energy spectrum or integrated quantities (H_s) but also in terms of time series. The LiDAR measurements of the surf and swash zones allowed a precise sensitivity analysis of computed run-up to model parameters. More specifically, the significant influence of the initial phase-distribution on the swash was highlighted, especially on the IG component. We showed that for accurate computations of the run-up, a complete description of the initial conditions is needed.

The model was then applied to a real case scenario, on the *Grande Plage* of Biarritz (GPB). The GPB is a meso-tidal engineered embayed beach exhibiting a double-barred profile with the presence of 3D morphological and geological features, such as rip channels, shoals and rocky islands. This configuration makes it one of the most challenging site to compute wave run-up as compared to sites found in the literature where open-beaches are generally well represented. The data-set, composed of pressure measurements and video-derived swash data, includes moderate ($H_s \simeq 1.5m$) to energetic ($H_s > 4m$) wave conditions under large spring tidal cycle. The model was found to perform fairly well at capturing wave and swash zone processes. The wide range of wave regimes, ranging from highly dissipative at low tide to reflective at high tide, were well reproduced by the model. This application of the BOSZ model to a real case study further proved the potential of phase-resolving depth-integrated models to estimate wave run-up under a large range of conditions and beach configurations. The possibility of implementing a 1D model configuration for operational purposes was also evaluated. In such highly heterogeneous environment, the use of 1D modeling provided large overestimations of the IG components near and at the shoreline, prescribing the use of a full 2D model in alongshore non-uniform environments.

5.1.2 What is the behavior of the swash in a geologically constrained meso-tidal environment ?

Based on the validated model results and observations, the swash motions at the GPB were first investigated, under moderate to energetic conditions for different tidal levels. The cross-shore profile, exhibiting two distinct sections with one low sloping area in the subtidal zone and one high sloping foreshore in the intertidal zone, resulted in a strong modulation of the hydrodynamics at the site. While SW energy was completely dissipated at low tide, released bound IG waves exhibited reflection at the shoreline, especially for low frequencies. The frequency-dependent reflection coefficient suggests IG wave breaking as the main energy dissipation mechanism. As a result, the swash exhibited a large range of values, for the same

offshore conditions. In addition, the relative contributions of the SW and IG bands to the swash varied significantly during the tidal cycle, ranging from completely IG dominated at low tide, to SW dominated at mid and high tide. Under energetic conditions the large waves tend to break further offshore than under moderate conditions, dissipating SW energy on the low sloping area even at high tide. As a result, the swash motions and general behavior of the site are less sensitive to the tidal variations under energetic than moderate conditions. Nonetheless, these results highlights the importance of the subtidal morphology on the swash values, even though most of the run-up parametrizations only account for the foreshore slope.

Secondly, the alongshore variability of the swash motions was addressed. The swash distribution was seen to be correlated both to the foreshore slope and to the wave distribution, suggesting an influence of the nearshore morphological and geological features on the wave field. The dominating features are however unclear, along with their exact influence on each frequency band. Understanding the driving factors contributing to the alongshore variability of the run-up is of paramount importance to mitigate coastal risks such as submersion. The potential use of a model configuration such as the one employed here to investigate the contributing factors to the distribution of the swash is detailed in the perspectives (section 5.2.2.1).

5.2 Further work

This work brought additional insights on the numerical modeling of the swash and the swash dynamics in a complex beach configuration. In this section, several perspectives are discussed, including ways to improve the model and its applications in terms of understanding the processes but also to help manage the risks of coastal flooding. Thus, the development of numerical models that could improve run-up predictions is discussed in section 5.2.1. The influence of the morphological features on the different frequency bands are still poorly understood and a validated model configuration could help bring new insights, as detailed in section 5.2.2.1. Finally, in section 5.2.2.2 the benefit of phase-resolving models to tackle climate change problems is highlighted by evaluating the efficiency of a coastal defense.

5.2.1 Nearshore wave model developments

The ever improving computational capabilities and evolving numerical formulations are constantly pushing the boundaries of numerical modeling. For instance, the wave breaking detection relied in this work on the wave height to water depth ratio. The associated energy dissipation was based on the momentary deactivation of the dispersive terms in the Boussinesq equations. The initiation of wave breaking is still an active field of research, and new methods could improve the accuracy of the modeling (Varing et al., 2021). Similarly, new dissipation mechanisms, such as the addition of an eddy viscosity term (Kennedy et al., 2000), are promising with more numerical stability. This would allow to capture wave transformations in the surf zone more accurately and potentially improve run-up predictions. It would also allow to refine the grid size, as instabilities with typical formulations arise in the surf zone with small grid

sizes.

In addition, the development of GPU (Graphics Processing Units) to solve depth-integrated equations offers a promising perspective to drastically reduce computational time (Mihami and Roeber, 2020, Brodtkorb and Holm, 2021). This would allow larger numerical domain, for instance larger than 10 km to make sure large scale longshore processes are captured, and finer grid sizes to resolve as accurately as possible local processes such as swash motions.

5.2.2 Model applications

5.2.2.1 Influence of morphology and geology

The site of the GPB displays highly 3D morphological features, inducing a significant alongshore variability in both the wave field and the swash distribution (see fig. 9 and 11 in section 4.3). However, the influence of the different features on the different frequency bands is still unknown and complex to quantify based on observations. The validated model configuration could be used as a numerical tank by altering the bathymetry to determine the driving features of the nearshore hydrodynamics.

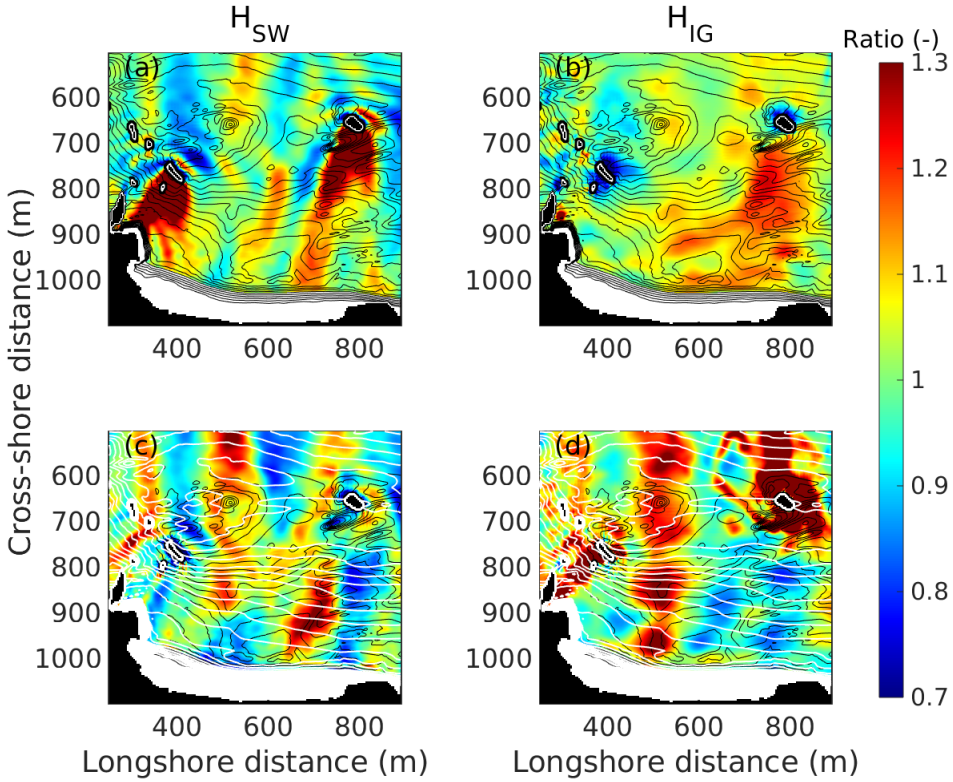

Figure 5.1: Comparisons (ratios) of the wave heights after and before the modification of the bathymetry. **(a)-(b)** rocks removed , **(c)-(d)** nearshore morphology homogenized (depth contours shown in white lines). Depth contours are shown in black lines.

Preliminary results are presented in the following to illustrate the potential of our model to analyse the influence of rocky islands and nearshore bathymetry on the wave field and swash motion. We performed two computations, one without the rocks (in $y = 400\,m$ and $y = 800\,m$

on figure 5.1) and one with an alongshore uniform morphology (white lines on figure 5.1). Both computations correspond to mid tide under moderate conditions $(H_s, T_p) = (1.5\,m, 11\,s)$.

The influence of the geology is mainly local (figure 5.1 **(a)** and **(b)**). An increase of SW energy is observed in the absence of the rocks which highlights the sheltering effect on the incident waves. Considering IG waves (panel **(b)**), some influence is visible on the right part of the domain, but on the left side the IG wave field appears unchanged, whereas the short waves are modified. This suggests a different influence on the two frequency bands. The initial nearshore bathymetry shows distinct features, such as a rip channel around $y = 600\,m$, no longer present with the alongshore uniform bathymetry (panels **(c)** and **(d)**). This time the influence is much more visible, on both the SW and IG bands. For instance, at the location of the rip channel a simultaneous decrease of SW energy and an increase of IG energy is observed. A possible reason for that is that this deeper region dissipates less SW energy through depth-induced wave breaking and therefore generates less IG waves.

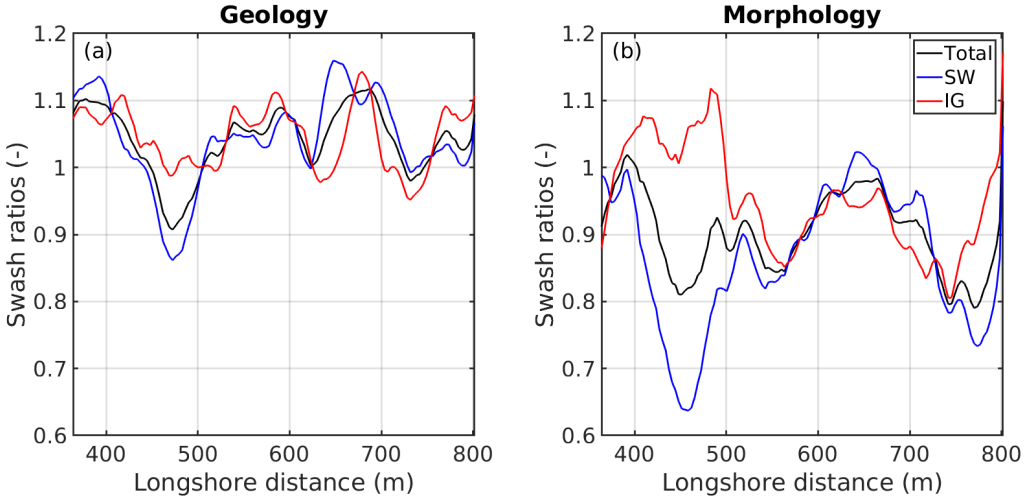

Figure 5.2: Comparisons (ratios) of the swash heights after and before the modification of the bathymetry. **(a)** rocks removed , **(b)** nearshore morphology homogenized. Black, blue and red lines respectively indicate the total, SW and IG swash heights.

The alongshore distributions of the swash for the two modified beach configurations are compared on figure 5.2. Similarly than for waves, the influence of the morphology on the swash is greater than the one of the geology. Near the location of the rip channel, a decrease by 40% of the SW swash is observed while an increase of about 10% of the IG swash is observed. This is consistent with the influence on the wave field noted on figure 5.1. In the case with no rock sheltering (panel **(a)**), the swash values are generally higher, up to 15% for both the SW and IG swash heights. However, the strongest variations are less than 20%, while it reaches 40% when the morphology is modified.

These preliminary results show that a better understanding of the influence of subtidal morphology on the run-up is crucial as it is a key driver to coastal inundation. Various studies showed significant alongshore variability in extreme water levels, causing various degrees of damage (Matsuba et al., 2021a). A better comprehension of these alongshore processes would

benefit the coastal community to better predict extreme sea level events and implement more efficient solutions.

5.2.2.2 Evaluation of a coastal defense efficiency

The study was carried out at an unprotected embayed beach. The implementation of coastal defenses, either permanent or temporary, would require an assessment of the impact on the wave field and swash motion. In this section, we propose to apply the *BOSZ* model

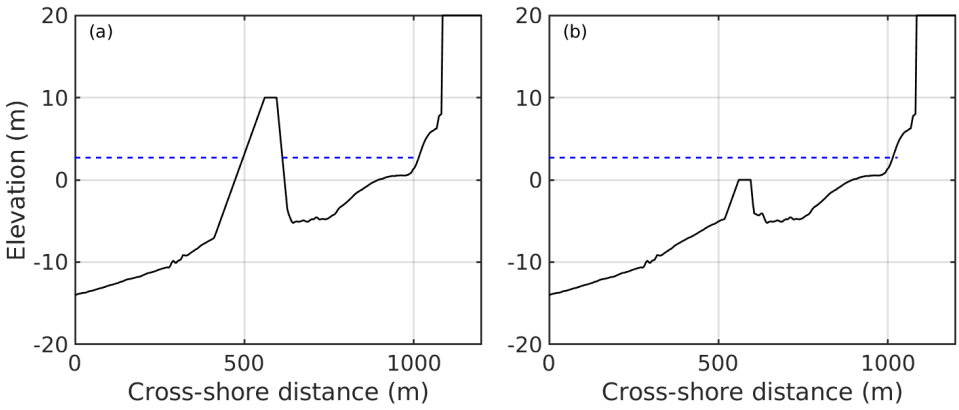

Figure 5.3: Cross-shore profile of the tested coastal defenses. **(a)** detached breakwater, **(b)** submerged breakwater. The horizontal blue lines represent the water level for the numerical experiment.

to study the influence of two offshore breakwater configurations. The first one consists in a detached breakwater (figure 5.3 panel **(a)**). It is located on the outer-bar and its top is at +10m. The seaward slope is 40% (1/2.5) while the shoreward slope is 150% (1.5/1). The second configuration (panel **(b)**) is similar to the first one, i.e. same location, same slopes on both sides, but it only reaches +0 m, hence it is always submerged. The advantage of such design lies in its social acceptability, as it is not visible from the beach. Both computations correspond to mid tide under energetic conditions $(H_s, T_p) = (3.5\,m, 14\,s)$.

The influence of the protection solutions on the wave field are shown on figure 5.4. As expected the sheltering effect of the emerged breakwater (**(a)** and **(b)**) is much larger than of the submerged one (**(c)** and **(d)**). Immediately behind the structure a reduction of 80% of H_{SW} is observed for the emerging breakwater against 40% for the submerged one. In addition, close to the shoreline H_{SW} appears almost not affected in the submerged case, as the ratio presents values close to one, suggesting no sheltering effect (panel **(c)**). In the case of H_{IG}, the dissipation is also much greater for the emerged case. In the submerged case, the SW depth-induced breaking might be happening on the structure, generating IG waves at this location.

Consistently with figure 5.4, the swash is much more attenuated with the emerged breakwater than with the submerged breakwater (figure 5.5). The two frequency bands show distinct behaviors. In both cases the IG swash is the most attenuated, almost twice as much as S_{SW}. In the case of the submerged breakwater (panel **(b)**), the SW swash is even increased at some

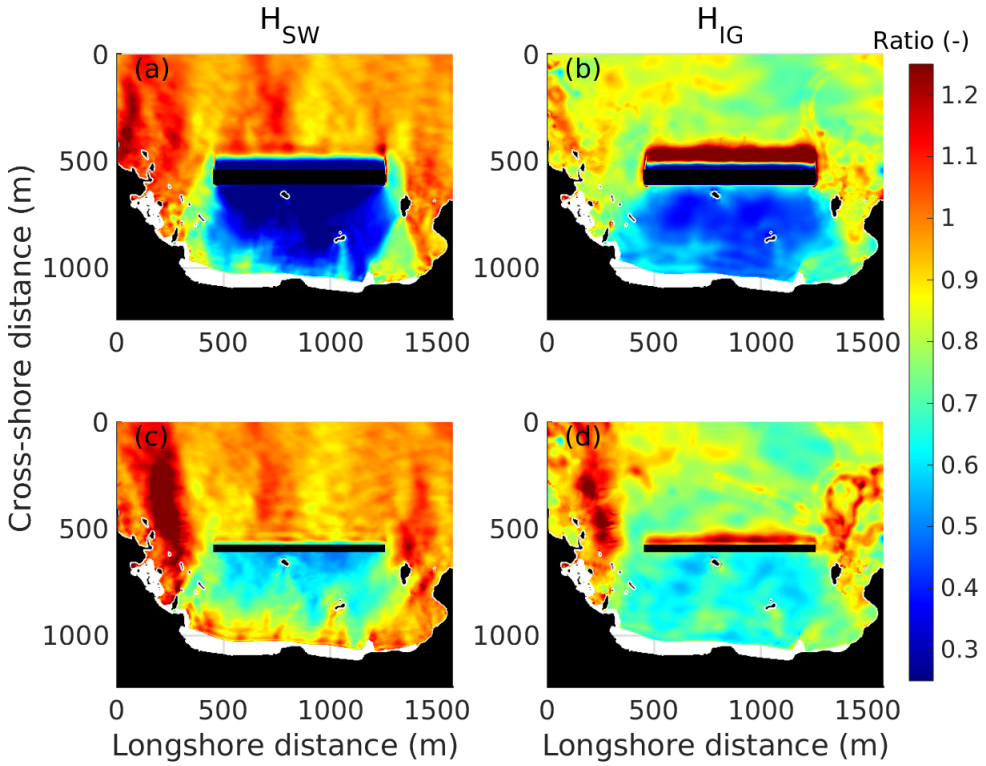

Figure 5.4: Comparisons (ratios) of the wave heights after and before the implementation of a coastal defense. **(a)-(b)** detached breakwater shown on figure 5.3 **(a)**, **(c)-(d)** submerged breakwater shown on figure 5.3 **(b)**.

locations (ratio> 1). This suggests that, as noticed with the waves on figure 5.4, both frequency bands are to be considered differently to fully quantify the efficiency of a coastal protection.

This preliminary work illustrates the potential of phase-resolving models to carry out numerical experiments for various coastal applications. It allows to investigate wave and run-up processes under a wide range of conditions and continuously along the beach. For a similar results, a field campaign would be extremely costly and complicated to set-up. It also allows to compute an infinite number of scenarios, for instance to assess the efficiency of different architectures of coastal defenses. Finally, in the context of climate change, such models can be applied to anticipate as accurately as possible the increasing coastal risks.

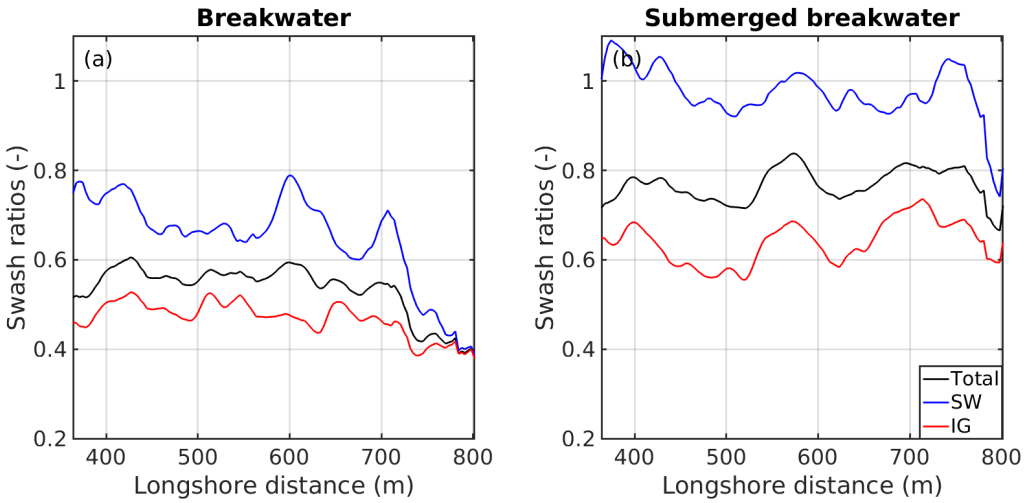

Figure 5.5: Comparisons (ratios) of the swash heights after and before the implementation of a coastal defense. **(a)-(b)** detached breakwater shown on figure 5.3 **(a)**, **(c)-(d)** submerged breakwater shown on figure 5.3 **(b)**. Black, blue and red lines respectively indicate the total, SW and IG swash heights.

Bibliography

Aarninkhof, S. G., Turner, I. L., Dronkers, T. D., Caljouw, M., and Nipius, L. (2003). A video-based technique for mapping intertidal beach bathymetry. *Coastal Engineering*, 49(4):275–289.

Abadie, S., Beauvivre, M., Egurrola, E., Bouisset, C., Degremont, I., and Arnoux, F. (2018). A database of recent historical storm impact on the french basque coast. *Journal of Coastal Research*, 85.

Abadie, S., Butel, R., Mauriet, S., Morichon, D., and Dupuis, H. (2006). Wave climate and longshore drift on the south aquitaine coast. *Continental Shelf Research*, 26(16):1924 – 1939.

Almar, R., Ranasinghe, R., Bergsma, E. W. J., Diaz, H., Melet, A., Papa, F., Vousdoukas, M., Athanasiou, P., Dada, O., Almeida, L. P., and Kestenare, E. (2021). A global analysis of extreme coastal water levels with implications for potential coastal overtopping. *Nature Communications*, 12:3775 [9].

Almar, R., Ranasinghe, R., Senechal, N., Bonneton, P., Roelvink, D. J., Bryan, K., Marieu, V., and Parisot, J.-P. (2012). Video-based detection of shorelines at complex meso-macro tidal beaches. *Journal of Coastal Research*, 28:1040–1048.

Andriolo, U. (2019). Nearshore wave transformation domains from video imagery. *Journal of Marine Science and Engineering*, 7(6).

Andriolo, U., Mendes, D., and Taborda, R. (2020). Breaking wave height estimation from timex images: Two methods for coastal video monitoring systems. *Remote Sensing*, 12(2).

Arnoux, F., Abadie, S., Bertin, X., and Kojadinovic, I. (2021). Coastal flooding event definition based on damages: Case study of biarritz grande plage on the french basque coast. *Coastal Engineering*, 166:103873.

Asbury H. Sallenger, J. (2000). Storm impact scale for barrier islands. *Journal of Coastal Research*, 16(3):890–895.

Atkinson, A. L., Power, H. E., Moura, T., Hammond, T., Callaghan, D. P., and Baldock, T. E. (2017). Assessment of runup predictions by empirical models on non-truncated beaches on the south-east australian coast. *Coastal Engineering*, 119:15–31.

Azouri, A., Roeber, V., and Luther, D. S. (2018). The response of harbor environments protected by irregular fringing reef systems to strong gravity wave forcing - a case study. *Coastal Engineering Proceedings*, 1(36).

Barbier, E. B., Hacker, S. D., Kennedy, C., Koch, E. W., Stier, A. C., and Silliman, B. R. (2011). The value of estuarine and coastal ecosystem services. *Ecological Monographs*, 81(2):169–193.

Battjes, J. A., Bakkenes, H. J., Janssen, T. T., and van Dongeren, A. R. (2004). Shoaling of subharmonic gravity waves. *Journal of Geophysical Research: Oceans*, 109(C2).

Battjes, J. A. and Janssen, J. P. F. M. (1978). Energy loss and set-up due to breaking of random waves. *Coastal Engineering*, pages 569–587.

Bellafont, F., Morichon, D., Roeber, V., Andre, G., and Abadie, S. (2018). Infragravity period oscillations in a channel harbor near a river mouth. In *Coastal Engineering Proceedings*, volume 1.

Berkhoff, J., Booy, N., and Radder, A. (1982). Verification of numerical wave propagation models for simple harmonic linear water waves. *Coastal Engineering*, 6(3):255–279.

Bertin, X., Bakker, A., Guérin, T., Chataigner, T., Martins, K., and Coulombier, T. (2018a). Transferts d'énergie et réflexion des ondes infragravitaires au niveau d'une plage dissipative. In *XVèmes Journées Nationales Génie Côtier – Génie Civil*, pages 9–18.

Bertin, X., de Bakker, A., van Dongeren, A., Coco, G., André, G., Ardhuin, F., Bonneton, P., Bouchette, F., Castelle, B., Crawford, W. C., Davidson, M., Deen, M., Dodet, G., Guérin, T., Inch, K., Leckler, F., McCall, R., Muller, H., Olabarrieta, M., Roelvink, D., Ruessink, G., Sous, D., Éléonore Stutzmann, and Tissier, M. (2018b). Infragravity waves: From driving mechanisms to impacts. *Earth-Science Reviews*, 177:774–799.

Bertin, X., Martins, K., Bakker, A., Chataigner, T., Guérin, T., Coulombier, T., and De Viron, O. (2020). Energy transfers and reflection of infragravity waves at a dissipative beach under storm waves. *Journal of Geophysical Research: Oceans*, 125.

Blenkinsopp, C., Bayle, P., Conley, D., Masselink, G., Gulson, E., Kelly, I., Almar, R., Turner, I., Baldock, T., Beuzen, T., McCall, R., H., R., Troch, A. R. P., Gallach-Sanchez, D., Hunter, A., O, B., Hennessey, G., Ganderton, P., Schimmels, S., and Kudella, M. (2019). Dynamic coastal protection: resilience of dynamic revetments (dynarev). *Proceedings of the HYDRALAB+ Joint User Meeting, Bucharest*.

Blenkinsopp, C., Bayle, P., Conley, D., Masselink, G., Gulson, E., Kelly, I., Almar, R., Turner, I., Baldock, T., Beuzen, T., McCall, R., Rijper, H., Reniers, A., Troch, P., Gallach-Sánchez, D., Hunter, A., Bryan, O., Hennessey, G., Ganderton, P., and Schimmels, S. (2021). High-resolution, large-scale laboratory measurements of a sandy beach and dynamic cobble berm revetment. *Scientific Data*, 8.

Blenkinsopp, C., Matias, A., Howe, D., Castelle, B., Marieu, V., and Turner, I. (2016). Wave runup and overwash on a prototype-scale sand barrier. *Coastal Engineering*, 113:88–103. Barrier Dynamics Experiment II: sediment processes across a large-scale sand barrier.

Blenkinsopp, C., Mole, M., Turner, I., and Peirson, W. (2010). Measurements of the time-varying free-surface profile across the swash zone obtained using an industrial lidar. *Coastal Engineering*, 57(11):1059–1065.

Blossier, B., Bryan, K. R., Daly, C. J., and Winter, C. (2017). Shore and bar cross-shore migration, rotation, and breathing processes at an embayed beach. *Journal of Geophysical Research: Earth Surface*, 122(10):1745–1770.

Bonneton, P., Bruneau, N., Castelle, B., and Marche, F. (2010). Large-scale vorticity generation due to dissipating waves in the surf zone. *Discrete & Continuous Dynamical Systems - B*, 13(4):729–738.

Bonneton, P. and Lannes, D. (2017). Recovering water wave elevation from pressure measurements. *Journal of Fluid Mechanics*, 833:399–429.

Bonneton, P., Lannes, D., Martins, K., and Michallet, H. (2018). A nonlinear weakly dispersive method for recovering the elevation of irrotational surface waves from pressure measurements. *Coastal Engineering*, 138:1–8.

Booij, N., Ris, R. C., and Holthuijsen, L. H. (1999). A third-generation wave model for coastal regions: 1. model description and validation. *Journal of Geophysical Research: Oceans*, 104(C4):7649–7666.

Boussinesq, J. (1872). Théorie des ondes et des remous qui se propagent le long d'un canal rectangulaire horizontal, en communiquant au liquide contenu dans ce canal des vitesses sensiblement pareilles de la surface au fond. *Journal de Mathématiques Pures et Appliquées*, pages 55–108.

Bouvier, C., Balouin, Y., Castelle, B., and Valentini, N. (2020). Video depth inversion at a microtidal site exposed to prevailing low-energy short-period waves and episodic severe storms. *Journal of Coastal Research*, 95:1021.

Bretschneider, C. L. (1959). Wave variability and wave spectra for wind generated gravity waves. In *Technical memo.*

Briggs, M., Thompson, E., and Vincent, C. (1995). Wave diffraction around breakwater. *Journal of Waterway Port Coastal and Ocean Engineering*, 121:23–35.

Brocchini, M. (2013). A reasoned overview on boussinesq-type models: the interplay between physics, mathematics and numerics. *Proceedings of the Royal Society A: Mathematical, Physical and Engineering Sciences*, 469(2160):20130496.

Brodie, K. L., Raubenheimer, B., Elgar, S., Slocum, R. K., and McNinch, J. E. (2015). Lidar and pressure measurements of inner-surfzone waves and setup. *Journal of Atmospheric and Oceanic Technology*, 32(10):1945 – 1959.

Brodtkorb, A. R. and Holm, H. H. (2021). Coastal ocean forecasting on the gpu using a two-dimensional finite-volume scheme. *Tellus A: Dynamic Meteorology and Oceanography*, 73(1):1–22.

Bruneau, N., Bonneton, P., Castelle, B., and Pedreros, R. (2011). Modeling rip current circulations and vorticity in a high-energy mesotidal-macrotidal environment. *Journal of Geophysical Research: Oceans*, 116(C7).

Callens, A., Morichon, D., Abadie, S., Delpey, M., and Liquet, B. (2020). Using random forest and gradient boosting trees to improve wave forecast at a specific location. *Applied Ocean Research*, 104:102339.

Castelle, B. and Coco, G. (2012). The morphodynamics of rip channels on embayed beaches. *Continental Shelf Research*, 43:10–23.

Chaigneau, A. A., Reffray, G., Voldoire, A., and Melet, A. (2021). IBI-CCS : a regional high-resolution model to evaluate western europe sea level changes. *Geoscientific Model Development Discussions*, 2021:1–35.

Cheriton, O. M., Storlazzi, C. D., and Rosenberger, K. J. (2020). In situ observations of wave transformation and infragravity bore development across reef flats of varying geomorphology. *Frontiers in Marine Science*, 7.

Christopher, S. and Robert, N. (2003). A global analysis of human settlement in coastal zones. *Journal of Coastal Research*.

Ciavola, P., Ferreira, O., Haerens, P., Van Koningsveld, M., Armaroli, C., and Lequeux, Q. (2011). Storm impacts along european coastlines. part 1: The joint effort of the micore and conhaz projects. *Environmental Science & Policy*, 14(7):912–923. Adapting to Climate Change: Reducing Water-related Risks in Europe.

Clamond, D. and Constantin, A. (2013). Recovery of steady periodic wave profiles from pressure measurements at the bed. *Journal of Fluid Mechanics*, 714:463–475.

Cohn, N. and Ruggiero, P. (2016). The influence of seasonal to interannual nearshore profile variability on extreme water levels : Modeling wave runup on dissipative beaches. *Coastal Engineering*, 115:79–92. Swash-zone Processes.

Collins, A. M., Brodie, K. L., Bak, A. S., Hesser, T. J., Farthing, M. W., Lee, J., and Long, J. W. (2020). Bathymetric inversion and uncertainty estimation from synthetic surf-zone imagery with machine learning. *Remote Sensing*, 12(20).

Conrady, A. E. (1919). Decentred Lens-Systems. *Monthly Notices of the Royal Astronomical Society*, 79(5):384–390.

Constantin, A. (2012). On the recovery of solitary wave profiles from pressure measurements. *Journal of Fluid Mechanics*, 699:376–384.

Da Silva, G., Gomes da Silva, P., Araujo, R., Klein, A., and Toldo, E. (2017). Wave run-up on embayed beaches. study case: Itapocorói bay, southern brazil. *Brazilian Journal of Oceanography*, 65:187–200.

Daly, C. J., Bryan, K. R., and Winter, C. (2014). Wave energy distribution and morphological development in and around the shadow zone of an embayed beach. *Coastal Engineering*, 93:40–54.

Davidson-Arnott, R., Bauer, B., and Houser, C. (2019). *Introduction to Coastal Processes and Geomorphology*. Cambridge University Press, 2 edition.

de Bakker, A., Tissier, M., and Ruessink, B. (2014). Shoreline dissipation of infragravity waves. *Continental Shelf Research*, 72:73–82.

de Bakker, A., Tissier, M. F. S., Marieu, V., Sénéchal, N., Ruju, A., Lara, J. L., and Ruessink, G. (2013). Infragravity wave propagation and dissipation on a low-sloping laboratory beach. In *Coastal Dynamics 2013*.

de Bakker, A. T. M., Tissier, M. F. S., and Ruessink, B. G. (2016). Beach steepness effects on nonlinear infragravity-wave interactions: A numerical study. *Journal of Geophysical Research: Oceans*, 121(1):554–570.

de Beer, A., McCall, R., Long, J., Tissier, M., and Reniers, A. (2021). Simulating wave runup on an intermediate–reflective beach using a wave-resolving and a wave-averaged version of XBeach. *Coastal Engineering*, 163:103788.

de Santiago, I., Morichon, D., Abadie, S., Reniers, A., and Liria, P. (2017). A comparative study of models to predict storm impact on beaches. *Nat Hazards*, 87:843–865.

Delpey, M., Lastiri, X., Abadie, S., Roeber, V., Maron, P., Liria, P., and Mader, J. (2021). Characterization of the wave resource variability in the french basque coastal area based on a high-resolution hindcast. *Renewable Energy*, 178:79–95.

Dessy, C., Schiaffino, C., Nicola, C., and Ferrari, M. (2008). Nourishment of levanto (italy): a webcam-aided evaluation of a mixed sand and gravel beach fill. *Beach Erosion Monitoring. Beachmed-e/OpTIMAL Project*, pages 119–128.

Didier, D., Caulet, C., Bandet, M., Bernatchez, P., Dumont, D., Augereau, E., Floc'h, F., and Delacourt, C. (2020). Wave runup parameterization for sandy, gravel and platform beaches in a fetch-limited, large estuarine system. *Continental Shelf Research*, 192:104024.

Do, K., Kobayashi, N., Suh, K.-D., and Jin, J.-Y. (2016). Wave transformation and sand transport on a macrotidal pocket beach. *Journal of Waterway, Port, Coastal, and Ocean Engineering*, 142(1):04015009.

Elsayed, S., Gijsman, R., Schlurmann, T., and Goseberg, N. (2022). Nonhydrostatic numerical modeling of fixed and mobile barred beaches: Limitations of depth-averaged wave resolving models around sandbars. *Journal of Waterway, Port, Coastal and Ocean Engineering*, 148.

Emery, W. J. and Thomson, R. E. (2001). Chapter 5 - time-series analysis methods. In Emery, W. J. and Thomson, R. E., editors, *Data Analysis Methods in Physical Oceanography*, pages 371–567. Elsevier Science.

Engsig-Karup, A. P., Hesthaven, J. S., Bingham, H. B., and Warburton, T. (2008). Dg-fem solution for nonlinear wave-structure interaction using boussinesq-type equations. *Coastal Engineering 55*, pages 197–208.

Enjalbert, C., Castelle, B., Rihouey, D., and Dailloux, D. (2011). High-frequency video observation of a geologically-constrained barred-beach: La grande plage de biarritz (france). *J. Coastal Res.*, SI 64.

Eskilsson, C., Sherwin, S., and Bergdahl, L. (2006). An unstructured spectral/hp element model for enhanced boussinesq-type equations. *Coastal Engineering*, 53(11):947–963.

Eskilsson, C. and Sherwin, S. J. (2006). Spectral/hp discontinuous galerkin methods for modelling 2d boussinesq equations. *Journal of Computational Physics*, 212(2):566–589.

Fiedler, J., Smit, P., Brodie, K., McNinch, J., and Guza, R. (2018). Numerical modeling of wave runup on steep and mildly sloping natural beaches. *Coastal engineering*, vol. 131.

Fiedler, J. W., Brodie, K. L., McNinch, J. E., and Guza, R. T. (2015). Observations of runup and energy flux on a low-slope beach with high-energy, long-period ocean swell. *Geophysical Research Letters*, 42(22):9933–9941.

Filipot, J.-F., Guimaraes, P., Leckler, F., Hortsmann, J., Carrasco, R., Leroy, E., Fady, N., Accensi, M., Prevosto, M., Duarte, R., Roeber, V., Benetazzo, A., Raoult, C., Franzetti, M., Varing, A., and Le Dantec, N. (2019). La jument lighthouse: a real-scale laboratory for the study of giant waves and their loading on marine structures. *Philosophical Transactions of the Royal Society A: Mathematical, Physical and Engineering Sciences*, 377.

Foote, M. and Horn, D. (2002). Using video and gis to measure two-dimensional water surface elevations in the swash zone. *Transition in GIS*, 6:43–68.

Gal, Y., Browne, M., and Lane, C. (2011). Automatic estimation of nearshore wave height from video timestacks. In *2011 International Conference on Digital Image Computing: Techniques and Applications*, pages 364–369.

Gallop, S., Bryan, K., Coco, G., and Stephens, S. (2011). Storm-driven changes in rip channel patterns on an embayed beach. *Geomorphology*, 127(3):179–188.

Gomes da Silva, P., Coco, G., Garnier, R., and Klein, A. H. (2020). On the prediction of runup, setup and swash on beaches. *Earth-Science Reviews*, 204:103148.

Gomes da Silva, P., Medina, R., González, M., and Garnier, R. (2018). Infragravity swash parameterization on beaches: The role of the profile shape and the morphodynamic beach state. *Coastal Engineering*, 136:41–55.

Gomes da Silva, P., Medina, R., González, M., and Garnier, R. (2019). Wave reflection and saturation on natural beaches: The role of the morphodynamic beach state in incident swash. *Coastal Engineering*, 153:103540.

Greenwood, B. and Brander, R. (2011). Far-infragravity and infragravity "pulses" in a rip current. *WIT Transactions on Ecology and the Environment*, 149.

Guedes, R. M., Bryan, K. R., and Coco, G. (2012). Observations of alongshore variability of swash motions on an intermediate beach. *Continental Shelf Research*, 48:61–74.

Guedes, R. M. C., Bryan, K. R., and Coco, G. (2013). Observations of wave energy fluxes and swash motions on a low-sloping, dissipative beach. *Journal of Geophysical Research: Oceans*, 118(7):3651–3669.

Guedes, R. M. C., Bryan, K. R., Coco, G., and Holman, R. A. (2011). The effects of tides on swash statistics on an intermediate beach. *Journal of Geophysical Research: Oceans*, 116(C4).

Guza, R., Thornton, E., and Holman, R. (1984). Swash on steep and shallow beaches. *Coastal Engineering Proceedings*, 1:48.

Guza, R. T. and Thornton, E. B. (1982). Swash oscillations on a natural beach. *Journal of Geophysical Research: Oceans*, 87(C1):483–491.

Guza, R. T. and Thornton, E. B. (1985). Observations of surf beat. *Journal of Geophysical Research: Oceans*, 90(C2):3161–3172.

Hasselmann, K. and Olbers, D. (1973). Measurements of wind-wave growth and swell decay during the joint north sea wave project (jonswap). *Ergänzung zur Deut. Hydrogr. Z., Reihe A (8)*, 12:1–95.

Hein, S. and Winter, C. (2019). Video monitoring of beach states, coastline migration and beach nourishments – a case study from sylt island, north sea. *Coastal structures*, pages 822–831.

Holland, K., Holman, R., Lippmann, T., Stanley, J., and Plant, N. (1997). Practical use of video imagery in nearshore oceanographic field studies. *IEEE Journal of Oceanic Engineering*, 22(1):81–92.

Holland, K. T. and Holman, R. A. (1999). Wavenumber-frequency structure of infragravity swash motions. *Journal of Geophysical Research*, 104:13479–13488.

Holland, K. T., Raubenheimer, B., Guza, R. T., and Holman, R. A. (1995). Runup kinematics on a natural beach. *Journal of Geophysical Research: Oceans*, 100(C3):4985–4993.

Holman, R. (1986). Extreme value statistics for wave run-up on a natural beach. *Coastal Engineering*, 9(6):527–544.

Holman, R. and Guza, R. (1984). Measuring run-up on a natural beach. *Coastal Engineering*, 8(2):129–140.

Holman, R. and Stanley, J. (2007). The history and technical capabilities of argus. *Coastal Engineering*, 54(6):477–491.

Holman, R. A., Jr., A. H. S., Lippmann, T. C., and Haines, J. W. (1993). The application of video image processing to the study of nearshore processes. *Oceanography*.

Holman, R. A. and Sallenger Jr., A. H. (1985). Setup and swash on a natural beach. *Journal of Geophysical Research: Oceans*, 90(C1):945–953.

Horrillo, J., Grilli, S., Nicolsky, D., Roeber, V., and Zhang, J. (2014). Performance benchmarking tsunami models for nthmp's inundation mapping activities. *Pure Appl. Geophys.*, vol. 172:869–884.

Hughes, M., Aagaard, T., Baldock, T., and Power, H. (2013). Wave runup (swash) spectra on natural beaches: Morphodynamic controls. *Coasts and Ports 2013*, pages 412–417.

Hughes, M. G. (1992). Application of a non-linear shallow water theory to swash following bore collapse on a sandy beach. *Journal of Coastal Research*, 8(3):562–578.

Hughes, M. G., Moseley, A. S., and Baldock, T. E. (2010). Probability distributions for wave runup on beaches. *Coastal Engineering*, 57(6):575–584.

Hughes, S. A. (1984). The tma shallow-water spectrum description and applications. In *Report*.

Hunt, I. A. (1961). Design of sea-walls and breakwaters. *Transactions of the American Society of Civil Engineers*, 126(4):542–570.

Huntley, D. A., Guza, R. T., and Bowen, A. J. (1977). A universal form for shoreline run-up spectra? *Journal of Geophysical Research (1896-1977)*, 82(18):2577–2581.

Iafrati, A. (2011). Energy dissipation mechanisms in wave breaking processes: Spilling and highly aerated plunging breaking events. *Journal of Geophysical Research: Oceans*, 116(C7).

Inch, K., Davidson, M., Masselink, G., and Russell, P. (2017). Observations of nearshore infragravity wave dynamics under high energy swell and wind-wave conditions. *Continental Shelf Research*, 138:19–31.

IUCN (2017). Ocean warming. *International Union for Conservation of Nature, Issues Brief*.

Janssen, T. T., Battjes, J. A., and van Dongeren, A. R. (2003). Long waves induced by short-wave groups over a sloping bottom. *Journal of Geophysical Research: Oceans*, 108(C8).

Kennedy, A. B., Chen, Q., Kirby, J. T., and Dalrymple, R. A. (2000). Boussinesq modeling of wave transformation, breaking, and runup. i: 1d. *Journal of Waterway, Port, Coastal, and Ocean Engineering*, 126(1):39–47.

Kim, K. O., Kim, D. C., Choi, B. H., Jung, K. T., Yuk, J. H., and Pelinovsky, E. (2015). The role of diffraction effects in extreme run-up inundation at okushiri island due to 1993 tsunami. *Natural Hazards and Earth System Sciences*, 15(4):747–755.

Kirezci, E., Young, I. R., Ranasinghe, R., Muis, S., Nicholls, R. J., Lincke, D., and Hinkel, J. (2020). Projections of global-scale extreme sea levels and resulting episodic coastal flooding over the 21st century. *Scientific Reports*, 10.

Klein, A. H., Óscar Ferreira, Dias, J. M., Tessler, M. G., Silveira, L. F., Benedet, L., de Menezes, J. T., and de Abreu, J. G. (2010). Morphodynamics of structurally controlled headland-bay beaches in southeastern brazil: A review. *Coastal Engineering*, 57(2):98–111. Hydrodynamics and Applications of Headland-Bay Beaches.

Knutson, T. R., Chung, M. V., Vecchi, G., Sun, J., Hsieh, T.-L., and Smith, A. J. P. (2021). Climate change is probably increasing the intensity of tropical cyclones.

Lashley, C. H., Bertin, X., Roelvink, D., and Arnaud, G. (2019). Contribution of infragravity waves to run-up and overwash in the pertuis breton embayment (france). *Journal of Marine Science and Engineering*, 7(7).

Lashley, C. H., Roelvink, D., van Dongeren, A., Buckley, M. L., and Lowe, R. J. (2018). Nonhydrostatic and surfbeat model predictions of extreme wave run-up in fringing reef environments. *Coastal Engineering*, 137:11–27.

Lastiri, X., Abadie, S., Maron, P., Delpey, M., Liria, P., Mader, J., and Roeber, V. (2020). Wave energy assessment in the south aquitaine nearshore zone from a 44-year hindcast. *Journal of Marine Science and Engineering*, 8(3).

Li, N., Roeber, V., Yamazaki, Y., Heitmann, T. W., Bai, Y., and Cheung, K. F. (2014). Integration of coastal inundation modeling from storm tides to individual waves. *Ocean Modelling*, 83:26–42.

Li, Y., Liu, S.-X., Yu, Y.-X., and Lai, G.-Z. (1999). Numerical modeling of boussinesq equations by finite element method. *Coastal Engineering*, 37(2):97–122.

Lin, P. and Liu, P. L.-F. (1998). A numerical study of breaking waves in the surf zone. *Journal of Fluid Mechanics*, 359:239–264.

Lippmann, T. and Holman, R. (1989). Quantification of sand bar morphology: A video technique based on wave dissipation. *J. Geophys. Res.*, 94.

List, J. H. (1991). Wave groupiness variations in the nearshore. *Coastal Engineering*, 15:475–496.

List, J. H. (1992). A model for the generation of two-dimensional surf beat. *Journal of Geophysical Research: Oceans*, 97(C4):5623–5635.

Liu, W.-j., Shao, K.-q., Ning, Y., and Zhao, X.-z. (2020). Numerical study of the impact of climate change on irregular wave run-up over reef-fringed coasts. *Journal of Coastal Research*, 34(2):162–171.

Liu, Y., Liao, Z., Fang, K., and Li, S. (2021). Uncertainty of wave runup prediction on coral reef-fringed coasts using swash model. *Ocean Engineering*, 242.

Lombardo, S., Salman, A., and Doody, P. (2004). Living with coastal erosion in europe: Sediment and space for sustainability. In *Directorate General Environment, European Commission.*

Longuet-Higgins, M. and Stewart, R. (1964). Radiation stresses in water waves; a physical discussion, with applications. *Deep Sea Research and Oceanographic Abstracts*, 11(4):529–562.

Loureiro, C., Óscar Ferreira, and Cooper, J. A. G. (2012). Geologically constrained morphological variability and boundary effects on embayed beaches. *Marine Geology*, 329-331:1–15.

Lubin, P., Vincent, S., Abadie, S., and Caltagirone, J.-P. (2006). Three-dimensional large eddy simulation of air entrainment under plunging breaking waves. *Coastal Engineering*, 53(8):631–655.

Lynett, P., Roeber, V., Heitmann, T., Cheung, K., David, C., and et al., J. B. (2017). Inter-model analysis of tsunami-induced coastal currents. *Ocean Modelling*, vol. 114:14–32.

Ma, G., Shi, F., and Kirby, J. T. (2012). Shock-capturing non-hydrostatic model for fully dispersive surface wave processes. *Ocean Modelling*, 43-44:22–35.

MacMahan, J. H., Reniers, A. J. H. M., Thornton, E. B., and Stanton, T. P. (2004). Infragravity rip current pulsations. *Journal of Geophysical Research: Oceans*, 109(C1).

Madsen, O. S., Poon, Y.-K., and Graber, H. C. (1988). Spectral wave attenuation by bottom friction: Theory. *Coastal engineering*, pages 492–504.

Madsen, P. A. and Sørensen, O. R. (1992). A new form of the boussinesq equations with improved linear dispersion characteristics. part 2. a slowly-varying bathymetry. *Coastal Engineering*, 18(3):183–204.

Mara Tonelli, M. P. (2009). Hybrid finite volume – finite difference scheme for 2dh improved boussinesq equations. *Coastal Engineering 56*, pages 609–620.

Martins, K., Blenkinsopp, C. E., Almar, R., and Zang, J. (2017). The influence of swash-based reflection on surf zone hydrodynamics: a wave-by-wave approach. *Coastal Engineering*, 122:27–43.

Martins, K., Bonneton, P., Mouragues, A., and Castelle, B. (2020). Non-hydrostatic, non-linear processes in the surf zone. *Journal of Geophysical Research: Oceans*, 125(2):e2019JC015521.

Martone, I., Galani, K., Gualtieri, P., Gualtieri, C., and Dimas, A. (2018). Experimental analysis on a low crested rubble mound breakwater. In 7^{th} *International Symposium on Hydraulic Structures*, Aachen, Germany.

Masselink, G. and Puleo, J. A. (2006). Swash-zone morphodynamics. *Continental Shelf Research*, 26(5):661–680. Swash-Zone Processes.

Masselink, G. and Russell, P. (2006). Flow velocities, sediment transport and morphological change in the swash zone of two contrasting beaches. *Marine Geology*, 227(3):227–240.

Matsuba, Y., Shimozono, T., and Tajima, Y. (2021a). Extreme wave runup at the seisho coast during typhoons faxai and hagibis in 2019. *Coastal Engineering*, 168:103899.

Matsuba, Y., Shimozono, T., and Tajima, Y. (2021b). Tidal modulation of infragravity wave dynamics on a reflective barred beach. *Estuarine, Coastal and Shelf Science*, 261:107562.

McCowan, J. (1894). Xxxix. on the highest wave of permanent type. *The London, Edinburgh, and Dublin Philosophical Magazine and Journal of Science*, 38(233):351–358.

McNinch, J. E. (2007). Bar and Swash Imaging Radar (BASIR): A Mobile X-band Radar Designed for Mapping Nearshore Sand Bars and Swash-Defined Shorelines Over Large Distances. *Journal of Coastal Research*, 2007(231):59 – 74.

Mehvar, S., Filatova, T., Dastgheib, A., De Ruyter van Steveninck, E., and Ranasinghe, R. (2018). Quantifying economic value of coastal ecosystem services: A review. *Journal of Marine Science and Engineering*, 6(1).

Melet, A., Meyssignac, B., Almar, R., and Le Cozannet, G. (2018). Under-estimated wave contribution to coastal sea-level rise. *Nature Climate Change*, 8.

Mihami, F.-Z. and Roeber, V. (2020). An efficient and robust gpgpu-based shallow water model. *Coastal Engineering Proceedings*, page 47.

Morichon, D., de Santiago, I., Delpey, M., Somdecoste, T., Callens, A., Liquet, B., Liria, P., and Arnould, P. (2018). Assessment of Flooding Hazards at An Engineered Beach during Extreme Events: Biarritz, SW France. *Journal of Coastal Research*, 85(sp1):801 – 805.

Morichon, D., Roeber, V., Martin-Medina, M., Bellafont, F., and Abadie, S. (2021). Tsunami impact on a detached breakwater: Insights from two numerical models. *Journal of Waterway, Port, Coastal, and Ocean Engineering*, 147(2):05021001.

Mouragues, A., Bonneton, P., Lannes, D., Castelle, B., and Marieu, V. (2019). Field data-based evaluation of methods for recovering surface wave elevation from pressure measurements. *Coastal Engineering*, 150:147–159.

Munk, W. (1949). Surf beats. *Eos Trans. AGU*, 30(6):849–854. cited By 1.

Naciri, M., Buchner, B., Bunnik, T., Huijsmans, R., and Andrews, J. (2004). Low frequency motions of lng carriers moored in shallow water. *23rd International Conference on Offshore Mechanics and Arctic Engineering 3*, 3.

Neumann, B., Vafeidis, A. T., Zimmermann, J., and Nicholls, R. J. (2015). Future coastal population growth and exposure to sea-level rise and coastal flooding - a global assessment. *PLOS ONE*, 10(3):1–34.

Nicholls, R. J. and Cazenave, A. (2010). Sea-level rise and its impact on coastal zones. *Science*, 328(5985):1517–1520.

Nicolae Lerma, A. and Bulteau, T. (2017). A numerical study of extreme wave runup behavior : spectral and statistical analysis. In *Coastal Dynamics 2017*.

Nicolae Lerma, A., Pedrero, R., Robinet, A., and Sénéchal, N. (2017). Simulating wave setup and runup during storm conditions on a complex barred beach. *Coastal engineering*, vol. 123.

Nwogu, O. (1993). An alternative form of the boussinesq equations for nearshore wave propagation. *Journal of Waterway, Port, Coastal, and Ocean Engineering*.

Ojeda, E. and Guillén, J. (2008). Shoreline dynamics and beach rotation of artificial embayed beaches. *Marine Geology*, 253(1):51–62.

Oliveras, K., Vasan, V., Deconinck, B., and Henderson, D. (2011). Recovering the water-wave profile from pressure measurements. *SIAM Journal on Applied Mathematics*, 72.

Orzech, M. D., Thornton, E. B., MacMahan, J. H., O'Reilly, W. C., and Stanton, T. P. (2010). Alongshore rip channel migration and sediment transport. *Marine Geology*, 271(3):278–291.

Otsu, N. (1979). A threshold selection method from gray-level histograms. *IEEE Transactions on Systems, Man, and Cybernetics*, 9(1):62–66.

Passarella, M., Goldstein, E. B., De Muro, S., and Coco, G. (2018). The use of genetic programming to develop a predictor of swash excursion on sandy beaches. *Natural Hazards and Earth System Sciences*, 18(2):599–611.

Peláez-Zapata, D., Montoya, R. D., and Osorio, A. F. (2018). Numerical study of run-up oscillations over fringing reefs. *Journal of Coastal Research*, 34(5):1065 – 1079.

Pengzhi Lin, C. M. (2007). A staggered-grid numerical algorithm for the extended boussinesq equations. *Applied Mathematical Modelling 31*, pages 349–368.

Peregrine, D. (1967). Long waves on a beach. *Journal of Fluid Mechanics*, vol. 27:815–827.

Peregrine, D. H. and Williams, S. M. (2001). Swash overtopping a truncated plane beach. *Journal of Fluid Mechanics*, 440:391–399.

Pierson, Willard J., J. and Moskowitz, L. (1964). A Proposed Spectral Form for Fully Developed Wind Seas Based on the Similarity Theory of S. A. Kitaigorodskii. *Journal of Geophysical Research*, 69(24):5181–5190.

Pinault, J., Morichon, D., and Roeber, V. (2020). Estimation of irregular wave runup on intermediate and reflective beaches using a phase-resolving numerical model. *Journal of Marine Science and Engineering*, 8(12).

Pitman, S. J. (2014). Methods for field measurement and remote sensing of the swash zone. In Cook, S., Clark, L., and Nield, J., editors, *Geomorphological Techniques*, pages 3.2.6.1–3.2.6.14. British Society of Geomorphology.

Poate, T., Masselink, G., Austin, M. J., Inch, K., Dickson, M., and McCall, R. (2020). Infragravity wave generation on shore platforms: Bound long wave versus breakpoint forcing. *Geomorphology*, 350:106880.

Pomeroy, A., Lowe, R., Symonds, G., Van Dongeren, A., and Moore, C. (2012). The dynamics of infragravity wave transformation over a fringing reef. *Journal of Geophysical Research: Oceans*, 117(C11).

Pranzini, E. and Williams, A. T. (2013). *Coastal erosion and protection in Europe*. Routledge.

Péquignet, A.-C. N., Becker, J. M., and Merrifield, M. A. (2014). Energy transfer between wind waves and low-frequency oscillations on a fringing reef, ipan, guam. *Journal of Geophysical Research: Oceans*, 119(10):6709–6724.

Quataert, E., Storlazzi, C., van Dongeren, A., and McCall, R. (2020). The importance of explicitly modelling sea-swell waves for runup on reef-lined coasts. *Coastal Engineering*, 160:103704.

Raubenheimer, B. and Guza, R. T. (1996). Observations and predictions of run-up. *Journal of Geophysical Research: Oceans*, 101(C11):25575–25587.

Raubenheimer, B., Guza, R. T., and Elgar, S. (1996). Wave transformation across the inner surf zone. *Journal of Geophysical Research*, 101:25589–25597.

Raubenheimer, B., Guza, R. T., and Elgar, S. (2001). Field observations of wave-driven setdown and setup. *Journal of Geophysical Research: Oceans*, 106(C3):4629–4638.

Raubenheimer, B., Guza, R. T., Elgar, S., and Kobayashi, N. (1995). Swash on a gently sloping beach. *Journal of Geophysical Research: Oceans*, 100(C5):8751–8760.

Ricchiuto, M. and Filippini, A. G. (2014). Upwind residual discretization of enhanced boussinesq equations for wave propagation over complex bathymetries. *Journal of Computational Physics*, 271:306–341.

Rijnsdorp, D. P., Ruessink, G., and Zijlema, M. (2015). Infragravity-wave dynamics in a barred coastal region, a numerical study. *Journal of Geophysical Research: Oceans*, 120(6):4068–4089.

Risandi, J., Rijnsdorp, D. P., Hansen, J. E., and Lowe, R. J. (2020). Hydrodynamic modeling of a reef-fringed pocket beach using a phase-resolved non-hydrostatic model. *Journal of Marine Science and Engineering*, 8(11).

Robertson, B., Gharabaghi, B., and Hall, K. (2015). Prediction of incipient breaking wave-heights using artificial neural networks and empirical relationships. *Coastal Engineering Journal*, 57(4):1550018–1–1550018–27.

Robinet, A., Castelle, B., Idier, D., Harley, M., and Splinter, K. (2020). Controls of local geology and cross-shore/longshore processes on embayed beach shoreline variability. *Marine Geology*, 422:106118.

Rodrigues, B. A., Matias, A. S. A., and Ferreira, Ó. (2012). Overwash hazard assessment. *Geologica Acta*, 10:427–437.

Roeber, V. and Cheung, K. (2012a). Bosz - boussinesq ocean and surf zone model. *NOAA, Special Report, Proceedings and Results of the 2011 NTHMP Model Benchmarking Workshop, Galveston, Texas, 437 p.*

Roeber, V. and Cheung, K. (2012b). Boussinesq-type model for energetic breaking waves in fringing reef environments. *Coastal Engineering*, vol. 70:1–20.

Roeber, V., Cheung, K., and Kobayashi, M. (2010). Shock-capturing boussinesq-type model for nearshore wave processes. *Coastal Engineering*, vol. 57:407–423.

Ruessink, B. G., Kleinhans, M. G., and van den Beukel, P. G. L. (1998). Observations of swash under highly dissipative conditions. *Journal of Geophysical Research: Oceans*, 103(C2):3111–3118.

Ruessink, B. G., Michallet, H., Bonneton, P., Mouazé, D., Lara, J. L., Silva, P. A., and Wellens, P. (2013a). Globex: wave dynamics on a gently sloping laboratory beach. In *7th International Conference on Coastal Dynamics*, pages 1351 – 1362, Arcachon, France.

Ruessink, G., Michallet, H., Bonneton, P., Mouazé, D., Lara, J., Silva, P., and Wellens, P. (2013b). Globex: wave dynamics on a gently sloping laboratory beach. In *7th International Conference on Coastal Dynamics*, Arcachon, France.

Ruggiero, P., Holman, R. A., and Beach, R. A. (2004). Wave run-up on a high-energy dissipative beach. *Journal of Geophysical Research: Oceans*, 109(C6).

Ruggiero, P., Komar, P., McDougal, W., Marra, J., and Beach, R. (2001). Wave runup, extreme water levels and the erosion of properties backing beaches. *Journal of Coastal Research*, 17(2):407–419.

Ruju, A., Lara, J., and Losada, I. (2014). Numerical analysis of run-up oscillations under dissipative conditions. *Coastal engineering*, vol. 86.

Ruju, A., Lara, J. L., and Losada, I. J. (2012). Radiation stress and low-frequency energy balance within the surf zone: A numerical approach. *Coastal Engineering*, 68:44–55.

Rutten, J., Torres-Freyermuth, A., and Puleo, J. (2021). Uncertainty in runup predictions on natural beaches using xbeach nonhydrostatic. *Coastal Engineering*, 166:103869.

Scott, T., Austin, M., Masselink, G., and Russell, P. (2016). Dynamics of rip currents associated with groynes — field measurements, modelling and implications for beach safety. *Coastal Engineering*, 107:53–69.

Scott, T., Masselink, G., and Russell, P. (2011). Morphodynamic characteristics and classification of beaches in england and wales. *Marine Geology*, 286(1):1–20.

Senechal, N., Coco, G., Bryan, K. R., and Holman, R. A. (2011). Wave runup during extreme storm conditions. *Journal of Geophysical Research: Oceans*, 116(C7).

Senechal, N., Coco, G., Plant, N., Bryan, K. R., Brown, J., and MacMahan, J. H. M. (2018). Field observations of alongshore runup variability under dissipative conditions in the presence of a shoreline sandwave. *Journal of Geophysical Research: Oceans*, 123(9):6800–6817.

Serafin, K. A. and Ruggiero, P. (2014). Simulating extreme total water levels using a time-dependent, extreme value approach. *Journal of Geophysical Research: Oceans*, 119(9):6305–6329.

Seto, K. C., Fragkias, M., Güneralp, B., and Reilly, M. K. (2011). A meta-analysis of global urban land expansion. *PLOS ONE*, 6(8):1–9.

Sheremet, A., Guza, R. T., Elgar, S., and Herbers, T. H. C. (2002). Observations of nearshore infragravity waves: Seaward and shoreward propagating components. *Journal of Geophysical Research: Oceans*, 107(C8):10–1–10–10.

Shi, F., Kirby, J. T., Harris, J. C., Geiman, J. D., and Grilli, S. T. (2012). A high-order adaptive time-stepping tvd solver for boussinesq modeling of breaking waves and coastal inundation. *Ocean Modelling*, 43-44:36–51.

Short, A. D. (2006). Australian beach systems—nature and distribution. In *Journal of Coastal Research*.

Stockdon, H., Thompson, D., Plant, N., and Long, J. (2014). Evaluation of wave runup predictions from numerical and parametric models. *Coastal Engineering*, 92:1–11.

Stockdon, H. F., Holman, R. A., Howd, P. A., and Sallenger, A. H. (2006). Empirical parameterization of setup, swash, and runup. *Coastal Engineering*, 53(7):573–588.

Stocker, T., Qin, D., Plattner, G.-K., Alexander, L., Allen, S., Bindoff, N., Bréon, F.-M., Church, J., Cubasch, U., Emori, S., Forster, P., Friedlingstein, P., Gillett, N., Gregory, J., Hartmann, D., Jansen, E., Kirtman, B., Knutti, R., Kumar, K. K., Lemke, P., Marotzke, J., Masson-Delmotte, V., Meehl, G., Mokhov, I., Piao, S., Ramaswamy, V., Randall, D., Rhein, M., Rojas, M., Sabine, C., Shindell, D., Talley, L., Vaughan, D., and Xie, S.-P. (2013). Climate change 2013. the physical science basis. working group I contribution to the fifth assessment report of the intergovernmental panel on climate change-abstract for decision-makers (IPCC).

Symonds, G., Huntley, D. A., Anthony, and Bowen, J. (1982). Two-dimensional surf beat: Long wave generation by a time-varying breakpoint. *J. Geophysical Research*.

Sénéchal, N., Dupuis, H., Bonneton, P., Howa, H., and Pedreros, R. (2001). Observation of irregular wave transformation in the surf zone over a gently sloping sandy beach on the french atlantic coastline. *Oceanologica Acta*, 24(6):545–556.

Sørensen, O. R., Schäffer, H. A., and Sørensen, L. S. (2004). Boussinesq-type modelling using an unstructured finite element technique. *Coastal Engineering*, 50(4):181–198.

Taborda, R. and Silva, A. (2012). Cosmos: A lightweight coastal video monitoring system. *Computers & Geosciences*, 49:248–255.

Thotagamuwage, D. and Pattiaratchi, C. (2014). Observations of infragravity period oscillations in a small marina. *Ocean Engineering*, 88:435–445.

Trenhaile, A. and Trenhaile, D. (1987). *The Geomorphology of Rock Coasts*. Oxford research studies in geography. Clarendon Press.

Tsai, C.-H., Huang, M.-C., Young, F.-J., Lin, Y.-C., and Li, H.-W. (2005). On the recovery of surface wave by pressure transfer function. *Ocean Engineering*, 32(10):1247–1259.

Turner, I. L., Whyte, D., Ruessink, B., and Ranasinghe, R. (2007). Observations of rip spacing, persistence and mobility at a long, straight coastline. *Marine Geology*, 236(3):209–221.

UNGA (2016). Report of the open-ended intergovernmental expert working group on indicators and terminology relating to disaster risk reduction : note /. page 41 p.

Valentini, N., Saponieri, A., Danisi, A., Pratola, L., and Damiani, L. (2019). Exploiting remote imagery in an embayed sandy beach for the validation of a runup model framework. *Estuarine, Coastal and Shelf Science*, 225:106244.

van Dongeren, A., Battjes, J., Janssen, T., Noorloos, J., Steenhauer, K., Steenbergen, G., and Reniers, A. (2007). Shoaling and shoreline dissipation of low-frequency waves. *Journal of Geophysical Research, 112, 2007 ; doi:10.1029/2006JC003701*, 112.

Van Dongeren, A., Lowe, R., Pomeroy, A., Trang, D. M., Roelvink, D., Symonds, G., and Ranasinghe, R. (2013). Numerical modeling of low-frequency wave dynamics over a fringing coral reef. *Coastal Engineering*, 73:178–190.

Varing, A., Filipot, J.-F., Delpey, M., Guitton, G., Collard, F., Platzer, P., Roeber, V., and Morichon, D. (2020). Spatial distribution of wave energy over complex coastal bathymetries: development of methodologies for comparing modeled wave fields with satellite observations. *Coastal Engineering*, page 103793.

Varing, A., Filipot, J.-F., Grilli, S., Duarte, R., Roeber, V., and Yates, M. (2021). A new definition of the kinematic breaking onset criterion validated with solitary and quasi-regular waves in shallow water. *Coastal Engineering*, 164:103755.

Vitousek, S., Barnard, P., Fletcher, C., Frazer, N., Erikson, L., and Storlazzi, C. (2017). Doubling of coastal flooding frequency within decades due to sea-level rise. *Scientific Reports*, 7.

Vousdoukas, M., Ferreira, P., Almeida, L. P., Dodet, G., Psaros, F., Andriolo, U., Taborda, R., Silva, A., Ruano, A., and Ferreira, O. (2011). Performance of intertidal topography video monitoring of a meso-tidal reflective beach in south portugal. *Ocean Dynamics*, 61:1521–1540.

Vousdoukas, M., Velegrakis, A., Dimou, K., Zervakis, V., and Conley, D. (2009). Wave run-up observations in microtidal, sediment-starved pocket beaches of the eastern mediterranean. *Journal of Marine Systems*, 78:S37–S47. Coastal Processes: Challenges for Monitoring and Prediction.

Vousdoukas, M., Wziatek, D., and Almeida, L. (2012). Coastal vulnerability assessment based on video wave run-up observations at a mesotidal, steep-sloped beach. *Ocean Dynamics*, 62:123–137.

Waddell, E. (1980). Wave forcing of beach groundwater. *Coastal Engineering*, pages 1436–1452.

Walkley, M. and Berzins, M. (2002). A finite element method for the two-dimensional extended boussinesq equations. *International Journal for Numerical Methods in Fluids*, 39(10):865–885.

Wei, G., Kirby, J. T., Grilli, S. T., and Subramanya, R. (1995). A fully nonlinear boussinesq model for surface waves. part 1. highly nonlinear unsteady waves. *Journal of Fluid Mechanics*, 294:71–92.

Welch, P. (1967). The use of fast fourier transform for the estimation of power spectra: A method based on time averaging over short, modified periodograms. *IEEE Transactions on Audio and Electroacoustics*, 15(2):70–73.

Whalin, R. W. (1971). The limit of applicability of linear wave refraction theory in a convergence zone. *Research report H-71-3, U.S. Army Corps of Engineers.*

Wright, L. and Short, A. (1984). Morphodynamic variability of surf zones and beaches: A synthesis. *Marine Geology*, 56(1):93–118.

Zijlema, M., Stelling, G., and Smit, P. (2011). Swash: An operational public domain code for simulating wave fields and rapidly varied flows in coastal waters. *Coastal Engineering*, 58:992 – 1012.

Appendix A

Analysis of infragravity waves

The analysis of low frequency motions such as IG waves requires the use of dedicated analytical tools. In this section the tools used throughout the study (mainly in section 4.5) are detailed.

A.1 Short-waves envelope

Nearshore IG waves are frequently investigated using cross-correlation between the SW envelope $\tilde{\eta(t)}$, representing the wave groups, and the IG waves $\eta_{IG}(t)$ (List, 1991, 1992, Janssen et al., 2003, Ruju et al., 2012, Matsuba et al., 2021b).

The SW envelope $\tilde{\eta}(t)$ is calculated here following the method of List (1991) :

$$\tilde{\eta}(t) = \frac{\pi}{2}|\eta_{SW}(t)|_{IG} \tag{A.1}$$

where the subscripts SW and IG denote successive high and low pass filtering, and $||$ represents absolute value. The filtering are performed using a cut-off frequency of $f_c = 0.05Hz$, consistently with the definition of the IG waves chosen in this study. An example of a wave signal along with the SW envelope $\tilde{\eta}(t)$ is given on figure A.1.

A.2 Separation between incident and reflected waves and reflection coefficient

If the IG waves are not dissipated they can be reflected at the shoreline. The IG wave signal recorded at one location is therefore the sum of the incoming and reflected IG waves. To separate the incoming from the reflected wave signal the methodology used here is the one described by Sheremet et al. (2002). Assuming that the IG waves are shore-normal propagating shallow water waves, the energy and cross-shore energy fluxes are estimated from collocated

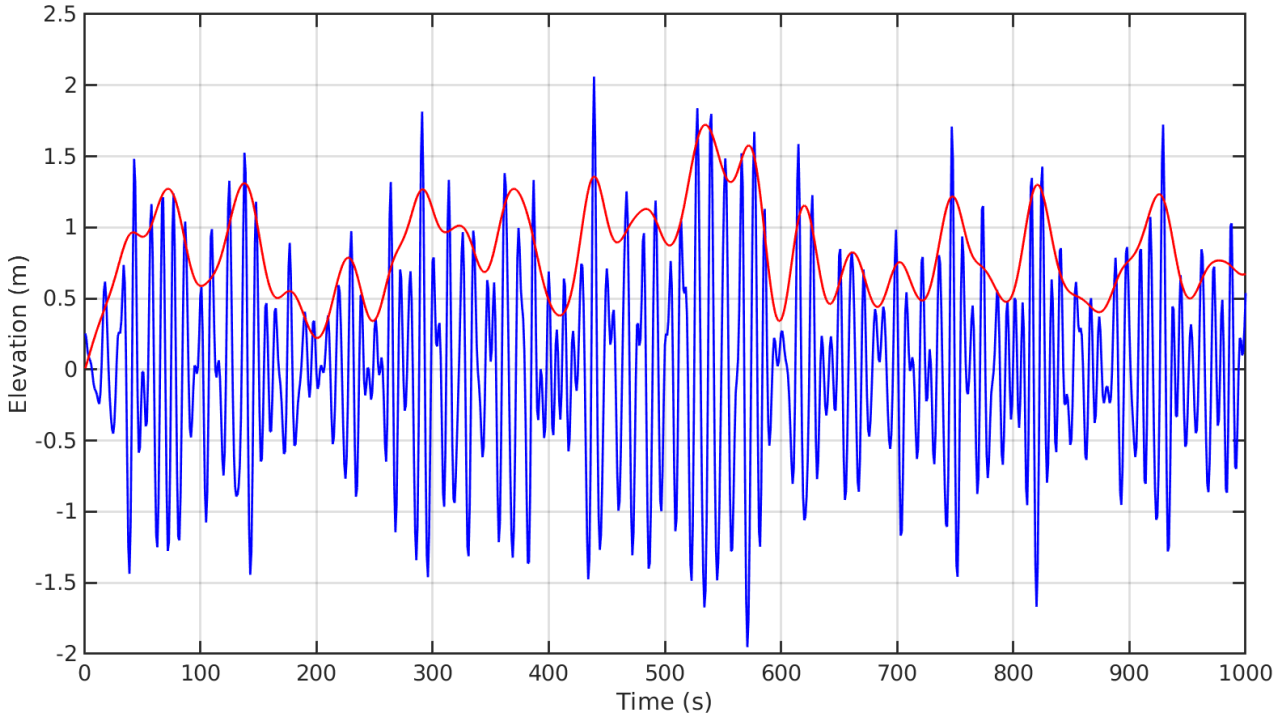

Figure A.1: Free surface elevation $\eta(t)$ (blue) and associated envelope $\tilde{\eta}(t)$ (red) time series calculated as in A.1.

pressure (or free surface elevation) and horizontal velocity measurements as :

$$E^{\pm}(f) = \frac{1}{4}\left[Co_{\eta\eta}(f) + \frac{h}{g}Co_{uu}(f) \pm \left(2\sqrt{\frac{h}{g}}Co_{\eta u}(f)\right)\right] \tag{A.2}$$

$$F^{\pm}(f) = E^{\pm}(f)\sqrt{gh} \tag{A.3}$$

where $Co_{\eta\eta}$ and Co_{uu} are the autospectra of the free surface elevation η and the horizontal velocity u respectively and $Co_{\eta u}$ is the $\eta - u$ cospectrum.

The frequency-dependant reflection coefficient $R(f)$, characterizing which amount of energy is being reflected at the shoreline, can be estimated as :

$$R(f) = \sqrt{\frac{E^{-}}{E^{+}}} \tag{A.4}$$

Incident and reflected wave heights were calculated using eq. 2.6a and eq. 2.6b using $E^{\pm}(f)$ instead of $E(f)$.

Bulk reflection coefficient R^2, which consists in the reflection coefficient integrated over a frequency band (Sheremet et al., 2002), is calculated as :

$$R^2 = \frac{\int_{f_1}^{f_2} E^{-}(f)\,df}{\int_{f_1}^{f_2} E^{+}(f)\,df} \tag{A.5}$$

where f_1 and f_2 are the bounds of the frequency range considered.

A.3 Travel time of reflected waves and natural frequencies

Possible reflection at the shoreline is often highlighted through cross-correlation as a lag corresponding to the travel time to the shoreline back and forth of the IG wave. The predicted travel round-trip time of long waves from a cross-shore location is calculated as in Ruju et al. (2012) :

$$\tau(x_0) = \int_{x_0}^{shore} \left(\frac{1}{C_g(x)} + \frac{1}{C(x)} \right) dx \tag{A.6}$$

where C_g and C respectively represent group and phase velocities and x_0 is the cross-shore position considered. This translates that waves are first considered group waves when traveling towards the shore at therefore the group velocity, but are then free reflected waves and the velocity considered becomes the phase celerity. Assuming that the IG waves travel at the shallow water celerity (Matsuba et al., 2021b), it yields :

$$\tau(x_0) = 2 \int_{x_0}^{shore} \frac{dx}{\sqrt{gh(x)}} \tag{A.7}$$

where $h(x)$ is the local depth.

At each cross-shore location x_0, an anti-node is generated if the incident and reflected wave crests are superimposed. It imposes that the round-trip time τ from this location up to the shoreline equals integer multiples of the wave period $1/f$. The corresponding natural frequencies are therefore calculated as :

$$f_n(x_0) = n/\tau(x_0) = n \frac{1}{2 \int_{x_0}^{shore} \frac{dx}{\sqrt{gh(x)}}}, n = 1, 2, 3, 4... \tag{A.8}$$

$n = 1$ corresponding to the fundamental frequency and $n = 2, 3, 4$ being respectively the 2^{nd}, 3^{rd} and 4^{th} harmonics (or modes).

Appendix B

Photogrammetry

B.1 Geo-referencing of oblique video data

Let O be the object to capture and I its projected image in the image plan. N is the projection center, the point in which all the projections meet. The definition of the variables is shown on figure 2.8. The coordinates of O and I are respectively $(x, y, z)_O$ and $(u, v)_I$. The subscript O and I respectively denotes the object-space and image-plan reference frame. The projection center N is positioned as $(x_c, y_c, z_c)_O$. The projection of N onto the image plan is denoted P (the principal point) and has for coordinates $(u_0, v_0, 0)$. Therefore, the coordinates of N in the image-plan reference frame can be expressed as $(u_0, v_0, f)_I$, where f is the focal distance of the camera. Points O,I and N are collinear. This collinearity condition is at the basis of the DLT method. It can be mathematically written as :

$$\mathbf{B} = c\mathbf{A} \tag{B.1}$$

where $\mathbf{B} = \vec{NI}$,$\mathbf{A} = \vec{NO}$ and c is a scalar. As $\mathbf{B} = \begin{pmatrix} u - u_0 \\ v - v_0 \\ -f \end{pmatrix}_I$ and $\mathbf{A} = \begin{pmatrix} x - x_c \\ y - x_c \\ z - z_c \end{pmatrix}_O$, $\mathbf{A}$ must be expressed in the same reference frame as $\mathbf{B}$:

$$\mathbf{A_I} = \mathbf{T_{I/O}}\mathbf{A_O} \tag{B.2}$$

where $\mathbf{T_{I/O}}$ is the transformation matrix from the object-space to the image-plan reference frame.

$$\mathbf{T_{I/O}} = \begin{pmatrix} r_{11} & r_{12} & r_{13} \\ r_{21} & r_{22} & r_{23} \\ r_{31} & r_{32} & r_{33} \end{pmatrix} \tag{B.3}$$

It yields :

$$\begin{pmatrix} u-u_0 \\ v-v_0 \\ -f \end{pmatrix} = c \begin{pmatrix} r_{11} & r_{12} & r_{13} \\ r_{21} & r_{22} & r_{23} \\ r_{31} & r_{32} & r_{33} \end{pmatrix} \begin{pmatrix} x-x_c \\ y-y_c \\ z-z_c \end{pmatrix} \tag{B.4}$$

Using the 3rd equation from eq. B.4, the scalar c is isolated and from equations 1 and 2 of eq. B.4 it yields :

$$\begin{aligned} u-u_0 &= -f\frac{r_{11}(x-x_c)+r_{12}(y-y_c)+r_{13}(z-z_c)}{r_{31}(x-x_c)+r_{32}(y-y_c)+r_{33}(z-z_c)} \\ v-v_0 &= -f\frac{r_{21}(x-x_c)+r_{22}(y-y_c)+r_{23}(z-z_c)}{r_{31}(x-x_c)+r_{32}(y-y_c)+r_{33}(z-z_c)} \end{aligned} \tag{B.5}$$

After reorganizing and isolating the object coordinates in the image-plan frame (u, v), the system is expressed as equation 2.1, where the coefficients L_i are defined as :

$$\begin{aligned} L &= -(x_c r_{31} + y_c r_{32} + z_c r_{33}) \\ L_1 &= \frac{(u_0 r_{31} + f r_{11})}{\lambda_u L} \\ L_2 &= \frac{(u_0 r_{32} + f r_{12})}{\lambda_u L} \\ L_3 &= \frac{(u_0 r_{33} + f r_{13})}{\lambda_u L} \\ L_4 &= -(L_1 x_c + L_2 y_c + L_3 z_c) \\ L_5 &= \frac{(v_0 r_{31} + f r_{21})}{\lambda_v L} \\ L_6 &= \frac{(v_0 r_{32} + f r_{22})}{\lambda_v L} \\ L_7 &= \frac{(v_0 r_{33} + f r_{23})}{\lambda_v L} \\ L_8 &= -(L_5 x_c + L_6 y_c + L_7 z_c) \\ L_9 &= \frac{r_{31}}{L} \\ L_10 &= \frac{r_{32}}{L} \\ L_11 &= \frac{r_{33}}{L} \end{aligned} \tag{B.6}$$

where λ_u and λ_v are respectively the horizontal and vertical scale factors. The r_{ii} coefficients are the successive camera rotations :

$$
\begin{aligned}
r_{11} &= \cos(\phi)\cos(\sigma) + \sin(\phi)\cos(\tau)\sin(\sigma) \\
r_{12} &= -\sin(\phi)\cos(\sigma) + \cos(\phi)\cos(\tau)\sin(\sigma) \\
r_{13} &= \sin(\tau)\sin(\sigma) \\
r_{21} &= -\cos(\phi)\sin(\sigma) + \sin(\phi)\cos(\tau)\cos(\sigma) \\
r_{22} &= \sin(\phi)\sin(\sigma) + \cos(\phi)\cos(\tau)\cos(\sigma) \\
r_{23} &= \sin(\tau)\cos(\sigma) \\
r_{31} &= \sin(\phi)\sin(\tau) \\
r_{32} &= \cos(\phi)\sin(\tau) \\
r_{33} &= -\cos(\tau)
\end{aligned}
\tag{B.7}
$$

where the different angles are defined according to figure B.1.

Figure B.1: Definition of the camera angles.

B.2 Intrinsic parameters

Due to the spherical shape of the lenses, most cameras impose a certain amount of distortion of the image and thus require rectification (known as inverse distortion) before applying the geo-rectification from eq. 2.1. The decentering distortion is composed of a radial and tangential components which are commonly called *intrinsic* parameters. Indeed,as opposed to extrinsic parameters which depend on the camera set-up (such as (ϕ, σ, τ) for example), the intrinsic parameters only depend on the camera and are determined in a laboratory using several images of a checkerboard at various angles for example. The distorted image can be corrected using the Brown-Conrady distorsion model (Conrady, 1919) :

$$u_u = u_d + (u_d - u_c)(K_1 r^2 + K_2^2 R^4) + P_1(r^2 + 2(u_d - u_c)^2) + 2P_2(u_d - u_c)(v_d - v_c) \tag{B.8}$$

$$v_u = v_d + (v_d - v_c)(K_1 r^2 + K_2 r^4) + 2P_1(u_d - u_c)(v_d - v_c) + P2(r^2 + 2(v_d - v_c)^2 \tag{B.9}$$

where (u_d, v_d) is the distorted image due to the actual lens, (u_u, u_u) is the undistorted image as projected by an ideal pinhole camera, (u_c, v_c) is the distortion center, K_n (P_n) is the n^{th} radial (tangential) distortion coefficient and $r = \sqrt{(u_d - u_c)^2 + (v_d - v_c)^2}$ represents the distance between the distorted image point and the distortion center. In fact, the distortion center is

the same point as the principal point P as defined on figure 2.8, i.e. $(u_c, u_v) = (u_0, v_0)$. The laboratory calibration performed prior to the field campaign yields values for the camera model parameters (K_n, P_n, (u_0, v_0),λ_u,λ_v), reducing the number of unknowns in the DLT parameters from eq. B.6 to 7 (τ,ϕ,σ,f,x_c,y_c,z_c). Each GCP bringing two new equations a minimum of 4 points are needed to solve the system. Holland et al. (1997) described a method to lower the number of unknowns to 4 by constraining the camera position (x_c, y_c, z_c), yielding a minimum number of GPCs of two.

Appendix C

Numerical study of longshore variability in run-up along an idealized embayed beach. *Proceedings from the Journées Nationales de Génie Civil - Génie Côtier (JNGCGC) 2020 (Le Havre, France)*

XVI[èmes] Journées Nationales Génie Côtier – Génie Civil
Le Havre, 2020
DOI:10.5150/jngcgc.2020.016 *© Editions Paralia CFL*
disponible en ligne – http://www.paralia.fr – available online

Numerical study of longshore variability in run-up along an idealized embayed beach

Jonas PINAULT [1], Denis MORICHON [1], Stéphane ABADIE [1], Volker ROEBER [1]

1. Université de Pau et des Pays de l'Adour, E2S UPPA, SIAME, Chaire HPC-Waves, Anglet, France.
jonas.pinault@univ-pau.fr ; denis.morichon@univ-pau.fr ; stephane.abadie@univ-pau.fr ; volker.roeber@univ-pau.fr

Abstract:
It is of common knowledge that energetic swell events bare the potential of threatening people and infrastructure in densely inhabited coastal regions. Parametric formulations, based on various data-sets, have been commonly employed to easily estimate wave run-up based on offshore conditions and beach parameters. These formulations are however mostly based on open beaches data-sets and their accuracy in complex 3D configuration such as an embayed beach is thus questionable.
In this numerical study, a phase-resolving Boussinesq-type model is used to investigate the longshore distribution of wave run-up in an idealized embayed beach from an oblique wave approach in order to isolate the sole effects of the geologically constrained configuration. The numerical model accounts for all major physical processes including refraction, diffraction, reflection, shoaling, breaking. Different scenarios are considered from moderately to extremely energetic incident wave conditions and bay orientations.
The run-up is found to vary significantly alongshore for the majority of the tested scenarios (run-up elevation can vary by a factor 3). A spectral analysis of the water levels shows that this variability is tightly connected to the infragravity waves (0.002 to 0.04 Hz). The relative contribution of those long waves to the total run-up varies along the beach displaying hotspots where wave energy focuses leading to highest run-up values. Those results, obtained for an idealized embayed beach, suggest to further investigation on the role of infragravity waves including the processes of nearshore wave transformation in more realistic embayement conditions in order to improve flooding risk assessment in this particular type of beach.
Keywords: Embayed beach, Run-up, Infragravity waves, Boussinesq-type model, Longshore variability.

1. Introduction

The total water elevation at the coast is composed of two components: the tide (astronomical and meteorological) and the incident waves - namely the run-up. Usually, wave run-up is divided into a static component, the wave set-up, and a dynamic component, the swash (HOLMAN & SALLENGER, 1986). The swash, as a time varying

component, can be subdivided into two frequency bands: the incident or short-wave band (usually from 0.04 to 0.25 Hz) and a lower frequency band (from 0.002 to 0.04 Hz) referring to the infragravity band (IG). The contributions of the spectral swash components mostly depend on the beach state (RUESSINK *et al*., 1998; RUGGIERO *et al.*, 2004; STOCKDON *et al*., 2006), given by the Iribarren number ξ (BATTJES, 1974). Infragravity dominated run-up is usually found under dissipative conditions (ξ<0.3) and incident dominated run-up under reflective conditions (ξ>1.25). The run-up has been extensively studied in the past decades. Field studies have focused on the relationships between run-up values, beach characteristics and offshore bulk wave parameters (HOLMAN, 1986; STOCKDON *et al*., 2006; ...). They were mostly conducted on open beaches and during low to mild energetic conditions. Their application to extreme events and beaches with complex geometries (embayed beaches, rocks, coastal structures…) is thus questionable. Several studies have highlighted these limitations (STOCKDON *et al*., 2014; POWER *et al*., 2013; ...).

Despite their common presence around the world, embayed (natural or artificial) beaches are still considered complex environments. They are constrained by headlands, and the hydrodynamics and morphological processes within the bay differ from the open beaches depending on the degree of embaymentisation (FELLOWES et al., 2019). Numerous studies were carried out to better understand the behaviors of these complex environments (CASTELLE & COCO, 2012; LOUREIRO *et al*., 2012) but have mostly focused on sediment transport or morphodynamics. The combined effects of refraction-diffraction processes in the lee of headlands have been intensively studied (GODA *et al.,* 1978) to describe wave heights distribution in embayed beaches but less is known about their effects on wave run-up at the coast.

Considering different storm scenarios and a highly idealized embayed beach configuration, this numerical study, based on a Boussinesq-type model, investigates the relative contribution of the incident and infragravity waves on the run-up intensity and variability.

2. Methodology

2.1 Bathymetry

An idealized bathymetry, comprising a sloping beach constrained between 2 headlands, is used in this study to assess the influence of a semi-enclosed basin on the longshore run-up distribution.

The beach cross-shore profile is based on a beach equilibrium profile (DEAN, 1991) given by $z=A(D_{50})x^{2/3}$, where A is the sediment scale parameter depending on D_{50}, the median grain diameter (taken equal to 0.3 mm in our study). It is completed with an 8% slope above the mean sea level, as the beach state considered is intermediate-reflective.

Furthermore, the beach is constrained between two headlands and isobaths within the bay are assumed to be curved (see figure 1).
The degree of embaymentisation (related to the length of the headlands compared to the width of the beach) is the main geological feature controlling the hydrodynamics and morphological processes. The embayment morphometric parameter for this study (FELLOWES *et al*., 2019) is chosen as 1 (length of the headlands being equal to the width of the beach) as it represents an embayed beach with high coastal indentation, and thus exhibiting different behaviors than open beaches. This idealized beach is 1km long and the headlands extend to 1km offshore from the shoreline. Mean sea level is fixed at 0m.

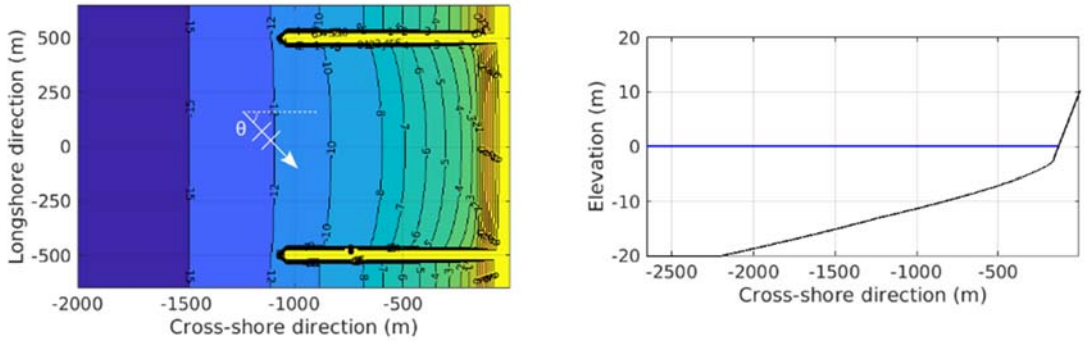

Figure 1. Contour lines of the bathymetry (area of interest) exposed to waves with an angle of incidence θ (left) and cross-shore transect in the middle of the embayed beach (right). The incident swell direction varies between 0 ˚and 30 ˚.

2.2 Wave conditions

Three different wave conditions are chosen to represent moderate, high, and very energetic swell conditions. Three swell directions are selected to study the influence of the propagation direction of the swell in relation to the orientation of the entrance of the idealized bay. All the scenarios are listed in table 1.

Table 1. Forcing conditions.

Event	*Case*	*H_s (m)*	*T_p (s)*	*Direction (°)*
Moderate	*1;4;7*	*2*	*12*	*0;15;30*
High	*2;5;8*	*3*	*15*	*0;15;30*
Stormy	*3;6;9*	*6*	*18*	*0;15;30*

A TMA wave spectrum is used to represent the nearshore incident wave conditions at the offshore boundary (depth = 20 m).

3160

2.3 Numerical model

The phase-resolving Boussinesq-type model BOSZ (ROEBER *et al.*, 2010; ROEBER & CHEUNG, 2012a) is used in this study. The model is based on the set of Boussinesq equations by NWOGU (1993) expressed in conservative form. Phases are randomly assigned to the different frequencies. This weakly non-linear and weakly dispersive model inherently accounts for relevant physical processes in coastal zones including refraction, diffraction, reflection, shoaling, dissipation and breaking. In addition, it allows to simulate the generation and transformation of IG waves, which have been shown to contribute to the run-up (STOCKDON *et al*., 2006). The model has been validated for the relevant processes in different benchmarks (HORRILLO *et al*. 2014; LYNETT *et al*. 2017; ROEBER & CHEUNG, 2012b).

The inside of the bay is 1x1 km and the whole computational domain extends 2.5km offshore and from 1 to 3km on the sides. The resolution is 5m in the longshore direction and 2.5 m in the cross-shore direction. The computation is carried out for one hour including a ramp up time of 15 minutes. The incident wave regime is kept constant during each run. The free surface is recorded at 2 Hz.

2.4 Post processing

The run-up time series is extracted at each longshore location by detecting the water elevation in the furthest wet cell with a threshold depth of 10 cm (STOCKDON *et al*. 2014).

Wave set-up $<\eta>$ is calculated as the time-averaged water-level elevation at the shoreline. The swash is obtained after subtracting the set-up from the run-up time series. The run-up 2% exceedance value is computed considering the cumulative distribution and its 98^{th} percentile (STOCKDON *et al*., 2006).

The 45 minutes long signal is separated into segments of 2048 points and is analyzed using a Hanning window with 50% overlapping. The significant swash height is calculated computing the power spectral density, PSD(f):

$$S = \sqrt{\sum PSD}(f)df \qquad (1)$$

The cut-off period chosen for the separation of the IG and incident band is 2Tp (SHEREMET *et al*., 2011). In literature the cut-off frequency is often given as 0.04 Hz but given the variability of Tp in the wave conditions a moving cut-off frequency gives a better representation of the infragravity band.

The significant swash height for the incident and the IG bands are computed by using eq. (1) within their specific ranges.

3. Results

3.1 Variability of $R_{2\%}$

To first assess the magnitude of the run-up variability, $R_{2\%}$ along the beach is computed for different incident wave conditions. The results are presented in table 2, where the coefficient of variation (CV) is calculated from the standard deviation (std) divided by the mean.

The analysis of std and CV values of $R_{2\%}$ shows that significant variations are found along the beach, the variability increasing with the wave field obliquity. For the most energetic scenarios (cases 3,6,9) the std ranges from 0.26 m to 0.62 m up to 0.87 m. An increase of more than 500% between the lowest and the highest longshore value of $R_{2\%}$ is observed in case 7 (moderate climate and 30° of incidence). For the most energetic case under the highest incidence (case 9), an increase of 212% is noted.

Due to the shadowing of the headlands, which reduces the area exposed to direct swell, the mean longshore $R_{2\%}$ is smaller in the cases of oblique wave fields regardless of the level of incident energy. For example, mean $R_{2\%}$ goes down from 3.89 m to 3.59 m for the stormy case. However, the highest $R_{2\%}$ values occur for oblique conditions. Indeed, the highest $R_{2\%}$ among all the runs is obtained for a 30° incident peak wave angle. It illustrates the fact that despite being partially sheltered by the headlands (reduction of the mean longshore value) under oblique conditions, the run-up is unevenly distributed, leading to the generation of hotspots where the energy is focused with subsequently higher run-up values.

Table 2. Longshore statistics of $R_{2\%}$ for the different incident wave conditions. Min, mean, max, std respectively refer to minimum, longshore mean and maximum value of $R_{2\%}$ (m), CV the coefficient of variation and min/max the ratio of the maximum over the minimum longshore value.

Angle	*Case*	*$R_{2\%}$*					
		min	*mean*	*max*	*std*	*CV*	*max/min*
0°	*1*	*1,12*	*1,36*	*1,45*	*0,08*	*5,95%*	*1,3*
	2	*1,88*	*2,2*	*2,39*	*0,13*	*5,95%*	*1,27*
	3	*3,41*	*3,89*	*4,17*	*0,26*	*6,60%*	*1,22*
15°	*4*	*0,69*	*1,24*	*1,58*	*0,24*	*19,39%*	*2,31*
	5	*1,45*	*2,14*	*2,68*	*0,33*	*15,29%*	*1,85*
	6	*2,95*	*3,84*	*4,8*	*0,62*	*27,57%*	*2,94*
30°	*7*	*0,31*	*1,08*	*1,73*	*0,35*	*32,09%*	*5,61*
	8	*0,87*	*1,82*	*2,84*	*0,5*	*27,57%*	*2,94*
	9	*2,49*	*3,59*	*5,29*	*0,87*	*24,34%*	*2,12*

3.2 Analysis of run-up components

Water motion close to the shore is controlled by both the short incident waves and IG waves (0.005-0.04 Hz). In the following, a spectral analysis of the computed swash signal is performed for each scenario to estimate the contribution of each frequency band to the water level variations.

The longshore anomaly (calculated as the difference between the local value and the mean longshore value) of the different run-up components is illustrated on figure 2 in order to understand how the uneven distribution is generated.

The comparison of the anomaly of total $R_{2\%}$ (top panel) with the anomalies of the incident (middle panel) and IG bands (lower panel) shows that the anomaly in the run-up is strongly related to the distribution of the IG swash. Indeed, the same trend and the same orders of magnitude (more than 1.5 m for the most energetic case) are observed. On the contrary, the incident band shows very little deviation, with a maximum anomaly of less than 0.5 m.

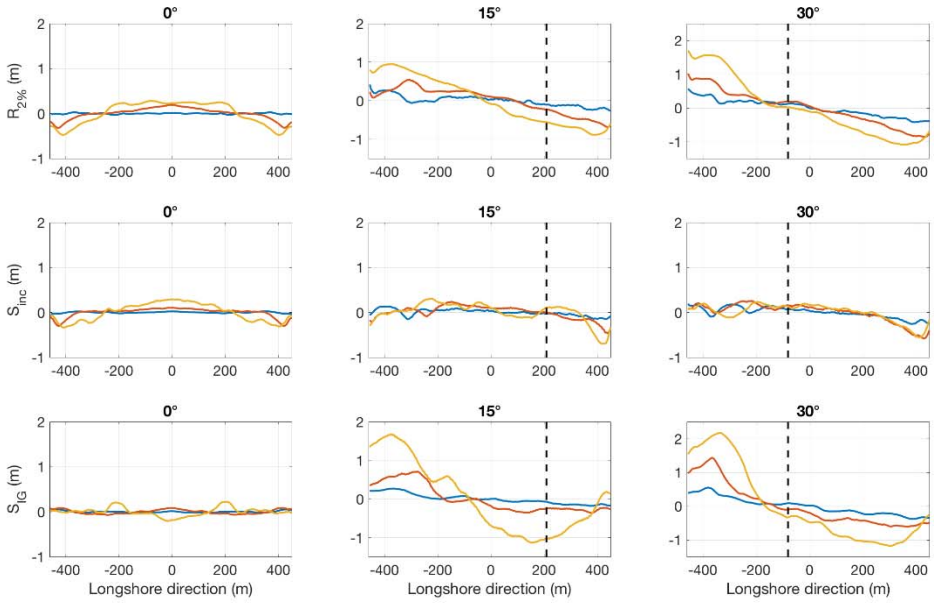

Figure 2. Longshore anomalies (difference between the local value and the mean longshore value) of $R_{2\%}$, the significant swash height IG S_{ig} and incident S_{inc}. Curve color: blue: moderate, red: high, yellow: storm, black dashed line: geometric shadow.

Figure 2 confirms that the wave angle induces a substantial anomaly in the run-up distribution. For the most energetic case, the anomaly can be well over 1 meter. As expected, in the shadow zone (right side of the black dashed lines), sheltered from the incident waves by the headland, the run-up anomaly is negative, meaning the values in this area are smaller than the mean value. Outside the shadow zone the run-up gradually

increases to a point of locally high values, in the area exposed to direct swell, close to the opposed headland. It appears that the headland plays a crucial role in focusing the energy leading to a high run-up.

3.3 Contributions of incident and infragravity bands

Figure 3 shows the distribution of the ratio S_{ig}/S_{inc} along the beach. For all wave conditions in the case of a normal incident swell the swash motions are IG dominated (S_{ig}/S_{inc} >1). For the most energetic conditions, the IG domination is stronger than for the two other cases, which is expected as the conditions are more dissipative. When the swell is approaching the embayed beach with an angle, the contributions of incident and IG-waves vary along the beach, meaning that the energy is redistributed spatially and also in the frequency domain. In the exposed zone, a clear increase of the IG energy is noticeable. The swash motions in all cases become strongly IG-dominated, with values of S_{ig}/S_{inc} higher than 1.5. This means that during a single event, sections of the beach can behave as dissipative, intermediate or reflective.

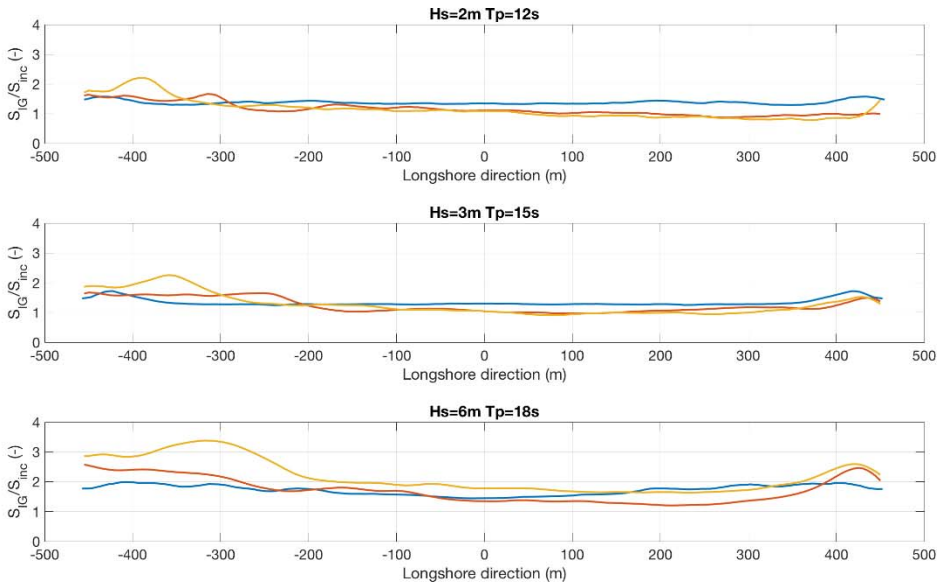

Figure 3. Longshore evolution of the ratio S_{ig} over S_{inc} for the different conditions. Curve color: blue: 0°, red: 15°, yellow: 30°.

Usually the beach state is given globally for a beach depending on the foreshore slope and offshore conditions (Iribarren number). However, in this configuration a different parametrization should be used to accurately define the beach state.

The different processes (diffraction, reflection) could contribute to the uneven longshore

distribution of the wave height and therefore impact the wave breaking. As a primary mechanism of energy dissipation and transfer, the distribution of the wave breaking is closely related to the one of the run-up and needs to be further investigated.

4. Conclusions

In this study, the variability of the run-up along an idealized simplified embayed beach was addressed based on the results of a phase-resolving model for different incident wave conditions and bay orientation. The results show that the run-up can vary significantly along this idealized beach, with alongshore hotspots where run-up values can be amplified by a factor of over 1.5 compared to the mean longshore value. As expected, under oblique incident wave conditions the mean longshore $R_{2\%}$ values are smaller due to increasing sheltering effect of the headlands, however this is also when the highest values of $R_{2\%}$ are observed. This study also highlights that the longshore variability of the run-up is essentially controlled by the variability of energy in the IG band. This result suggests that the consideration of IG waves might be critical to correctly address run-up characteristics in an embayed beach including their uneven contribution along the beach, which can vary according to incident wave conditions. This should be confirmed under more realistic beach configurations.

5. References

BATTJES J.A. (1974). *Surf similarity*. Proceedings 14th International Conference on Coastal Engineering, pp 466–480. https://doi.org/10.9753/icce.v14.26

CASTELLE B., COCO G. (2012). *The morphodynamics of rip channels on embayed beaches*, Continental Shelf Research, Vol. 43, pp 10-23. https://doi.org/10.1016/j.csr.2012.04.010

DEAN R.G. (1991). *Equilibrium beach profiles: characteristics and applications*. Journal of Coastal Research, Vol.7, pp 53-84.

FELLOWES T.E., VILA-CONCEJO A., GALLOP S.K. (2019). *Morphometric classification of swell-dominated embayed beaches*, Marine Geology, Vol. 411, pp 78-87. https://doi.org/10.1016/j.margeo.2019.02.004

GODA Y., TAKAYAMA T., SUZUKI Y. (1978). *Diffraction diagrams for directional random waves*. 16th International Conference on Coastal Engineering. https://doi.org/10.1061/9780872621909.037

HOLMAN R. (1986). *Extreme value statistics for wave run-up on a natural beach*. Coastal Engineering. Vol. 9(6), pp 527-544. https://doi.org/10.1016/0378-3839(86)90002-5

HOLMAN R.A., SALLENGER A.H. (1986). *Longshore variability of wave run-up on natural beaches*. 19th International Conference on Coastal Engineering, pp 1896-1912. https://doi.org/10.1061/9780872624382.128

HORRILLO J., GRILLI S.T., NICOLSKY D., ROEBER V., ZHANG J. (2014). *Performance benchmarking tsunami models for NTHMP's Inundation mapping activities*. Pure Appl. Geophys. Vol. 172, pp 869–884. https://doi.org/10.1007/s00024-014-0891-y

LOUREIRO C., FERREIRA Ó., COOPER J.A.G. (2012). *Geologically constrained morphological variability and boundary effects on embayed beaches*. Mar. Geol., Vol. 329, pp 1–15. https://doi.org/10.1016/j.margeo.2012.09.010

LYNETT P.J., ROEBER V., HEITMANN T.W., CHEUNG K.F., DAVID C.G. BRIKER J.D. *et al*. (2017). *Inter-model analysis of tsunami-induced coastal currents*. Ocean Modelling, Vol. 114, pp 14-32. https://doi.org/10.1016/j.ocemod.2017.04.003

NWOGU O. (1993). *Alternative form of Boussinesq equations for nearshore wave propagation*. Journal of Waterway, Port, Coastal and Ocean Engineering, Vol. 119. https://doi.org/10.1061/(ASCE)0733-950X(1993)119:6(618)

POWER H., ATKINSON A., HAMMOND T., BALDOCK T. (2013). *Accuracy of wave runup formula on contrasting southeast Australian beaches*. Coasts and Ports 2013, 21st Australasian Coastal and Ocean Eng. Conf. & 14th Australasian Port and Harbor Conf., 6 p.

ROEBER V., CHEUNG K.F., KOBAYASHI M.H. (2010). *Shock-capturing Boussinesq-type model for nearshore wave processes.* Coastal Engineering, Vol. 57(4), pp 407–423. https://doi.org/10.1016/j.coastaleng.2009.11.007

ROEBER V., CHEUNG K.F. (2012a). *Boussinesq-type model for energetic breaking waves in fringing reef environments*. Coastal Engineering. Vol. 70, pp 1-20. https://doi.org/10.1016/j.coastaleng.2012.06.001

ROEBER V., CHEUNG K.F. (2012b). *BOSZ - Boussinesq Ocean and Surf Zone model.* NOAA, Special Report, Proceedings and Results of the 2011 NTHMP Model Benchmarking Workshop, Galveston, Texas, 437 p.

RUESSINK B.G., KLEINHANS M.G., VAN DEN BEUKEL P.G.L. (1998). *Observations of swash under highly dissipative conditions*. J. Geophys. Res., Vol. 103, pp 3111–3118. https://doi.org/10.1029/97JC02791

RUGGIERO P., HOLMAN R.A., BEACH R.A. (2004). *Wave run-up on a high-energy dissipative beach.* J. Geophys. Res. 109, C06025. https://doi.org/10.1029/2003JC002160

SHEREMET A., KAIHATU J.M., SU S.-F., SMITH E.R., SMITH J.M. (2011). *Modeling of nonlinear wave propagation over fringing reef*. Coastal Engineering, Vol. 58, pp 1125-1137. https://doi.org/10.1016/j.coastaleng.2011.06.007

STOCKDON H., HOLMAN R., HOWD P., SALLENGER A. (2006). *Empirical parameterization of setup, swash, and runup*. Coastal Engineering. Vol. 53(7), pp 573-588. https://doi.org/10.1016/j.coastaleng.2005.12.005

STOCKDON H., THOMPSON D., PLANT N., LONG J. (2014). *Evaluation of wave runup predictions from numerical and parametric models*. Coastal Engineering. Vol. 92, pp 1-11. https://doi.org/10.1016/j.coastaleng.2014.06.004

Appendix D

PhD outcomes

Peer-reviewed papers

- Pinault, J., Morichon, D. and Roeber, V. (2020). "Estimation of Irregular Wave Runup on Intermediate and Reflective Beaches Using a Phase-Resolving Numerical Model" *Journal of Marine Science and Engineering* 8, no. 12: 993. https://doi.org/10.3390/jmse8120993

Conference proceedings

- Pinault, J., Morichon, D., Abadie, S. and Roeber, V. (2020). Numerical study of the longshore variability in run-up along an idealized embayed beach. In *XVI èmes Journées Nationales Génie Côtier – Génie Civil*, pages 139–148. https://doi.org/10.5150/jngcgc.2020.016.

- Roeber, V., Nestler, J. D., Pinault, J., Azouri, A. and Bellafont, F. (2020). MULTI-SCALE INFRA-GRAVITY WAVE DYNAMICS - THE FRENCH BASQUE COAST. *Coastal Engineering Proceedings*. https://doi.org/10.9753/icce.v36v.waves.46

- Roeber, Volker; Pinault, Jonas; Morichon, Denis; Abadie, Stephane; Azouri, Assaf; Guiles, Martin; Luther, Doug; Delpey, Matthias; Danglade, Nikola (2019): Improving Wave Run-up Forecasts – Benefits from Phase-resolving Models. In *Coastal Structures 2019*. https://doi.org/10.18451/978-3-939230-64-9_075.

Conference presentation

- Pinault, J.; Morichon, D.; Roeber, V. (2020, November 4–5). LONGSHORE VARIABILITY OF WAVE RUN-UP ALONG AN EMBAYED BEACH DURING ENERGETIC EVENTS [Conference presentation]. UHINAK : Cross border conference on climate and coastal change, Irun, Spain.

- Pinault, J.; Roeber, V.; Lastiri, X.; Delpey, M.; Morichon, D.; Abadie, S. (2021, June 16-18). Spatial and temporal wave variability at the Basque Coast : From wave energy

at regional scales to runup of individual waves [Conference presentation]. B'Waves21, Bordeaux, France.

- Pinault, J.; Morichon, D.; Roeber, V.; Delpey, M. (2021, July 1-2). Numerical study of wave transformations and runup variability along an embayed beach - Grande Plage of Biarritz, France [Conference presentation]. Coastal Dynamics 21, Delft, The Netherlands.

Teaching

- Introduction to water wave mechanics (2019-2020-2021). *Computations in Coastal and Civil Engineering (CCCE)*, Université de Pau & des Pays de l'Adour.
- Risques de submersion et ouvrages de protection côtière (2020). *Qualité des milieux aquatiques (QUAMA)*, Université de Pau & des Pays de l'Adour.